IMPERIAL

Developing a long-term microfluidic system to study the mesoscopic dynamics of Piezo1 activity.

See Swee Tang

January 2024

Supervisor: Dr Periklis Pantazis

Department of Bioengineering

Imperial College London

Submitted in part fulfilment of the requirements for the degree of

Doctor of Philosophy in Bioengineering Research at Imperial College London

Abstract

The cellular microenvironment (or cell niche) is a complex and specialised environment, consisting of physical, chemical, and biological factors that collectively influence the cells residing within. Interactions within this dynamic microenvironment play a critical role in regulating and maintaining cellular activities and function. Within the cellular microenvironment, resident cells constantly experience various mechanical force stimuli, which previous *in vitro* studies cannot fully recapitulate. Hence, the inclusion of mechanical forces (for example fluid shear stress) in the cell culturing system would yield a more physiologically relevant investigation of cellular behaviour.

Cells commonly express mechanosensitive proteins and receptors to sense and transduce external mechanical stimuli to respond appropriately. A widely expressed mechanosensitive ion channel, Piezo1, has been shown to play an important role in cellular mechanotransduction. Our lab previously generated a genetically-encoded Piezo1 sensor (GenEPi), which allows precise detection of Piezo1-specific activities. To investigate the activities of Piezo1 in near-physiological conditions, I developed a microfluidic-based system to study the dynamics of Piezo1 in mammalian cells using our GenEPi sensor.

Using my developed system, I discovered that Piezo1 clusters exhibit more directed diffusive motion after fluid shear stress. By studying the dynamics of the protein, I revealed differential Piezo1 responses across fluid shear stress magnitudes. I also reported a mechanical threshold to HEK-Piezo1 activation during constant fluid shear stress. Through the GenEPi dynamic responses, I observed that cellular Piezo1 activations are synchronised to mechanical shear triggers but become increasingly asynchronous under sustained shear stress.

Crucially, the characteristics of Piezo1's dynamic within cells reported here will significantly advance our understanding of the interplay between mechanical forces and cellular behaviour within the cellular microenvironment. This system can also be a model for others to adopt in investigating the dynamics of other mechanosensitive proteins expressed in the cells.

Statement of Originality

I hereby declare that the work presented in this thesis my own, except otherwise acknowledged. All contributions and assistance received have been acknowledged in the text. This work was performed in the Department of Bioengineering at Imperial College London, under the supervision of Dr Periklis (Laki) Pantazis.

All published and unpublished materials used in the thesis have been given full acknowledgement. This work has not been previously submitted, in whole or in part, to any other academic institution for a degree, diploma, or any other qualification.

See Swee Tang
January 2024

Copyright Declaration

The copyright of this thesis rests with the author, See Swee Tang. Unless otherwise indicated, its contents are licensed under a Creative Commons Attribution-Non Commercial 4.0 International Licence (CC BY-NC).

Under this licence, you may copy and redistribute the material in any medium or format. You may also create and distribute modified versions of the work. This is on the condition that: you credit the author and do not use it, or any derivative works, for a commercial purpose.

When reusing or sharing this work, ensure you make the licence terms clear to others by naming the licence and linking to the licence text. Where a work has been adapted, you should indicate that the work has been changed and describe those changes.

Please seek permission from the copyright holder for uses of this work that are not included in this licence or permitted under UK Copyright Law.

Acknowledgements

"Accept the things to which fate binds you,
And love the people with whom fate brings you together,
But do so with all your heart."
– Marcus Aurelius

There is an ancient African proverb saying, "It takes a village to raise a child." To a small extent, finishing this PhD journey has been like raising an intellectual child – it took a whole village. To everyone I have met along this journey: Thank you for being my village.

I would first like to express my gratitude to my supervisor and mentor, Dr. Periklis (Laki) Pantazis. Thank you for creating an environment that shaped and supported my scientific ideas. My experience in the Pantazis lab has not only been fruitful in the technical and scientific aspects, but also in the soft skills that would allow me to further my research career.

I would also like to thank my PhD viva committees, Dr. Victoria Salem and Dr. Nordine Helassa. Thank you for taking the time to be my chairing, and for challenging me during my defense session. Your invaluable inputs, and critical perspectives had led to a fruitful discussion and my completion of this thesis.

Past and present members of the Pantazis group, it has been a delight to be able to work alongside and learn from many of you.

Konstantinos Kalyviotis, Edagül Uluçay, Julian Boecker, Aysen Unsal, Fabian Kohlbacher, Harry Hsu, Kim Donghyeon (Alex), Fauzi Alhakim, Papavee Phongsopa (Prim), Vishnu Seshan, Athina Apostolelli, Andrew Kloska, Pomone Bollier.

I would especially like to thank:

- Konstantinos – In all the times we worked together to midnight, you have been a great company and support during my PhD. Please, never stop smiling.
- Edagül – For all the kindle-ling conservations we have had. You have been a great listener in times when I need one.
- Fabian – Thank you for bringing the fun and light to the over-30s group!
- Prim – Your curiosity for science and hardworking attitude kept me on my toes. I hope you're doing Abba-ly well.

I am also extremely grateful for the various past and present members of the bunker lab (B001) – Moore, Overby and vBS labs.

Simon Tupin, Jacques Betram, Ester Reina-Torres, Jennifer Frattolin, Foivos Chatzidimitriou, Elizabeth (Lizzy) Wheeler, Eva Zeringa, Beatrice (Bea) Bezdadea, Larry O'Connell, Alice Barocco, Saverio Charalambous, Loïck Behr, Kinga Suba.

You have adopted me as an honorary member of your labs and the kindness you have shown me made my PhD experience a better one. From the bottom of my heart, thank you for making each day so much easier for me – You have been the rays of sunlight in the windowless lab I was allowed to share. To Simon, Jacques, and Ester, thank you for being my "over-30s" pack, I guess we are friends now!

A special thank you to my work-wife, my fellow sister of Singapore, and my dearest friend – Adele Lam Jing Ying. The hats you wear throughout our friendship have been the most invaluable gift of this PhD experience. I still look back fondly at the numerous long days we shared in the tissue culture room.

Throughout these four years, I have also been blessed with many friendships which started off with a nod along the corridor or a "hi" in the TC room. From then, we have had multiple coffee chats, and some after-work drinks. I am sure there will be more drinks and coffee to come.

- Vermont lab: Emmanuelle Steib and Christina Vagena-Pantoula

- Au lab: Julian Ashby, Julia Perea Paizal, Angelos Vrynas, Neelima KC, Shusei Kawara.
- Green lab: Estelle Cuttaz, Martina Genta, Sophia Peressotti, Roberto Portillo Lara, Christopher Chapman.
- Higgins lab: Summik Limbu and Lee Jia Jun (JJ).
- Crew of B127 office: Magdalene Ho, Konstantinos Tsikonofilos (Kosta), Namphung Peimyoo, Grace Lim, John Goodwin.
- Department of Bioengineering Technician Team: Miguel Hermida Ayala, Sharad Patel, Elina Zalite, Marta Da Silva Moreira, Ji Young Yoon, Joel Eustaquio, Florent Seichepine, Olivier Dubois, Shahrzad Forouzanfar, Marta Garcia Bellmunt, Nana A. Asamoah-Danso, Hamid Samivand, Greg Casson, Morgan Edmonds, Katie Giles.

To my family and loved ones, in blood and by extension, this journey would not have happened without each one of you. The Tang-Lie family back in Singapore, thank you for providing for me in my young days and raising me to be the man I am today. Thank you for letting me venture out of my comfort bubble and away from home. To the Selous family – Gerald, Lina, Grace, Joy, Andrew, Sarah, and the little Bulls – I feel privileged to be welcomed into the family. Your love and kindness have been a source of motivation for me during these four years. And to the Hoffmuller unit – Niki, Pia and little Otto – thank you for always being more excited in my progress than I have been with myself.

And finally, Edmund Selous, my precious, thank you for allowing me to put our lives on hold while I went on this crazy doctorate journey. I am forever grateful for your patience, kindness, and the quiet sacrifices you have made for our lives. For all the times that I am lost and weary, thank you for building me up and sending me out into the world as the strongest and “bestest” version of me. Thank you for being a rock and my home.

Contents

Abstract **2**

Statement of Originality **4**

Copyright Declaration **5**

Acknowledgements **6**

Contents **9**

List of Figures **14**

List of Tables **18**

List of Abbreviations **19**

1. Introduction **22**

1.1. The cellular microenvironment. 23

1.1.1. Components of cellular microenvironment. 23

1.1.2. Importance of cell microenvironment in biomedical research. 25

1.1.3. *in vitro* static models and their insufficiencies to inform cell niche. 27

1.1.4. Advances in creating near-physiological experimental conditions. 28

1.2. The role of mechanical forces within the cellular microenvironment. 30

1.2.1. Mechanosensation and mechanotransduction within cells. 31

1.2.2. Mechanobiology of the cell membrane. 32

1.2.3. Means and methods of studying cellular mechanics. 35

1.3. Mechanosensitive ion channels and the Piezo family. 36

1.3.1. Piezo1 – Properties and structure. 37

1.3.2. Piezo1's mode of action. 40

1.3.3. Piezo1 in development, homeostasis and pathophysiology. 41

1.3.4. Methodologies used to study Piezo1 function. 45

1.4. Genetically-encoded calcium indicators and GenEPi. 48

1.4.1. Calcium signalling and calcium microdomains. 48

1.4.2. Genetically encoded calcium indicators (GECIs). 50

1.4.3. GenEPi, a Piezo1-specific optical readout. 52

1.5. Aims of the thesis. 55

2. Designing and generating an inducible, yet stable expression of GenEPi within mammalian cells 57

2.1. Generating an inducible, yet stable GenEPi expression construct. 57

2.2. Materials & Methods. 58

2.3. Creation of an inducible Piezo1 sensor – XLGenEPi. 66

2.3.1. Selection of an appropriate inducible system. 66

2.3.2. Inducible Piezo1-reporter engineering. 69

2.3.3. Generating the piggyBase construct for XLGenEPi co-transfection in mammalian cells. 71

2.4. *in vitro* characterisation of XLGenEPi. 72

2.4.1. Transfected HEK 293T cells remain viable after co-transfection of XLGenEPi and CMV-pBase constructs. 72

2.4.2. Establishing a stable, GenEPi-expressing cellular clone via the XLGenEPi plasmid. 74

2.4.3. XLGenEPi-HEK cells express GenEPi-sensor under Dox-inducible treatment. 79

2.4.4. GenEPi sensor responds reliably to Piezo1 chemical perturbations. 83

2.5. Discussion. 85

2.5.1. The "XLone-" cloning & selection strategy. 86

2.5.2. The difficulty of XLGenEPi strategy with primary cell-line models. 89

2.5.3. *in vitro* GenEPi-signal characterisation on the XLGenEPi-HEK clones. 91

2.5.4. XLGenEPi, an inducible Piezo1-specific reporter for mammalian cells. 94

2.6. Statement of contribution. 95

3. Developing a microfluidic-based system for the imaging of dynamics of Piezo1 96

3.1. Importance of imaging the dynamics of Piezo1 and other mechanosensitive proteins. 96

3.1.1. Time-lapse, live-imaging to capture mechanosensitive dynamics. 97

3.1.2. Models of applying mechanical stimulation during live-imaging. 97

3.2. Materials & Methods. 99

3.3. Devising a microfluidic platform adapted for precision optical imaging. 106

3.2.1. Microfluidics models. 106

3.2.2. Criteria of a microfluidic-based system for imaging GenEPi dynamics. 107

3.4. Microfluidic Culturing Platform Design. 108

3.4.1. Microchannel device design. 108

3.4.2. Microfluidic flow system setup. 110

3.4.3. Microfluidic flow profile. 111

3.4.4. Establishing confluence of XLGenEPi clones within the microfluidic system. 114

3.5. A time-lapse, live-imaging system fit for mechanosensitive proteins dynamics. 117

3.6. Discussion. 119

3.6.1. The versatility of our developed system. 123

3.6.2. Mechanical stretch-based system to study mechanosensitive proteins and cell processes. 124

3.7. Statement of Contribution. 125

4. Piezo1 dynamics dissected through GenEPi time-lapse, live-imaging system 126

4.1. A microfluidic-based, live-imaging system for studying Piezo1 dynamics. 126

4.2. Fluid shear stress on HEK 293 cells. 127

4.3. Materials & Methods. 128

4.4. Functional characterisation of Piezo1 dynamics. 133

4.4.1. GenEPi fluorescence intensity increases after shear induction. 133

4.4.2. Cellular Piezo1 exhibits diffusive dynamics following shear stress induction. 135

4.4.3. GenEPi responses are modulated dependent on the shear magnitudes. 138

4.4.4. GenEPi responses are graded over increasing shear stress of 1 – 5 dynes/cm^2 stimulation. 140

4.4.5. Shear stress stimulated XLGenEPi-HEK cells display a response threshold at 5 dynes/cm^2. 142

4.4.6. HEK-Piezo1 mechanical threshold triggers nuclei shrinkage within cells. 144

4.4.7. Repeated mechanical stimulation at lower shear stress eventually triggers the HEK-Piezo1 mechanical threshold effect in GenEPi response. 145

4.4.8. Temporary downregulation of Piezo1 expression following sustained shear stress exposure in HUVECs. 149

4.4.9. GenEPi response is synchronised to mechanical shear triggers that becomes increasingly asynchronous under sustained shear stress. 151

4.5. Discussion. 153

4.5.1. The use of GenEPi sensor reveals unique Piezo1 functional dynamics in HEK cells upon exposure to different shear stress magnitudes. 153

4.5.2. Signal depression of GenEPi during persistent shear stress stimulation. 155

4.5.3. Piezo1 downregulation from cell membrane as cellular mechanoprotective response. 157

4.6. Statement of Contribution. 158

5. Discussion 159

5.1. GenEPi, an optical tool for dissecting physiological Piezo1 dynamics. 160

5.2. Limitations to our "XL-", microfluidic-based system. 164

5.2.1. Limitations to the "XL"-approach in GenEPi construct. 164

5.2.2. Limitations to a GCaMP-based approach. 165

5.2.3. The HEK 293 cell model. 166

5.2.4. Limitations in our fluidic handling method in the system. 168

5.2.5. The shortfalls of a confocal-based system. 169

5.3. Ongoing work and future outlook. 170

5.3.1. Red-GenEPi. 170

5.3.2. Endogenous Piezo1/GenEPi-tagging. 174

5.3.3. Compound screening and drug discovery pipeline. 174

5.3.4. Understanding Piezo1 activity modulation. 175

5.4. Concluding remarks. 176

6. Bibliography 177

Appendix 198

List of Figures

Chapter 1:

Figure 1.1. Cellular microenvironment and the main components. 25

Figure 1.2. Global overview of physiological phenomenon induced by microenvironment-associated mechanical cues. 27

Figure 1.3. The extracellular mechanical environment which cells experienced from their microenvironment. 31

Figure 1.4. Mechanical forces that induce cell membrane deformation. 34

Figure 1.5. Cryo-EM revealed that mouse Piezo1 forms a homotrimer structure. 39

Figure 1.6. Proposed gating mechanisms of mechanosensitive ion channels (MSCs). 41

Figure 1.7. Piezo1-mediated mechanotransduction pathways. 44

Figure 1.8. Biomechanics methodologies commonly used to study Piezo1 activity. 47

Figure 1.9. The Piezo1 calcium microdomain hypothesis. 49

Figure 1.10. Two main classes of genetically-encoded calcium indicators (GECIs). 51

Figure 1.11. Piezo1-specific optical reporter, GenEPi. 54

Chapter 2:

Figure 2.1. XLone-EGFP construct gene map. 69

Figure 2.2. Molecular cloning strategy for XLGenEPi. 70

Figure 2.3. XLGenEPi construct integrity and quality screening. 71

Figure 2.4. Molecular cloning of CMV-pBase construct. 72

Figure 2.5. XLone-GFP and XLGenEPi co-transfection efficiency evaluation. 74

Figure 2.6. Timeline for blasticidin-resistance selection of XLGenEPi-transfected cells. 76

Figure 2.7. Optimal concentration of blasticidin (BSD) treatment for XLGenEPi-positive cell selection. 77

Figure 2.8. Gel electrophoresis confirmed successful genome integration of XLGenEPi construct into selected HEK 293 clones. 79

Figure 2.9. GenEPi is only expressed in XLGenEPi-positive HEK clones under the influence of Doxycycline (Dox). 80

Figure 2.10. Live GenEPi-signal tracking revealed re-inducible expression in HEK clones lasting three days. 82

Figure 2.11. XLGenEPi-HEK clones expressing GenEPi-sensor respond to Piezo1-specific agonist, Yoda1. 84

Figure 2.12. *in vitro* characterization of GenEPi-sensor shows that the reporter has functional specificity without affecting Piezo1 channels inherent features. 85

Figure 2.13. Fluorescence intensity differences between XLone-GFP and XLGenEPi. 88

Figure 2.14. XLGenEPi co-transfection and selection efficiency fare less in primary cell-lines, like HUVECs. 90

Figure 2.15. GenEPi signal exhibits broad emission spectrum. 94

Chapter 3:

Figure 3.1. Overview of our *in vitro* microchannel model developed for investigating Piezo1 dynamics in HEK cells. 109

Figure 3.2. Schematics of different magnification objectives and their relative working distances on an inverted microscope set-up. 110

Figure 3.3. Microfluidic flow circuit to establish flow delivery within our microchannel device. 111

Figure 3.4. Characterisation of flow profile within the microchannel flow circuit. 113

Figure 3.5. Fibronectin-coating is favourable for culturing XLGenEPi-HEK clones within the microchannels. 115

Figure 3.6. Overnight perfusion of culture media ensured proper cellularisation of microchannels. 117

Figure 3.7. Experimental workflow for capturing and analysing GenEPi (Piezo1) dynamics. 118

Figure 3.8. An overview of the protocol for setting up our microfluidic-based system. 120–122

Figure 3.9. Culturing timeline for cellularising the rectangular microchannel with HUVECs. 123

Chapter 4:

Figure 4.1. GenEPi fluorescence intensity increases after shear stress induction on XLGenEPi-HEK clones. 134

Figure 4.2. GenEPi (Piezo1) clusters displayed less confined diffusive motion within cell membrane during shear stress stimulation. 137

Figure 4.3. GenEPi (Piezo1) response-time and -pattern differed across shear stress magnitudes. 139

Figure 4.4. GenEPi (Piezo1) responses are graded over increasing shear stress level. 141

Figure 4.5. GenEPi (Piezo1) response peak is accompanied by signal depression after shear stress threshold. 143

Figure 4.6. Nuclei shrinkage observed after 5 and 10 dynes/cm^2 stimulatory cycle in XLGenEPi-HEK cells. 145

Figure 4.7. GenEPi (Piezo1) response depresses over time during sustained shear stimulation at lower magnitudes. 146

Figure 4.8. GenEPi (Piezo1) declining response exhibits two different slope depressive trends. 148

Figure 4.9. Endothelial-Piezo1 expression temporarily downregulated after 24 hours of constant 10 dynes/cm^2 shear stress. 150

Figure 4.10. GenEPi dynamics are synchronised at the onset of mechanical stimulation, but becomes increasingly asynchronised under sustained stimulation. 152

Chapter 5:

Figure 5.1. GenEPi (Piezo1) activation occurs in a graded and progressive manner. 162

Figure 5.2. Engineering the red version of GenEPi. 172

Figure 5.3. Red-GenEPi (or RGenEPi) is successfully expressed in HUVECs after transient transfection. 173

List of Tables

Table 3.1. Common methods of fluid administering in bio-microfluidic models. 107

Table 3.2. Microscope objectives specification of Leica SP8 used in our experiments. 110

Table 3.3. Averages of profilometry measurements across the length of the channel mould. 112

Table 4.1. List of shear stress magnitude ranges previous used on HEK 293 cells in literatures. 127

Table. 4.2. Definition of the four basic motion types. 135

Table 5.1. List of potential red-GECIs for generating red-GenEPi. 171

Table A1. Primer sequence for XLGenEPi sequencing. 198

Table A2. Primer pair sequence for four key elements of XLGenEPi construct. 199

Table A3. Primer pair sequence for the PCR cloning of CMV-pBase constuct. 199

List of Abbreviations

2D	Two-dimensional
3D	Three-dimensional
AFM	Atomic force microscopy
ATP	adenosine-triphosphate
bp	base pair
BSD	blasticidin
CMV	cytomegalovirus immediate early enhancer
cpFP	circularly-permutated fluorescent protein
DAPI	diamino-2-phenylindole
DHS	dehydrated hereditary stomacytosis
DMSO	dimethyl sulfoxide
DNA	deoxyribonucleic acid
Dox	doxycycline
ECM	extracellular matrix
EMT	epithelial-mesenchymal transition
ER	endoplasmic reticulum
FACS	fluorescence-activated cell sorting
FAK	focal adhesion kinases
FP	fluorescent protein
FRET	Förster/fluorescence resonance energy transfer
GCaMP	genetically-encoded green calcium indicator, based on GFP, Calmodulin and myosin light chain kinase M13 peptide

GECI	genetically-encoded calcium indicator
(e)GFP	(enhanced) green fluorescent protein
GLD	general lymphatic dysplasia
GSGG	Glycine-Serine-Glycine-Glycine peptide linker
GsMTx-4	*Grammostola spatulate* mechanotoxin #4
H2B	Histone H2B
HEK 293T	Human Embryonic Kidney 293T cells
HeLa	Cervical cancer cell line isolated from Henrietta Lacks HFF Human foreskin fibroblasts
HUVEC	Human Umbilical Vein Endothelial cells
IP3	inositol 1,4,5- trisphosphate
K2P	Two-pore-domain potassium channel
mRNA	messenger RNA
MSC	mechanosensitive ion channel
ORF	open reading frame
PCR	polymerase chain reaction
PDMS	polydimethyl siloxane
PECAM-1	platelet/endothelial cell adhesion molecule-1
R-GECO	genetically-encoded red calcium indicator, based on mApple
RBC	red blood cell
RCaMP	genetically-encoded red calcium indicator, based on mRuby
RFP	red fluorescent protein
RNA	ribonucleic acid
RR	ruthenium red
rtTA	reverse tetracycline transactivator
SAC	stretch-activated channels

siRNA	small interfering RNA
Taz	transcriptional co-activator with PDZ binding motif
TIRFM	total internal reflection fluorescence microscopy
TRE	tetracycline-responsive element
TREK	TWIK-related potassium channel
WGA	wheat germ agglutinin, a plant lectin that binds to the glycoproteins or glycolipids present in the plasma membrane
WT	wild type, the phenotype found in nature, generated by the unmodified version of a gene
Yap	Yes-associated protein, transcriptional co-activator

1. Introduction

“天下难事，必作于易，天下大事，必作于细。
千里之行，始于足下。” **– 老子**

“Do the difficult things while they are easy, and do the great things while they are small.
A journey of a thousand miles must begin with a single step.” ***– Lao Tzu***

Pantazis lab previously introduced the first Piezo1-specific sensor, termed GenEPi. The GenEPi reporter is a genetically-encoded sensor carefully designed and engineered to detect Piezo1-specific activities across different biological scales[1]. With this sensor, we can further our understanding of how Piezo1 functions under near-physiological conditions. Hence, I developed this microfluidic-based system to capture in real-time Piezo1 activity dynamics under mechanical stimulation. The product of this workflow (a microfluidic-based, inducible cell model) will help advance our understanding of Piezo1’s function within the cellular microenvironment.

My PhD research is divided into three main themes, and this introductory chapter presents an overview of those themes. First, the chapter explores the cellular microenvironment and the importance of creating a near-physiological model to study intricate cellular phenomena such as Piezo1 functional dynamics. Subsequently, the chapter summarises the role of mechanical forces and how cells sense these forces within their microenvironment. This part is followed by an in-depth review of the Piezo1 research and its importance in the physiological context. Finally, I end this introductory chapter with the aims of my PhD thesis.

1.1. The cellular microenvironment

The cellular microenvironment (or cell niche) is the immediate surrounding and the specialised environment in which a cell resides[2–4]. The cell microenvironment provides signals and conditions distinct and unique to the different cell types. It consists of physical, chemical and biological factors that collectively influence the cell's behaviour, fate and function. Cell niches are dynamic and constantly interact with the present cells, playing a pivotal role in regulating cellular activities, including self-renewal, differentiation and maintenance[5–7]. Recent research on the cellular microenvironment has found that imbalance within the niche can be associated with certain pathophysiologies[8,9]. Therefore, understanding the intricacies of this environment is crucial for studying cellular processes in health and disease.

1.1.1. Components of cellular microenvironment

Cell niches are often unique and specific to the cell- and tissue- types[10,11]. The uniqueness of one lies in its ability to tailor their properties to support the specific needs and functions of the different cell types. While the individual factors present within the cellular microenvironment are specialised to specific cell types, the overall categories of components are similar. Here, I have listed some of the most common, yet crucial contributors to the cellular microenvironment (**Figure 1.1**).

(I) Extracellular Matrix (ECM)

The extracellular matrix (ECM) is a complex network of proteins and carbohydrates that forms a three-dimensional (3D) scaffold surrounding the cells or tissue[12,13] (**Figure 1.1(ii)**). The ECM's primary role is to provide structural support and signalling cues to the cells within the niche. In recent years, more research has concluded that ECM plays a vital role in various physiological and pathological processes. For example, ECM proteins and structures are important in determining cell migration and cell-state transition events like epithelial-mesenchymal transitions or EMT during embryogenesis[14,15]. Some of the most common components include collagen, elastin, fibronectin, laminin, proteoglycans, glycoproteins and many more[4].

(II) Chemical Signalling

Cell niches often contain signalling molecules, including growth factors, cytokines, and hormones, to trigger signalling pathways and regulate cell processes that are important for maintaining tissue homeostasis and orchestrating development[4,14,16]. These signalling events can be for cellular self-renewal and differentiation or signalling in response to certain stimuli and pathological cues. Most importantly, chemical signalling enables cells within the microenvironment to communicate with each other and coordinate activities[16].

(III) Physical Properties

The physical properties of the microenvironment, such as stiffness, topography, and mechanical forces, can influence cellular behaviour and function[4] (**Figure 1.1(iii)**). These properties can impact processes like cell adhesion, migration, proliferation, differentiation and even overall tissue development[17,18]. For example, the exposure of mechanical forces in the cell niche is crucial to the behaviour and responses of cells, especially the mechanosensitive cells. For example, the manipulation of cell culturing stiffness is crucial in guiding neuronal differentiation from neural stem cells[19,20]. Furthermore, culturing vascular and endothelial cells under consistent laminar flow was shown to ensure proper cell adhesion, alignment, and responses to shear changes *in vitro* and *ex vivo* set-ups[21,22].

(IV) Metabolic Requirements

Different cell types have different metabolic requirements, therefore, it is not surprising that the cell niches adapt to provide the required support for the resident cells. The present cellular niches not only provide the required nutrient factors to the cells, but also provide an environment where metabolites are exchanged and waste products are removed to maintain cellular health[4].

In summary, the add-ups of all these contributing factors create a dynamic and intricate environment to sustain cellular events, which maintain tissue homeostasis and functioning.

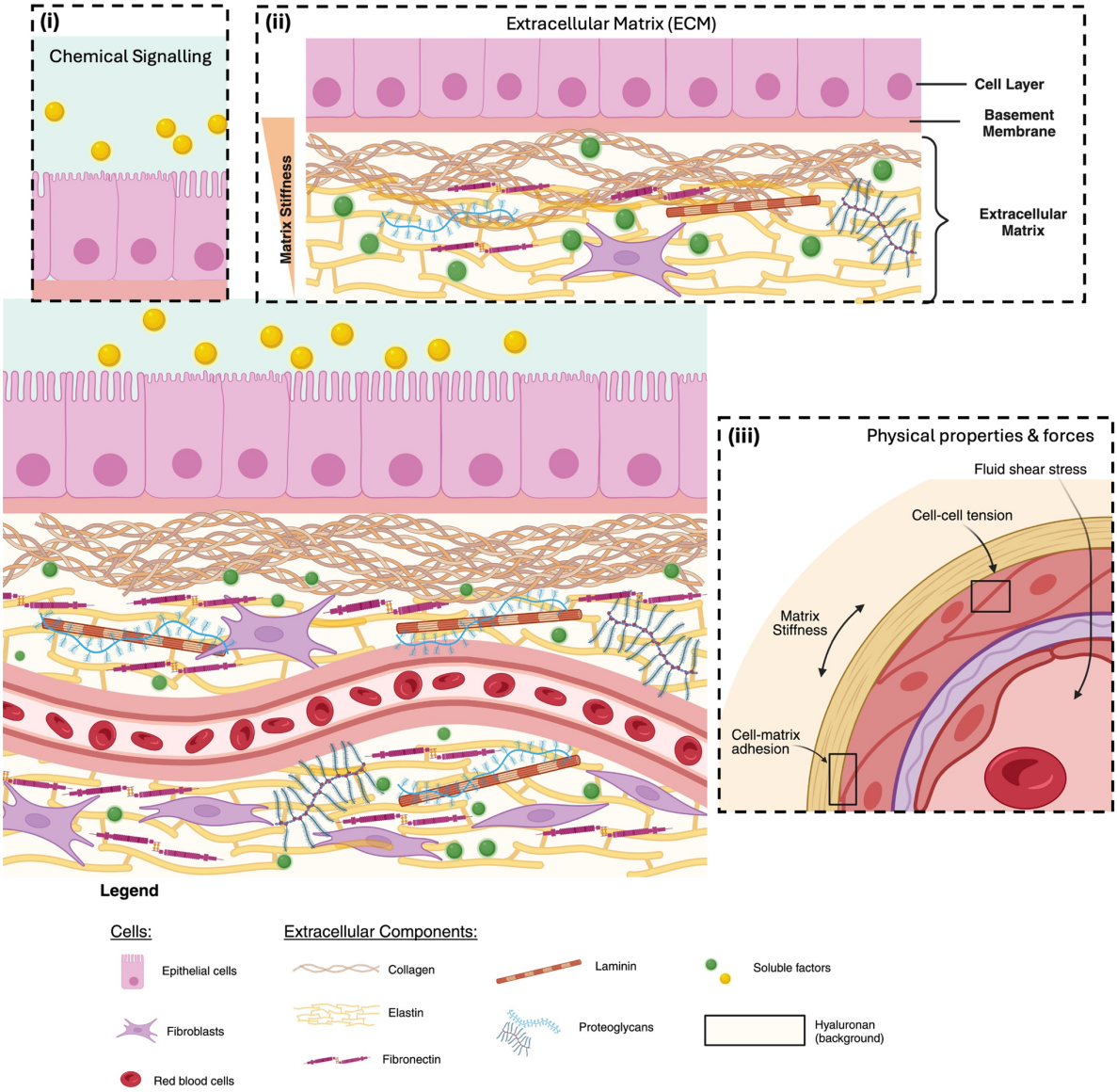


Figure 1.1. Cellular microenvironment and the main components. The cellular microenvironment is a specialised environment consisting of physical, chemical, and biological factors that support the cells residing within. Key components of the cell microenvironment include neighbouring cells, soluble factors **(insert i)**, the extracellular matrix (ECM) **(insert ii)**, and biophysical fields (e.g., shear stress and other physical forces) **(insert iii)**. Schematics created using BioRender.com.

1.1.2. Importance of cell microenvironment in biomedical research

Understanding the cellular microenvironment is not only important to further our knowledge about cell biology, but it is of paramount importance in other applications of biology and medicine. As it profoundly influences cell behaviour and tissue homeostasis, dissecting and possibly replicating cell niches in biomedical research

better inform us about the physiological conditions and disease pathophysiology (**Figure 1.2**). In cancer research, the tumour microenvironment is often emphasised during the progression of cancer. Interactions between cancer cells and the surrounding microenvironment can promote invasion, angiogenesis and immune evasion[23,24]. Consequently, targeting the tumour microenvironment is a promising approach to cancer treatment. For example, the tumour microenvironment, specifically the ECM mechanical stiffness has been implicated in regulating the epithelial-to-mesenchymal transition (EMT) process during primary epithelial tumour metastatsis[25]. Furthermore, the tumour microenvironment stiffness in breast tumours has been associated with a poor survival rate[26,27]. The effective use of pharmacological inhibition of focal adhesion kinases (FAK) in a recent phase I clinical trial has shown significant stabilisation in patients who are unresponsive to existing cancer interventions[28,29]. Thus, modulating the tumour microenvironment is a potential therapeutic approach to controlling cancer progression. Knowledge gained in establishing the interactions within cell niches can potentially be harnessed for strategies in regenerative medicine and tissue engineering applications. Furthermore, studying the cellular microenvironment can help us identify potent factors that may enhance or hinder drug efficacy. For instance, the interaction of tumour cells with other stromal cells within the microenvironment, including endothelial cells and fibroblasts, can lead to the formation of desmoplastic tumour stroma. This tumour stroma becomes a physical barrier, which influences drug delivery and efficacy[30]. Therefore, advancing our knowledge of the cellular microenvironment, in this case, the tumour microenvironment, will guide the development of more effective treatments for pathological conditions[31]. Ultimately, understanding the cellular microenvironment is key to a wide range of fields, from basic biology to clinical applications, with significant implications for health and disease.

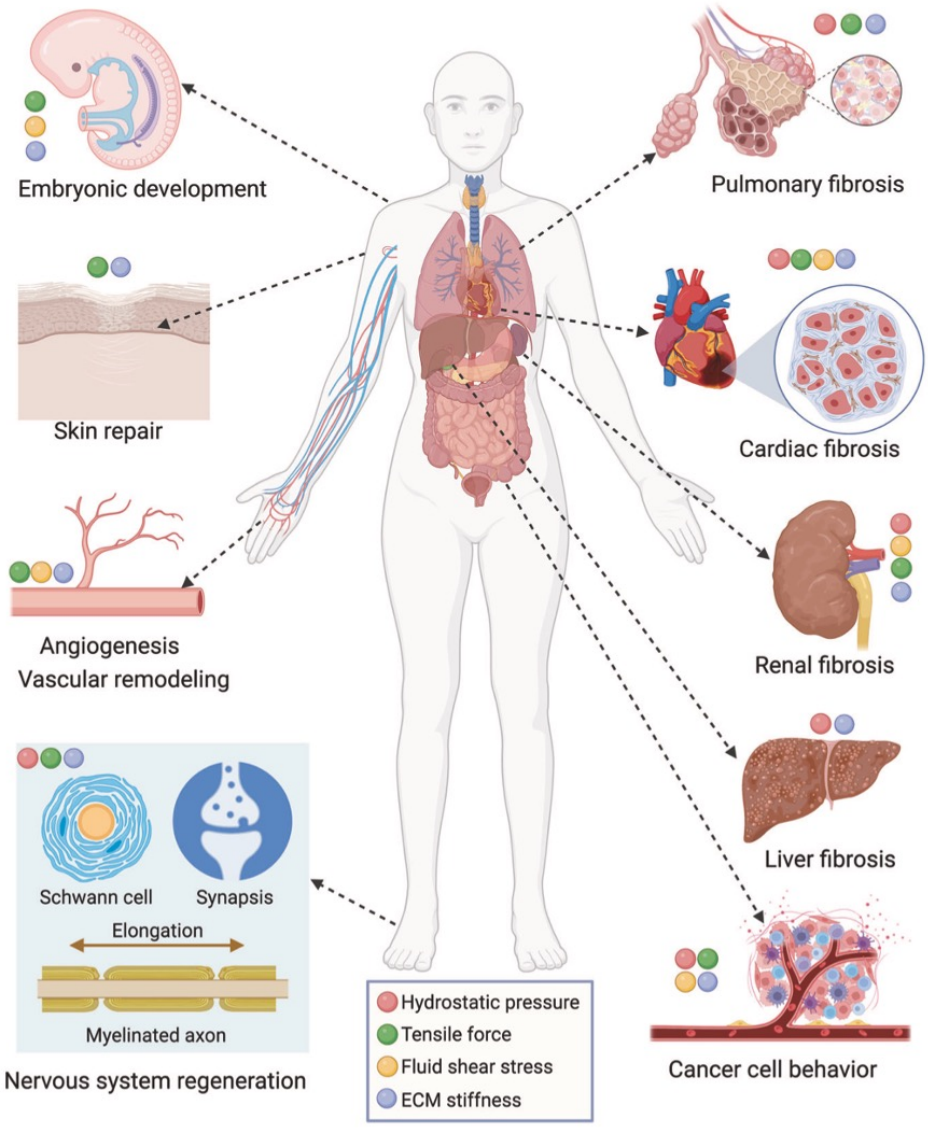


Figure 1.2. Global overview of physiological phenomenon induced by microenvironment-associated mechanical cues. Cellular microenvironments are specialised to the biological context, and they are unique to support their residing cells. Changes in the cellular microenvironment can (i) induce certain developmental processes, (ii) upset homeostasis balance, or (iii) potentiate disease pathogenesis. Image adapted from Di *et al.* (2023)[49].

1.1.3. In vitro static models and their insufficiencies to inform cell niche

Traditionally, in *in vitro* experiments, cells were simply cultured on plates and flasks. These we termed the static cellular models, as there are no other physical or mechanical elements incorporated into the culturing platform. These *in vitro* static cellular models have been essential tools in biological research for decades, allowing researchers to study various cellular processes, like proliferation and differentiation. These simple, controlled and non-dynamic models present both advantages and disadvantages in investigating the cellular microenvironment. Having a highly controlled model makes it

easy to isolate and study the effects of individual factors on cellular behaviour. In addition, a simple experimental setup allows careful manipulation of specific variables to monitor cellular responses. For example, we can investigate the effect of cellular proliferation or differentiation in the presence or absence of certain chemical compounds in the culturing media. Other than being more cost-effective than *in vivo* models for preliminary research and large-scale studies, *in vitro* static cellular models offer a high level of reproducibility for data acquisition and analysis.

However, more studies in recent years have concluded that *in vitro* static models often fall short of representing the physiological conditions[32]. This is because they fail to replicate the dynamic and multifaceted conditions present within a cellular niche. An *in vitro* static setup, being a simplistic model, cannot fully capture the complexity of the multi-dimensional and heterogeneous nature of a tissue. Furthermore, cells grown in a typical two-dimensional (2D) monolayer fail to mimic the 3D structural architecture of a microenvironment. Many *in vitro* static models lack the absence of physiological forces, such as shear stress and fluid flow, which play a significant role in cell behaviour and function *in vivo*[33,34]. The absence of a dynamic experimental condition may result in certain cells, like endothelial and epithelial cells, behaving differently under static conditions as they would *in vivo*[34,35]. Therefore, the suitability of *in vitro* models varies depending on the cell type and cellular context being studied.

1.1.4. Advances in creating near-physiological experimental conditions

In vitro static cellular models remain limited in their capability to replicate the dynamic and multifaceted conditions of cell niches. Advanced models and approaches that better mimic physiological conditions are critical for addressing these challenges and advancing our knowledge of cellular processes. In recent years, technologies and engineering strategies have significantly improved our ability to create controlled and physiologically relevant microenvironments for experiments. 3D culture systems, such as scaffolds, hydrogels and organoids, allow cells to grow in a more representative microenvironment with the support of other relevant cell types and structural biomaterials[36–38]. Improvements in biomaterials have produced substrates and scaffolds with tailored mechanical, topographical and biochemical properties that

further enhance the specific tissue microenvironments[38–40]. In addition, the incorporation of essential mechanical cues, like shear stress, compression and cellular tension, enhances the experimental models by providing a more physiologically relevant microenvironment[37,38,40]. These mechanical cues play a crucial role in influencing cell behaviour, function, and responses, as they closely mimic the physical forces experienced by cells in their native niches[38,40]. By adjusting the matrix stiffness or scaffold design and by introducing microfluidic systems or mechanical stretch platforms, cells can be encouraged to behave as they do in their *in vivo* context. For instance, neural stem cells cultured on stiffer substrates are encouraged to differentiate into neurons, while softer substrate promotes their differentiation into the astrocyte lineage[41–43]. Also, the integration of microfluidic systems and perfusion bioreactors into experimental models can provide a near-physiological niche condition for culturing endothelial cells *in vitro*. Thereby, allowing us to better understand innate cell response and behaviours within the microenvironment[44,45].

Recreating the microenvironment ensures that experiments can be conducted with a high degree of consistency and reproducibility, which is essential for drawing meaningful conclusions about the *in vivo* physiological context. Yet, challenges remain in tissue engineering technologies for us to fully realise a faithful replica of specific cellular niches. As the *in vivo* cellular microenvironment is heterogeneous and highly complex, it is difficult to replicate the exact condition in our *in vitro* or *ex vivo* experiments[37,39,40]. Integrating all components of the niche, while at the same time ensuring (i) dynamic interactions between cells, (ii) a functional network of vascular vessels for nutrient supply and (iii) the presence of mechanical cues are just a few of the challenges in the quest of reproducing the cellular microenvironment. Not to mention, maintaining the long-term viability and stability of dynamic models is also a difficult task.

Overcoming these challenges is an ongoing area of research in the tissue engineering field. Therefore, advances in biomaterials, cell culture techniques, tissue culture systems and our understanding of the cellular microenvironment will contribute to addressing these issues. Even though there is yet a faithful replica of the cellular microenvironment, near-physiological conditions can unquestionably be incorporated

into *in vitro* experimental setups. This will enhance the research impact and allow us to gain a deeper understanding of cellular behaviours, study disease processes and develop novel therapies and regenerative medicine approaches based on more relevant models.

In summary, the cellular microenvironment is a complex and dynamic entity that exerts significant influence over cell behaviour and function[4–6]. While *in vitro* static cellular models have been valuable in many respects, they fall short in replicating the dynamic and multifaceted nature of the cellular microenvironment. Creating near-physiological conditions, through advanced culture models, co-culture systems, and biomimetic materials, is essential for producing more accurate and relevant experimental outcomes. The near-physiological models will be critical for improving our understanding of cellular processes, developing better disease models, and advancing therapeutic strategies.

1.2. The role of mechanical forces within the cellular microenvironment

The presence of mechanical forces within the cell microenvironment is integral to many physiological and pathophysiological processes[46–48]. The forces experienced within the cellular niche can be both endogenous (generated by the cells themselves) and exogenous (applied from external sources) (**Figure 1.3**). Cells are finely tuned to sense and respond to mechanical cues present in their microenvironment, which help regulate their behaviour and maintain the overall health and functionality of the tissue and organ[49]. Within the cell niche, mechanical forces often play the pivotal role of supporting structural architecture, maintaining tissue homeostasis and guiding development and maturation[8,49,50]. Besides enhancing our experimental outcomes, the inclusion of mechanical cues into experimental models has proven to be critical in helping us understand how cells interact with their respective microenvironments[36,37,47]. Therefore, it is essential that we appreciate the role of mechanical forces within the cellular

microenvironment and, more importantly, understand how cells sense and respond to those mechanical cues.

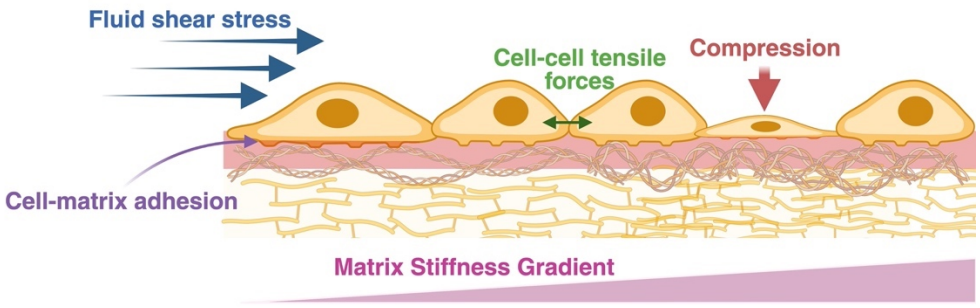


Figure 1.3. The extracellular mechanical environment which cells experience from their microenvironment. Cells are constantly exposed to mechanical forces within their microenvironment. These mechanical forces include (i) fluid shear stress, (ii) cell-matrix adhesion, (iii) tension forces from neighbouring cells, (iv) compression, and (v) extracellular matrix stiffness. Changes in any of these mechanical forces can induce mechanotransduction signalling in cells, which in response lead to various cellular behaviours and processes. Schematics created using BioRender.com.

1.2.1. Mechanosensation and mechanotransduction within cells

All living entities down to the basic units of life, the cells, are constantly exposed to mechanical stimuli from their surroundings. To respond and adapt to the continuously dynamic changes from their microenvironment, cells need the ability to perceive and transduce those mechanical cues into useful information[51–53]. Mechanosensation is the process by which cells (or organisms) sense mechanical forces or physical changes in their environment. Mechanotransduction, on the other hand, is the conversion of mechanical signals (gathered from the mechanosensation process) into biochemical signals and cellular responses. This conversion involves a series of biochemical events within the cells, termed signalling pathways, that transmit the mechanical information into a cellular response. Once mechanosensation occurs, mechanotransduction pathways often lead to changes in gene expression, protein activation or cytoskeletal rearrangement as a cellular reaction[53–55].

Mechanosensation and mechanotransduction have become increasingly crucial to cell biology research. The insights gathered from the research help us understand how cells sense and respond to mechanical forces, ultimately affecting various cellular processes. In recent years, many processes previously thought to depend solely on

specific, patterned biochemical signalling, are influenced by mechanical cues. For example, during embryogenesis and tissue morphogenesis, mechanical forces were proven to play a central role in shaping and organising cells within the niche[54,55]. Mechanosensation pathways have been identified to guide the spatial arrangement of cells, contributing to the formation of functional tissues and organs[49]. The multitude of developmental, physiological, and pathophysiological processes influenced by mechanobiological pathways ranges from cellular organisation[56,57], homeostasis[58], wound healing[59] and tissue regeneration[50] to cancer metastasis[60,61]. Furthermore, the importance of cellular mechanics reaches into more contained processes, like cell adhesion, locomotion, cell-cell coordination, proliferation, differentiation as well as apoptosis[62].

Within the cell microenvironment, resident cells constantly perceive external mechanical cues and simultaneously generate intracellular forces. To sense and transduce these diverse and ubiquitous mechanical signals, cells possess specialised structures and proteins[49,51,62]. Some of these specialised machinery include structural cell elements (e.g. the actomyosin network), cell junction and adhesion proteins (e.g. PECAM-1, cadherins and integrins), mechanosensitive channel proteins (e.g. Piezo1), transcription factors (e.g. YAP and TAZ) and more[49,63]. These cellular factors are often highly regulated by the cellular and microenvironmental context. They help cells detect and transduce physical forces, like tension, compression, shear and fluid flow, rendering them mechanosensitive and mechanoresponsive[63]. In this thesis, I will closely investigate the dynamics of cellular mechanosensation, occurring mostly on the cell membrane at near-physiological conditions.

1.2.2. Mechanobiology of the cell membrane

The cell membrane is a dynamic, lipid bilayer embedded with various proteins and receptors and channels. Some of which can sense mechanical stimuli exerted on the cell that originate either internally or externally. For a protein to be mechanosensitive, it must be able either (i) to detect changes in the membrane's mechanical properties like flexibility, curvature and tension or (ii) to interact directly with both extracellular and intracellular tethers[64,65]. Mechanical forces which cause deformation to the cell

membrane can trigger either (or both) mechanosensation phenomena. Examples of mechanical forces strong enough to induce membrane deformation include (**Figure 1.4**):

(I) Compression

Compression involves the application of external forces that exceed the membrane's resistance, leading to structural changes, commonly the reduction of cell volume[66]. Compressive stress is commonly observed during cell migration and invasion[67]. For example, migrating cancer cells travel through narrow capillaries[68,69]. Compression leads to an increase in local pressure on the cell membrane. Membrane buckling or invaginations will form upon the localised pressure, but if the compression force is substantial, it may sometimes cause membrane blebbing or rupture[69,70].

(II) Stretching

Stretching, frequently exerted by tensile forces, pulls the cell in opposite directions, leading to an expansion of the cell's surface area and a temporary increase in membrane thickness[71]. Both deformations cause an increase in membrane tension. Physiologically, the phenomenon of cellular cyclic stretching is commonly observed during respiration, when the inflation action stretches the epithelial cells in the lungs[71,72].

(III) Bending and Curvature

Bending or curvature forces involve localised changes in the shape of the cell membrane[73]. These localised membrane deformations are vital during processes like endocytosis and exocytosis, where the formation of vesicles or the fusion of membrane compartments occurs.

(iv) Shear Stress

Shear stress is the force applied parallel to the cell membrane, most commonly during strong fluid flow current[74,75]. It creates a differential movement across adjacent membrane layers, leading to the lateral displacement of membrane proteins and changes in membrane fluidity[74]. Common physiological processes which produce

shear stress include blood flow, particle flow in the gut, or contact between migratory cell clusters and their substrate[75].

(v) Cytoskeletal Force

This intracellularly exerted force originates from the cytoskeletal network[76,77]. The cytoskeleton, consisting of actin filaments, microtubules and intermediate filaments, can exert mechanical forces on the cell membrane. Forces originating from the cytoskeleton would exerted similar deformations to compression, stretching, and even bending on the cell membrane.During cellular reorganisation or locomotion, actin filaments can push against the cell membrane, leading to protrusions, membrane ruffling and changes in cell shape[77].

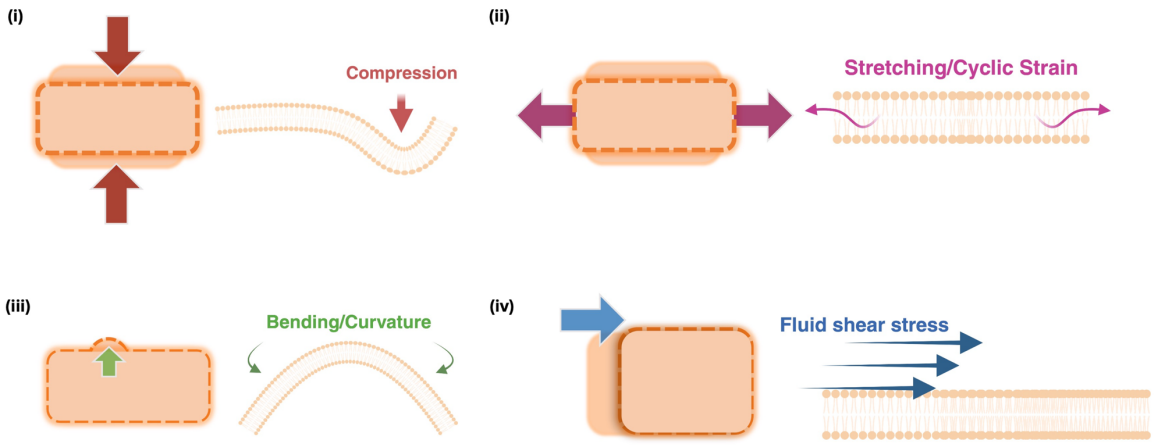


Figure 1.4. Mechanical forces that induce cell membrane deformation. Mechanical forces which cause deformation to the cell membrane can trigger cellular mechanosensation and mechanotransduction. Mechanical forces include **(i)** compression, **(ii)** stretching or cycle strain, **(iii)** bending or curvature, and **(iv)** fluid shear stress. Schematics were partly created using BioRender.com.

Understanding the mechanobiology of cell membrane and how its components affect its properties will provide insights into how cells sense and respond to mechanical curs from their microenvironment. Central to this understanding lies the fluid mosaic model of the plasma membrane, proposed by Singer and Nicolson in 1972. This model describes the cell membrane as a fluid lipid bilayer embedded by proteins, cholesterol, and carbohydrates, resembling a mosaic pattern. The composition of various components within the cell membrane is controlled and regulated. Changes in the

distribution of these macromolecules can profoundly impact the membrane mechano-properties, such as fluidity and stability. For example, an increase of cholesterol on the phospholipid bilayer stiffens the cell membrane, which negatively impacts the membrane deformability and influence mechanosensing and mechanotransduction processes.

Over the last decades, various methods have been developed to study how these forces change the membrane's mechanical properties and how cells adapt and respond to the stressor[78,79]. No matter the mechanical forces, deformations on the cell membrane are essential for the cell to adapt to its mechanical microenvironment. Hence, it is key to incorporate the relevant mechanical stimuli into experimental models to accurately study dynamic, mechanosensitive phenomena occurring on the cell membrane.

1.2.3. Means and methods of studying cellular mechanics

Advancements in technologies have brought about improvements in methodologies used to study cellular mechanics within the microenvironment. A considerable amount of time and effort has been invested to yield a wide range of strategies in which mechanical forces can be established experimentally to study cell responses. A widely used method that allows us to measure cellular mechanics is using a mechanical manipulation system. Mechanical manipulation systems allow studying the role of cellular mechanics on samples such as cells and tissue by applying controlled mechanical forces to the experimental sample of interest[80,81]. These systems offer various scales of forces depending on the tools employed. For example, tensile and compression testers measure the tensile strength of tissues at macroscale, while an atomic force microscope (AFM) studies the mechanical properties of a cell at nanoscale[81–84]. Other methods of exerting external forces, like optical[85] and magnetic[86,87] tweezers, involve the manipulation of microscopic particles using a probe. While mechanical manipulation systems are sophisticated and versatile in teasing single cell mechanics, mechanical forces applied are mostly localised[88]. A common approach to exert global mechanical stimulation is to incorporate bioengineering methods within the experimental model. Biomaterial and bioprinting technologies can be used to create substrates and scaffolds to simulate physiological conditions and manipulate tissue

mechanical properties within a controlled culturing model[89]. The inclusion of microfluidic systems or tissue stretcher chambers is another popular method to exert global mechanical forces on cells. Devices can control forces in a controlled manner while allowing us to study the mechanoresponsive phenomenon of cells[36,37]. Lastly, computational simulation methods, such as finite element analysis (FEA), have further informed our understanding of how cells and tissue respond to forces[90]. Simulating mechanical forces and their effects on potential biological samples, can also guide experimental design and complement findings.

1.3. Mechanosensitive ion channels and the Piezo family

Mechanosensing on the cell membrane takes many forms. Cells express mechanosensitive proteins on the lipid bilayer membrane to sense changes in the mechanical environment surrounding them. Transmembrane proteins at the focal adhesion sites, such as integrins and other cell adhesion molecules, couple the intracellular cytoskeletal element, like the actomyosin filaments, to the extracellular microenvironment[49,63]. Coupled focal adhesion sites physically bind the cells' intracellular network to the microenvironment, allowing the transmission of external forces from either neighbouring cells or ECM to the actomyosin cytoskeletal network or vice versa[91,92]. Further studies have shown that other transmembrane proteins associated with the focal adhesion sites are crucial in mechanosensation or part of the mechanotransduction pathways[93].

Another mechanism which allows cells to perceive and transduce external mechanical cues is through mechanosensitive ion channels (MSCs). Like other ion channels, MSCs are pore-forming membrane proteins that are activated by mechanical stimuli experienced by the cell[94,95]. As a class of transmembrane proteins, MSCs open or close in response to changes in membrane tension, deformation or shear stress, allowing passage of ions (typically calcium (Ca^{2+}), sodium (Na^{+}), or potassium (K^{+})) across the cell membrane[96]. Gated by mechanical stimuli, activation of MSCs can trigger a cascade of

biochemical signalling pathways, leading to a wide range of cellular processes and physiological functions[96–98].

Among the class of MSCs expressed on the cell membrane, the Piezo family has been well-studied over the years. First discovered in 2010 by the Patapoutian group, the Piezo proteins are stretched-activation, non-selective cation channels that do not possess homology to any other mechanosensitive proteins in mammalian cells[99]. There are two known members within the Piezo proteins family, Piezo1 and Piezo2[99]. Both Piezo channels remain conserved across species and organisms, suggesting their physiological importance[99,100]. First described in mouse neuroblastoma cell line, Neuro2A cells, it was later found that the human Piezo1 amino acid sequence shares 24% identity with *Drosophila melanogaster*-Piezo1, 59.2% identity with zebrafish Piezo1, and 82% identity with mouse Piezo1 (mPiezo1)[99,100]. Between human Piezo1 and Piezo2, 47% identity was reported, with no similarity found with any other protein[100]. While Piezo2 channels mainly function in the peripheral nervous system, Piezo1 is widely expressed across various cell and tissue types[100,101]. Out of the family of two, Piezo1 channels have been studied more closely. Still, Piezo1 activity dynamics, like its modulation mechanisms, and the downstream signalling of the channel remain largely unanswered and an exciting area of research[102,103]. Below I will summarise knowledge of Piezo1 structure, activation mechanism, and function derived from previous research efforts.

1.3.1. Piezo1 – Properties and structure

Piezo1 is one of the largest mechanosensitive ion channels described, with a protein size of 900 kDa and more than 2500 amino acids[99,104]. Cryogenic electron microscopy (CryoEM) studies of the mouse Piezo1 channel have determined that it has three identical subunits arranged in a tri-blade propeller-like formation with a central ion-permeating pore to form a homotrimeric structure[105,106] (**Figure 1.5 a and b**). Each subunit of the trimer consists of nine transmembrane helical units (THU) which are formed by bundles consisting of four transmembrane (TM) helices, accompanied by the outer and inner helices (TM37 and TM38 respectively)[105–107] (**Figure 1.5 c**). Monomers trimerise to form the three curved propeller-like blades at the extracellular domain,

which is stabilised by the long, helical, intracellular beams of each subunit. The intracellular beams bridge the external domains to the central ion-conduction pore module, enabling the flux of cations intracellularly[105,107] (**Figure 1.5 c**). Further analysis has assigned distinct functions to different domains of the Piezo1 protein complex. For example, mechanotransduction is facilitated by the peripheral helices (residues 1 – 2190), while ion conduction and mechanosensing lie between residues 2187 – 2547 that form the central pore[107,108].

Piezo1 channels have been shown to respond to a multitude of external and internal mechanical stimuli, ranging from shear stress[110,111], substrate stiffness[41], membrane or cell stretch[99,112], membrane indentation[98,99], osmotic shock[113,114], pressure[115] and intracellular traction forces[116]. Structurally, the activation of Piezo1 is orchestrated like a lever-like action by its tri-blades and long intracellular beams. Changes in membrane tension brought about by mechanical forces can change Piezo1's distal tri-blades conformation. The change in tri-blades conformation results in a "pull" on the intracellular beam that bridges the distal ends to the cap of Piezo1, thereby converting the mechanical force into opening the channel[117] (**Figure 1.5 d**). The Piezo1 trimers also induce membrane curvature wherever the channels are localised. This curvature of the membrane is thought to be important in enhancing Piezo1's sensitivity to changes in membrane tension[118]. Although Piezo1 is a non-selective cation channel, when opened, the ion conducting pore has a slight preference, around 80% conductance, for divalent cations, such as Ca^{2+}. In addition, Piezo1's conductance of divalent cations, like Ca^{2+}, reduces the permeability of monovalent ions, like Na^{+} and K^{+} [119]. The conductance of Piezo1 channel plays an important in cell signal, as Ca^{2+} is a key secondary messenger for numerous intracellular signalling pathways and processes. Therefore, the downstream effect of Piezo1 activity is multifaceted, ranging from cell reorganisation to gene transcription, and cell differentiation to apoptosis.

While the activation of Piezo1 channel is well understood, Piezo1 inactivation mechanism is less studied. A proposed mechanism of Piezo1 inactivation involves the process of "fast inactivation", which occurs shortly after the ion channel's activation. It is suggested that there is a structural changes within the Piezo1 complex, specially the

ion-conducting pore cap subdomain, causing a termination of ion conductance through the pore[120]. This “fast inactivation” conformational changes of Piezo1 channel, following activation, may be influenced by the alteration of the membrane environment or certain associated proteins. Alternatively, it was hypothesized a Ca^{2+} negative feedback mechanism may contribute to modulating Piezo1 activity. Ca^{2+}-dependent mechanisms, such as Ca^{2+}-dependent inactivation or desensitisation, can render Piezo1 channels less responsive to subsequent mechanical cues, leading to channel inactivation. Further research efforts are still required to identify molecular determinants involve in the mechanisms of Piezo1 channel activation and inactivation.

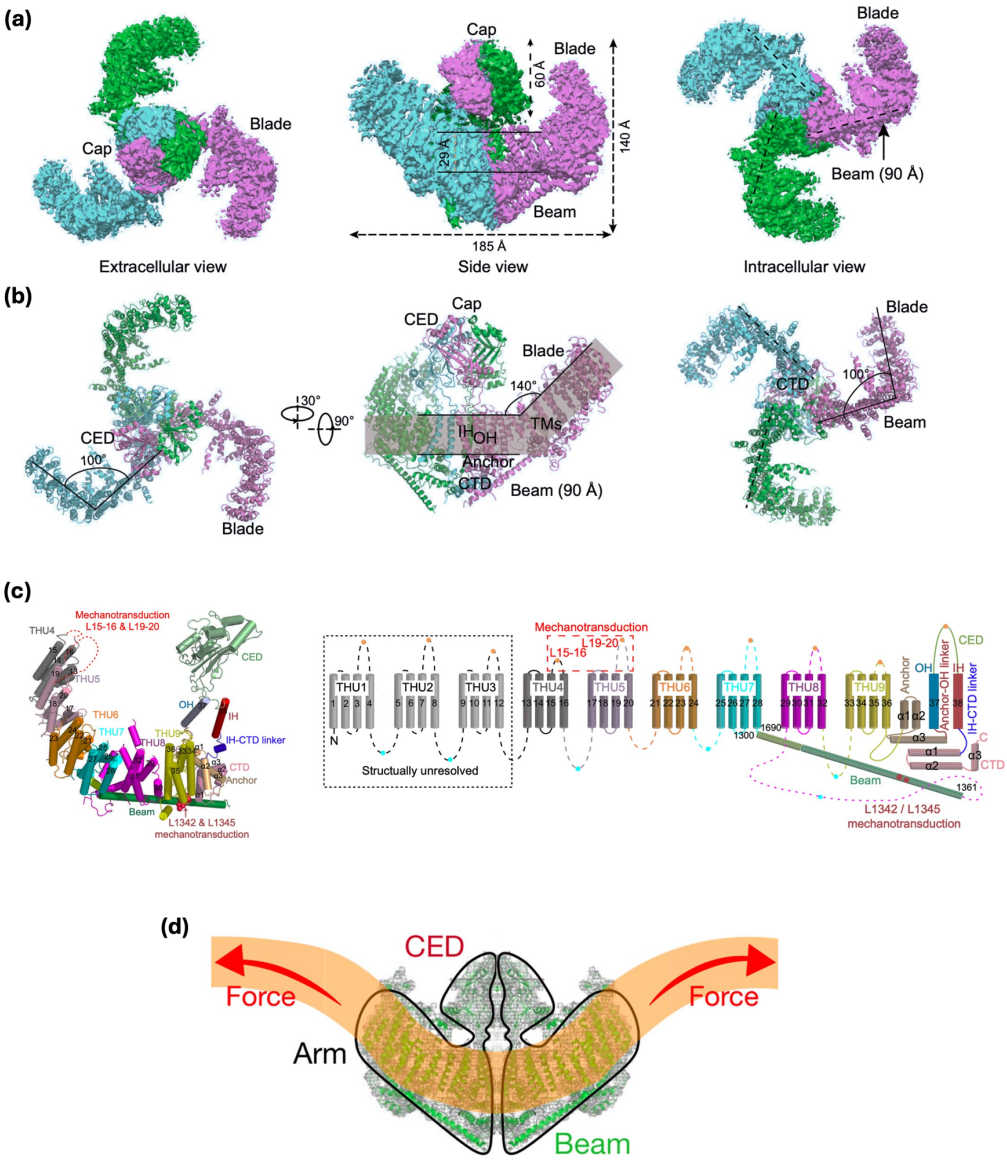


Figure 1.5. Cryo-EM revealed that mouse Piezo1 forms a homotrimer structure. Mouse Piezo1 (mPiezo1) structure in **(a)** surface and **(b)** cartoon mode showing the secondary structures of the protein from extracellular, side, and intracellular views. **(c)** Cartoon view and the 38-TM topology model showing

a single subunit of Piezo1, with individual THUs and featured structural domains colour-coded. **(d)** Schematic model of membrane Piezo1 doming mechanism. Membrane tension causes a change in membrane curvature, which leads to the activation of Piezo1 ion channels. Images (a – c) adapted from Zhao *et al*. (2019)[108], (d) adapted from Fang *et al*. (2019)[117].

1.3.2. Piezo1's mode of action

Though the precise mechanism of gating Piezo1 activity remains elusive, previous research has proposed two paradigms of Piezo1 gating: gating by force-from-lipids and by force-from-filaments (**Figure 1.6**). Apart from the two membrane-associated gating paradigms of Piezo1 activity, there is currently no known proteins which is associated to the gating of Piezo1 channel activities. In the force-from-lipids hypothesis, changes in the membrane dynamics alter the protein-lipid interface, leading to changes in the conformation of Piezo1 channels. In the absence of other cellular components, it was shown that force transmission through a lipid bilayer is sufficient enough to trigger Piezo1 activity[114]. This suggested changes in lipid bilayer tension alone can activate mechanosensitive ion channels present on the cell membrane. Other examples of ion channels gated by membrane dynamics are the mechanosensitive hyperpolarising K2P channels, TREK and TRAAK[121]. In addition, there was evidence showing that Piezo1 channel activity can be modulated by membrane mechanics, reported membrane fluidity[122]. For example, the recruitment of cholesterol molecules by STOML3 to increase membrane stiffness appears to facilitate Piezo1 activation[123]. In contrast, disrupting the membrane cholesterol domains, which soften the membrane, was shown to impair Piezo1 function[94].

On the other hand, the force-from-filament model suggests that the ion channel activities are gated by the conformational changes of both the cytoskeletal and ECM protein network upon mechanical stimulation[98,114]. Interestingly, in the presence of intracellular cytoskeletal elements, Piezo1 activation has a higher force threshold[98]. Cox et al. (2016) also found that Piezo1 activation came easier in membrane blebs (cell membrane component, lacking cytoskeletal elements) than in cell-attached patches. In addition, Gaub and Müller (2017) observed that cell-ECM contact is important in sensitising Piezo1's mechanical force responses[84]. Overall, these studies underscore the important role of Piezo1 as a bona fide mechanosensitive ion channel in the cell. Yet,

the complexity of its functioning is still a conundrum that leaves researchers racing to uncover.

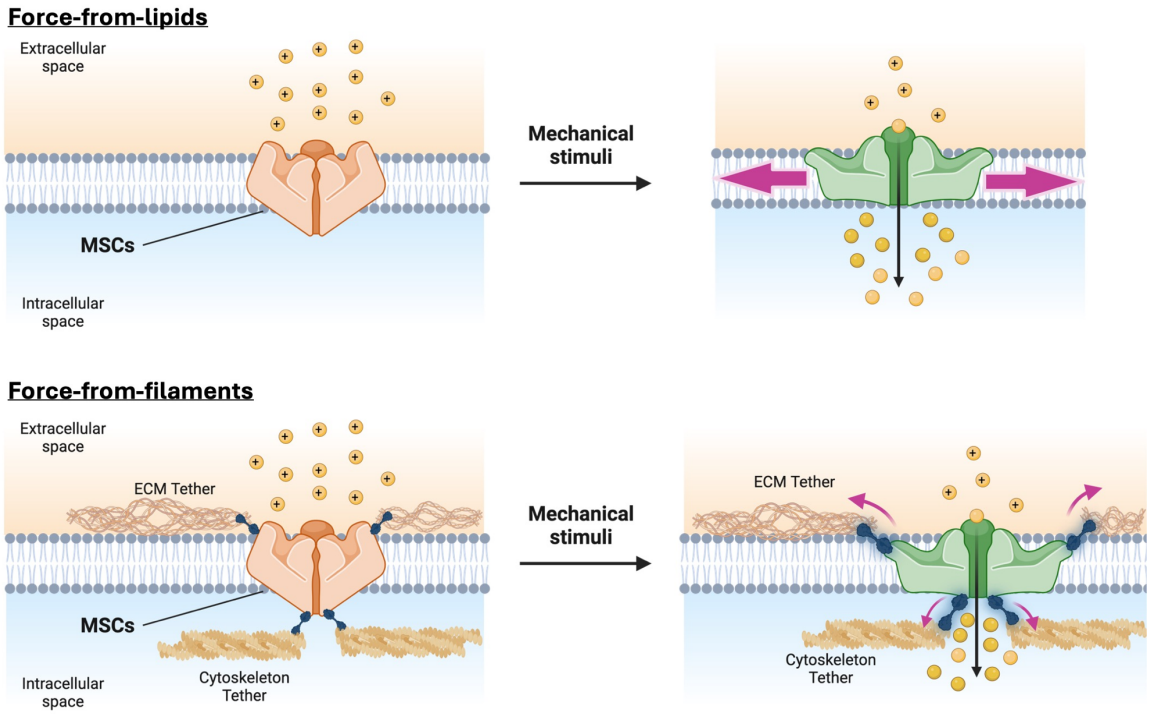


Figure 1.6. Proposed gating mechanisms of mechanosensitive ion channels (MSCs). There are two paradigms of gating mechanism for MSCs, like Piezo1 – (i) Force-from-lipids and (ii) Force-from-filaments. In the force-from-lipids model, forces are transmitted through membrane lipids directly onto MSCs, without implicating other cytoskeletal components. On the other hand, the force-from-filament model proposed that the tethering of the MSCs with cytoskeletal or ECM components leads to activation. Schematics were created using BioRender.com.

1.3.3. Piezo1 in development, homeostasis and pathophysiology

The discovery of the Piezo channel family by the Patapoutian group in 2010 has fuelled a wide range of research efforts in the field of mechanobiology. A plethora of recent work using both animal and cellular models and primarily focussed on Piezo1 has provided evidence that this channel plays a crucial role during development, homeostasis and pathophysiology[124] (**Figure 1.7**). Various gain-of-function and knockout studies in both cellular and animal models have yielded valuable insights into the physiological contributions of Piezo1 functioning. Mutations in the human *PIEZO1* gene have been associated with two main human genetic diseases: dehydrated hereditary stomacytosis (DHS)[125,126] and general lymphatic dysplasia (GLD)[127,128]. Mechanistically, DHS is caused by an inherited autosomal dominant gain-of-function mutation in the *PIEZO1*

gene. This mutation altered the mechanosensing properties of the ion channel, leading to an increase in cation permeability in red blood cells (RBCs)[126,129]. In contrast, GLD is caused by an autosomal recessive, *PIEZO1* loss-of-function mutation and is characterised by a widespread lymphoedema affecting all segments of the body[127].

Furthermore, the global knockout of the mouse Piezo1 gene is embryo-lethal due to failure in vasculogenesis, highlighting the channel's importance in embryonic development[110,111]. Conversely, a gain-of-function variant of Piezo1 was shown to confer significant protection against severe malaria[130]. Below, I attempt to highlight a few examples of Piezo1's functional importance in different biological and physiological contexts.

(I) Vascular System

Piezo1 plays a crucial role in the vascular system by enabling proper endothelial cell functioning and responses to shear stress and stretching[110,111]. Highly expressed across the different populations of endothelial cells, Piezo1 mechanosensing activity regulates the alignment of cells in the direction of laminar flow during prolonged fluid shear stress[110]. Endothelial-Piezo1 activation in response to increased shear stress has also been shown to facilitate the release of nitric oxide (NO), a molecule that causes blood vessels to dilate[131,132]. Interestingly, Piezo1 activity has shown to regulate the permeability of the blood-brain barrier (BBB)[133]. Zhang *et al*. (2020) demonstrated that ultrasonic stimulation (USS) increased HUVECs permeability via Piezo1, while the inhibition of Piezo1 decreased cell barrier permeability. These studies highlighted Piezo1's role in regulating blood flow and maintaining vascular tone within the cardiovascular system.

(II) Epithelial Layer

Besides endothelial cells, Piezo1 is also highly expressed in epithelial cells, particularly in the epithelial cells of the lung, bladder and skin[134–137]. As the main surface lining and protective barrier against the outside world, these cells are constantly exposed to physical and mechanical forces, such as shear stress, stretching and pressure. In the skin epithelial microenvironment, Piezo1's mechanosensing activities determine

whether epithelial cells undergo proliferation or live cell extrusion[134,135]. Results in the studies emphasise the importance of Piezo1 in crowd sensing and epithelial tissue homeostasis. In the renal tissues, Piezo1 was found to be responsible for stretch-activated currents and modulation of the lower urinary tract enteroception[136,137].

(III) Stem Cells and Niche

Piezo1 is also increasingly recognised for its importance in stem cell biology and the stem cell niche. The unique pluripotent nature of stem cells makes them critical for tissue repair, regeneration and homeostasis, because they can differentiate into different types of cells[138]. Piezo1 activation in response to mechanical cues like substrate stiffness can regulate the differentiation lineage choices of mesenchymal and neural stem cells into osteocytes[139,140] and neurons[19,20,41], respectively. Piezo1 activity in neural stem cells was also shown to be crucial for precursor cell migration in the developing brain[141,142]. Recently, Piezo1 activity has been shown to regulate the regenerative capacity of muscle stem cells by priming them to adopt a responsive state[143].

(IV) Cancer Pathophysiology

The importance of Piezo1 extends beyond development and physiology into disease pathophysiology. Piezo1 has been implicated in the mechanosensory abilities of cancer stem cells (CSCs) and the regulation of CSC properties, such as self-renewal, differentiation and therapy resistance[144]. Piezo1 in cancer cells can sense these mechanical cues within the tumour microenvironment, like increased tissue stiffness, and trigger signalling pathways to support tumour progression[144,145]. Furthermore, studies done with HeLa and lung epithelial cells have shown that Piezo1 is crucial for cell adhesion, and the loss of Piezo1 function increases cancer cell migration[135]. Yet in human gastric adenocarcinoma cells and malignant mammary epithelial cells, Piezo1 function increases cell mobility[145]. Combined, these studies reveal the complexity of Piezo1's downstream effects, which are highly dependent on tissue types and physiological context.

Overall, Piezo1 function spans a variety of cellular and physiological processes, presenting an essential component of many mechanosensory processes. Increasingly, various studies have come to appreciate that Piezo1's activities and downstream processes are dependent on the cells' microenvironment and biological context. Piezo1 enables cells to sense and respond to mechanical cues that originate in their respective niche. The understanding of Piezo1 function is constantly evolving and has far-reaching implications for understanding cellular mechanics in health and diseases.

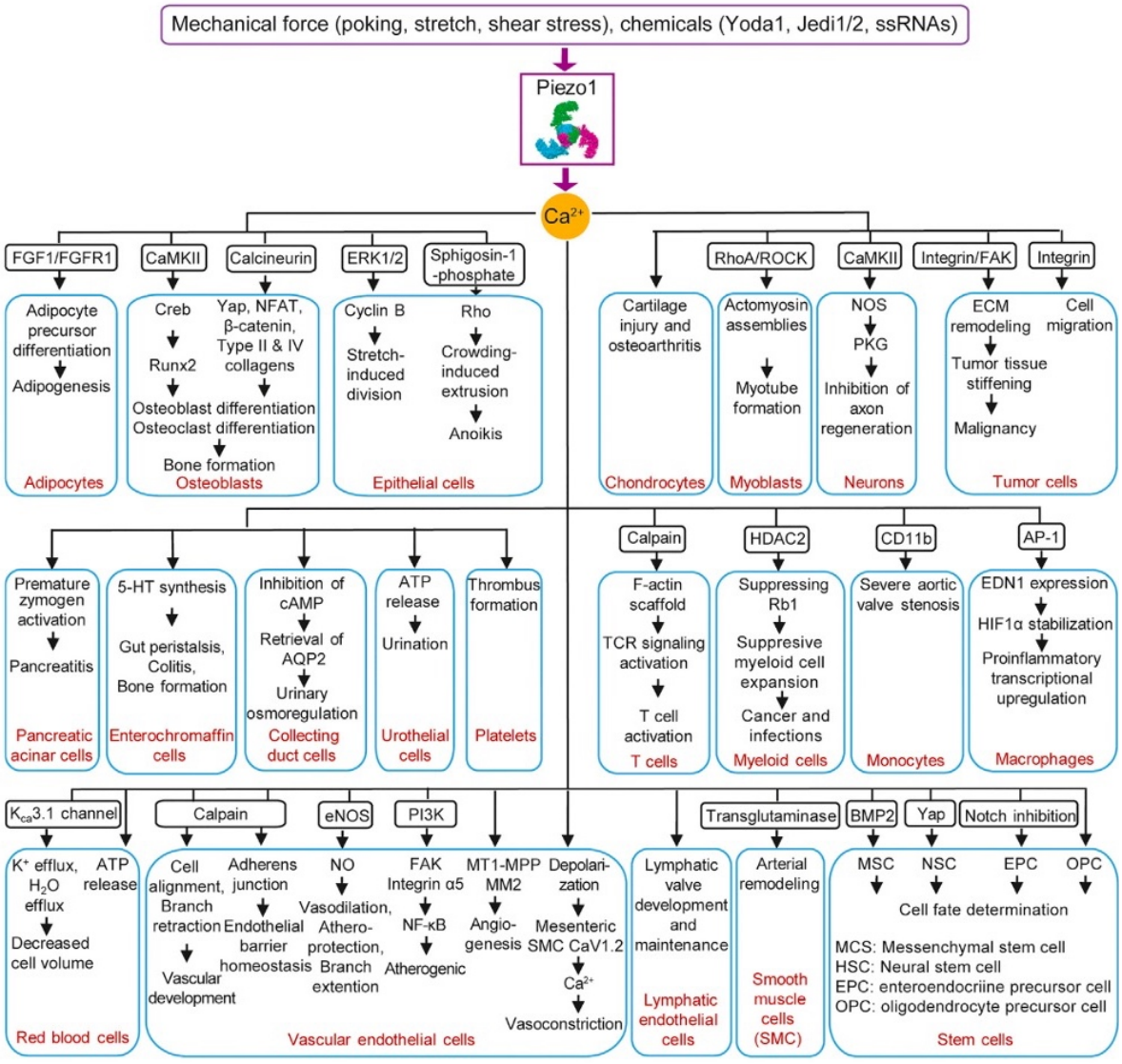


Figure 1.7. Piezo1-mediated mechanotransduction pathways. A wide range of biological processes in development, homeostasis, and disease pathophysiology, in which Piezo1 is involved. Piezo1 serves as a bona fide mechanosensitive ion channel for transducing distinct Ca^{2+} signalling pathways in various cell types.

1.3.4. Methodologies used to study Piezo1 function

Since the discovery of Piezo1, various methods and techniques have been employed to exert mechanical forces in an experimental setup to study different aspects of Piezo1 function[102]. Techniques widely used to study the dynamics of MSCs mostly measure the output of the ion channels, such as patch-clamp electrophysiology, cytosolic Ca^{2+} imaging and other molecular biology analyses (**Figure 1.8**). For example, patch-clamp recordings were used to monitor the electrical activity of Piezo1 in real-time. The application of mechanical forces to cells while simultaneously measuring the ion channel conductance provided insights into the gating dynamics and ion selectivity of Piezo1[109]. Similarly, cytosolic Ca^{2+} imaging allowed for the real-time visualisation of intracellular Ca^{2+} dynamics associated with Piezo1 activation. In association with Piezo1 activation, researchers have outlined mobile Ca^{2+} speckles in response to the mechanical force[59,116]. Though proven useful, these techniques are indirect measures of Piezo1 dynamics and conclusions are often drawn in the conjuncture of Piezo1 activation and its cations conductance.

Below, I summarise common methods of experimentally exerting mechanical stimulation to trigger and study Piezo1 activity.

(I) Contact- and Probe-based Methods

Contact- and probe-based methodologies remain one of the most common methods to study the activity of any mechanosensitive or mechanoresponsive protein. Extremely robust, these methods are useful in investigating surfacial, intracellular and intramolecular forces within a single cell[102]. Methods include atomic force microscopy (AFM), microindenters and micropipette aspiration that allow measuring the stiffness, tension and mechanical properties of biological samples[146]. Probe-based methods, like optical and magnetic tweezers, allow precise measurement of forces at micro- to macro-scale with the manipulation of laser or magnetic probes, respectively[147,148]. These direct force application and measurement methods are mostly localised to single cells at once, therefore requiring dissociated tissue[102]. Therefore, these techniques are limited in their mechanical force delivery and multicellular outlooks. The involvement of mechanical

indenters or force-inducing probes can easily damage tissue, which limits access to samples and complicates experiments.

(II) External Mechanical Force Applications

Piezo1 channels can be activated upon a range of global mechanical stimuli, such as shear stress, stretching and compression. Therefore, the external application of mechanical stimulation is another way to elicit Piezo1 response in cells globally. By culturing cells on stretchable membrane or flexible substrate, cells can be exposed to physical strain and mechanical deformation by mechanical stretching apparatus[149]. In addition, *in vitro* cell cultures can also be subjected to controlled fluid flow within a microfluidic device to recreate fluid shear stress on the cell surface. Employing microfluidic techniques replicates, for example, the mechanical forces experienced by endothelial cells in blood vessels and allows researchers to assess Piezo1 activation in response to shear stress[150,151]. Overall, these global mechanical stimulations can mimic dynamic physiological conditions cells are constantly exposed to in their microenvironment, providing insights into Piezo1's response to dynamic mechanical conditions in a controlled setting. However, the process of incorporating external mechanical stimulations into the culturing system can be complicated, requiring specialised equipment and careful optimisation.

(III) Chemical Perturbations

Compound screening efforts have made pharmacological modulation possible in controlling the MSCs' activities without the use of mechanical stimuli. In 2015, the first Piezo1-specific agonist, Yoda1, was reported[152]. As a potent gating modifier of Piezo1, Yoda1 acts by reducing the channel's mechanical threshold, without affecting Piezo1's constitutive activity[152,153]. With an EC_{50} value of ~ 17 μM and ~ 26 μM for mouse and human Piezo1 respectively, Yoda1 affects Piezo1's sensitivity by stabilising the open state of the channel. Structurally, Yoda1 is believed to wedge between the central cap structure and the transmembrane beams, which potentiates the conformational change of the Piezo1 structure induced by mechanical forces. Subsequently, additional chemical agonists of Piezo1 were described (Jedi1 and Jedi2, with EC_{50} values of 200 μM

and 158 μM, respectively)[154]. Both Jedi1 and Jedi2 activate Piezo1 through the extracellular side of the tri-blades.

Pharmacological antagonists for Piezo1 activity are still non-specific. Commonly used Ca^{2+} channel inhibitors, like ruthenium red[155] and gadolinium[99], are currently used in Piezo1 perturbation experiments. These inhibitors act by blocking Piezo1's ion conductance, along with other Ca^{2+} channels. Another commonly used antagonist against MSCs is the peptide GsMTx-4[156,157]. Initially isolated from the venom of a tarantula, *Grammostola spatulate*, GsMTx-4 is highly potent against MSCs[156]. Due to its lack of stereospecificity, GsMTx-4 acts as a gating modifier and pore inhibitor[158,159]. It binds on the lipid membrane bilayer to alter the mechanical properties of the cell membrane, thereby inhibiting MSC activation[157–159]. As chemical perturbations are fundamentally unspecific, the interpretation of results needs to be performed carefully.

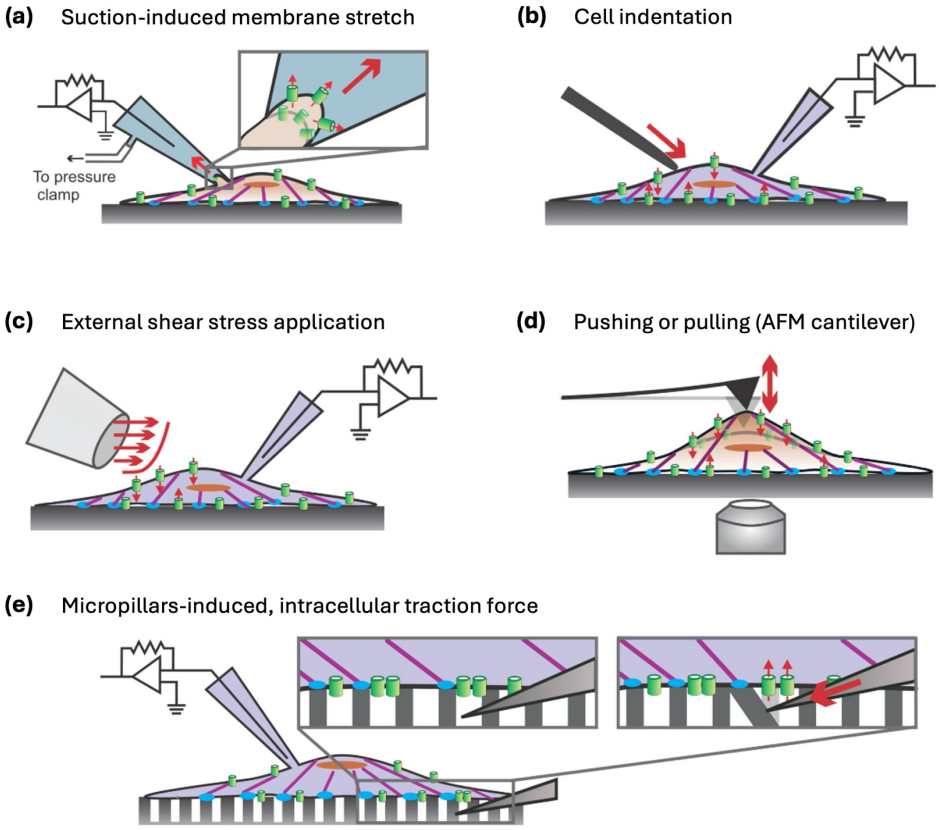


Figure 1.8. Biomechanics methodologies commonly used to study Piezo1 activity. Piezo1 senses and transduces mechanical forces from the cellular microenvironment. Common techniques employed in previous studies mainly involve recording outputs, such as electrophysiological recordings, cytosolic Ca^{2+} imaging and transcriptomic changes, in response to direct mechanical force stimulation. Image adapted from Nourse & Pathak (2017)[102].

1.4. Genetically-encoded calcium indicators and GenEPi

Previous studies of Piezo1's activity have been largely performed using outputs, such as electrophysiological recordings, cytosolic Ca^{2+} imaging and transcriptomic changes, in response to extracellular mechanical stimuli[102,160,161] (**Figure 1.8**). However, these experimental approaches present two major shortfalls of causation – (i) the recorded outputs cannot be directly correlated with Piezo1-specific activity, or (ii) the recorded outputs do not inform any spatiotemporal resolution of Piezo1-specific activity. The necessity for a non-invasive, and direct measure of Piezo1 activity led to the generation of a genetically-encoded reporter of Piezo1, termed GenEPi, by our lab[1].

1.4.1. Calcium signalling and calcium microdomains

Cells require signalling mechanisms to affect specific downstream cellular processes in response to changes in their extracellular microenvironment. Through signalling mechanisms and pathways, cells can integrate extracellular inputs into intracellular adaptive responses. Ca^{2+} is one of the most essential secondary messengers employed in different signalling pathways. As a prominent signalling molecule, it is involved in a wide range of cellular and physiological processes throughout the body[120,162]. Cellular Ca^{2+} signalling is initiated upon the rapid increase of cytosolic Ca^{2+} concentration by either (i) Ca^{2+} influx across the cell membrane or (ii) Ca^{2+} release from the intracellular endoplasmic reticulum (ER) stores[163,164]. Across the cell, Ca^{2+} concentrations are tightly regulated, with Ca^{2+} being mainly in the extracellular milieu or within the ER stores, within the µM to mM range at resting. The huge difference in intracellular Ca^{2+} concentration at rest (~ 100 nM [Ca^{2+}]) creates the steep gradient for speed, amplitude, and spatiotemporal patterning, which upon activation, initiates a spectrum of downstream signalling cascades[163,164]. The extracellular influx of Ca^{2+} is mediated by various Ca^{2+}-permeable ion channels and other metabotropic receptors expressed on the cell membrane surface. While Ca^{2+} release from intracellular stores is normally activated by the inositol 1,4,5- trisphosphate (IP3) receptor pathway. The surge in cytosolic Ca^{2+} triggers several Ca^{2+}-dependent enzymes and Ca^{2+}-binding molecules, like the protein

kinase C (PKC) and calmodulin (CaM), respectively, to initiate cellular processes. Ca^{2+} pumps and exchanges will actively transport Ca^{2+} across the cell membrane (to the extracellular environment) or back into the intracellular stores, which restores the resting Ca^{2+} homeostasis after signalling events.

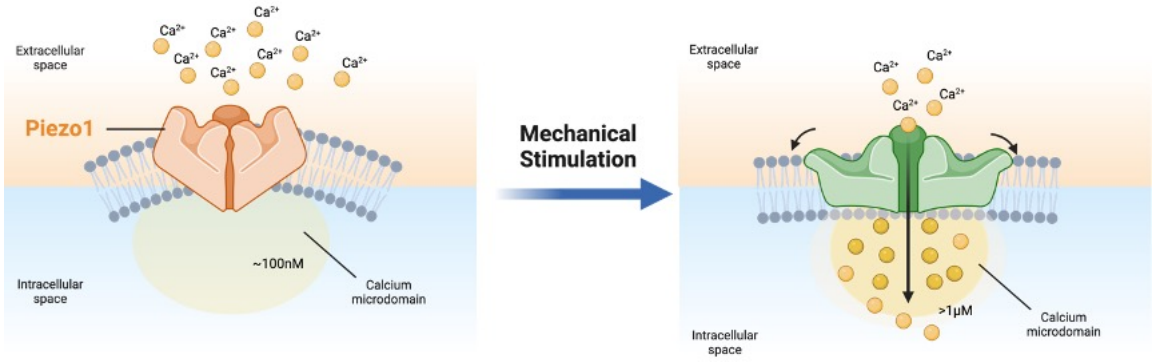


Figure 1.9. The Piezo1 calcium microdomain hypothesis. The calcium (Ca^{2+}) microdomain hypothesis implies that when the channel is active due to mechanical stimulation (or chemical agonism), the Ca^{2+} concentration near the vicinity of the ion-conducting pore increases dramatically. The increase in Ca^{2+} concentration creates a Ca^{2+} microdomain near the ion channel. Schematics were created using BioRender.com.

Being a ubiquitous signalling molecule, intracellular Ca^{2+} levels are spatiotemporally controlled to ensure the specificity of distinct signalling cascades[120,162]. The intracellular Ca^{2+} signalling event is heavily governed by (i) concentration, (ii) timing and (iii) localisation of the cytosolic Ca^{2+}. The steep Ca^{2+} gradient between the extracellular environment (or ER stores) and cytosol allows for a strong flux of Ca^{2+} into the cytosol within milliseconds after activation of Ca^{2+} channels. Due to localised chelation mechanisms within the cytoplasm, the influx of Ca^{2+} is spatially restricted to the activated region(s) of the open ion channels[162]. These regions with high Ca^{2+} concentration are nanodomains of 100 nm, when a single Ca^{2+} channel is activated, or a microdomain, when a cluster of channels within the region is activated[165]. This spatiotemporal restriction and regulation of Ca^{2+} movements within the cytosol allow parallel transmission of Ca^{2+}-dependent signalling[166]. In addition, different Ca^{2+}-dependent enzymes and Ca^{2+}-binding molecules have varying affinities to Ca^{2+}, thus allowing distinct signalling pathways to be effected using the same secondary messenger. With such stringent regulation over the intracellular Ca^{2+} signalling event, a wide bandwidth of signal transmission can be achieved simultaneously within the cells.

1.4.2. Genetically-encoded calcium indicators (GECIs)

In order to visualise the intracellular Ca^{2+} domains *in situ*, synthetic Ca^{2+} indicators or genetically-encoded calcium indicators (GECIs) were developed. GECIs are a class of molecular tools designed to monitor intracellular Ca^{2+} dynamics in living cells with high spatiotemporal resolution[167–169]. They are engineered protein sensors that change their fluorescent properties, such as intensity or wavelength, in response to changes in the intracellular Ca^{2+} concentration. Typically, GECIs are composed of a Ca^{2+}-binding module and a fluorescent protein (FP) module[170]. When bound to Ca^{2+} ions, the Ca^{2+}-binding module undergoes a conformational change, resulting in a change in the fluorescence properties of the attached fluorescent protein. The change in either fluorescent intensity or wavelength provides a measurable readout based on the Ca^{2+} concentration changes locally[170,171]. Being genetically-encoded, GECIs are non-invasive and can be introduced into living cells without significant damage. The expression of GECIs can be targeted to specific cellular regions or organelles, like the ER, to monitor Ca^{2+} dynamics within the local Ca^{2+} domains. In addition, optimised GECIs allow for real-time visualising of intracellular Ca^{2+} dynamics with high temporal resolution, making them a reliable tool for studying rapid Ca^{2+}-dependent cellular events, like the activation of a mechanosensitive ion channel. These indicators have become invaluable as specific reporters for Ca^{2+}-conducting ion channels and for studying intracellular Ca^{2+} signalling events.

Over the years, GECIs have been modified and optimised with various protein engineering technologies to suit different applications of research. Briefly, there are two main GECI sensor classes: the single-FP intensiometric GECIs[170,171] and the FRET-based two FPs ratiometric GECIs[172] (**Figure 1.10**). In the single-FP intensiometric method, a circular permutated version of the FP (cpFP) is created and fused with the Ca^{2+}-binding module. The Ca^{2+}-binding module normally consists of a Ca^{2+}-binding effector protein and its binding peptide, calmodulin (CaM) and M13 peptide. In the presence of Ca^{2+}, CaM and M13 interact and bind to each other, leading to a conformational change in the GECI and a chromophore-favoured environment for the cpFP[170] (**Figure 1.10 a**). In addition to cpFP, split-FP has also been fused to the separated CaM-M13 module. Here, the split

parts of the FP would be brought together in the presence of Ca^{2+}, therefore allowing fluorescence. Well-established single-FP intensiometric GECIs, like the GCaMPs and GECOs, have been widely used in cell biology research to report intracellular Ca^{2+} signalling events[173]. Similarly, in the FRET-based two FPs ratiometric approach, the Ca^{2+}-binding module (CaM-M13 proteins) is separately fused to two different FPs. In the presence of Ca^{2+}, CaM and M13 interact and bind to each other, which in turn brings the two FPs closer together[172] (**Figure 1.10 b**). Instead of reporting the fluorescence intensity, the FRET-based approach calculates the fluorescence ratio between the two FPs, to yield the FRET efficiency.

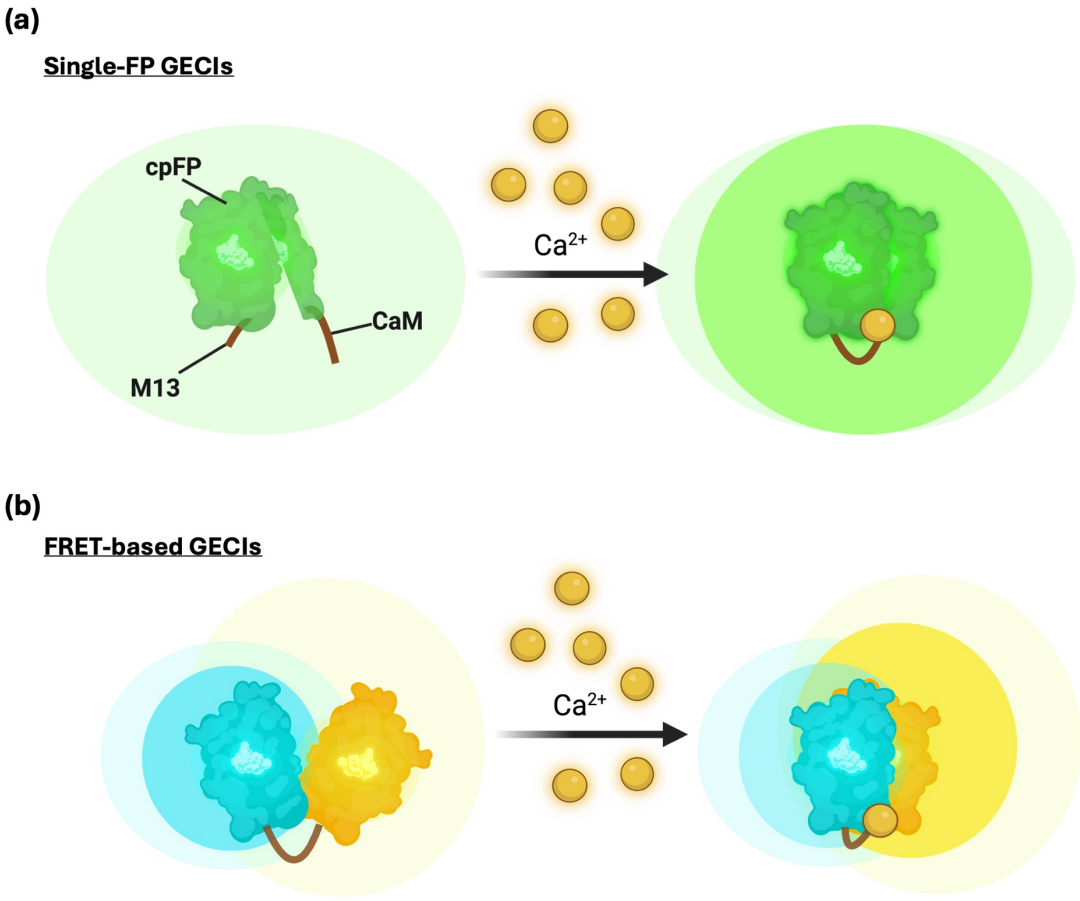


Figure 1.10. Two main classes of genetically-encoded Ca^{2+} indicators (GECIs). (a) Single-FP intensiometric GECIs consist of circularly permuted fluorescent protein (cpFP), calmodulin (CaM) and the binding peptide (M13). Binding of Ca^{2+} to CaM results in a conformational change of the Ca^{2+}-CaM-M13 interaction leading to an increase in fluorescence. **(b)** FRET-based ratiometric GECIs are generated by fusing FPs of a FRET-pair to either terminus of a CaM-M13 fusion. In the presence of calcium, CaM can interact with M13 and the associated conformational changes bring the two FPs closer together. In this state, the excitation of donor FP leads to FRET, and therefore, increases the fluorescence of the acceptor FP.

To report and monitor the dynamics of intracellular Ca^{2+}-dependent events, properties such as localisation, Ca^{2+} affinity, GECI kinetics and dynamic range must be considered when selecting the GECI to employ[174]. GECIs generated have different affinities to Ca^{2+} and their affinities should ideally be informed by the localisation of Ca^{2+} signalling events of interest. Hence, localisation of the Ca^{2+} signalling will inform the choice of GECIs, based on Ca^{2+} affinity. The GECIs' kinetics is another important factor to consider. A fast-proceeding event, like Ca^{2+} ion channel activation, will require a fast kinetic GECI to record the rapid Ca^{2+} influx. Whereas a slow-acting GECI could be beneficial for a longer-spanning Ca^{2+} event [172,174]. Finally, the dynamic range of the GECIs would determine the optical resolution capabilities. Dynamic range is the fluorescence fold change between the GECI's saturated and non-saturated states. The dynamic range of the GECIs should complement the differences occurring during the Ca^{2+} dynamics of the signalling event. Overall, the selection of GECI for use is ultimately dependent on the cellular context of the Ca^{2+} signalling event.

1.4.3. GenEPi, a Piezo1-specific optical readout

Previous studies on Piezo1 have clearly outlined the critical role it plays in sensing the mechanical cues from the microenvironment. Its importance in cell physiology, tissue homeostasis and disease pathophysiology has highlighted the need to measure and investigate Piezo1's dynamics and function within cells. Researchers have been working to investigate how cells integrate their Piezo1's activities in response to the mechanical cues from the microenvironment by various methods. Methods used in previous studies to dissect Piezo1's activity include ion channel electrophysiology, genetic transcriptional activities, protein expression, cell morphological changes, and behavioural processes insights. While these are invaluable insights into the downstream mechanotransduction effects of Piezo1, they provide neither the Piezo1-specific readouts nor any information regarding Piezo1 channel activities and functional regulation.

To address the need for a non-invasive, yet direct measurement of Piezo1-specific activity, the Pantazis lab recently introduced a genetically-encoded fluorescent-based

Piezo1 reporter, termed GenEPi[1]. The creation of GenEPi was achieved by fusing a GCaMP GECI to the C-terminal end of a human Piezo1 sequence, with a flexible linker (GSGG amino acid sequence) (**Figure 1.11 a**). The design and generation of GenEPi-sensor was based on (i) the GCaMP's low Ca^{2+} affinity, (ii) the GECI's high dynamic range (i.e. changes in fluorescence intensity, F_{max}/F_{min}), and (iii) the sensor's ability to reliably report Piezo1-activation specific Ca^{2+} influx[1]. With a Ca^{2+} affinity of 1.4 μM and a dynamic range of 31-fold, GCaMP-G4 was selected for the generation of the GenEPi construct, following a series of experiments to establish the reliability to detect and report Piezo1 activation specific Ca^{2+} influx from other intracellular Ca^{2+} events[1]. The GenEPi's GCaMP-G4 consist of a circular-permeated EGFP (cpEGFP) fused with the Ca^{2+}-binding module, CaM and M13 peptide (**Section 1.4.2**). Therefore, with an optimised linker length (1x GSGG peptide), the GCaMP-G4 within can only detect the Ca^{2+} concentration increase within the localised Ca^{2+} microdomain resulted from Piezo1 activation.

In response to mechanical stimulation or chemical agonist, Yoda1, Piezo1 activation leads to the influx of Ca^{2+}. Ca^{2+} ions that permeate interact with the Ca^{2+}-binding module (CaM-M13 protein) of the GCaMP-G4. The interaction causes structural changes to the GCaMP molecule within the GenEPi-sensor, which provide a chromophore-favoured environment for the cpEGFP to fluorescence (see **Figure 1.10 a** for the functioning of cpFP intensiometric GECIs). Thus, leading to an overall increase in green fluorescence intensity, which serves as the readouts of Piezo1 activity[1] (**Figure 1.11b**). The GenEPi construct has shown great reliability in reporting Piezo1 activities during chemical and mechanical stimulations. In addition, GenEPi preserves the endogenous Piezo1 electrophysiological activities upon stimulation, proving a functional mechanosensitive ion channel[1]. These results demonstrate that GenEPi is a unique optical tool that allows detecting and monitoring cellular Piezo1's activity and dynamics in real-time.

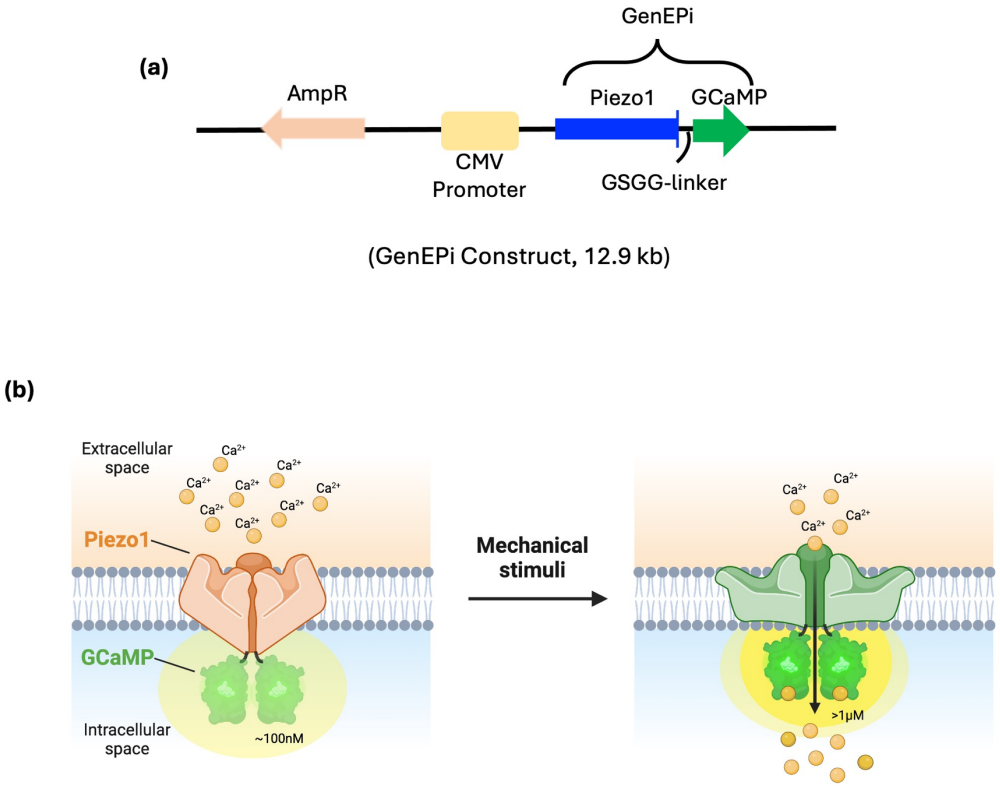


Figure 1.11. Piezo1-specific optical reporter, GenEPi. GenEPi was designed and generated by tagging a low affinity GECI to the C-terminus of a human Piezo1 sequence. With GenEPi, we can detect Piezo1-specific activation in response to mechanical stimulation or chemical agonist, Yoda1, treatment. **(a)** A simplified, linearised schematic view of the original GenEPi construct with the main features described. **(b)** Schematics of GenEPi working principle. When Piezo1 is activated by mechanical stimuli, incoming Ca^{2+} (in yellow) binds to GCaMP, causing an increase in green fluorescence. Schematic created using Biorender.com is adapted from Yaganoglu & Kalyviotis *et al.* (2023)[1].

1.5. Aims of the thesis

Piezo1 is a key mechanosensor expressed by cells to perceive and translate mechanical cues from the cellular niche. The procedure of sensing, translating, and transducing mechanical information both externally and intracellular has increasingly been shown to play a critical role in various cellular processes. As cells are constantly exposed to external cues (including mechanical stimuli) from their microenvironment, it is important to be able to have a reliable *in vitro* model to study how cells receive and respond to these continuous streams of information. Whether or not cells react to the external stimulus depends on the sensory mechanism on the cell membrane, which is the role Piezo1 plays for mechanical stimuli.

Despite having many insights about the downstream effects of Piezo1 activity in response to mechanical forces, still little is known about the dynamics and regulatory mechanism of Piezo1 activity itself on the cell membrane. My PhD research aims to develop a system which allows us to reliably measure and monitor the dynamics of Piezo1-specific activity in real-time within a near-physiological cellular model. Specifically, my aims are:

(I) Design and generate an inducible version of GenEPi.

Presented in Chapter 2, I designed and generated an inducible version of GenEPi, termed XLGenEPi, by changing the genetic construct's backbone that was previously used by the Pantazis lab. In addition, I included a piece of genomic integration machinery into the new construct to allow for positive clonal cell selection. These positive clonal cells reliably express the GenEPi-sensor when induced and allow investigation of Piezo1-specific activity.

(II) Develop a microfluidic-based culturing system which is adaptable for live-time imaging on a commercial confocal microscope.

Presented in Chapters 3 & 4, I developed a microfluidic-based culturing system, which allowed me to culture our positive clonal cells with exposure to near-physiological range shear stress. The incorporation of microfluidic technologies helped me to create a cellular model which is closer to the cells' *in vivo* microenvironment. Furthermore, the developed system is adaptable for doing time-lapse, live-imaging on a commercial confocal microscope. Our microfluidic-based system allows culturing and experimenting in a close setting to measure and investigate cellular Piezo1 activities under different shear stress conditions.

(III) Piezo1 activity dynamics were dissected through our GenEPi time-lapse, live-imaging system.

Presented in Chapter 5, I used the established microfluidic-based system developed under aim (II) to dissect the dynamics of Piezo1 mechanosensing activity. With my developed system, I reiterate the phenomenon previously associated with Piezo1 activity through indirect experimental methods. In addition, I report novel Piezo1 activity dynamics in response to varying shear stress perturbations.

2. Designing and generating an inducible, yet stable expression of GenEPi within mammalian cells

"Everything is theoretically impossible, until it is done."
– Robert A. Heinlein

2.1. Generating an inducible, yet stable GenEPi expression construct

The original GenEPi sensor was developed as a tool to display Piezo1's mechanosensation and activities. GenEPi reliably displayed the ability to report Piezo1's response to both Piezo1-specific agonist, Yoda1, and mechanical stimuli in the form of high-contrast fluorescent readouts. However, there are limitations to this genetic system of GenEPi expression.

Firstly, in the original construct, the GenEPi sensor expression is driven by a strong genetic promoter, a CMV-promoter. CMV-promoter poses the limitation of overexpression in cells for the duration that the cells retain the construct. Even though Yaganoglu, Y. & Kalyviotis, K. *et al.* (2023) showed that the overexpression of GenEPi is not detrimental or toxic to cells, long-term effects on the cells and intricate cellular processes remain unclear[1]. Overexpression of any protein could cause undesirable

effects on cellular processes and behaviour subsequently, including cellular identity and homeostasis, cell-state transition, and differentiation.

Secondly, the GenEPi construct was built for transient expression in transfected cells. As the original GenEPi construct is not integrated into the genome of the host cell, GenEPi expression is only retained for a limited number of cell cycles period. Upon cell proliferation, the DNA plasmids encoding for GenEPi will be diluted out, limiting the time the GenEPi signal can be observed in transfected cells to only a few cell division cycles.

Lastly, the original GenEPi construct transfection method poses a variability in GenEPi sensor expression among the cell population. In this case, imaging would include a population of both successfully transfected and untransfected cells, which do not express the GenEPi sensor. Having a mixed group of cells (GenEPi-expressing and non-expressing WT cells) complicates the analysis of populational cellular behaviour and makes clonal analysis of Piezo1 dynamics impossible.

To overcome the limitations described, I proposed an inducible system to be adapted into the original GenEPi construct. An inducible construct allows more precise control of GenEPi expression within the host cell. Here, I first describe the molecular cloning process and validation of the inducible GenEPi construct, named XLGenEPi. I then discuss the characterisation of the integrity and functionality of the XLGenEPi construct in mammalian cell models.

In the rest of this thesis, I will refer to the inducible Piezo1 sensor-carrying construct as XLGenEPi, and the expressed protein and its acquired fluorescence signal as GenEPi.

2.2. Materials & Methods

2.2.1. Molecular cloning

Molecular cloning procedure was undertaken to create the XLGenEPi and CMV-pBase constructs, which were used throughout the research described in this thesis. XLone-

GFP was a gift from Xiaojun Lian (Addgene plasmid #96930; http://n2t.net/addgene:96930; RRID: Addgene_96930). The hGFAPmin-pBase was previously generated in our lab by inserting the hGFAPMIN promoter from pAAV-GFAP-EGFP (a gift from Bryan Roth, Addgene # 50473) into pCAG-PBase plasmid (a gift from Paolo Salomoni)[200]. The CMV promoter and GenEPi sensor sequences were derived from the original GenEPi construct (Addgene #140236), which was previously generated in the Pantazis lab by Sine Yaganolu[1].

The cloning procedure for XLGenEPi construct was as follow: Restriction digestion of the GenEPi plasmid by HindIII and SphI enzymes (NEB; R3104S and R3182L respectively) allowed us to get the full GenEPi sensor sequence. In addition, the XLone background sequence was derived from restriction digestion using KpnI and SphI (NEB; R3142S and R3182L respectively). Digestion products were subsequently separated by agarose gel (1%) electrophoresis and the correct-sized DNA products were isolated using NEB Gel Extraction kit (NEB, T1020L). 5' overhang flanking sites were either filled in or removed by the Quick Blunting Kit (NEB; E201) from GenEPi or XLone sequences respectively. Ligation of GenEPi sequence to the XLone backbone was performed using T4 ligase (NEB; M0202) at 24°C for 1 hour.

The overview of the CMV-pBase construct cloning process was as follow: PCR amplification of the CMV promoter was done using Phusion high-fidelity DNA polymerase (NEB; M0530) on the original GenEPi construct. pBase transposase sequence was derived from restriction digestion of pGFAPmin-pBase construct using SalI enzyme (NEB, R3138S). Both PCR and restriction digestion products were separated by agarose gel (1%) electrophoresis and the correct-sized DNA products were isolated using NEB Gel Extraction kit (NEB, T1020L). DNA fragments with homologous ends generated above were then incubated in the Gibson Assembly mix (NEB; E2611L) at 50°C for 1 hour to clone the CMV-pBase construct.

Following the assembly of both constructs, heat-shock transformation at 37°C was carried out using competent *E coli.* cells (NEB; K12 strain) and grown on Agar LB (Thermo Fisher; Q60120 and Q61020) and LB liquid media (BD Bioscience; 244610)

supplemented with 100 µg/ml ampicillin (Sigma-Aldrich, A9393). Bacterial clones were screened using restriction digestion and DNA sequencing by Eurofins Genomics (https://eurofinsgenomics.eu/) using our custom-made sequencing primers (see **Appendix A1.**) to confirm the identity and integrity of the plasmid DNAs. Once successfully, both plasmid constructs were isolated using Mini- (NEB, T2010S) and MaxiPrep (Invitrogen; BenchPro™ 2100 machine).

2.2.2. Cell Culture

Different cell types were used in this section, namely HEK293T, HeLa, HFFs, A549, primary rat astrocytes and HUVECs. Culturing condition differ slightly for the different cell types (due to the difference in culturing requirements), experimenting conditions were kept the same.

HEK 293T, HeLa, and HFFs cells: All three cell-types were originally obtained from ATCC (ATCC CRL-3216, ATCC CCL-2, and ATCC SCRC-1041). All three cell-types were cultured at 37°C, 5% CO_2, in DMEM complete media, consisting of high glucose DMEM with GlutaMAX (Gibco™, 10569010), supplemented with 10% FBS (Sigma-Alrdrich, F7524) and 1x Penicillin-Streptomycin antibiotic solution (Thermo Fisher, 15140122). HEK 293T cells used in this series of experiment were of P7-8, where the XLGenEPi-HEK 293T clones generated are of P8. HeLa cells used in this series of experiment were of P6-7. HFFs used here were of P8-9.

HUVECs: HUVECs were previously obtained from Lonza (Lonza, C2519A) and established within the lab. HUVECs used in this series of experiment were of P3-4. Cells were cultured at 37°C, 5% CO_2, in EGM™-2 Endothelial Cell Growth Medium-2 BulletKit™ (Lonza, CC-3162). Medium kit system contains EBM™-2 Basal Medium (Lonza, CC-3156) and EGM™-2 SingleQuots™ Supplements (Lonza, CC-4176).

Primary Rat Astrocytes: Primary rat astrocytes were harvested and a gift from Rylie Green's lab. Astrocytes were cultured at 37°C, 5% CO_2, in DMEM/IMDM at 1:1 ratio (Gibco™, 12440053) supplemented with GlutaMAX (Gibco™, 35050061), supplemented

with 2% FBS (Sigma-Alrdrich, F7524) and 1x Penicillin-Streptomycin antibiotic solution (Thermo Fisher, 15140122).

All cultures were routinely tested for mycoplasma infection using Mycoplasma detection kit (LuBioScience GmBH, B39032). For routine maintenance, culture media was changed every two days and passaged at ~ 70% confluence by incubating with TrypLE™ (Gibco™, 12604-013) at 37°C for 5-minutes. Cells were routinely cryopreserved at -140°C to ensure continuation of cell lines. For cell cryopreservation, cells were dissociated from culture platforms using TrypLE™ (Gibco™, 12604-013) at 37°C for 5-minutes and frozen in their respective culture media, supplemented with 10% FBS and 10% DMSO.

2.2.3 Cell Transfection

Plasmid DNAs used for the co-transfected were isolated from bacterial cultures grown in 150 – 200 ml LB liquid media (BD Bioscience, 244610) supplemented with 100 µg/ml ampicillin (Sigma-Aldrich, A9393). The isolation process was undertaken using MaxiPrep kit (Invitrogen, BenchPro™ 2100 machine), according to the manufacturer's instruction. The amount of plasmid DNAs was measured using NanoDrop One$_c$ Spectrophotometer (Thermo Fisher). 500 ng of each plasmid (XLone-EGFP or XLGenEPi and CMV-pBase) were used for each transfection reaction. As mentioned before, cells were also co-transfected with CMV-pBase plasmid, which contains the genetic sequence of transposase, the enzyme that integrates our target gene into the host cell genome. The volume of the plasmid DNAs for each reaction was scaled by the individual plasmid's molecular size ratio. This ratio is needed before XLGenEPi construct size is almost times larger than both the CMV-pBase and XLone-EGFP constructs. Mammalian cell transfection was performed when cultures were at 70 – 80% confluence using the Lipofectamine® 3000 Reagent kit (Thermo Fisher, L3000001) as according to manufacturer's protocol. In brief, the co-transfection reaction was introduced to the cells in Opti-MEM (Gibco™, 31985062) and incubated at 37°C, 5% CO_2 for overnight (approximately 16 hours). After which, cells were given fresh media and left to recover for at least 24-hours before further intervention. For the transfection of HUVECs and

primary rat astrocytes, cells were incubated with the same co-transfection reaction at 37°C, 5% CO_2 for 6 hours, before the change of fresh cell culture media.

For transfection efficiency imaging, the XLone-EGFP- or XLGenEPi- transfected cells were dissociated 24-hours post transfection and seeded onto 0.1% gelatin pre-coated 20 mm-wide cover-glass bottom confocal dishes (VWR, 734-2906), at a density of 200,000 cells per dish. 200 ng/ml doxycycline (Merck, D9891) was added to induce GenEPi 's expression at 18-hours prior to imaging. 200 ng/ml doxycycline was used to induce GenEPi's expression and generate sufficient contrast which is in the lower range of previously used concentrations[175].

2.2.4. Clonal Selection and Analysis

Wild-type (WT) XLGenEPi-transfected HEK 293T cells were dissociated using TrypLE™ (Gibco™, 12604-013), at 37°C for 5-minutes, and plated into 12-wells plate containing 22 mm coverslips (0.1% gelatine pre-coated), at a seeding density of 100,000 cells per well. At 70 – 80% confluence, cells were treated with 4, 6, 8, 10, 12, and 14 µg/ml blasticidin (BSD) in DMEM complete media (described in **Section 2.5.2**). After the removal of BSD at Day 7, cells were left to recover in fresh complete media for 3 days.

To evaluate the effective of positive clone selection by BSD-treatment, treated cells were subsequently subjected to 200 ng/ml doxycycline (Merck; D9891) was added to induce GenEPi 's expression at 18-hours prior to cell fixation. During cell fixation, 4% ice-cold paraformaldehyde (PFA) (diluted from 16% concentrate solution, Thermo Fisher, 28908) was added into each well and incubated for 10 minutes at 37°C. After which, fixed cells were washed and stored under fresh DPBS -/- (Sigma-Aldrich, D8537) at 4°C until subsequent immunofluorescence staining procedure.

To select for XLGenEPi-HEK 293 colonies, transfected-HEK 293T cells were dissociated using TrypLE™ (Gibco™, 12604-013), at 37°C for 5-minutes, and plated into 6-wells plate, at a seeding density of 250,000 cells per well. At 70 – 80% confluence, cells were treated with 10 µg/ml BSD (Sigma-Aldrich, 203350) in DMEM complete media (described in **Section 2.5.2**). After the removal of BSD at Day 7, cells were left to recover in fresh

complete media for 3 days. Colonies visible under the EVOS microscope (AMEX1000) at 10x objective were manually picked by pipetting them off the culture-ware and transferring them into a fresh 12-wells plate with fresh DMEM complete media. Each colony was transplanted into its own individual well for expansion. Expanded clones are generated when WT HEK 293T cells were P8 but was cryopreserved as XLGenEPi-HEK 293T P1 clones. Like all the other cell lines, all selected XLGenEPi clones were cryopreserved in basal DMEM media, supplemented with 10% FBS and 10% DMSO, at -140°C.

To inspect the XLGenEPi-positive HEK 293T clones for successful genome integration, WT cells and XLGenEPi-HEK 293T clones were dissociated and resuspended in PBS three times. After the final resuspension, cells were pelleted by centrifuging at 300 g for 10 minutes at 4 ℃. Cell pellets were stored at -20 ℃ until DNA extraction. Genomic DNA was extracted from each harvested cell pellet (WT cells and XLGenEPi-HEK 293T clones) using Purelink™ Genomic DNA Mini Kit (Invitrogen, K182001). We performed four different polymerase chain reactions (PCR) on the DNA sample from each clone to confirm the presence of GCaMP, TRE3G inducible promoter, Tet-On transactivator protein, and BSD resistance gene. PCR was performed using the standard *Taq* DNA Polymerase kit (NEB, M0273S). Primer pairs targeting those four elements have been specifically designed and listed in **Appendix A2**. XLGenEPi plasmid prepared by Maxiprep (described in **Section 2.5.1**), and WT cells genomic DNA were used as a positive and a negative control, respectively. Gel electrophoresis was performed to confirm product size with 1% agarose gel (Appleton Woods, AG001) with precast GelRed™ dye (Merck, SCT123) added.

2.6.5. Immunofluorescence Staining

For antibody staining after BSD clonal selection, cells were fixed in 4% PFA (diluted from 16% concentrate solution, Thermo Fisher, 28908) for 10 minutes at 37°C, permeabilized with PBS supplemented with 0.1% TritonX-100 (Sigma-Aldrich, T8787) and blocked with 10% Donkey Serum (Jackson ImmunoResearch, 17-000-121) in PBS supplemented with 0.1% TritonX-100. Samples were then incubated with goat anti-GFP antibody (Abcam, ab6673) diluted in 5% Donkey Serum (Jackson ImmunoResearch, 17-000-121) in PBS

supplemented with 0.1% TritonX-100. After several washing steps with PBS, the samples were incubated with donkey anti-goat IgG (H+L) Alexa Fluor Plus-488 (Thermo Fisher, A32814), as well as DAPI (Thermo Fisher, 62248). Finally, the coverslip samples were mounted onto microscope slides (VWR, 631-0905) with Mowiol® 4-88 mounting medium (Sigma-Aldrich, 81381-50G).

2.2.6. Confocal Imaging and Chemical Perturbation

Images were acquired on a Leica SP8 confocal laser scanning microscope equipped with a white light laser (WLL, Leica) using an HC PL APO CS2 20x/0.75 dry objective. Images of cells were acquired at 8- or 16-bit depth, excited with 405 nm for DAPI, and 488 nm for GenEPi- or Alexa488- reporter, respectively. To ensure fast image acquisition, we imaged small regions of interest within the field of view, recording a single z-plane over several minutes (pinhole size ranged from 3 Airy units to maximum pinhole size) using the maximum acquisition speed. When imaging was performed on the Leica SP8 confocal, bidirectional scanning with off-set correction was used to increase acquisition speed even more. Live imaging of cells was carried out in Live Cell Imaging Solution (Thermo Fisher, A14291DJ), with the stage-top incubator set at 37°C.

For immunofluorescence staining imaging: Images of cells were acquired at 8-bit depth, with xyz planes, at 1024 x 1024 format, excited with 405 nm for DAPI, 488 nm for Alexa Fluor Plus-488 reporter, respectively. An optical zoom factor up to 3 might be used to obtain higher magnification of the cells and their subcellular structures. Z-stack images were acquired with an average z-stack size 20 µm at 0.88 µm optimal step-size.

For Piezo1 chemical perturbation experiments, cells were plated on a 35-mm glass-bottomed confocal dish (VWR, 75856-742) and imaged at 37°C on a stage-top incubator. During the live-imaging session, XLGenEPi-HEK 293T clones were subjected to Yoda1 and RR treatments directly on the imaging stage by adding the respective Yoda1 and RR solution into the Live Cell Imaging Solution (Thermo Fisher, A14291DJ). Cells were imaged for 30 minutes with each perturbatory conditions. We used 10 µM Yoda1 (Tocris Bioscience, 5586) diluted in DMSO (D8418, Sigma- Aldrich) for Piezo1-specific agonistic

perturbation. And 10 μM Ruthenium Red (Sigma-Aldrich, R2751) diluted in Ultrapure Distilled Water (Invitrogen, 10977-035) was used for Ca^{2+} ion channels inhibition.

2.2.7. Image Processing and Analysis

Image analysis of the cellular responses of GenEPi-sensor in the XLGenEPi-HEK 293T clones experiments was performed using ImageJ/Fiji [199] (release 1.53f51). For the immunofluorescence-stained confocal images, the maximum (X-Y plane) projection of the Z-stack images were made and subsequently merged to form the realised fluorescence images, which cells positive for GFP-stain were counted. For the live-imaging processing, the mean GenEPi-fluorescence intensity fold-change was derived by normalising each single cell fluorescence intensity values against one of the following: (a) the WT cells fluorescence intensity values (**Figure 2.9 b and Figure 2.11 b**), or (b) the negative-Dox condition single cell fluorescence intensity values (**Figure 2.10 d and Figure 2.14)**, or lastly (c) the T0/before perturbation condition single cell fluorescence intensity values (**Figure 2.10 c and Figure 2.12 b**). Data were further analysed and plotted using GraphPad Prism 9.

2.2.8. Statistical Analysis

All data are expressed means ± SEM. Sample sizes (n) are provided in the text or figure legend of each experiment. Each experiment has been repeated independently at least 3 times. To determine whether the data set has a Gaussian distribution, data subjected to the Shapiro-Wilk normality test; $p>0.05$ indicated it has a Gaussian distribution, and $p<0.05$ indicated it did not. With Gaussian distribution confirmed for each data set, two-tailed Student's t-test was applied to compare two independent datasets; with an F-test to compare variances. When F-test resulted in $p<0.05$, Welch's correction was applied to the t-test. When more than 2 datasets were present with Gaussian distribution, one-way ANOVA was used to compare datasets, followed by multiple comparisons test. When at least one of the compared data sets did not have a Gaussian distribution, Mann-Whitney test was applied to compare two independent datasets; and Wilcoxon rank-sum test was applied when the data sets were paired. When more than 2 datasets were present without Gaussian distribution, Kruskal-Wallis test was applied, followed by

Dunn's post hoc multiple comparisons test. For all statistics, either p-value number was reported or with n.s.=p>0.05, *=p<0.05, **=p<0.01, ***=p<0.001 and ****=p<0.0001.

2.3. Creation of a stable, inducible Piezo1 sensor – XLGenEPi

2.3.1. Selection of an appropriate inducible system

To visualise Piezo1 dynamics in cellular behaviour, the adapted construct will have to possess the following criteria: (1) allow for temporal control over the sensor's expression, (2) achieve increased imaging contrast during image acquisition and (3) the ability to produce stable clones of cell expressing GenEPi. By fulfilling these key requirements, we can image and investigate cellular Piezo1 dynamics, while minimising cytotoxicity and other negative cellular effects.

The GenEPi construct (**Figure 1.11**), created previously in the Pantazis lab[1], is controlled by the CMV promoter (**Figure 1.11 a, yellow block**), which strongly drives the expression of GenEPi in the successfully transfected host cells. The CMV-promoter system renders an overexpression of GenEPi, which poses limitations as mentioned above (Chapter 2.1). To address the limitations and fulfil the above-listed qualities, the genetic system generated for Piezo1-reporter has to be able to generate cell clones with stable, yet inducible expression of GenEPi-sensor.

To adapt our Piezo1-specific reporter to possess the three criteria described above, several gene editing methods, each with its own strengths and limitations, were considered.

(I) CRISPR-Cas9 System

The CRISPR-Cas9 system has gained immense popularity as a powerful genetic editing tool due to its simplicity, versatility, and efficiency. The system utilises a guide RNA (gRNA) to target specific genomic DNA sequences (e.g. gene or target genome site), and the Cas9 nuclease will induce a double-strand breaks (DSBs) at the target site. This system exploits the cellular genome repair process, like non-homologous end joining

(NHEJ) or homology-directed repair (HDR), to introduce gene mutations, insertions, deletions, or replacements. With the CRISPR-Cas9 system, we could potentially insert the GCaMP-sensor to the C-terminal of the cell's endogenous Piezo1 sequence. While this system offers high editing efficiency and the ability to introduce precise modifications, it may also lead to off-target effects and unintended mutations within the host cell genome.

(II) Transposon-Based Systems

Transposons are mobile genetic elements capable of moving from one location to another within the genome. Transposon-based systems, such as the Sleeping Beauty and PiggyBac systems, harness the transposons as vehicles for gene delivery and integration in various organisms, including mammalian cells. The transposon can efficiently integrate target DNA sequence into the host cell's genome with precision, making it a powerful tool for gene delivery and manipulation. Unlike viral vectors, the transposon-based systems do not induce significant immune responses or insertional mutagenesis, making it safer for use in gene therapy applications. However, the usage of these genetic delivery systems must be carefully titrated to prevent multiple copies integration, which may generate unintended side-effects.

(III) Viral Vectors Gene Delivery Systems

Viral vectors, such as Lentiviral vectors and Adeno-Associated Virus (AAV) vectors, are commonly used for their gene delivery and efficient transduction capabilities. Both Lentiviral and AAV vectors offers low immunogenicity transduction of both dividing and non-dividing cells. These viral vectors can be engineering to carry and delivery specific genetic payloads, including the CRISPR-Cas9 components and transposons systems, to targeted cells and tissues. Despite offering efficient gene delivery and long-term transgene expression, the viral vectors system carries the risk of insertional mutagenesis on host cells, and requires specialised viral production expertise and facilities.

Among these genetic editing methods, transposon-based systems, specifically the PiggyBac System, has been identified as my preferred tool for GenEPi-sensor construct genetic modification due to the following advantages:

(I) **Efficient Transposition:** The PiggyBac transposon exhibits efficient transposition activity, allowing for stable integration of transgenes into the host genome with high efficiency. This makes the PiggyBac System well-suited for integrating our GenEPi-sensor into the host cell's gene. In addition, a PiggyBac-based GenEPi expression system allows long-term expression of GenEPi-sensor, which is advantageous for generation of transgenic animal models.

(II) **Large Cargo Capacity:** The PiggyBac transposon can accommodate large DNA payloads, including entire genes or gene clusters, making it suitable for delivering our GenEPi-sensor, which is 13 kb in size.

(III) **Low Genomic Disruption:** Unlike viral vectors such as AAV or lentiviral vectors, which may disrupt endogenous genes upon integration, the PiggyBac System exhibits minimal genotoxicity and preferentially integrates into transcriptionally active genomic regions. This reduces the risk of unintended mutagenesis and enhances the safety profile of our GenEPi system.

(IV) **Broad Applicability:** The PiggyBac System is compatible with a wide range of host organisms, including mammalian cells, plants, and insects. This versatility makes it an attractive tool for the integration of our GenEPi-sensor across different biological systems.

From extensive literature and well-known genetic construct deposition databases survey, the XLone-GFP construct (**Figure 2.1**) was identified as the most suitable genetic system to adapt into the GenEPi construct. The XLone-GFP construct uses a Tet-On 3G inducible PiggyBac system[175]. Chemical regulation is the most common method used in biological setup to induce gene expression, due to the simplicity of its application. For example, in the tetracycline-ON (Tet-On) system, gene expression can be induced by simply adding tetracycline/doxycycline into the culture media[176].



(XLone-EGFP construct, 6.3kb)

Figure 2.1. XLone-EGFP construct gene map. A simplified, linearised schematic view of the XLone-EGFP construct[175] with the main features described – Tet-On 3G promoter (yellow) driving the EGFP (green) expression, reverse transactivator (maroon), Blasticidin-resistance gene sequence (orange), Ampicillin-resistance gene (beige) and piggyBac repeats (blue).

Key elements present in the XLone-GFP construct allowed us to fulfil the three qualities set out for an ideal inducible-GenEPi construct.

1. A third-generation TRE promoter (**TRE3GS; Figure 2.1, yellow block**), which will only be activated in the presence of Doxycycline (Dox) and is less likely to display leaked expression compared to previous versions.
2. A reverse transactivator (**rtTa; Figure 2.1, maroon arrow**), a crucial factor to the Tet-On inducible system that drives transcription activity in the presence of Dox.
3. A blasticidin-resistance gene (**BsdR; Figure 2.1, orange arrow**), which allows for selection in mammalian cells using blasticidin (BSD).
4. piggyBac inverted repeats (**Figure 2.1, blue triangle**), the site marks which enable high efficiency transposase-mediated gene integration into the host's genome.

Therefore, by employing XLone-GFP, an inducible-GenEPi construct will allow for temporal expression control with good imaging contrast and the ability to generate positive transgenic clones for stable GenEPi expression.

2.3.2. Inducible Piezo1-reporter engineering

To create an inducible version of GenEPi construct, I sub-cloned our GenEPi-sensor sequence into the XLone- genetic backbone, downstream of the TRE promoter site. In brief, restriction digestions were performed to (1) cut out the GenEPi (hPiezo1 + GCaMP-G4) sequence from the original construct (**Figure 2.2a**), and (2) remove the EGFP sequence from the XLone-GFP vector (**Figure 2.2b**). Digested products were then extracted and purified, before ligating together to create the XLGenEPi construct (**Figure 2.2 c**).

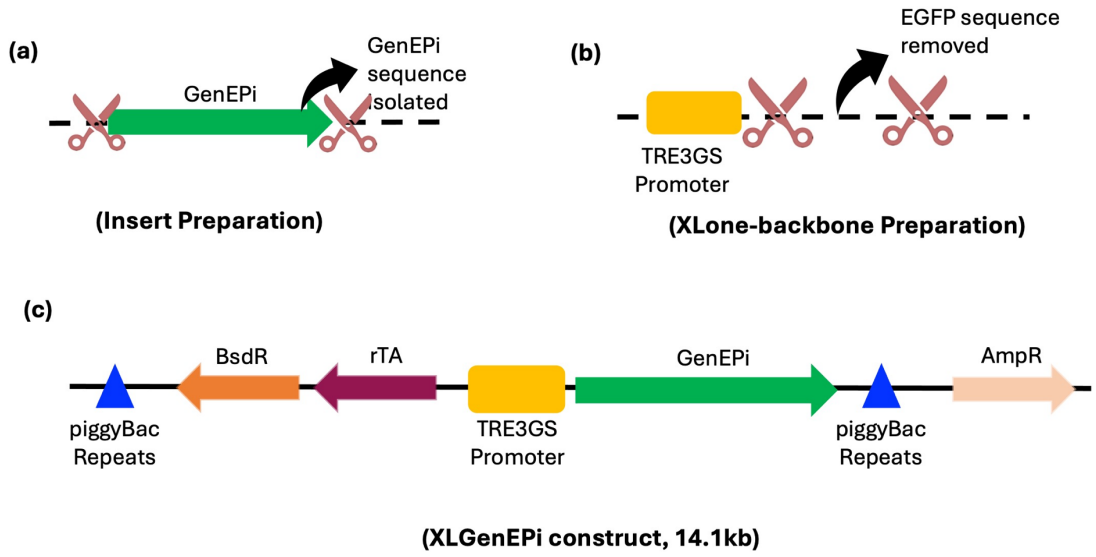


Figure 2.2. Molecular cloning strategy for XLGenEPi. (a) A representative schematic view of the GenEPi sequence prepared by performing restriction digestion on the original GenEPi construct. **(b)** A representative schematic view of the empty XLone vector with the EGFP sequence removed by performing restriction digestion of the original XLone-GFP vector. **(c)** A simplified, linearised schematic view of the XLGenEPi construct generated from molecular cloning.

The integrity of the cloned XLGenEPi product was first screened by performing restriction digestion (**Figure 2.3 a and b**) at different sites of the construct. Subsequently, the XLGenEPi cloning product was sent for gene sequencing (**Figure 2.3 c**), with a total of 14 primers (see Appendix 1) to ensure the quality of the construct, especially the GenEPi sequence. The cloned product which showed good nucleic acid quality from the confirmatory assays and no mutations in the XLGenEPi sensor sequence was selected as the final XLGenEPi construct, which was used in all subsequent experiments in this project to study the dynamics of Piezo1 activities.

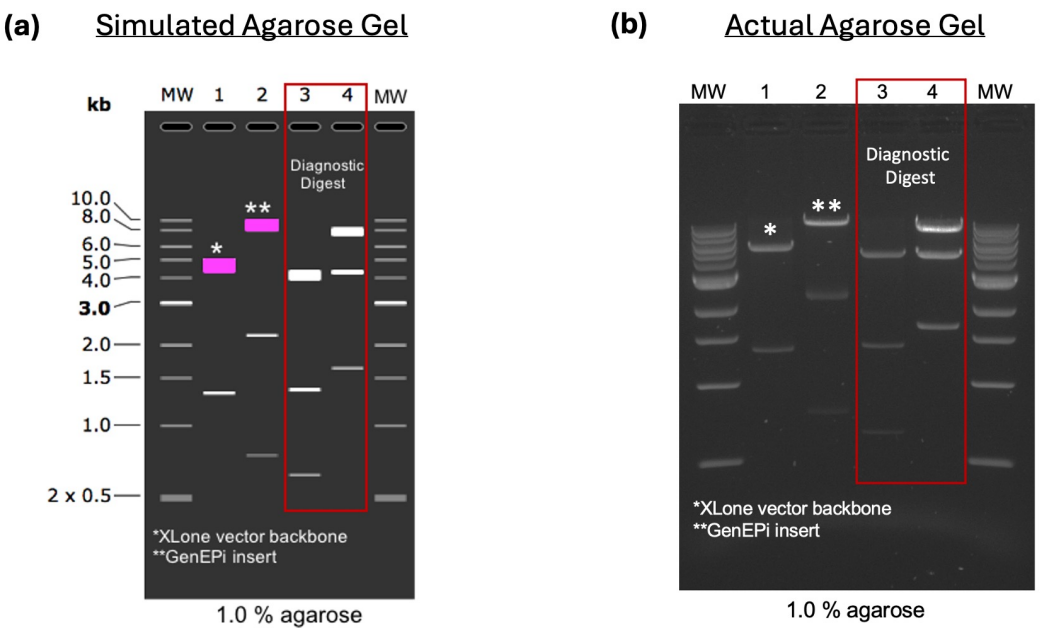




Figure 2.3. XLGenEPi construct integrity and quality screening. (a) A representative gel picture simulated with Snapgene® software was used to plan for the restriction digestion and confirmation of XLGenEPi. **(b)** Gel electrophoresis picture was taken after the actual restriction digestion to confirm the XLGenEPi construct. In both picture (a and b): Molecular weight ladder used = 1 kb ladder; Lane 1 = XLone-GFP digested with KpnI and SphI; Lane 2 = GenEPi construct digested with HindIII and SphI; Lane 3 = Original GenEPi digested with (Negative control); Lane 4 = XLGenEPi construct digested with (Positive). **(c)** A snapshot of the XLGenEPi gene sequencing results. XLGenEPi sequence and the sequencing results were aligned to confirm the integrity of the clones. Individual nucleotides have been recorded and the quality of the sequencing is displayed as a bar chart at the bottom.

2.3.3. Generating the piggyBase construct for XLGenEPi co-transfection in mammalian cells.

In order to integrate our GenEPi-sensor sequence, from the XLGenEPi construct, into the host cells' genome, I generated a second construct carrying the genetic sequence of the transposase protein. The transposase protein expressed transiently in the transfected cells will recognise and act on the piggyBac inverted repeats within the XLGenEPi construct. This piggyBase construct was created by cloning the CMV-promoter,

amplified from the original GenEPi construct, into a plasmid carrying the piggyBase sequence, termed hGFAP-pBase (**Figure 2.4 a**). The CMV-pBase construct will allow the host cells to constitutively express the transposase enzyme required for successful genomic integration of sequence between the piggyBac inverted repeats (**Figure 2.2 c, blue triangles**). Therefore, allowing me to integrate our GenEPi-sensor sequence into mammalian host cells when I co-transfect this CMV-pBase construct with our XLGenEPi construct (**described in Section 2.3.2**).

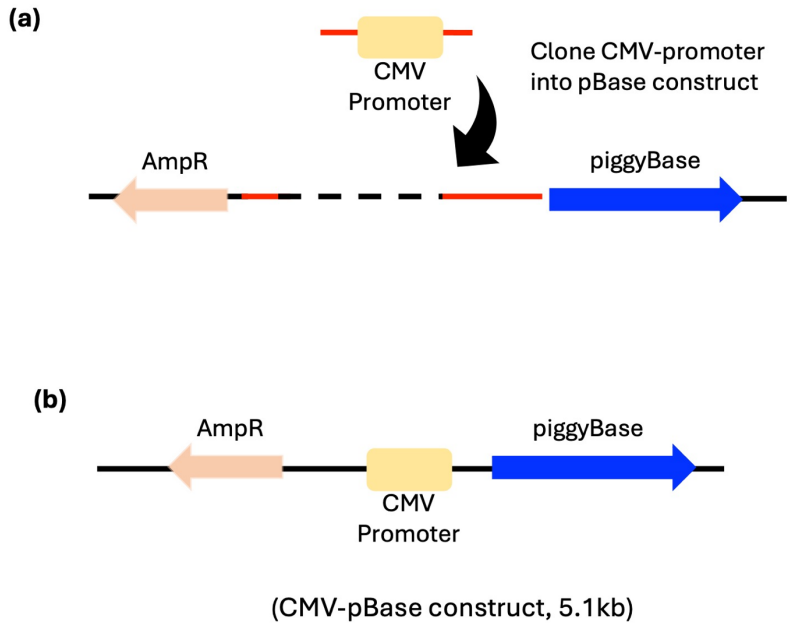


Figure 2.4. Molecular cloning of CMV-pBase construct. (a) A representative schematic view of the molecular cloning strategy to create the piggyBase construct. **(b)** A simplified, linearised schematic view of the CMV-pBase construct generated the co-transfection with XLGenEPi construct in mammalian cells.

2.4. *In vitro* characterisation of XLGenEPi

2.4.1. Transfected HEK 293T cells remain viable after co-transfection of XLGenEPi and CMV-pBase constructs

With both the XLGenEPi and CMV-pBase constructs ready, I first evaluated the efficiency of the co-transfection of both plasmids on a mammalian cell line, human embryonic kidney (HEK) 293T cells. The co-transfection reactions were prepared based on a 1:1 plasmid molecular ratio (XLone-GFP or XLGenEPi : CMV-pBase) because the final

genomic size of the XLGenEPi construct is three times the size of the XLone-GFP and CMV-pBase plasmids. To evaluate the transfection efficiency, I performed confocal live imaging under 488 nm laser excitation after Dox-induction to visualise for fluorescence signal. Transfected HEK 293T cells were treated with either DMSO (control group) or with 200 ng/ml Dox to induce either EGFP or XLGenEPi expression. I observed that transfected-HEK 293T cells treated with DMSO (- Dox groups) did not display any fluorescence under 488 nm excitation. In contrast, Dox-induced cells (+ Dox groups), which are successfully transfected, exhibited fluorescence signal under 488 nm excitation (**Figure 2.5 a**). This fluorescence observed after 488 nm excitation is indicative of cells expressing either EGFP or XLGenEPi after the Dox-induction procedure. The co-transfection efficiencies were evaluated based on the percentage of EGFP- or XLGenEPi-positive cells counted from the total imaged cell population. The transfection efficiencies of XLone-GFP and XLGenEPi were reported to be 15% and 78% respectively (**Figure 2.5 b**).

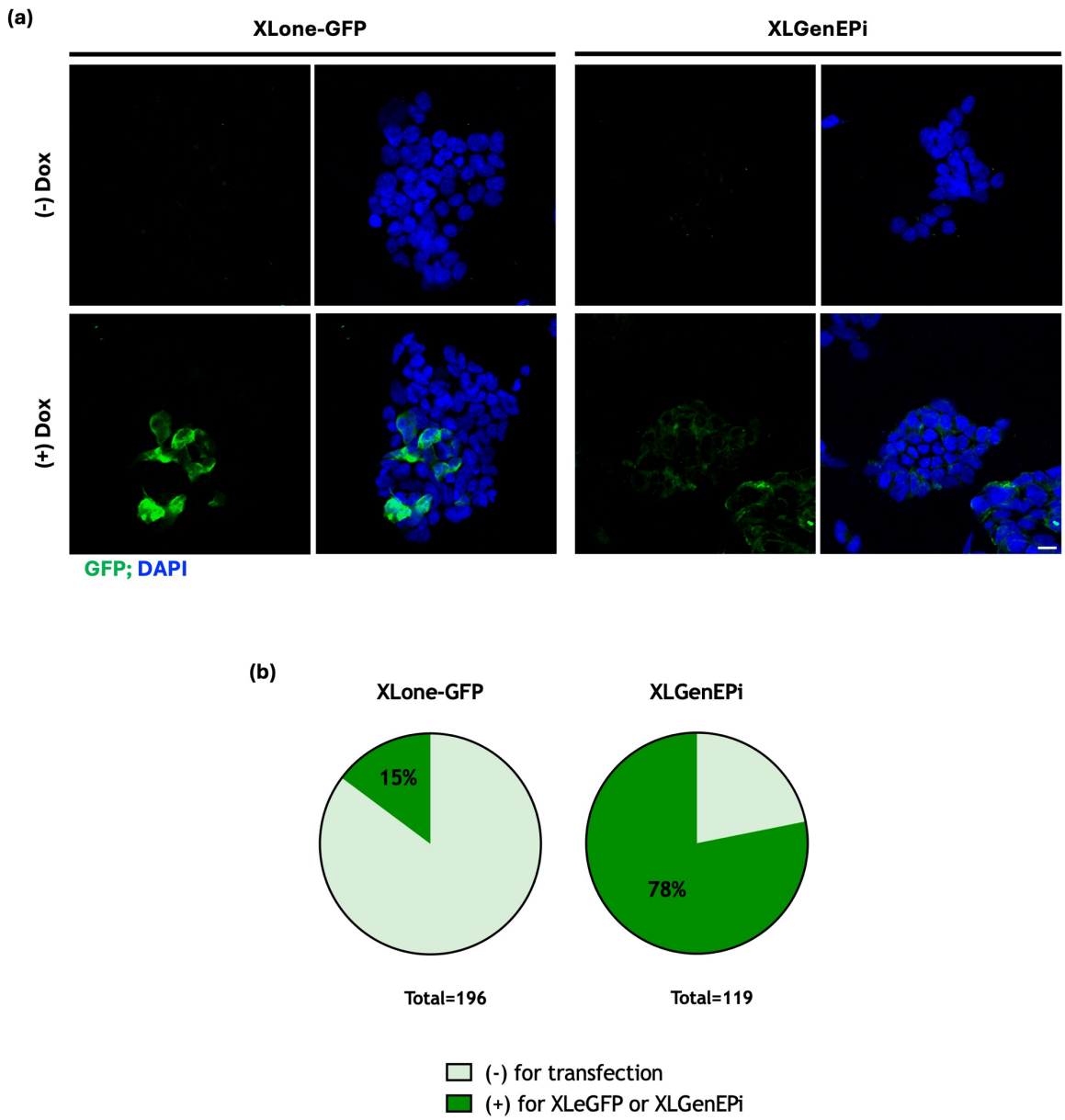


Figure 2.5. XLone-GFP and XLGenEPi co-transfection efficiency evaluation. (a) Representative confocal images of HEK 293T cells co-transfected with either XLone-GFP or XLGenEPi, with CMV-pBase construct. Co-transfected cells were either treated with either DMSO (control group) or 200 ng/ml of Dox (treatment group). Confocal images presented at 60x magnification (taken with 20x dry objective, and 3x optical zoom factor). Scale bar = 15 µm. **(b)** Pie charts showing the co-transfection efficiencies of XLone-GFP and XLGenEPi. Population distributions are successful for XLone-GFP and XLGenEPi co-transfection concluded at 15% and 78% respectively.

2.4.2. Establishing a stable, GenEPi-expressing cellular clone via the XLGenEPi plasmid

To investigate the efficiency of genome integration into mammalian host cells, I challenged co-transfected HEK 293T cells with the antibiotic, blasticidin (BSD). Successful co-transfection ensures host cells constitutively express transposase enzyme through the CMV-pBase construct. The expression of the transposase enzyme

allows genome integration of XLGenEPi through the piggyBac inverted repeats. Therefore, a successful genome integration renders host cells BSD-resistance capability. We first tested the selectability of the BSD-resistance gene and second outlined the conditions for positive selection in positively co-transfected cells. Even though the manufacturer's instruction and previous literature have advised BSD working treatment protocols, the BSD-treatment conditions vary for cell-types[177–178]. Therefore, both the ideal concentration of BSD and the length of BSD treatment need to be determined for GenEPi-positive cell selection. To this end, both WT and transfected cells were cultured in a six-well plate until they reached 70-80% confluency. Then the cells were subjected to varying concentrations of BSD, ranging from 4 – 14 µg/ml, over several days. The criteria for a positive selection of XLGenEPi-transfected cells are:

1. Total eradication of GenEPi-negative cells (determined by the clearing of all WT cells at a given BSD concentration); and
2. Survival of GenEPi-positive cells to create individual clones.

From this experiment, all WT cells being treated with 10 – 14 µg/ml were dead by day(s) 6 and 7. This served as an indication that GenEPi-negative cells were also eliminated from the transfected cell population. Surviving transfected cell populations at Day 7 were mostly distributed single-cellularly across the culturing surface of the six-well plate (**Figure 2.6; Day 7**). BSD-treated HEK 293T cells were left in fresh DMEM complete media (without BSD) for another three days for the cells to recover and for the singular positive cells to grow into a cell colony suitable for colony picking (**Figure 2.6; Day 10**).

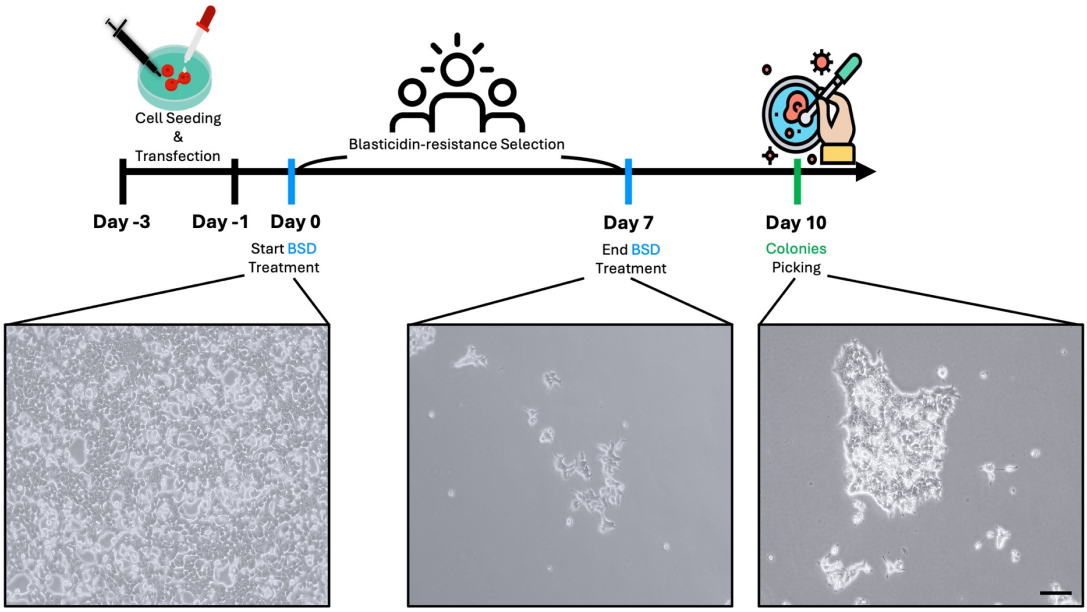


Figure 2.6. Timeline for blasticidin-resistance selection of XLGenEPi-transfected cells. Co-transfected cells were treated with the ideal concentration of blasticidin (BSD) antibiotic for a period of 7 days consecutively. Surviving cells are positively co-transfected cells with successful genome integration for our XLGenEPi construct.

With the length of time for BSD treatment established, the selection efficiency of the respective BSD concentrations was determined by calculating the percentage of GenEPi-expressing cells from the survival colonies. As before, Dox-induction was implemented on Day 10 post-BSD-selection (**Figure 2.7 a**). Then cell populations were imaged and tallied for fluorescence under 488 nm excitation (**Figure 2.7 b**). The three lower BSD concentrations were ineffective for selecting XLGenEPi-positive cells because the total cell population expressing GenEPi amounted to less than 25% (**Figure 2.7 c**). While 10 µg/ml of BSD treatment was the most effective, with more than 70% GenEPi-expressing cells within the surviving population (**Figure 2.7 c**). Therefore, I conclude that 10 µg/ml of BSD, over seven consecutive days, is the optimal treatment for selecting GenEPi-positive HEK 293T cells.

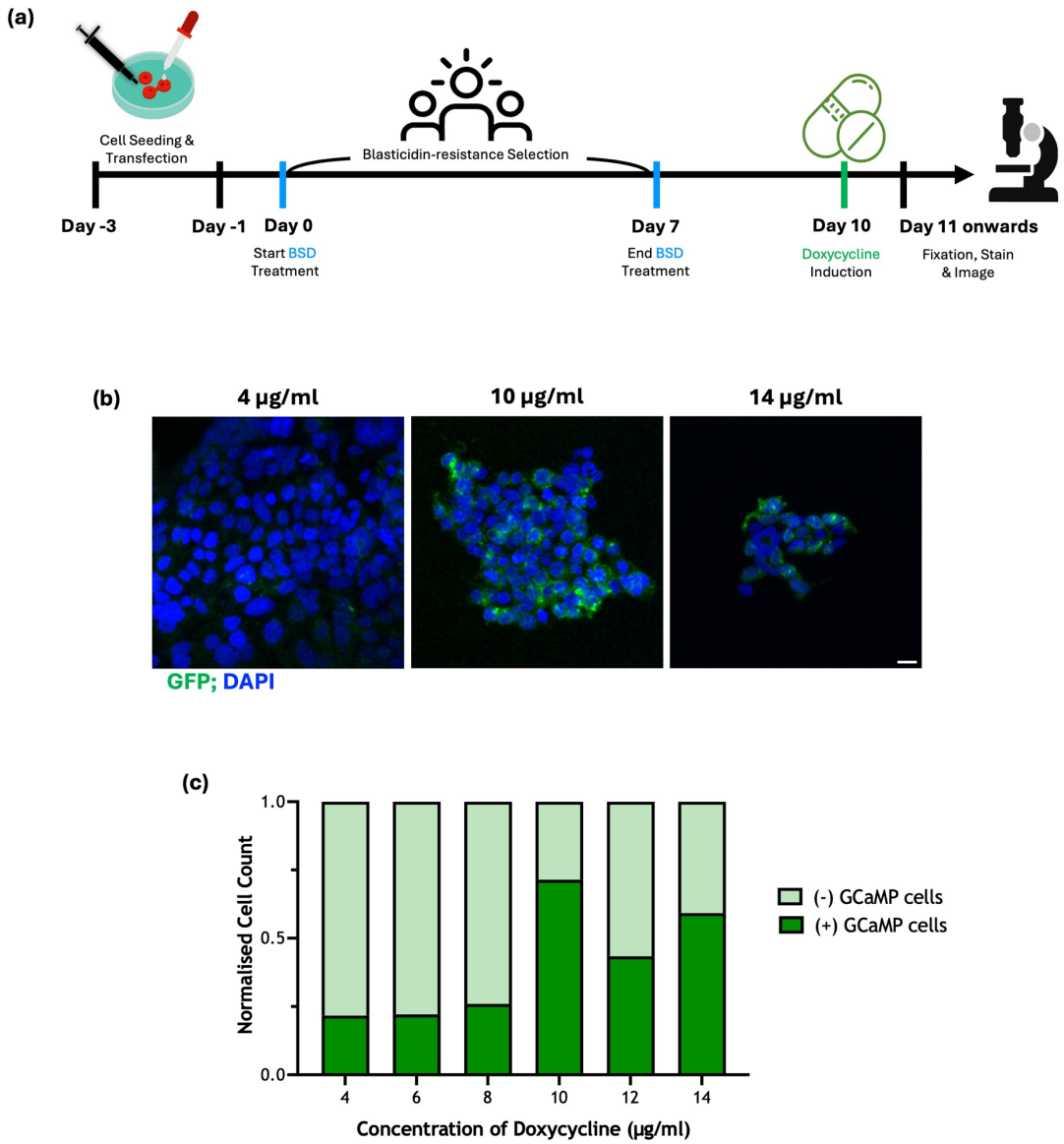


Figure 2.7. Optimal concentration of blasticidin (BSD) treatment for XLGenEPi-positive cell selection. (a) Representative timeline for evaluating BSD-selection efficacy in co-transfected HEK 293T cells. **(b)** Representative confocal images showing the surviving population of co-transfected cells after 7 days of BSD treatment at different concentrations, namely 4, 10 and 14 µg/ml. Green fluorescence represents the GenEPi signal under 488 nm illumination, while blue fluorescence represents DAPI staining under 405 nm illumination. Confocal images presented at 60x magnification (taken with 20x dry objective, and 3x optical zoom factor). Scale bar = 15 µm. **(c)** Bar charts depicting the BSD-selection efficiency for XLGenEPi-positive cells at various BSD concentrations, ranging from 4 to 14 µg/ml. From these results, it seemed BSD-treatment of 10 µg/ml for 7 days is the most effective at selecting XLGenEPi-positive HEK cells.

Using the BSD resistance as a cell selection method, I was able to isolate positively-transfected and successfully integrated cells by subjecting the cells to an appropriate treatment of BSD. Following the BSD treatment (**Figure 2.6**), individual cell colonies were manually isolated for clonal expansion. I manually picked a total of six clones for

individual clonal expansion. These colonies were presumed to be identical cell clones of a particular single cell derived after the BSD-selection period. To verify that the clones isolated were truly carrying the XLGenEPi construct in their genome, I performed four different polymerase chain reactions (PCRs) to identify the presence of four main elements of the XLGenEPi construct. The four elements detected from the PCRs are: (1) GCaMP part of the GenEPi sequence, (2) TRE3G promoter sequence, (3) Tet-On transactivator gene sequence, and (4) part of the BSD resistance gene sequence.

Genomic DNA samples were harvested from the six presumed GenEPi-positive HEK 293T clones for the confirmation of the XLGenEPi integration. Although at slightly different PCR band intensities, all six clones showed positive bands for the PCRs of the four elements (**Figure 2.8**). This is indicative of successful XLGenEPi integration into the host cell's genome in all isolated HEK 293T clones. Clone B consistently displayed brighter band intensity in the PCRs for all four XLGenEPi construct elements, which might suggest that there are more copies of XLGenEPi integrated into the genome. However, a normal PCR (like this) is hardly an accurate indication of the gene copy numbers, and rather only a suggestion.

Thus far, I have confirmed that our new construct is suitable and safe for mammalian cell application; and can create stable, GenEPi-expressing cell clones. Thereafter, my *in vitro* construct characterisation effort focused on interrogating and assessing the XLGenEPi construct's potential to: (1) allow for temporal control over the sensor's expression, (2) achieve increased imaging contrast during image acquisition, and (3) function like an endogenous Piezo1 protein – so that I can examine Piezo1-specific activity. The XLGenEPi-positive clones generated, allow me to extend our investigation into the dynamics of cellular Piezo1 activities.

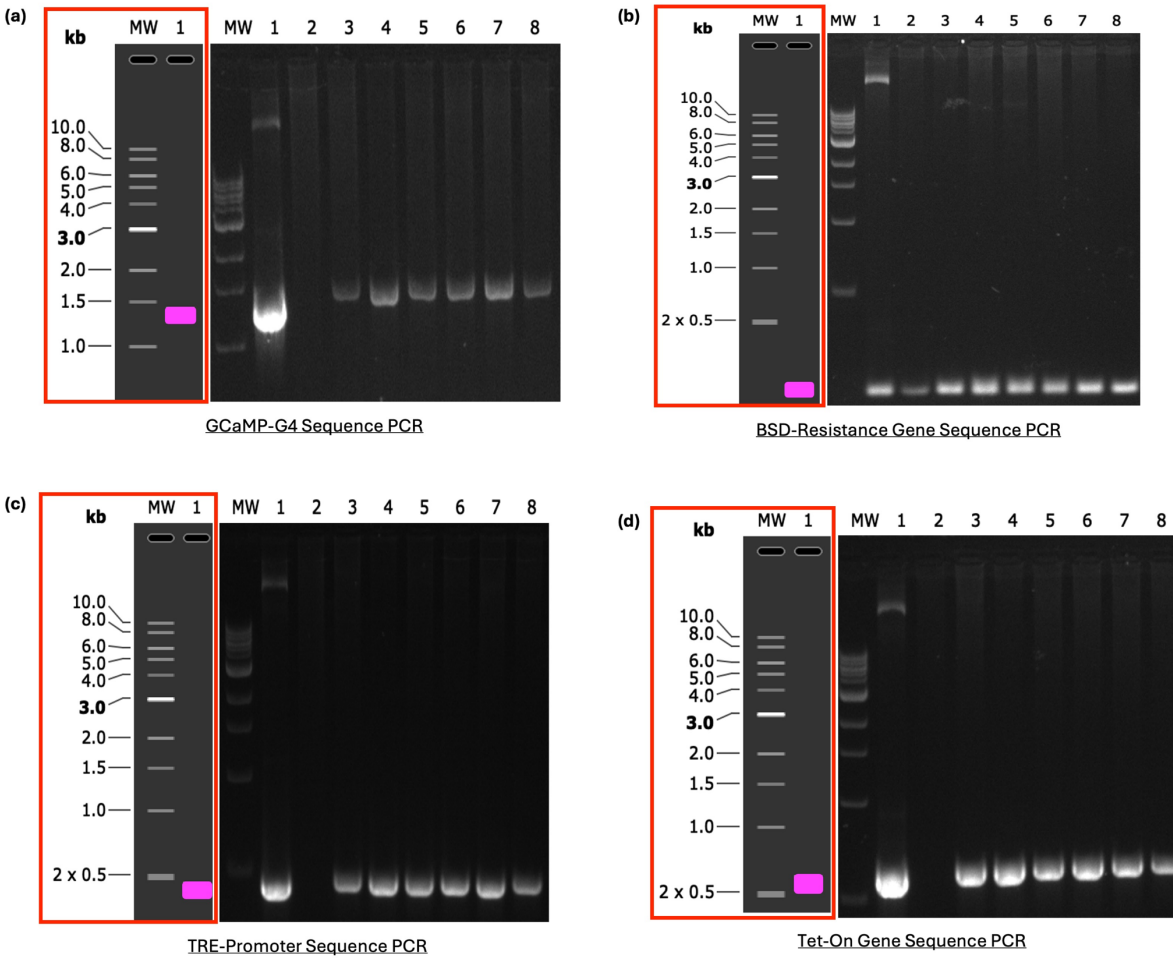


Figure 2.8. Gel electrophoresis confirmed the successful genome integration of the XLGenEPi construct into selected HEK 293 clones. Image(s) of the respective simulated agarose gel products generated by Snapgene® software are presented on the left of each PCR picture. PCR electrophoresis was performed on 1% agarose gel of PCR products for all four gene segments, namely: **(a)** GCaMP gene. Product size = 1414 bp. **(b)** BSD-resistance gene. Product size = 153 bp. **(c)** TRE3G promoter. Product size = 472 bp. **(d)** Tet-On protein. Product size 614 bp. MW = 1 kb molecular weight ladder. In simulated agarose gel pictures: Lane 1 = PCR product of respective genes. In actual agarose gel pictures: Lane 1 = XLGenEPi plasmid DNA (Positive control); Lane 2 = PCR product from wild type HEK 293 genomic DNA (Negative control); Lanes 3 - 8 = PCR products from Clones A – F.

2.4.3. XLGenEPi-HEK cells express GenEPi-sensor under Dox-inducible treatment

By introducing our GenEPi-sensor sequence into the XLone- backbone, I am capitalising the Tet-On 3G system for its increased temporal control of the downstream gene expression. With the doxycycline-inducing system, consisting of a doxycycline-binding transactivator protein (rtTa; **Figure 2.1, maroon arrow**) and low background promoter (TRE3GS promoter; **Figure 2.1, yellow box**), I can efficiently control GenEPi expression within host mammalian cells.

Using the XLGenEPi-HEK clones I generated (described above in **Section 2.4.2**), I can characterise and assess the GenEPi function. I first evaluated their inducibility of GenEPi expression (under the Tet-On 3G system) on the cultured HEK 293T clones by subjecting them to 200 ng/ml of Dox treatment for more than 18 hours, before conducting live, fluorescence imaging. By measuring the basal fluorescence intensity under 488 nm excitation, I can evaluate the reliability of the inducible expression of GenEPi post Dox-treatment (**Figure 2.9 a**). Following Dox-induction, there is a 4.86-fold increase in basal fluorescence intensity detected under 488 nm excitation (**Figure 2.9 b**). Whereas, HEK 293T clones not treated with Dox exhibited minimal fluorescence under 488 nm excitation (**Figure 2.9 a**), similar to WT HEK 293T cells. This, therefore, validated the reliability of inducible GenEPi-expression in the generated HEK 293T cell clones. However, any relative GenEPi fluorescence intensity differences brough about by my XLGenEPi construct modifications could not be comment, due to the lack of original GenEPi construct control in my transfection experiment.

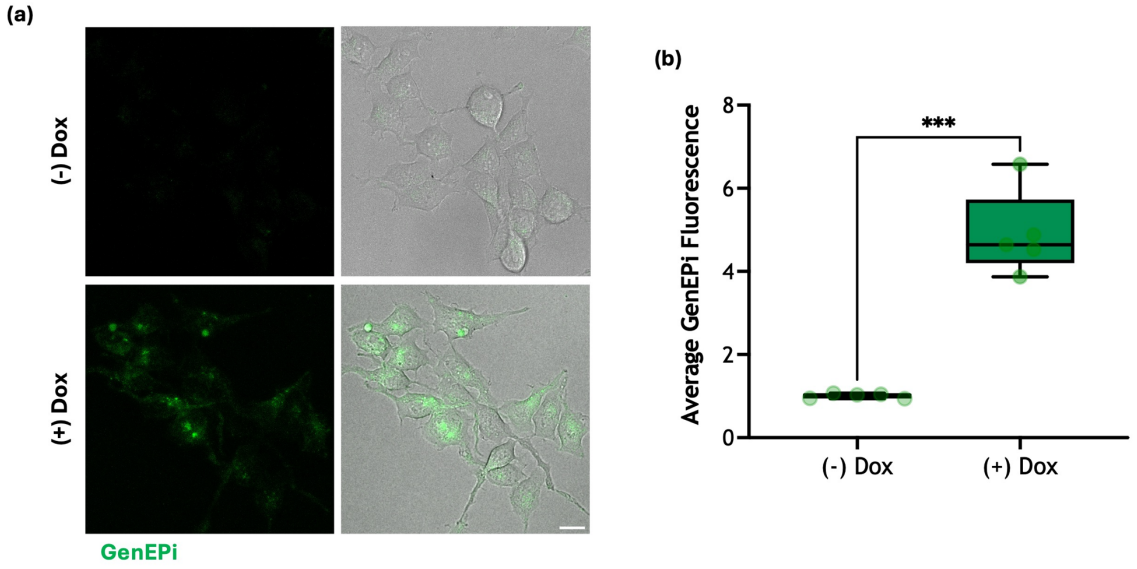


Figure 2.9. GenEPi is only expressed in XLGenEPi-positive HEK clones under the influence of Doxycycline (Dox). (a) (Top panel) Dox-inducible XLGenEPi- HEK cells do not show any fluorescent signal before Dox treatment. (Bottom panel) Dox-induced XLGenEPi- HEK cells displayed GenEPi (green) expression after Dox induction. Confocal images presented at 60x magnification (taken with 20x dry objective, and 3x optical zoom factor). Scale bar = 15 µm. **(b)** Representative graph showing the basal fluorescence intensity differences in XLGenEPi-positive HEK clones before and after Dox induction. N = 5 experimental repeats (with average of 56 cells for (-) Dox, and 42 cells for (+) Dox) *** , $p < 0.001$.

In addition to evaluating the inducibility of GenEPi expression in my XLGenEPi-positive HEK 293T clones, I characterised the expression pattern of the sensor after Dox-induction. Like the original GenEPi construct, which carries a CMV-promoter, our XLGenEPi construct still exists as an overexpression system, once the cells are treated with Dox. An overexpression system was shown to confer mechanical sensitivity to our HEK 293T clones, as HEK cells innately express low levels of Piezo1[1,180,181]. However, the expression of GenEPi-sensor is now governed by the presence of Dox. Without Dox, the GenEPi-sensor should not be expressed and any GenEPi-sensor already present should follow the endogenous Piezo1 protein recycling timeline. Consequently, it is crucial to investigate (i) how long will GenEPi be expressed after an episode of Dox-induction and (ii) if the GenEPi-expression can be re-induced.

To investigate that, I performed a Dox-withdrawal experiment to track the GenEPi-signal initiation and decay. By measuring the fluorescence intensity of the Dox-induced, XLGenEPi-positive HEK 293T clones over days after the first Dox-initiation and re-applying Dox after the GenEPi-signal is diminished, I can monitor the sensor's expression under the influence of the Tet-On 3G system. HEK 293T clones were cultured up to 70% confluence prior to the first Dox-induction. After this, daily live-imaging sessions were performed to image and analyse changes in the fluorescence intensity under 488 nm excitation after Dox was removed from the culture (**Figure 2.10 a**). Following Dox-induction, GenEPi fluorescence intensity decreased over the next 72 hours until it returned to the minimal basal fluorescence level under 488 nm excitation (**Figure 2.10 b and c**). By fitting my fluorescence intensity decay data to an exponential decay curve, the half-life of GenEPi in the HEK 293T clones was predicted to be approximately 30 – 32 hours. It was observed that HEK 293T clones remained healthy and normal, even after the overexpression of the GenEPi-sensor for three days – as we tracked the GenEPi-expression decay pattern (**Figure 2.10 b**). The same cultured XLGenEPi-clones were inducted with Dox-treatment, a second time, the day after the GenEPi-fluorescence signal returned to basal (Day 5; **Figure 2.10 a**). Live-imaging was again performed the day after the second Dox-induction to measure the the fluorescence intensity under 488 nm excitation (**Figure 2.10 b**). The GenEPi-fluorescence intensity measure after the second Dox-induction was compared to that of the first Dox-induction (0 hrs point; **Figure 2.10**

a). To which, I detected no significant difference in the fluorescence intensity between the first- and second- inductions (**Figure 2.10 d**). This result implies that my XLGenEPi-positive HEK 293T clones can be used and re-induced to express GenEPi, without any compromising to the expression level.

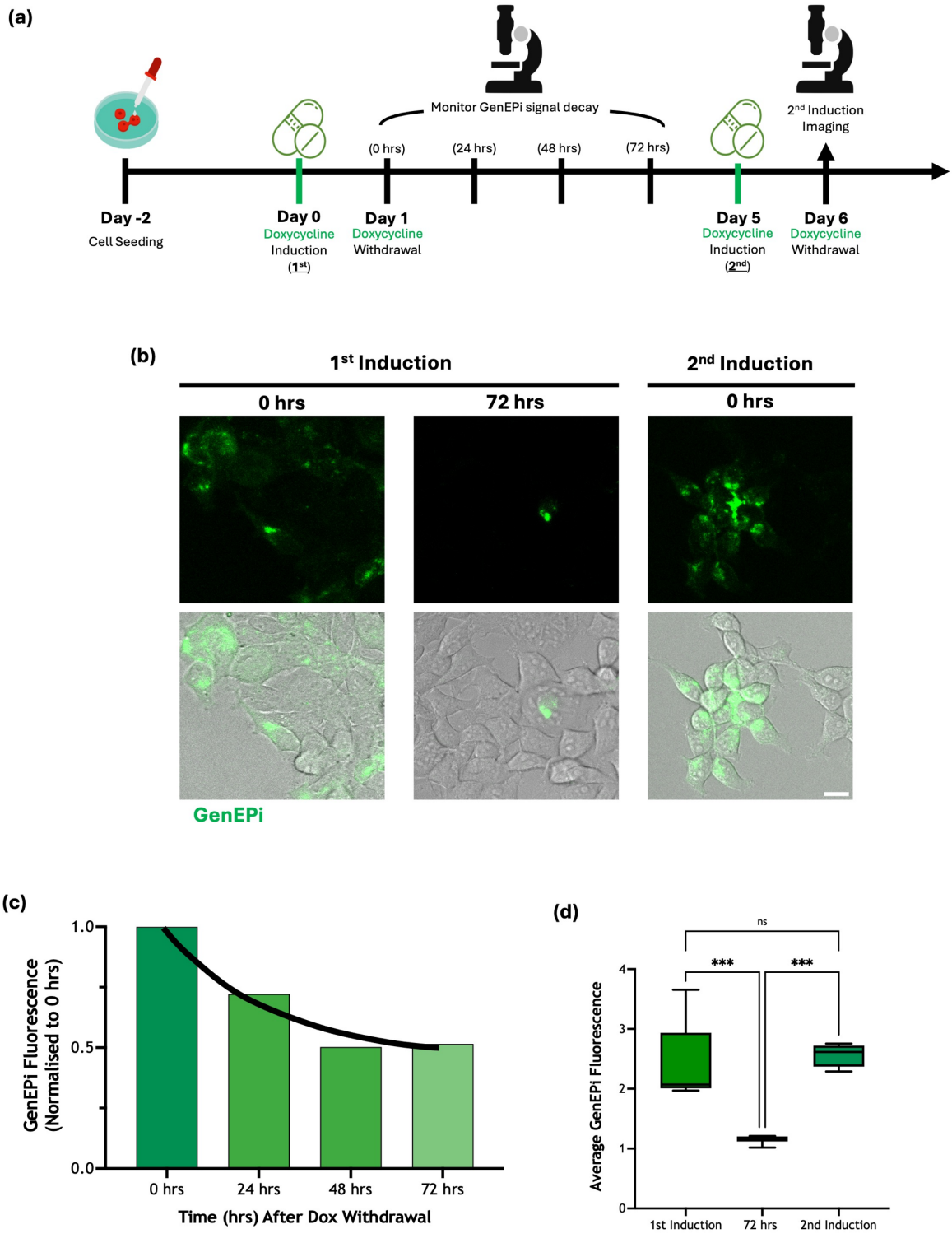


Figure 2.10. Live GenEPi-signal tracking revealed re-inducible expression in HEK clones lasting three days. (a) Timeline of Dox-withdrawal and re-induction experiment. After initial Dox-induction, XLGenEPi-clones were imaged every 24 hours for four days to monitor the fluorescence decay. Cells were re-induced on Day 5 and imaged again after 24 hours. Each time point shown on the timeline is 24 hours apart. (b) Representative confocal images of GenEPi- (green) expressing HEK clones at different time points. Confocal images presented at 60x magnification (taken with 20x dry objective, and 3x optical zoom factor). Scale bar = 15 µm. **(c)** Normalised GenEPi fluorescence intensity over the course of four days. Data (black line) was fitted with an exponential decay model. The data was normalised against the fluorescence intensity at 0 hrs, as 1. (d) Representative bar charts of GenEPi fluorescence intensity differences at three different time points. GenEPi fluorescence intensities displayed no significant differences between the first and second Dox-inductions. N = 3 experimental repeats (with average of 52 cells analysed for each time-point). n.s, non-significance, $p>0.05$, and *** , $p < 0.001$.

2.4.4. GenEPi sensor responds reliably to Piezo1 chemical perturbations

Finally, in the characterisation of our XLGenEPi-strategy, I validated the integrity of the expressed GenEPi-sensor within the clones, primarily the functionality of the Piezo1 channel module. Using chemical perturbations, both agonistic and antagonistic, we tested GenEPi's functionality in the XLGenEPi-positive clones.

Among millions of screened compounds, Yoda1 has been identified as a Piezo1-specific agonist, and remained the only compound known to target Piezo1 specifically. I exposed the XLGenEPi-positive clones to 10 µM of Yoda1 (post Dox-induction) and measured the fluorescence intensity changes under 488 nm excitation. The fluorescence intensity increased significantly after Yoda1 treatment (**Figure 2.11 a**). When calculating the F/F_0 differences, I noted that there was an increase of at least a 4-fold in fluorescence intensity after Yoda1 application (**Figure 2.11 b**). This result confirms that GenEPi-recorded responses are specific to Piezo1's activity.

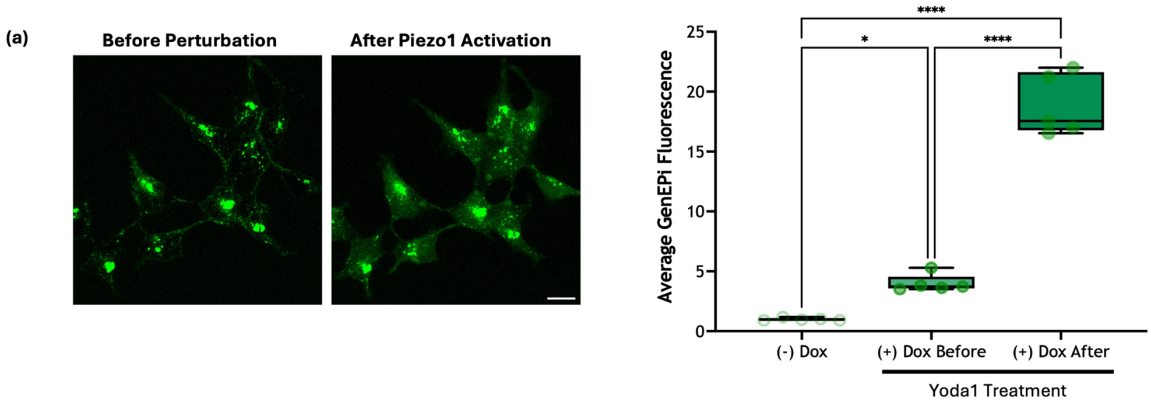


Figure 2.11. XLGenEPi-HEK clones expressing GenEPi-sensor respond to Piezo1-specific agonist, Yoda1. (a) Representative confocal images of GenEPi-signal (green) activation before and after 10 μM Yoda1 treatment. Images taken under 60x optical magnification. Scale bar, 15 μm. **(b)** Representative graph showing 10 μM Yoda1 treatment increase the GenEPi fluorescence intensity in XLGenEPi-HEK 293T clones. Single cell fluorescence intensity values measured before and after Yoda1 treatment normalised against WT control cells. The experiment was independently repeated thrice, with three biological and three technical repeats. N = 5 experimental repeats (with average of 32 cells for (-) Dox, and 38 cells for (+) Dox Before/After). *, $p<0.05$, and **** , $p<0.0001$.

In addition to Piezo1-specific activation (by Yoda1), we conducted an antagonistic perturbation to inhibit the Ca^{2+} ion channels. Here, I subjected the XLGenEPi-HEK clones to ruthenium red (RR), a generic Ca^{2+} ion channel inhibitor, to inhibit the activation of Piezo1, along with other Ca^{2+} ion channels. I first saw a spike in GenEPi fluorescence signal after the introduction of Yoda1 (agonist), but GenEPi-signal returned to baseline shortly after the addition of RR (antagonist) (**Figure 2.12**). By interrogating our inducible construct and the XLGenEPi-positive HEK 293T clones, I reinforce that the channel functionality and ion selectivity of Piezo1, within the GenEPi-sensor, were preserved, in the sensor's response to Piezo1-specific agonist, Yoda1 (**Figure 2.11 and Figure 2.12**), and the generic Ca^{2+} ion channel, RR (**Figure 2.12**).

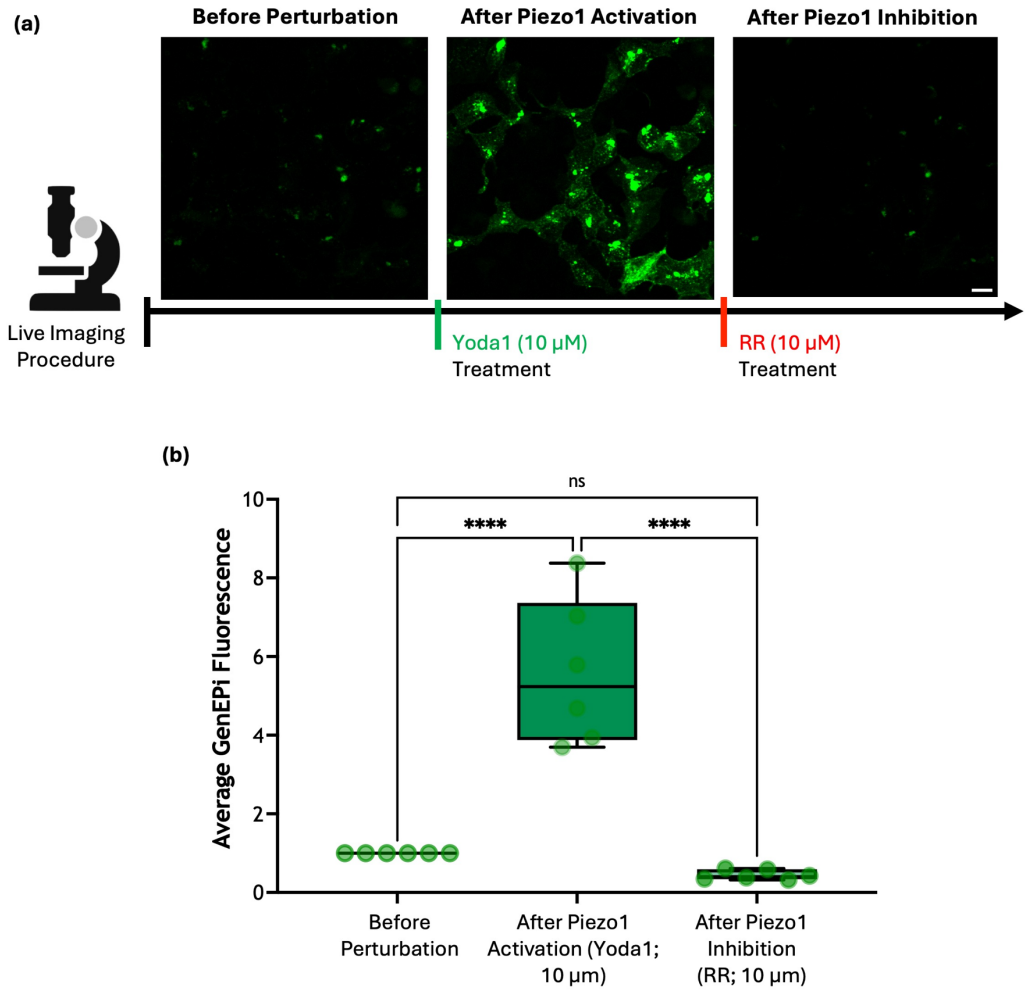


Figure 2.12. *in vitro* characterization of the GenEPi-sensor shows that the reporter has functional specificity without affecting Piezo1 channels inherent features. (a) Representative live-imaging example of GenEPi-signal (green) activation after 10 μM Yoda1 treatment and signal inhibition after 10 μM RR treatment. Images taken under 60x optical magnification. Scale bar, 15 μm. **(b)** Representative graph showing 10 μM Yoda1 treatment increase the GenEPi fluorescence intensity in XLGenEPi-HEK 293T clones, and GenEPi-signal returned close to baseline after application of RR. Single-cells fluorescence intensity values measured before and after Piezo1 perturbations normalised against single-cells fluorescence intensity values from before chemical perturbations. Experiment independently repeated thrice, with three biological and three technical repeats. N = 5 experimental repeats (with average of 31 cells analysed for the live-imaging data). n.s, non-significance, $p>0.05$, and **** , $p<0.0001$.

2.5. Discussion

Piezo1, like other ion channels on the cell membrane, has dynamic activities, which occurrences take place within nano- to micro- seconds. Being mechanosensitive, Piezo1's activity is triggered by the changes in membrane tension, resulting from mechanical forces. GenEPi has been generated as a targeted tool for distinguishing

Piezo1-specific activities within cells, as optical readouts[1]. In this chapter, I described my modification approach by introducing the following key new features to the original construct:

(1) A Tet-On 3G promoter system upstream of our GenEPi-sensor sequence which ensures inducible expression of GenEPi, through Dox-treatment.
(2) The BSD-resistance gene which provides an option of selection for positively transfected cells.
(3) piggyBac repeats which allow construct-genome integration into transfected host cells, in the presence of transposase enzyme (in our case, the form of CMV-pBase construct).

Whilst showing the benefits of the new elements in the XLGenEPi construct, I also proved the preservation of the reliability of GenEPi as a Piezo1-specific output. However, the lack of the original GenEPi construct controls in my experiments disallowed me to compare and comment the relative influence in the GenEPi-sensor fluorescence intensity after our XLGenEPi construct modification.

2.5.1. The "XLone-" cloning & selection strategy

The GenEPi-sensor has proven robust and reliable as an optical tool for Piezo1's functional output, yet the genetic backbone of the construct carrying the sensor sequence presents limitations once transfected into a cell model (**described in Section 2.1**). One of the main limitation we prioritise to address in the original GenEPi-construct[1], in the adaptation elaborated in this chapter, is the transient overexpression of GenEPi-sensor within transfected cells. By replacing the backbone of the construct with an inducible and selectable version, we aimed to have a new construct, XLGenEPi, adequate for the study of more intricate cellular phenomena involving Piezo1. The molecular cloning process of replacing the backbone of the original construct has been described in **Section 2.4.2**. After ensuring the genetic integrity of the XLGenEPi, we characterised the inducible construct's transfection efficiency, new genetic elements, as well as the functionality of the GenEPi-sensor as a Piezo1-specific optical readout.

Co-transfection with the CMV-pBase construct was carried out to allow genome integration by a transposase-mediated cut-and-paste mechanism. In evaluating the

efficiency of our co-transfection, a control reaction was set up with the XLone-GFP plasmid, where our XLone-backbone was derived. The transfection efficiency of XLGenEPi-transfected cells reported here is 78%, as compared to the 15% from the XLone-EGFP co-transfection reaction (**Figure 2.5**). With a molecular size ratio of 1:2.2 (XLone-EGFP : XLGenEPi), it seems unlikely that the XLGenEPi co-transfection reaction would be 5 times more effective than that of XLone-GFP[182]. In addition, the reported transfection efficiency for XLGenEPi co-transfection in HEK 293T cells was higher than previous transfection study done using Lipofectamine P3000® and single-stranded oligonucleotides[183]. During the co-transfection, the amount of DNA used in transfection was scaled by a factor of 2.2, using XLGenEPi as the reference, to account for the size difference between the two plasmids. This is to ensure that there are an equal number of plasmids introduced, as well as equal chances of the two different plasmids (XLGenEPi or XLone-GFP and CMV-pBase) entering a cell during transfection. With 1 µg of XLGenEPi plasmid DNA as the reference, it is possible that the amount of XLone-GFP DNA used was not sufficient. Hence, the significantly lower co-transfection efficiency in the XLone-GFP reaction.

In addition, the derivation of the co-transfection efficiency was manual counting of samples from fluorescence images, which potentially opened up room for human errors. When doing manual counting from fluorescence images, it is crucial to have a sufficiently balanced image contrast so that one can accurately discern between true positive and false positive signals. As shown in **Figure 2.5 a**, the fluorescence intensity readout for the XLone-GFP reaction is significantly brighter than that of XLGenEPi's. The fluorescence intensity comparison was at least a 5-fold difference between eGFP and GCaMP-G4 (**Figure 2.13**). With the GenEPi fluorescence signal being much dimmer, the margin of error to conduct manual counting will be larger. The molecular size difference of the translated protein may be a contributor to the difference in fluorescence intensity after Dox-induction. Our GenEPi-sensor is approximately 35 times larger than an EGFP molecule, sitting at ~ 950 kDa for GenEPi (Piezo1 + GCaMP-G4) to 26.9 kDa for EGFP[184–186]. As smaller gene/protein tend to have higher rate of gene translation and protein production[187], it is possible that more molecules of EGFP were being produced within the XLone-GFP transfected cells creating a large difference in fluorescence intensity.

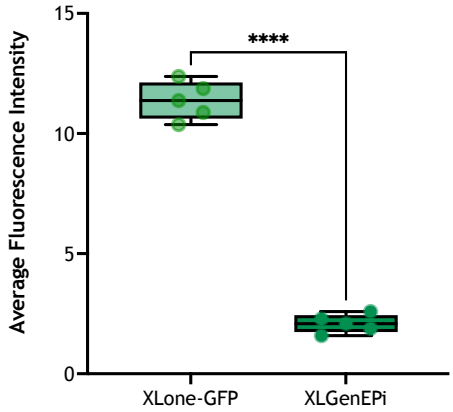


Figure 2.13. Fluorescence intensity differences between XLone-GFP and XLGenEPi. Normalised fluorescence intensity of both Dox-induced XLone-GFP and XLGenEPi co-transfected HEK cells. XLone-GFP-positive HEK cells exhibited significantly higher fluorescence intensity than XLGenEPi-positive HEK cells. N = 5 experimental repeats (with average of 25 cells analysed for each transfection condition). **** , $p<0.0001$.

Furthermore, GenEPi and EGFP are fundamentally very different proteins because of their innate ability to fluoresce. EGFP fluoresces after the 488 nm excitation from the tripeptide X65Tyr66Gly67 chromophore hidden in the β-barrel scaffold. Upon excitation, the Tyr66 amino acid will oxidise, yielding a large delocalised π-system within the β-barrel[188]. In contrast, the GCaMP-G4 within the GenEPi molecule is essentially a circularly permuted green fluorescent protein (cpGFP), or in other words an EGFP with a broken β-barrel[185]. As described in **Section 1.4.3**, GCaMP-G4 relies on the binding of Ca^{2+} ions to the calmodulin (CaM) module of the GCaMP-G4, which triggers CaM interaction with the M13 kinase and consequently alters the protonation state of the cpGFP, allowing it to fluorescence. In this case, without the activation of Piezo1, there are insufficient levels of Ca^{2+} ions within the microdomain of the channel to allow for the CaM-M13 interaction to take place. At the basal level, the GCaMP-G4 signal will be much dimmer (**Figure 2.13**), and therefore, smaller image contrast than the EGFP fluorescence.

Conversely, a more precise method to discriminate the outcome for our XLGenEPi co-transfection is to perform fluorescence-activated cell sorting (FACS). FACS not only enables the separation of individual cells into subpopulations based on their fluorescence, but it also offers a larger sample size application for cell enumeration.

Thus, resulting in a more reliable outcome, with a reduced margin of error. Moreover, in contrast to cell fixation, FACS permits the isolation and collection of individual cells for subsequent live cell experiments post-sorting. Therefore, FACS could also serve as a superior substitute method to BSD treatment for clonal selection. Given that Piezo1 activation, by agonist Yoda1, resulted in a heightened fluorescence imaging contrast of the GenEPi-sensor (**Figure 2.11 a**), introducing Yoda1 before FACS may simplify cell gating and enhance sorting precision.

2.5.2. The difficulty of XLGenEPi strategy with primary cell-line models

In this research (and the rest of my thesis), I am utilising the XLGenEPi-HEK 293T clones I generated (elaborated in **Section 2.4.2**) as an exemplary mammalian cell model to realise the potential of our GenEPi sensor. However, the compatibility of my XLGenEPi construct with other mammalian cell-lines and -types might differ. In the efforts to test the compatibility of my XLGenEPi construct with other mammalian cells, I performed the same co-transfection procedure on other mammalian cells of different types and nature, including HeLa, HFFs, A549, HUVECs and primary astrocytes. I observed that the co-transfection efficiency and clonal selection achievability differ across the different cells, especially when comparing between cell nature/origin. Co-transfection efficiency is similar for immortalised WT (e.g. HEK 293T and HFFs) and cancerous (HeLa and A549) cells, at averages of 68% and 65% respectively (**Figure 2.14 a**). Whereas the efficiency reported for primary cell-types (HUVECs) was 5% (**Figure 2.14 a**), despite optimisation efforts.

In addition to the successful HEK 293T clonal selection presented above (**Section 2.4.2**), XLGenEPi-positive clones were also generated for HeLa cells, but not for HUVECs (**Figure 2.14 b**). After using the BSD-resistance selection method to isolate XLGenEPi-positive HUVECs, cells appeared to have lost their endothelial nature. Cell morphology transformed entirely, and no longer resembled the original HUVECs or a typical endothelial cell morphology (**Figure 2.14 b**). It is well known that primary cells are delicate and impervious to genetic manipulation. Coupled with the complexity of doing a co-transfection, the size of our XLGenEPi construct is at least 2 – 3 times larger than the ideal plasmid size of 3 – 6 kb. Thus, it is unsurprising that the transfection efficiency

and the BSD-resistance clonal selection were ineffective and abortive in primary cells, like HUVECs. The failure of XLGenEPi construct to have successive usage on primary cells suggests that our “XL”-strategy is mainly suitable for hardier, immortalised cell-lines.

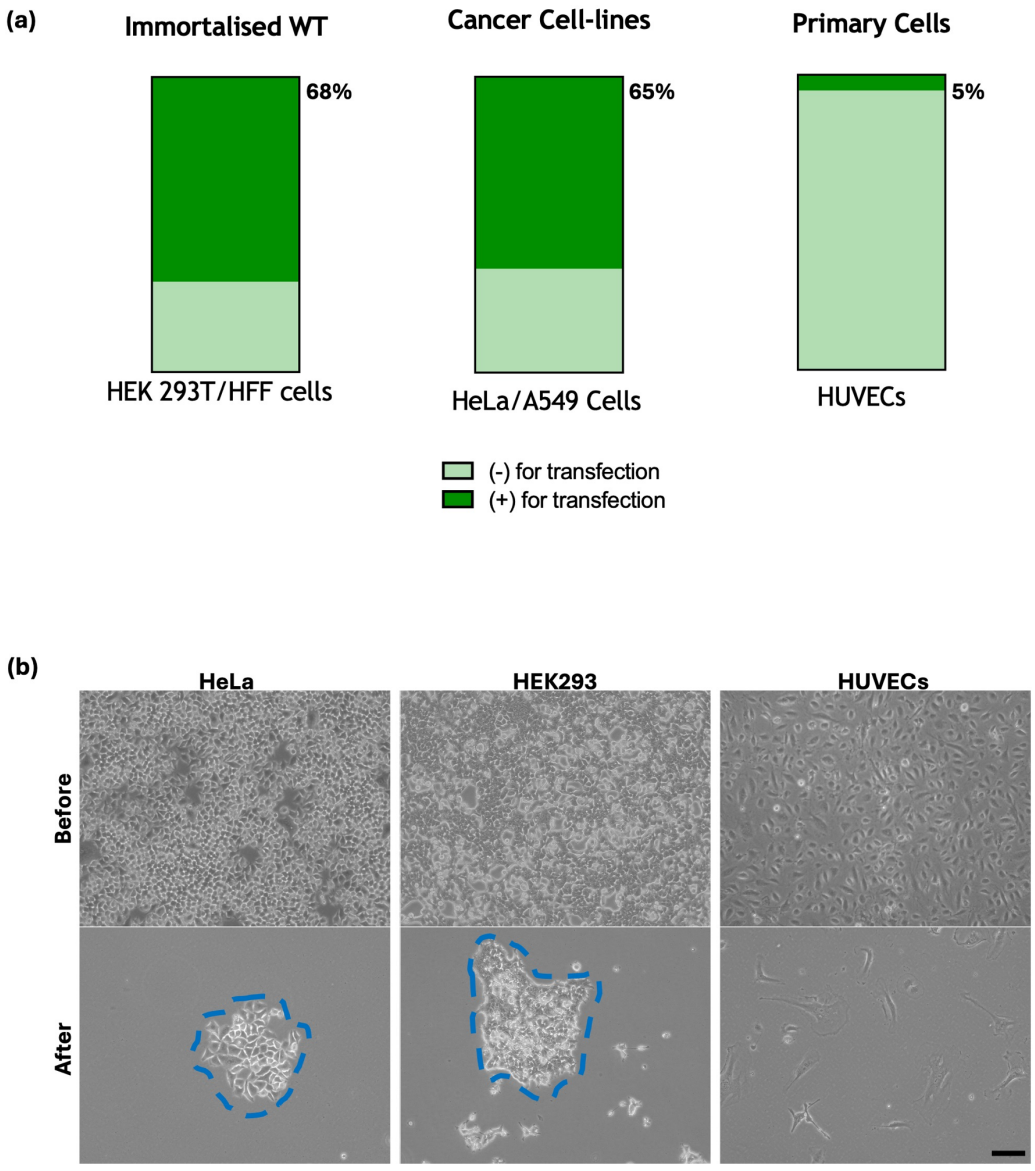


Figure 2.14. XLGenEPi co-transfection and selection efficiency fare less in primary cell-lines, like HUVECs. The XLGenEPi construct was evaluated based on the stability and temporal control of XLGenEPi expression in different cell-types. **(a)** Bar charts showing the co-transfection efficiency in three different types of cell-lines available, namely immortalised wild-type (WT) cells, cancerous cells, and primary cell-lines. XLGenEPi co-transfection is significantly less effective e in primary cell-line, HUVECs, than other types of cells. **(b)** Representative brightfield images of XLGenEPi-transfected cells after blasticidin (BSD) selection regimen. Through this treatment, cells that did not have our XLGenEPi-construct integrated into their genome started dying. Surviving cells/colonies after the BSD treatment (marked within the dashed area) were isolated for XLGenEPi characterisation. Images taken under 20x magnification. Scale bar, 10 µm.

2.5.3. in vitro GenEPi-signal characterisation on the XLGenEPi-HEK clones

The XLGenEPi construct (with the BSD-resistance selection gene) provides the option of isolating and expanding single GenEPi-expressing clones. When co-transfected with our CMV-pBase construct, the transposase enzyme encoded in the CMV-pBase construct can recognise and incise at the inverted piggyBac repeats within the XLGenEPi construct and the host cell's genome to make an integration. The selection for XLGenEPi-positive cells was done by treating the co-transfected cells with 10 µg/ml of BSD over the course of 7 days. Surviving cells were isolated manually and expanded to cultures that were used for subsequent experimentation. With the XLGenEPi-positive HEK 293T clones selected, it is important to first test the functionality of these clones on reporting Piezo1-specific activations within the cells. In the earlier sections (**Sections 2.4.3 and 2.4.4**), I emphasised that the GenEPi-sensor remains functional as an optical reporter of Piezo1-specific activities. I proved, using my XLGenEPi-HEK clones, the inducibility of GenEPi-sensor expression under Dox-treatment, and GenEPi's heightened imaging contrast to ensure reliable analysis of Piezo1 activity in my future work.

When using the BSD-resistance capability for the selection of positive clones, the BSD treatment dosage and duration were intended to end when all WT cells were eliminated. This is under the assumption that non-transfected cells would naturally be WT in nature, and so be eliminated during the same timeline. However, during the BSD concentration titrating experiment, we still observed non-fluorescent cells remaining in the treated population, even at our most effective concentration (10 µg/ml; **Figure 2.7 c**). It appeared that in some colonies, there were non-transfected cells mixed in the population, and possibly acquired BSD resistance due to exposure to the neighbouring XLGenEPi-positive cells. Similarly, it was shown that direct tumour-tumour cell interaction or tumour-stromal cell interaction can render tumour cells to acquire contact-mediated drug resistance[189]. This cell contact-mediated drug resistance could often lead to failure of treatment within the tumour cell population, despite being seemingly efficient at the single-cell level and in homogeneous cell population[190,191].

Also, this mixed-in population of non-transfected cells could arise due to differences in proliferation rate. Successfully transfected HEK 293T cells might be growing and proliferating at a slower rate than WT cells, as is often the case especially when overexpression of the target protein is induced[192]. This can contribute to the existence of WT background cells within the selected population, as they could have outgrown the XLGenEPi-positive cells or the BSD treatment. Even though the non-transfected cells outgrew the positive clones when we were doing colony picking, a better alternative to isolate purer clones of XLGenEPi-positive cells is to perform FACS.

In addition to investigating the BSD-resistance capability in the XLGenEPi-positive clones, I studied the reliability of the Dox-inducible system and GenEPi-sensor expression after the induction. In my experiments, I observed that GenEPi-sensor expression becomes detectable within 24 hours after the initial Dox-induction. And following Dox-withdrawal, GenEPi expression remained measurable for up to 72 hours, until it returned to baseline (**Figure 2.10 b**). A regression curve was fitted to the expression decay pattern (**Figure 2.10 c**). The half-life of the GenEPi-sensor extrapolated from the exponential decay curve is within 30 – 32 hours. In a recent study, it was reported that overexpressed Piezo1 expression remained stable long after 8 hours[193]. Furthermore, the half-life for a cluster of sodium (Na^+) ion channels in cardiomyocytes was 35 hours[194]. This could be evident that, as previously reported in endogenous Piezo1[94,97,116], GenEPi-sensors form nanoscale clusters on the plasma membrane. This would explain the 30 – 32 hours half-life I observed in GenEPi expression (**Figure 2.10 c**). However, it is important to note that for the same protein, half-life may still differ depending on cell age, cell types and tissues, specific membrane partners, and the cellular location of the proteins[195–197]. Hence, the GenEPi-sensor expression pattern might still vary with cell passage number and cell-lines used.

The use of fluorescence intensity differences to analyse GenEPi-sensor expression pattern is an indirect method that could potentially be influenced by signal background noises. To accurately investigate the processes of GenEPi-sensor synthesis, assembly, and turnover, a more precise method like Western Blotting should be employed. By isolating and separating the total cellular protein content, one may identify the target

protein by antibody staining[198]. Then, the analysis of band intensities could elucidate information on protein quantity within the cells at the point of time proteins were harvested from cells. That way, the absolute quantification of GenEPi level can be compared between different timepoints after Dox-induction to show how GenEPi-sensor is turned over in cells.

Interestingly, during the process of characterising GenEPi-sensor's induced expression in the positive clones, I noticed that the GenEPi-signal has a broad emission profile. Under the 488 nm excitation, the GenEPi fluorescence signal was detected in both the green wavelengths (i.e. 500—550 nm), and the orange/red wavelength range (i.e. 600—650 nm) (**Figure 2.15 a**). In addition, lambda scan confirmed that the emission spectrum of GenEPi-signal ranges from 500 – 700 nm (**Figure 2.15 b**). Although the leak into the orange/red detectable wavelength range might not cause problems when we are just investigating solely Piezo1-specific activities, GenEPi-signal detection and analysis will require careful calibration and interpretation when combined with other fluorescent markers within the 600 – 700 nm range.

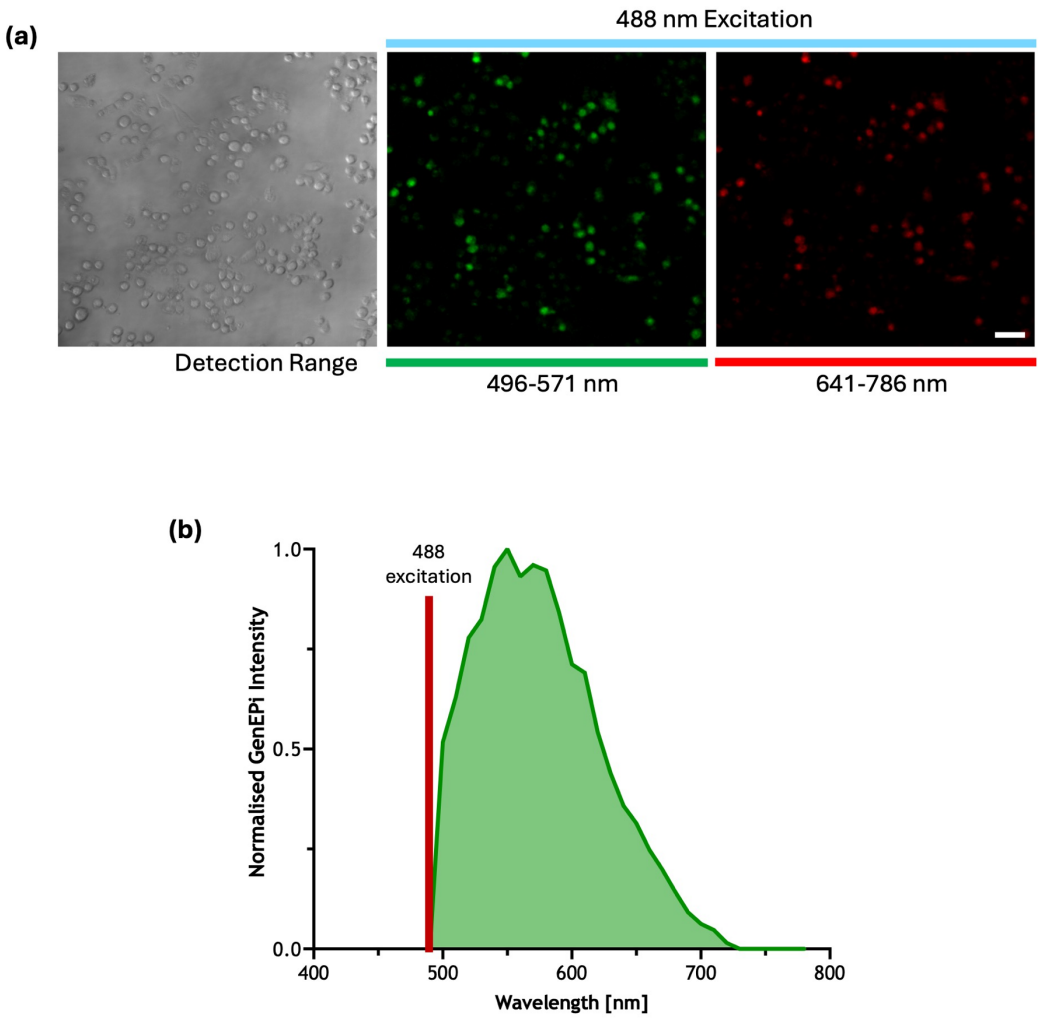


Figure 2.15. GenEPi signal exhibits a broad emission spectrum. (a) Representative images of XLGenEPi-transfected HeLa cells displaying a wide optical spectrum. Images taken under 20x magnification. Scale bar, 50 µm. **(b)** Representative emission spectrum curve derived from lambda scan after following 488 nm excitation. The emission spectrum of XLGenEPi shows that XLGenEPi fluorescence signal peaks at around 550, but is still observable within the orange/red wavelength range.

2.5.4. XLGenEPi, an inducible Piezo1-specific reporter for mammalian cells

In summary, I adapted the original GenEPi construct to create a Dox-inducible version, which we referred to as XLGenEPi. By switching the plasmid backbone (CMV-promoter based) into a XLone-based backbone, key elements were introduced into the XLGenEPi construct allowing us to (i) generate positive mammalian cell clone, which expresses GenEPi-sensor stably; (ii) faithfully induce expression of the GenEPi-sensor in host cells, through Dox-treatment; and (iii) provide increased imaging contrast to ensure reliable analysis of Piezo1 activity in the rest of my PhD work. In this research, I outlined that the GenEPi-sensor remains expressed on cells for up to 72 hours after the initial Dox-induction. In addition, I showed that re-induction of GenEPi-sensor expression did not

compromise the fluorescence intensity for imaging. Overall, the modified XLGenEPi construct provides high spatial and temporal resolution on GenEPi-sensor expression, while reliably reports Piezo1-specific dynamics as GenEPi-fluorescence signal outputs. With the generated XLGenEPi-HEK 293T clones which stably express GenEPi-sensor when induced, I can extend our investigation into the dynamics of Piezo1 functioning.

2.6. Statement of contribution

Credits for part of the work described in this chapter belong to Mr Konstantinos Kalyviotis (a fellow PhD student, at the point of the experiment), and Ms Phongsopa Papavee (BSc student under my supervision, at the point of the experiment), both in the Pantazis group. Some experiments and analyses were carried out in collaboration with them.

3. Developing a microfluidic-based system for the imaging of dynamics of Piezo1

"言之，吾听；示之，吾明；行之，吾知之矣。" ***— 孔夫子***

"Hear, I listen; See, I understand; Do, and I know." ***– Confucius***

3.1. Importance of imaging the dynamics of Piezo1 and other mechanosensitive proteins

Mechanosensitive ion channels, like Piezo1, are pivotal components of cellular mechanotransduction signalling. They allow cells to sense and respond to mechanical forces within their microenvironment. Understanding their real-time dynamics is therefore key to unravel their roles within the larger physiological and pathological processes. However, this remains challenging to the study of mechanosensitive proteins (and Piezo1, in particular), mainly due to the nature of their activities and responses. Piezo1 channels, like other ion channels, sense and respond to changes in the membrane tension rapidly, within nano- to micro-seconds. Conventional static imaging or immunofluorescence staining imaging, like previous Piezo1 studies, cannot capture

those rapid activities, which will inform us about the dynamics of Piezo1 within the cells. In addition, there are findings which suggest that Piezo1 channels function in clusters and exhibit some extent of mobility within the lipid membrane layer[1,59]. These further discourage the usage of conventional static imaging to characterise mechanosensitive ion channels, like Piezo1.

3.1.1. Time-lapse, live-imaging to capture mechanosensitive dynamics

Time-lapse, live-imaging has long been a powerful tool in cell biology, allowing the acquisition of dynamic processes within living cells over an extended time period. It is a unique technique which offers a window into the dynamics of cellular processes, like the activation of mechanosensitive ion channels, that conventional static imaging can never provide. Besides providing insights into the real-time dynamics of Piezo1, time-lapse, live-imaging allows for longitudinal studies of a region of interest over extended periods. This is invaluable for observing gradual cellular changes and adaptations in response to mechanical stimuli. Therefore, incorporating time-lapse, live-imaging as a method for our system to investigate the dynamics of Piezo1 and other mechanoresponsive proteins within cells.

As described before, GenEPi is an optical tool generated by incorporating a GCaMP molecule into the C-terminal of the human Piezo1 sequence (**Figure 1.11 a**). As previously shown, by electrophysiology data[1] and our chemical perturbations results (**Section 2.3.4**), the GenEPi-sensor expressed within the cells is still a functional Piezo1 channel, reacting to mechanical and chemical stimulations. Therefore, the time intervals and signal acquisition settings of the time-lapse, live-imaging need to be precisely optimised in order to faithfully capture the intricate dynamics of Piezo1 activity. In addition, robust data analysis pipelines should be established to extract meaningful information from the time-lapse datasets, which could help inform novel characteristics of Piezo1 activities within the cell membrane.

3.1.2. Models of applying mechanical stimulation during live-imaging

Studying the dynamics of Piezo1, and other mechanosensitive channels, through live-imaging with mechanical stimulation is of great importance. It allows researchers to

investigate how the channel reacts and responds to external physical forces in real-time. The dynamic information of Piezo1 is essential to help us understand its role in mechanotransduction. It is also crucial in helping us dissect Piezo1's behaviour in diverse cellular contexts. By incorporating GenEPi, our Piezo1-specific sensor, into our system, we provide the unique opportunity to correlate Piezo1 dynamics with other cellular processes, like calcium influx and membrane deformation, in response to external mechanical stimulation.

In developing our system, we have highlighted the following factors which are crucial for us in choosing which mechanical stimulation model to incorporate into our investigative system:

(i) Precise control of mechanical forces – The method of choice should offer precise control over the magnitude, duration, and pattern of mechanical stimulation. This level of control allows us to design experiments that closely mimic physiological conditions, making it ideal for studying Piezo1 responses to specific force profiles.

(ii) High spatiotemporal resolution – Having a high spatiotemporal resolution is crucial for optical imaging. It is essential for capturing rapid and localized changes in Piezo1 behaviour in response to the elicited mechanical forces.

(iii) Versatility of method – The method of choice should have the versatility to adapt to a wide-range of applications and models of experiment. High-throughput capabilities in the experimenting system will allow us to study multiple conditions or cell types simultaneously. This can significantly increase the efficiency of data collection and analysis.

(iv) Compatible with cell culture procedure – Importantly, the mode of administering mechanical force needs to be compatible with cell culture procedure. In addition, the incorporation of the method into the culturing of cells will expose cells to a near-physiological condition. This ensures that we

are observing cellular behaviour baseline close to their *in vivo* physiological behaviour.

Different models of applying external stimulation in real-time to study Piezo1's activities have been presented in **Section 1.3.4**. These methods include AFM, optical/magnetic tweezers, cell stretching devices, and microfluidic devices. Among these popular options, microfluidics technology has proven its precision, versatility, and compatibility with a broad range of applications. Therefore, developing a microfluidic-based system is the preferred choice for us to investigate the dynamics of cellular Piezo1 activities in response to mechanical forces, in the form of fluid shear stress.

3.2. Material & Methods

3.2.1. Cell Culture.

The XLGenEPi-HEK clones generated (see **Chapter 2**) were used in the development and optimisation of tis microfluidic-based system. XLGenEPi clones were cultured at 37°C, 5% CO_2, in DMEM complete media, consisting of high glucose DMEM with GlutaMAX (Gibco™, 10569010), supplemented with 10% FBS (Sigma-Alrdrich, F7524) and 1x Penicillin-Streptomycin antibiotic solution (Thermo Fisher, 15140122).

HUVEC cultures were used to investigate the versatility of our flow system. HUVECs were cultured at 37°C, 5% CO_2, in EGM™-2 Endothelial Cell Growth Medium-2 BulletKit™ (Lonza, CC-3162). The medium kit system is composed of EBM™-2 Basal Medium (Lonza, CC-3156) and EGM™-2 SingleQuots™ Supplements (Lonza; CC-4176).

XLGenEPi-HEK 293T clones used were of P9-10, and HUVECs were of P3-4. All cultures were routinely tested for mycoplasma infection using Mycoplasma detection kit (LuBioScience GmBH, B39032). For routine maintenance, culture media was changed every two days and passaged at ~ 70% confluence using TrypLE™ (Gibco™, 12604-013) at 37°C for 5-minutes. Cells were routinely cryopreserved at -140°C to ensure continuation of cell lines. For cell cryopreservation, cells were dissociated from culture

platforms using TrypLE™ (Gibco™, 12604-013) at 37°C for 5-minutes and frozen in their respective culture media, supplemented with 10% FBS and 10% DMSO.

3.2.2. PDMS-based Straight Channel Device

To fabricate our microfluidic device using soft lithography method, a mould (**Figure 3.1 b**) was designed in Inventor 2022 (Autodesk, USA) for 3D printing. The Objet 500 3D printer (Stratasys, USA) was used to print the mould, with VeroWhite (Stratasys, USA) as the print material. The final product is a mould which is used to fabricate the microfluidic device for all the experiments described in this thesis.

The brief outline of producing a cellularised microfluidic device for each experiment has been detailed as schematics in **Figure 3.8**, and the methodology is as follows:

(A) Device Fabrication

The device top material, PDMS (Sylgard 184, Dow, USA), was prepared as a 10:1 weight ratio mixture of base polymer to curing agent, as per manufacturer's instructions. The PDMS mixture was then placed in a glass vacuum chamber for degassing. After which, 5 grams of the optically transparent and bubble-free PDMS mixture was poured over the 3D-printed mould. Polymerisation of the material was done so by baking the PDMS-filled mould on a hot-plate set at 80°C for more than 4 hours, usually overnight. The device PDMS top material could be carefully cut out from the mould and trimmed using a scalpel. The inlet and outlet ports were created by applying a 1 mm biopsy punch (Kai Medical, BPP-10F). To create the whole device, the PDMS top material is plasma bonded to a rectangular thickness #1 (24 x 50 mm) borosilicate coverglass (VWR, 631-0146), using a hand-held Piezobrush PZ2 (Relyon Plasma, Germany). To ensure secure and strong bonding between the PDMS and glass surfaces, the whole device was set on the hot-plate at 80°C for 5 mins.

(B) Device Preparation and Coating

Completed microfluidic devices were sent for sterilisation (121°C for 15 mins) using the autoclave machine, to ensure that devices are suitable for cell culturing. Sterilised devices were subsequently dried in an 70°C oven before being used. Channels within the

devices were wet by washing with with 1X DPBS (Sigma-Aldrich, D8537) for at least three times. Subsequently, the microfluidic channels were coated with either fibronectin or 0.1% gelatine solutions, before cells were seeded and cultured within the devices.

Fibronectin-coating: On ice, fibronectin coating solution was prepared by diluting 1 mg/ml of fibronectin stock solution (Sigma-Aldrich, F0895) to 1x DPBS supplemented with Ca^{2+} and Mg^{2+} (Gibco™, 14040083). This fibronectin coating solution was prepared such that we achieve 1.5 µg/cm^2 coating density on the coverglass surface in the microchannel. The fibronectin coating solution was carefully pipetted into each microchannels from the inlet and outlet ports at least twice, making sure that a small amount of coating solution (approximately 30 µl) sits at both port ends of the channel (**see Figure 3.8, step 5**). This helps to seal the channel off from getting any air bubbles during incubation period. Devices were then placed into the humidity chamber and incubated in a 37 °C, 5% CO_2 cell culture incubator overnight.

0.1% gelatine-coating: 0.1% gelatine solution was prepared by dissolving gelatine (Sigma-Aldrich, G9391) in 1x DPBS supplemented with Ca^{2+} and Mg^{2+} (Gibco™, 14040083). The 0.1% gelatine solution was sterilised by autoclave (121°C for 15 mins) and filtered through 0.22 µm filter for sterile, tissue culture usage. The sterile 0.1% gelatine solution was carefully pipetted into each microchannels from the inlet and outlet ports at least twice, making sure that a small amount of coating solution (approximately 30 µl) sits at both port ends of the channel (**see Figure 3.8, step 5**). This helps to seal the channel off from getting any air bubbles during incubation period. Devices were then placed into the humidity chamber and incubated in a 37 °C, 5% CO_2 cell culture incubator overnight.

(C) Device Seeding

The day prior to cell seeding, HEPES-supplemented culture media was prepared by adding up to 10 mM of HEPES solution (Gibco™, 15630080) into either complete DMEM for XLGenEPi-HEK 293T clones or complete EGM2 for HUVECs. HEPES-supplemented culture media was then syringe-filtered through 0.22 µm filter into a T25 flask, which

would be placed up-right in a 37 °C, 5% CO_2 cell culture incubator overnight to allow media degassing.

Following the overnight coating incubation, microfluidic channels were washed with 1x DPBS supplemented with Ca^{2+} and Mg^{2+} (Gibco™, 14040083) and HEPES-supplemented culture media and returned into the humidity chamber, to be equilibrated at room temperature (RT).

XLGenEPi-HEK 293T clones (or HUVECs) were harvested by trypsinisation with TrypLe (Gibco™, 12604-013) for 5-minutes at 37°C. Harvested cells were resuspended in HEPES-supplemented culture media to a concentration of 10 million cells/ml and carefully pipetted into the devices to achieve a seeding density of 40,000 cells/cm^2.
For the seeding of HEK 293T cells, the culture media was supplemented with a further 10% of FBS before the resuspension. As this has been shown to help increase HEK cells viability within microchannels[201]. It is important that the cells be seeded (and any further administering of fluids be done) from the designated inlet port of the channels to establish a one-way direction within the channel. Seeded devices were returned to the incubator (in the humidity chamber) for at least 20 minutes to allow for cell attachment (**Figure 3.8, step 7**). After that, the seeding process was repeated for each channel with the 10 million cells/ml cell suspension (**Figure 3.8, step 8**). Devices were incubated for another 4 hours to ensure proper cell attachment within the microchannels, before the microfluidic flow circuit was connect to the devices.

(D) Microchannel Cell Culturing

Once proper cell attachment has been established across the channel, cells were fed with fresh HEPES-supplement culture media (further 10% FBS added for the XLGenEPi-HEK 293T clones) by gently pipetting 15 µl of culture media through the channels, from the designated inlet ports.

Simultaneously, the microfluidic flow circuit (**Figure 3.3**) was assembled and connected to the device channels at the respective inlet and outlet ends. Briefly, a 10/20 ml syringe (Terumo, MDSS10SE and MDSS20ESE respectively) will be filled with 3-4 ml of pre-

warmed culture media and connected to a three-way vial (vyclic, 876-70876), with the other two ports connected to another filled 1 ml syringe (Terumo, MDSS01SE) and a luer connector that leads to the outlet tubing respectively (**see Figure 3.8**). Media would fill the PTFE outlet tubing (Darwin microfluidic, 1608-20) from the connected 10/20 ml syringe, ensuring that there is no air gaps or air bubbles within. The outlet tubing was then connected inserted into the device channel outlet, and the three-way vial switched to a close position (**Figure 3.8, step 10a**). This prevents the cells within the channel from any sudden fluid shear or minute backflow of fluid brought about by the movement of tubings or device. A 10 ml glass bottles with three open ports (Duran®, 29 231 28 01) were put together (**see Figure 3.3, insert 2 or Figure 3.8, step 10b**) and filled with enough pre-warmed, HEPES-supplemented culture media. One of the glass bottle ports should hold the connector to the PTFE inlet tubing, which was filled with culture media, before connecting to the device channel inlet (**Figure 3.8, step 11**).

After setting up the flow circuit within the tissue culture hood, it was transferred gently to a cell culture incubator. The media reservoir (glass bottle filled with culture media and connected to the inlet of device channel) and the humidity chamber containing the connected devices were brought into the cell culture incubator. The outlet end (tubing connected to the syringe) will be installed onto the syringe pump, placed outside but near the cell culture incubator. Once everything is in place and secured, the three-way valve would be switched to an open orientation and the flow circuit was allowed to sit and equilibrate for 5-10 mins, while the flow parameters were being keyed into the syringe pump. After equilibration, the pump was switch on with the program of withdrawing fluid at the rate of 1.12 µl/min for 24 hours (this corresponded to 0.1 dyne/cm^2 shear within our rectangular cross-section channel).

3.2.3. Fluid Shear Stress Applications.

Fluid shear stress application was established using the PhD Ultra™ programmable syringe pump (Harvard Apparatus, 70-3007). Fluid flow rate was calculated and calibrated according to the channel's dimension to correspond to the respective shear levels. Briefly, the flow rate (Q ; µl/s) through a device can be calculated by *Eq. 1*, where h and w refer to the channel height and width respectively, μ (Pa.s) refers to the dynamic

viscosity of the fluid, and the pre-determined shear level (τ; dyne/cm^2) across the rectangular channel is determined beforehand. A range of shear stress levels, from 0.1 to 50 dynes/cm^2, were used in my experiments, and therefore used to calculate the corresponding flow rate (Q) to apply on the syringe pump machine.

$$\tau = \frac{6\mu Q}{wh^2} \qquad \textit{Eq. 1}$$

Depending on the level of fluid shear stress intended, the respective fluid flow rate will be input into the syringe pump system. Fluid flow rates corresponding to 0.1 – 10 dynes/cm^2 fluid shear stress were used, where 0.1 dyne/cm^2 for cell culturing and 1 – 10 dynes/cm^2 for shear experiments. The syringe pump is set on "Withdrawal" mode for cell culturing, and "Infusion" mode for shear stress application.

3.2.4. Brightfield Imaging

During seeding and culturing of cells within the device, visualisation of the microchannel and brightfield image acquisition were performed using the cell culture hood-compatible EVOS XL Core microscope (Thermo Fisher, AMEX1000) under the 10x magnification.

3.2.5. Immunofluorescence Staining

To fix and stain the cells within the microfluidic device, the design of the system has allowed for direct pipetting of fixing and staining solutions through the microchannel from the inlet and outlet interfaces. Cells were fixed in 4% PFA (diluted from 16% concentrate solution, Thermo Fisher, 28908) for 10 minutes at 37°C, permeabilized with DPBS supplemented with 0.1% TritonX-100 (Sigma-Aldrich, T8787) and blocked with 10% Donkey Serum (Jackson ImmunoResearch, 17-000-121) in DPBS supplemented with 0.1% TritonX-100. Samples were then incubated with anti-Piezo1 antibody (Proteintech, 15939-1-AP) diluted in 5% Donkey Serum (Jackson ImmunoResearch, 17-000-121) in DPBS supplemented with 0.1% TritonX-100. After several washing steps with DPBS, the samples were incubated with donkey anti-rabbit IgG (H+L) Alexa Fluor Plus-488 (Thermo Fisher, A32790), Alexa Fluor-647 Phalloidin (Invitrogen, A22287), as well as DAPI (Thermo Fisher, 62248). Finally, washing with 1x DPBS was repeated at least five times, before filling the microchannel with 15 µl of 1x DPBS (Sigma-Aldrich, D8537),

making sure that a small amount of DPBS solution (approximately 30 µl) sat at both ends of the channel. Samples were stored in 4°C until imaging.

3.2.6. Confocal Image Acquisition

All images were acquired on a Leica SP8 confocal laser scanning microscope equipped with a white light laser (WLL, Leica) using an HC PL APO CS2 20x/0.75 dry objective.

For fixed, immunofluorescence staining imaging: Images of cells were acquired at 8-bit depth, with xyz planes, at 1024 x 1024 format, excited with 405 nm for DAPI, 488 nm for Alexa Fluor Plus-488 reporter, and 647 nm for Alexa Fluor-647 Phalloidin, respectively. An optical zoom factor up to 3 might be used to obtain higher magnification of the cells and their subcellular structures. Z-stack images were acquired with an average z-stack size 20 µm at 0.88 µm optimal step-size.

For time-lapse, live-imaging: Images of cells were acquired at 8-bit depth, at 512 x 512 format, excited with 488 nm for Alexa Fluor Plus-488 reporter, with photon-counting mode. An optical zoom factor up to 3 might be used to obtain higher magnification of the cells and their subcellular structures. To ensure fast image acquisition, we imaged small regions of interest within the field of view, recording a single z-plane over several minutes (pinhole size ranged from 3 Airy units to maximum pinhole size) using the maximum acquisition speed. When live-imaging was performed on the Leica SP8 confocal, bidirectional scanning with off-set correction was used to increase acquisition speed even more. Live imaging of cells was carried out in culture medium.

3.2.7. Image Processing and Analysis

ImageJ/Fiji [199] (release 1.53f51) was used for the post-processing of the confocal images acquired. For the immunofluorescence-stained confocal images, the maximum (X-Y plane) projection of the Z-stack images were made and subsequently merged to form the realised fluorescence images. For the live-imaging processing, GenEPi (Piezo1) clusters were segmented using the respective 8-bit single channel confocal images. Images were masked by (i) subtracting background (rolling ball radius of 2 pixels), (ii) applying a median filter (radius of 2 pixels) and (iii) thresholding (Otsu). The mask image was then

subsequently watersheded, dilated before using it to obtain quantitative data, such as mean gray value, from the built-in "Analyse Particles" function of Fiji/ImageJ. Single-pixel measurements due to masking artifacts were excluded from the subsequent analysis. Any average camera noise was subtracted from images that are displayed.

To compare the differences in 488 nm signal saturation on images acquired with Intensity-analog mode and Photon-counting mode, the quantitative data of the $\frac{F}{F_0}$ changes over time were collected from individual cells or regions of interest using the plot z- axis profile (where z dimension was time, usually in milliseconds or seconds). The resultant $\frac{F}{F_0}$ images were pseudo-coloured with the mpi- Inferno LUT to better represent the signal saturation differences within the field of view.

3.3. Devising a microfluidic platform adapted for precision optical imaging

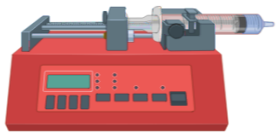
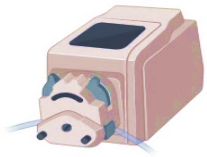
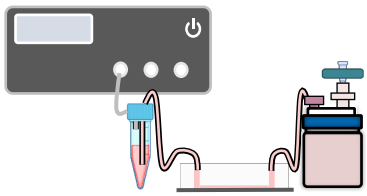
3.3.1. Microfluidics models

Microfluidics is a rapidly growing field that involves the manipulation and control of small volumes of fluids, typically in the range of microlitres to picolitres, using channels and chambers that are on the order of micrometres. The precise control of fluids at this small scale has numerous applications in biomedical research, chemical synthesis and analytical chemistry.

The most common method for controlling fluid flow in microfluidic devices is the use of pumps. Pumps can be broadly classified into two categories: pressure-based pumps and displacement-based pumps. Pressure-based pumps rely on the application of a pressure difference across the fluid to drive flow, while displacement-based pumps rely on the mechanical displacement of the fluid to create flow. Each methodology has its own merits and shortfalls (outlined in **Table 3.1**). The selection of fluid handling methods ultimately depends on the purpose and intended outcomes of the system. With the

primary purpose and intended outcome of integrating the microfluidic culturing platform into a sensitive imaging setup, displacement-based microfluidic handling is preferred. Here, I employed a syringe pump fluid handling setup. This setup is characterised by (i) precise control of fluid administration, (ii) low pulsatility, (iii) wide flow rate and (iv) big volume range, rendering the syringe pump suitable for my research.

Table 3.1. Common methods of fluid administering in bio-microfluidic models.

	Methods of Fluid Handling	Advantages	Disadvantages
Displacement-based System	 **Syringe Pump**  **Peristaltic Pump**	• Simple setup. • Precise fluid control. • Low pulsatility. • Wide range of flow rates and volumes. • Broader fluid compatibility. • Easily portable. • Integration to imaging system.	• Expensive. • Complex tubing configuration during multiple inputs. • Perfusion duration may be limited by syringe or reservoir. • Poor accuracy at very low flow rates.
Pressure-driven System		• Simple setup – better tubing configuration. • Rapid flow control. • High throughputs easily achieved. • Lower oscillations in flow rate. • Fully automated and programmable.	• Expensive. • Susceptible to hydrostatic pressure complications. • Limited portability (compressed gas needed). • More complex integration to imaging system.

Illustrations of the different fluid handling systems created using BioRender.com.

3.3.2. Criteria of a microfluidic-based system for imaging GenEPi dynamics

To build a microfluidic system that is suitable for precision optical imaging, the following design and practicality criteria needed to be fulfilled:

a) Simple, yet practical channel design that allows for precise imaging of Piezo1 dynamics.

b) Biocompatible and sterilisable material makeup to achieve long-term cell culturing within the device.

c) Optically clear and adaptable chamber to accommodate for commercial confocal microscopes and to accomplish imaging of GenEPi dynamics in mammalian cells.
d) Cheap and easy to fabricate in the lab.

3.4. Microfluidic Culturing Platform Design

In this section, I optimised the microfluidic device design, culturing procedure, and imaging setup in the system, such that they fulfil the key requirements of our microfluidic-based platform (listed above). The resultant system will allow me to culture our XLGenEPi-HEK clones within the microfluidic device under near-physiological shear conditions and to capture Piezo1 behaviour in real-time under shear conditions.

3.4.1. Microchannel device design

The design of our microfluidic device is crucial, as the device will need to provide reliable delivery of desired fluid flow through the channel as well as imaging the dynamics of Piezo1 activity in cells using the fluorescent/optical readout provided by GenEPi. I aimed for a simple microfluidic channel design that can accommodate a confluent monolayer of cells and an optically compatible glass base for confocal imaging (**Figure 3.1 a**). To realise the microchannel device design, I employed soft the lithography method for my device fabrication. A 3D-printed mould with four parallel, raised details was made (**Figure 3.1 b**). Microchannels were fabricated by soft lithography with the 3D-printed mould with the dimension of 31.4 mm (L) x 0.8 mm (W) x 0.1 mm (H), creating a rectangular cross-section (**Figure 3.1 c**). At these dimensions, it allows for up to 25 mm^2 culturing surface and 2.5 µl of holding volume within the channel.

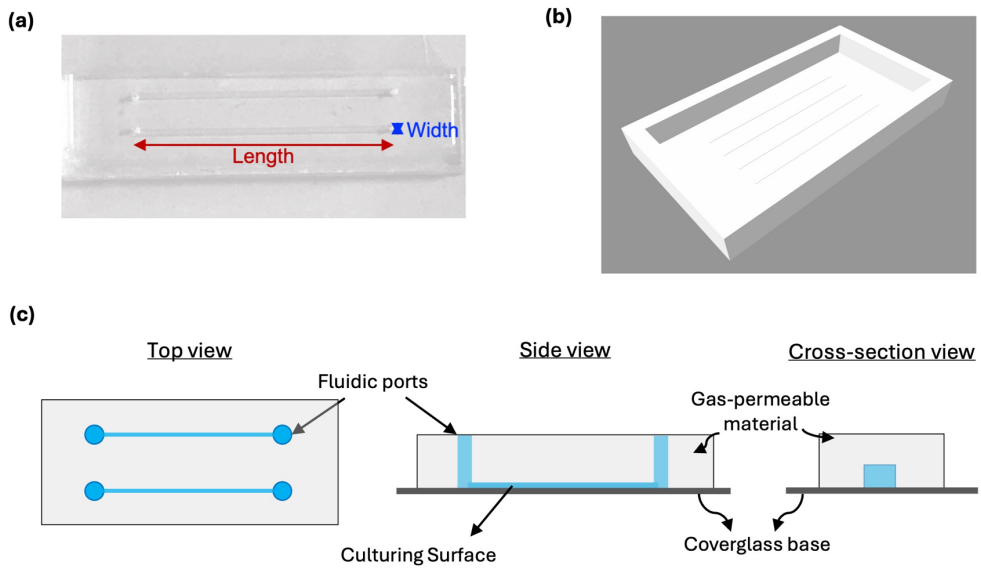


Figure 3.1. Overview of our *in vitro* microchannel model developed for investigating Piezo1 dynamics in HEK cells. (a) Brightfield image of our end-product microfluidic device after fabrication. The device was fabricated by plasma-bonding the soft-lithography produced PDMS top-material to a No. 1 thickness coverglass. **(b)** Representative drawing of the 3D-printed mould used for fabricating the device's top-material. Design of the mould consists of four raised details aligned in parallel. **(c)** Top, side and cross-section views of the developed microchannel device, not drawn to scale. Key features are indicated in the schematics.

Polydimethyl siloxane (PDMS) was chosen as the material for our device's top material. PDMS is a flexible material which can be customised to different sizes and shapes, making it compatible with soft lithography in our fabrication method. In addition, PDMS is gas permeable, allowing gaseous exchange within the device during cell culturing. Capitalising on these recognized benefits, PDMS has become the favoured polymer for our approach due to its adeptness in fulfilling the specified design criteria described in **Section 3.2.2**. Therefore, I used PDMS as the polymer for soft lithography in casting my device's top-material.

Furthermore, I have selected a glass base for our microchannel device design. The use of a cover glass base for our microfluidic device not only allows me to perform optical imaging using a standard confocal microscopy, but also presents the option of using higher magnification objectives during imaging. I use the commercial confocal microscope Leica SP8 which has the following objectives (**Table 3.2**):

Table 3.2. Microscope objectives specification of Leica SP8 used in our experiments.

Correction	Magnification	NA	Immersion	Coverglass	Working Distance	Others
HC Plan APO	10x	0.40	Dry	0.17	2740 µm	CS2
HC Plan APO	20x	0.75	Dry	0.17	620 µm	CS2
HC Plan APO	40x	1.30	Oil	0.17	240 µm	CS2
HC Plan APO	63x	1.40	Water	0.17	140 µm	CS2

(NA = Numerical aperture of the respective objectives)

To ensure that the imaging of GenEPi (Piezo1) dynamic under shear stress was acquired without compromising the depth resolution, I chose to use a No.1 thickness cover glass as the device base. Contrary to using a standard microscope glass slide as the device base, like in most microfluidic devices, a No.1 thickness coverglass is that it is only 170 µm in thickness (instead of a thickness of 1 mm or 1000 µm). The use of No.1 cover glass (i.e glass of 170 µm thickness) in my microfluidic device was compatible with the working distance (i.e. the maximal distance from the objective lens to keep the sample in-focus (**Figure 3.2**)) of the 10x, 20x, and 40x objectives (**Table 3.2**). Using these microscope objectives, I can capture finer cellular details, like the GenEPi-signal on cell membranes, without compromising the imaging resolution.

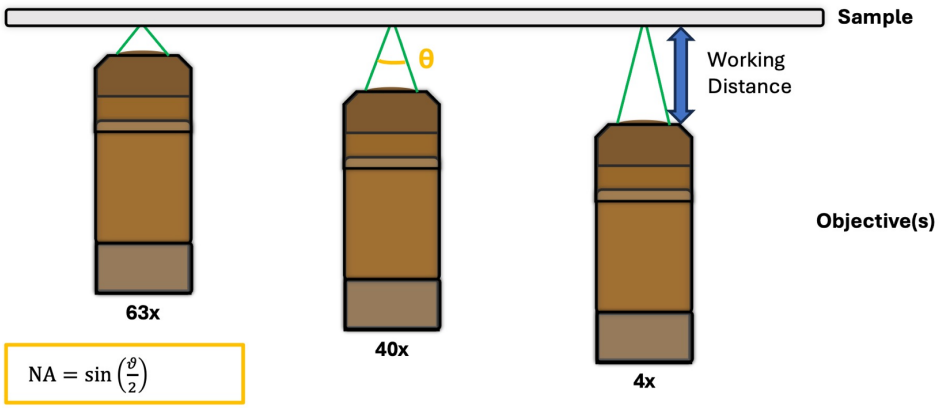


Figure 3.2. Schematics of different magnification objectives and their relative working distances on an inverted microscope set-up. The higher the objective magnification, the smaller the working distance (the minimum distance between the objective lenses and the in-focus sample). Therefore, the thickness of the microfluidic base has to be carefully considered during the device designing.

3.4.2. Microfluidic flow system setup

To establish fluid flow conditions within the microchannel environment, I connected a syringe pump to my microfluidic device. A flow circuit (**Figure 3.3**) was designed such that the system is suitable to deliver maintenance flow during cell culturing and

perturbating shear conditions during my live experiments. By altering the set parameters (i.e. rate, volume and time) on the syringe pump display setting, I can easily switch between the two modes of flow administered onto our XLGenEPi-HEK cells within the microchannel. The fluid circuit was run in the fluid withdrawal mode, meaning cell culture media, from a media reservoir, was being drawn through the microfluidic device to the syringe via biocompatible tubings (**Figure 3.3**).

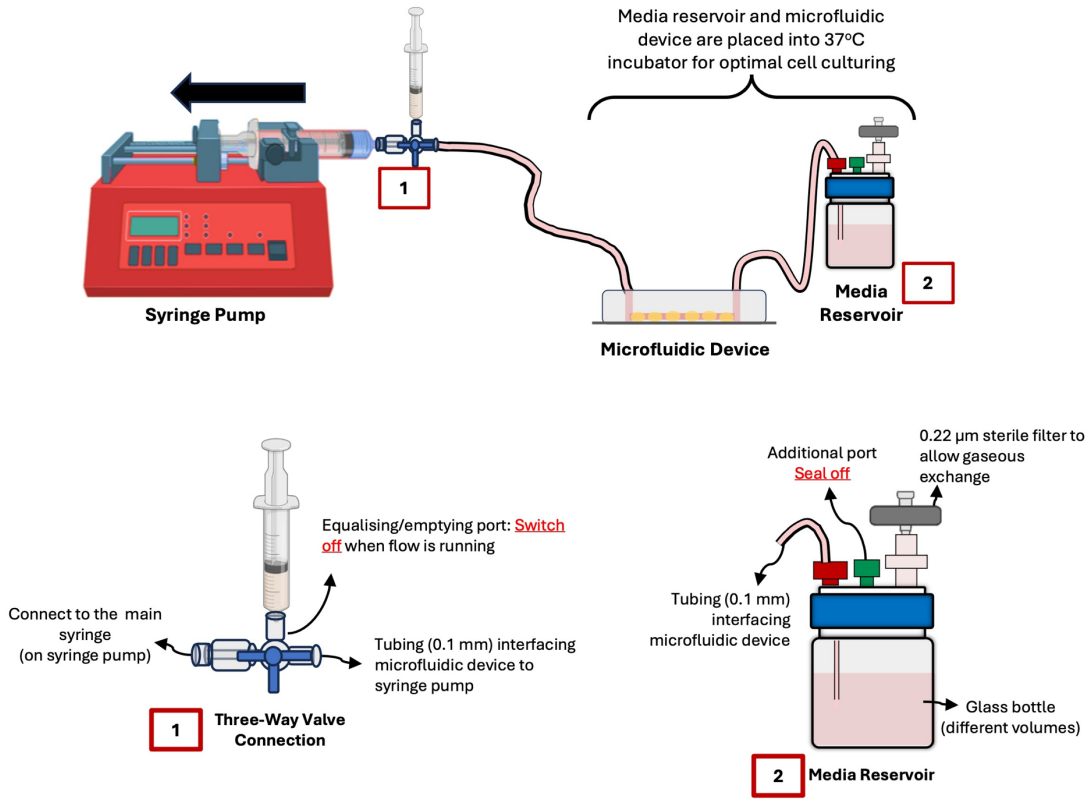


Figure 3.3. Microfluidic flow circuit to establish flow delivery within our microchannel device. Illustrations of an assembled, closed flow circuit used to administer culture media through the microfluidic device for culturing and shear stress application. **(Insert 1)** Schematic drawing of the fluid circuit set-up at the outlet end, consisting of a three-way valve connector. **(Insert 2)** Schematic drawing of the inlet end, consisting of the glass bottle-based media reservoir. Flow circuit illustrations are not drawn to scale. Schematics were partly created using BioRender.com.

3.4.3. Microfluidic flow profile

To ensure that I administered a uniform flow rate across the microchannel, profilometer measurements were taken on the 3D-printed mould. These measurements confirmed the consistency of height and width across the length of the resultant channel (**Figure 3.4 a**). With an accuracy of ± 10 µm, I concluded that the channel height and width after fabrication were on average 120 µm and 839 µm, respectively (**Table 3.3**). These values

were eventually used to calculate the microchannel hydraulic resistance, R_{ch}, and flow rate, Q, parameters needed to correspond to the desire flow rate (and shear level) through my microfluidic device.

Table 3.3. Averages of profilometry measurements across the length of the channel mould. The height of three regions of the 3D-printed mould raised details were measured using the profilometer. The measurements confirmed that the channels fabricated by the mould will be 120 µm high and 839 µm wide. The channel dimension measurements helped us to calculate accurately the required flow rates in order to elicit the desired shear levels during the experiment.

Averages of Profilmetry Measurements	
Inlet	120.3 µm
Mid-Channel	118.3 µm
Outlet	119.7 µm

Subsequently, I run a flow sensor measurement to investigate the consistency of the fluid flow with my flow circuit design (see **Figure 3.3**). By incorporating a flow sensor on the outlet side of the circuit (**Figure 3.4 b**), I could confirm that the flow rate output coming from the channel remained the same as the input into the syringe pump programme. The flow rates and regimen tested were what I subsequently used in my live-imaging experiment (see **Chapter 4, Section 4.3.3**)– 0.1, 5 and 10 dynes/cm^2. According to the flow sensor readings, fluid flow within the whole flow circuit remained consistent and as intended. The ramping up of the fluid flow rate occurred within 10 seconds (**Figure 3.4 c**). Despite minor oscillations at higher flow rates, the fluid flow within the flow circuit remained smooth and had a laminar flow profile (**Figure 3.4 c**). Overall, I have shown here that my fluid flow setup has been able to elicit the intended shear stress within the microchannel reproducibly.

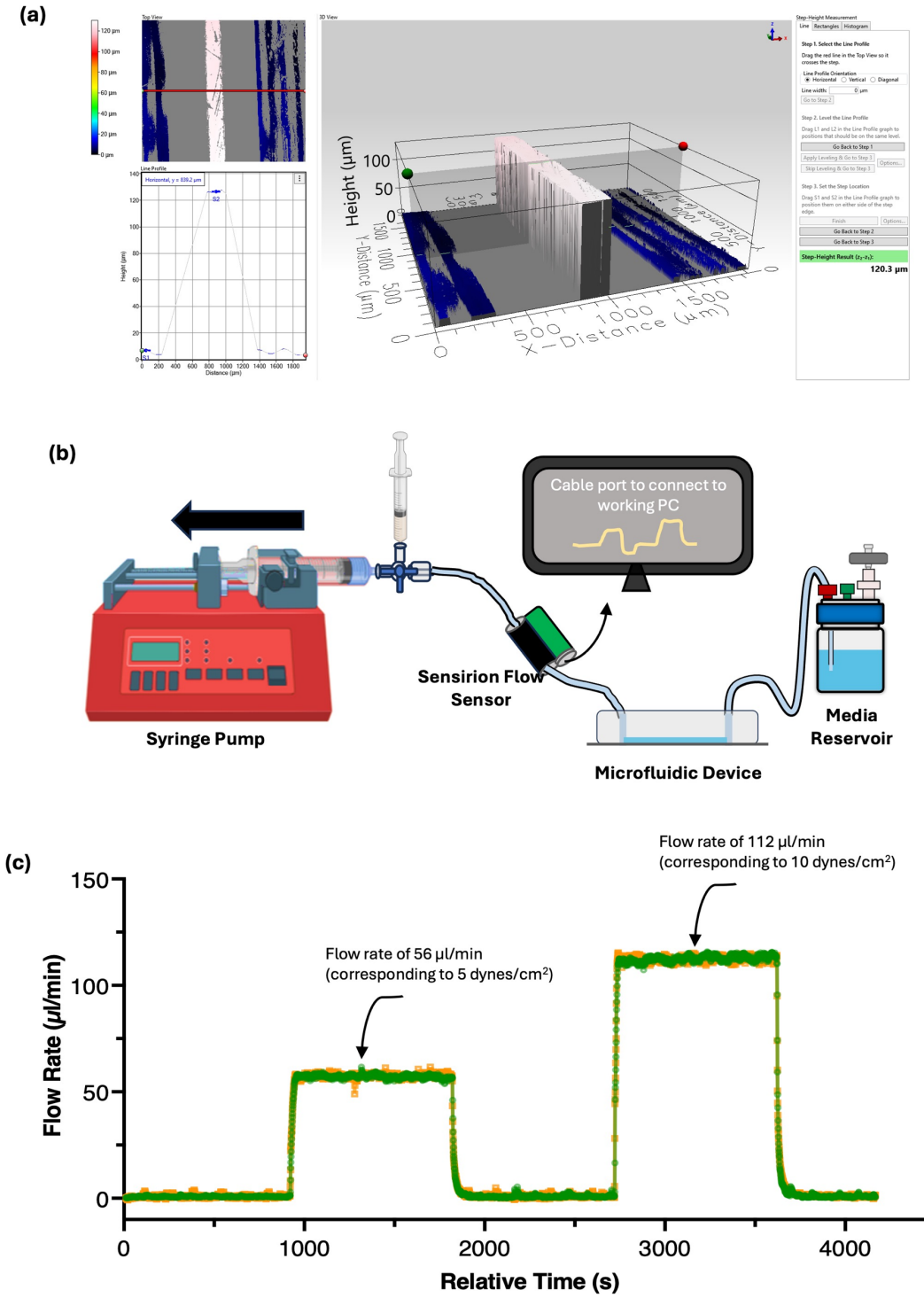


Figure 3.4. Characterisation of flow profile within the microchannel flow circuit. (a) Representative profilometer measurement of the width of the 3D-printed mould raised detail. The measurement corresponds to the resultant microchannel width. Recorded measurements were used to calculate the flow rates needed to elicit the respective shear stress magnitude within the microchannel. **(b)** Schematic drawing of the flow circuit used for flow sensor measurement. The Sensirion flow sensor was incorporated into the flow circuit at the outlet end to record the flow rate through the microchannel. Illustration not drawn to scale. Schematics were partly created using BioRender.com. **(c)** Graph of the recorded flow rate across the microfluidic channel. Given the measured dimensions of our microchannel, the recorded 56 and 112 µl/min flow rates corresponded to 5 and 10 dynes/cm^2 respectively.

3.4.4. Establishing confluence of XLGenEPi clones within the microfluidic system

To investigate the dynamics of GenEPi (Piezo1) during the application of external physical forces, I established a protocol for culturing and imaging XLGenEPi-HEK clones (described in **Chapter 2**) within the designed microfluidic device. XLGenEPi-HEK cells cultured within the microchannel will stably express the GenEPi-sensor during Dox-induction treatment. Within my microfluidic-based system, I can image and capture Piezo1-specific activities under fluid shear stress application. I discuss below culturing factors, such as surface coating and media perfusion rate, which have been carefully optimised to maintain my XLGenEPi-HEK culture within the microfluidic-based system.

(A) Fibronectin-coating is favourable for culturing XLGenEPi clones.

Within the microchannel, the culturing conditions to which the cells are subjected are dramatically different from those of culture plates and dishes. To achieve a monolayer of cells within the microchannel, the adhereability of the culturing surface is crucial for adherent cells, like our model cell-type, HEK 293T cells. Here I investigated how well the XLGenEPi-positive clones adhere and eventually grow on the culturing surface within the microfluidic device. Seeding of the XLGenEPi-HEK cells into the microchannel was performed at high density, 10 million cells/ml. Once seeded, the XLGenEPi-positive HEK 293T clones readily adhere to glass and plastic surfaces when cultured on tissue culture imaging dishes and culture flasks when growing in static condition, they failed to settle on the cover glass surface of my microfluidic device (**Figure 3.5, first row**). Cells became clustered together after seeding, which eventually died out and were washed out of the channel.

Hereafter, I shortlisted two commonly used coating substrates, gelatine and fibronectin, for my microfluidic culturing surface. Both gelatine and fibronectin are natural components of the extracellular matrix. I, therefore, reasoned that coating the culturing surface with either would encourage cells to settle and adhere. 0.1% gelatine coating is sometimes used in static, live-imaging cultures. Within the microchannel, XLGenEPi-positive cells showed initial attachment to the 0.1% gelatine surface, but cells were not spreading out, and the population was sparse across the channel four hours post-seeding (**Figure 3.5, middle row**). This suggested poor cell adhesion, and consequently,

cells would unlikely proliferate and form a uniform monolayer across the microchannel. In comparison, XLGenEPi-HEK 293T cells seeded in fibronectin-coated channels presented favourable adhesion and spreading within four hours post-seeding (**Figure 3.5, last row**). The XLGenEPi-HEK cells cultured in the fibronectin-coated channels assumed and remained in their typical adherent morphology, with dendritic-like processes. Whereas, cells cultured in the other two conditions (no coating and 0.1% gelatine) appeared rounded up and non-adherent even after 4 hours of incubation. By seeding cells into differentially coated microchannel surfaces, I conclude that the addition of favourable ECM material, like fibronectin, encourages cell adhesion and settling, and therefore contributes to healthy and stable cell growth.

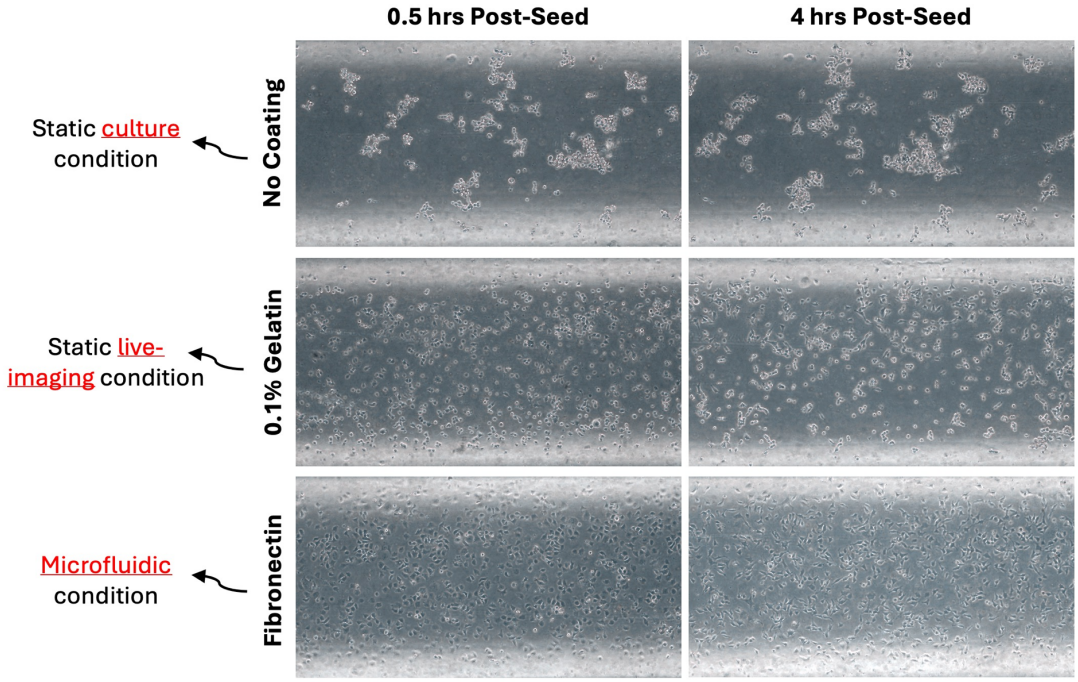


Figure 3.5. Fibronectin-coating is favourable for culturing XLGenEPi-HEK clones within the microchannels. (Top row) No coating, static culture condition. XLGenEPi-positive HEK cells failed to adhere and survive within the uncoated, glass-based microchannel. **(Middle row) 0.1% gelatine-coated, static live-imaging condition.** XLGenEPi cells displayed initial attachment onto the 0.1% gelatine-coated surface, but did not survive within the channel after four hours. **(Bottom row) Fibronectin-coated, microfluidic condition.** XLGenEPi-HEK clones stably adhered and favourably proliferated with the fibronectin-coated microfluidic channels. Brightfield images were taken using 10x magnification.

(B) Acclimatisation flow ensures XLGenEPi clone survival.

I then investigated if administering a consistent flow of media through the channel shortly after cell adherence would be beneficial for cell culturing within the microfluidic

device. As described earlier (**Section 3.3.2**), the channel has a small holding volume capacity of 2.5 µl. Therefore, it is not sustainable for the cells to survive and grow without a constant flow of culture media shortly after adherence is established.

Following the seeding and attachment of cells, I connected the devices as according to the flow circuit designed (**Figure 3.3**) and incubated the setup in standard cell culturing conditions (i.e. 37°C, with 5% CO_2). The calculated flow rate corresponding to 0.1 dyne/cm^2 was 1.12 µl/min according to the actual measured dimensions (**Section 3.4.3**) of the microchannel (calculation described in **Section 3.2.3**). Cells were cultured within the microchannel overnight, at 1.12 µl/min perfusion rate, and allowed to acclimatise to fluidic flow conditions before the actual shear experiment. At this flow rate, media exchange was ensured across the channel, while having the shear level kept low to not trigger any potential changes in cell behaviour that could complicate the investigation of Piezo1 dynamics within the cell layer. I observed that after an overnight incubation with consistent media flow, XLGenEPi-positive HEK 293T cells remained healthy and kept proliferating within the microchannel (**Figure 3.6**). The XLGenEPi-HEK cells assumed their typical spread and adherent morphology, with dendritic-like processes. When seeded at 10 million cells/ml density, I was able to achieve a near-confluence state within each microchannel after 18-hours of culturing under 0.1 dyne/cm^2 shear level. Conversely, when cells were not exposed to an acclimatisation flow overnight, they appeared rounded up and started dying off within the microchannel.

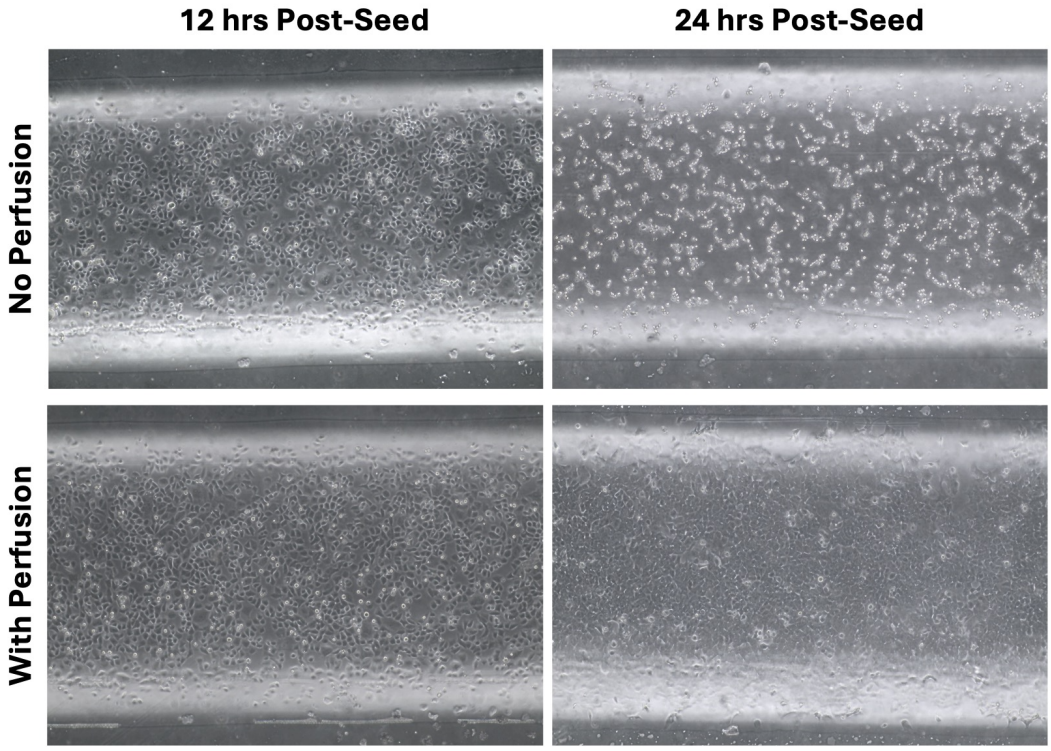


Figure 3.6. Overnight perfusion of culture media ensured proper cellularisation of microchannels. In the absence of overnight media perfusion, XLGenEPi-HEK cells did not survive within the microfluidic channel post-seeding **(Top row).** On the other hand, XLGenEPi-HEK clones proliferate to confluence within the microchannel after overnight perfusion at a flow rate of 1.12 µl/min. This flow rate corresponded to 0.1 dyne/cm^2 shear stress level; which we termed as acclimatisation flow) **(Bottom row)**.

3.5. A time-lapse, live-imaging system fit for mechanosensitive protein dynamics

To visualise and capture cellular GenEPi-signal, I adapted the microfluidic-based setup to be readily insertable into a commercial confocal microscope (here: Leica SP8), and streamlined the image acquisition process to image the fluorescence signal of our GenEPi-sensor within cells. The GenEPi-sensor is a fluorescence-based indicator of Piezo1-specific activities. Therefore, capturing the fluorescent changes reported by my GenEPi-provides real-time information on the activities of the mechanosensitive ion channel, which typically occurs within microseconds. In order to capture the dynamic activities of GenEPi (Piezo1) under shear stress, the live-imaging system had to be optimised with (i) quick scanning speed, (ii) precise imaging intervals across time, and

(iii) significant imaging quantification power. The streamlined image acquisition pipeline we optimised for our microfluidic-based system is summarised below in **Figure 3.7**.

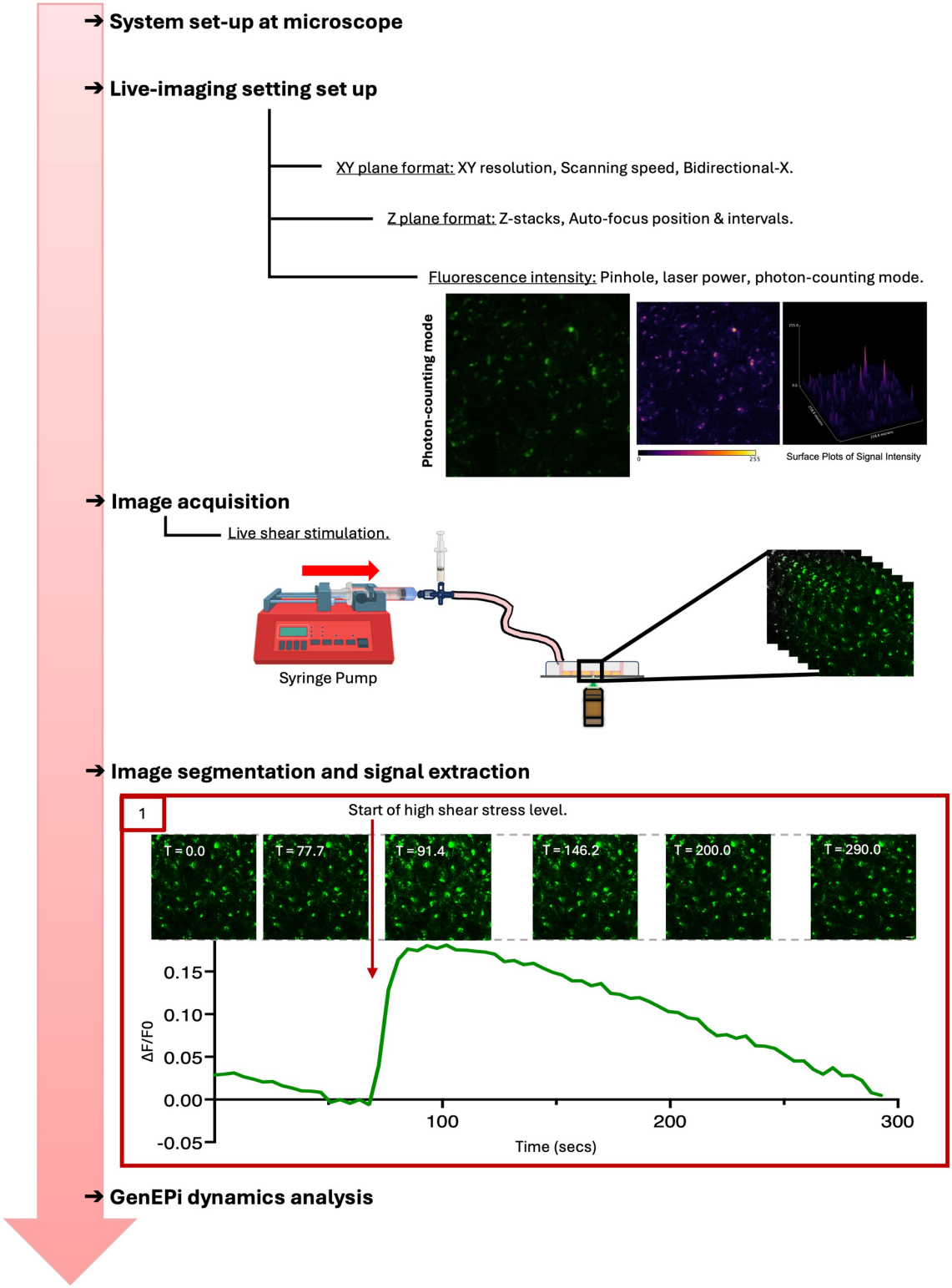


Figure 3.7. Experimental workflow for capturing and analysing GenEPi (Piezo1) dynamics. XLGenEPi-HEK clones cultured successfully cultured in microchannel will have been induced to express the GenEPi-sensor. 24 hours after seeding will see the microchannel being confluent, which would be ready for our time-lapse, live-imaging experiment. Live-imaging settings have been

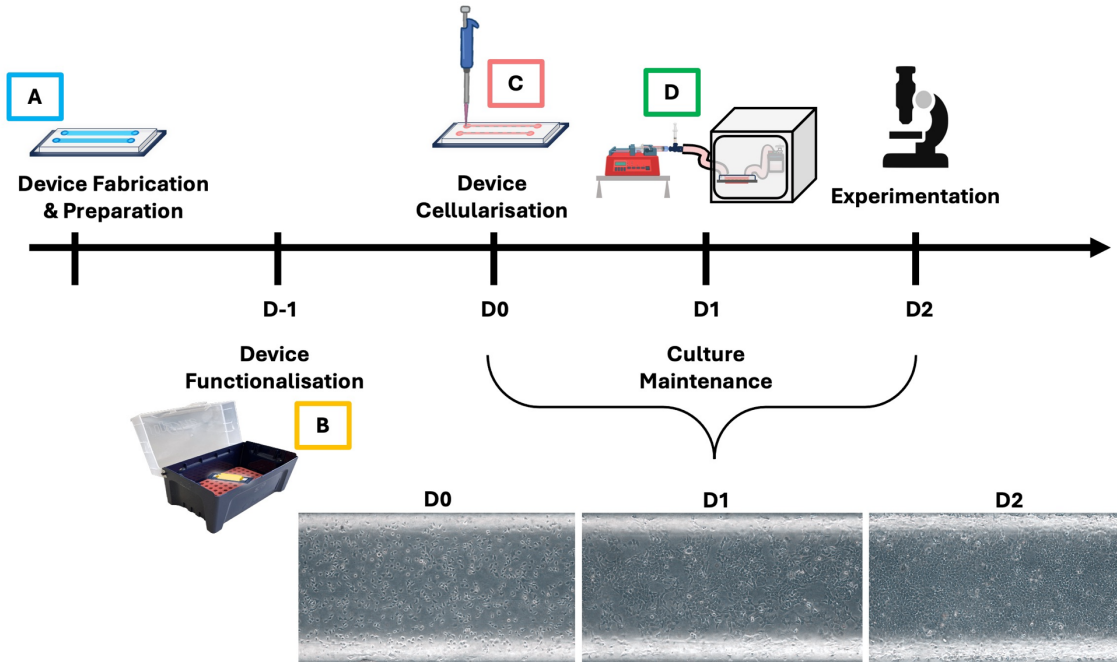
established to acquire (i) quick scanning speed, (ii) precise imaging intervals across time, and (iii) significant imaging quantification power. Mechanical shear perturbation will be conducted in real-time during image acquisition in order to capture the GenEPi fluorescence signal over time. Post-processing of the time-lapse images will help extract data on the GenEPi fluorescence intensity changes ($\Delta F/F_0$) over time. Other dynamics of GenEPi activities in response to shear stress stimuli can be dissected from the set of data.

Using the optimised workflow we developed, I was able to capture in real-time the changes in the GenEPi fluorescence signal in response to the mechanical shear stimulation. Data extracted from the time-lapse images showed that the GenEPi fluorescence intensity changes ($\Delta F/F_0$) over time increased shortly after shear stress application (**Figure 3.7, insert 1**). In summary, this microfluidic-based system I have developed proved reliable in acquiring GenEPi dynamic changes in real-time, which provides us insights into Piezo1-specific activation to shear stress.

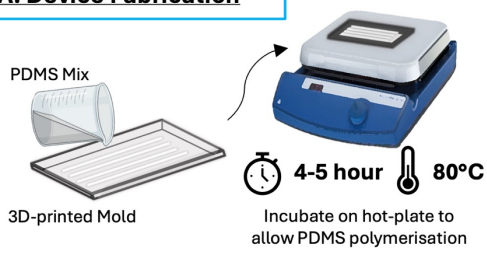
3.6. Discussion

In this chapter, I have reviewed the importance of building a microfluidic-based culturing setup for our system and described the process of optimising the setup. Here, I detailed a summarised timeline and the procedure of my microfluidic-based culturing setup in the following schematics (**Figure 3.8**).

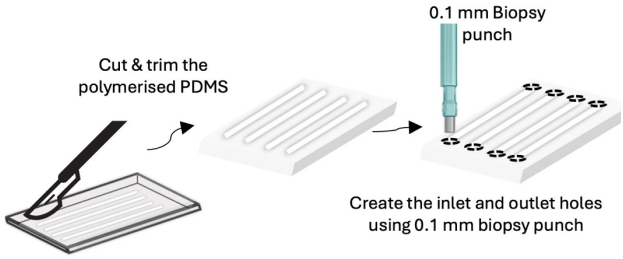
Timeline of Microfluidic-Based System Setup



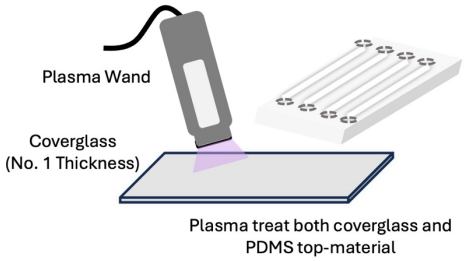
A. Device Fabrication



1 PDMS (device top-material) casting



2 PDMS (device top-material) trimming

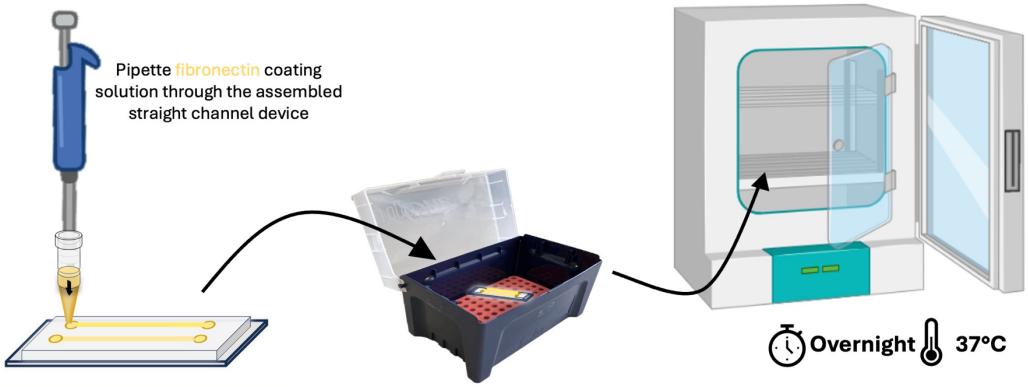


3 Surface activation (Plasma Treatment)



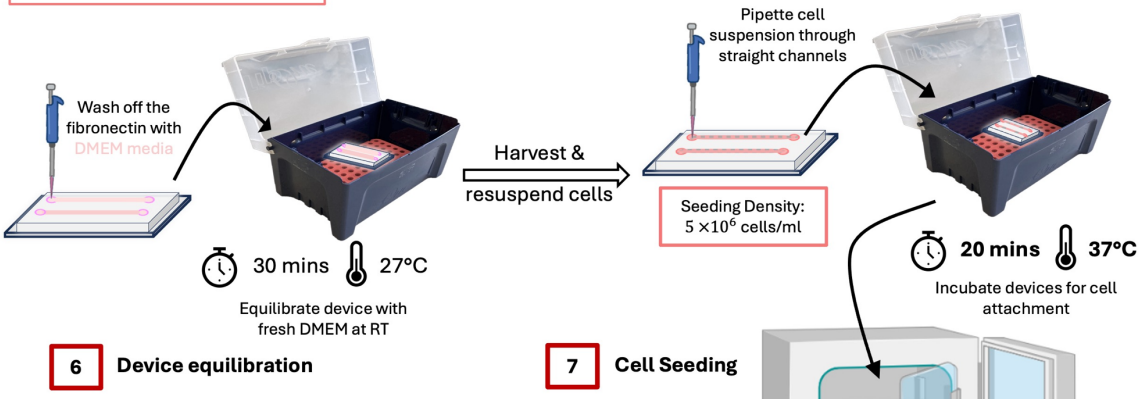
4 Device assembly

B. Device Functionalisation



5 **Fibronectin coating**

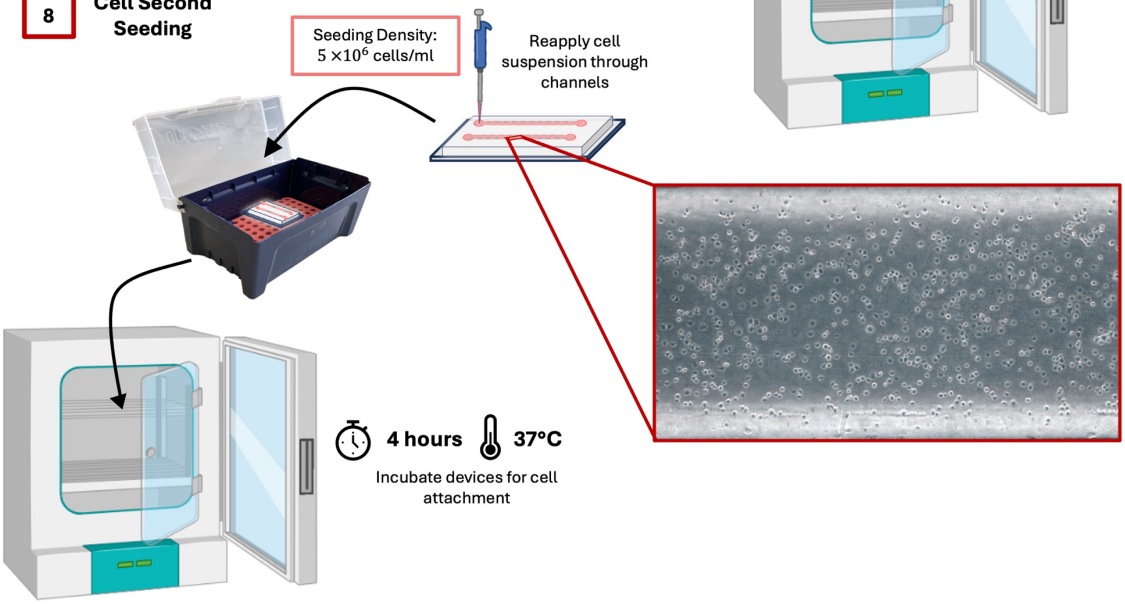
C. Device Cellularisation



6 **Device equilibration**

7 **Cell Seeding**

8 **Cell Second Seeding**



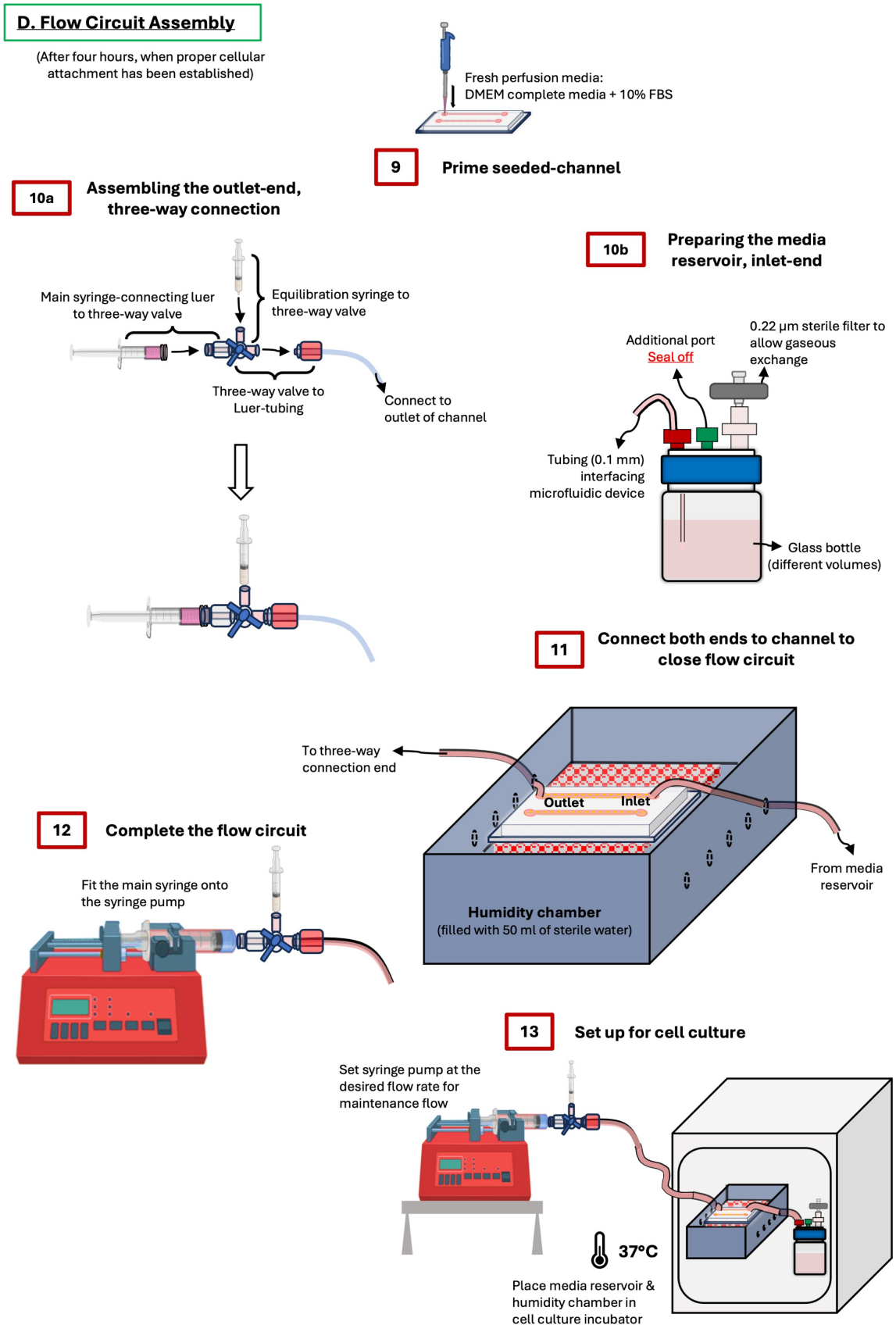


Figure 3.8. An overview of the protocol for setting up our microfluidic-based system. A summarised timeline for the full process of the protocol set-up has been represented at the top of the figure. Individual procedures have been labelled (A to D) within the timeline. **(A) Device Fabrication – Day -2 or before.** A brief illustration showing how our device top-material (PDMS) is being cast and

bonded to the No.1 thickness coverglass base to form the resultant microfluidic device. **(B) Device Functionalisation – Day -1. Schematic drawing of how the microfluidic device is coated (with fibronectin) before cells can be seeded and cultured within the channels. (C) Device Cellularisation – Day 0.** The illustrated procedure of seeding and culturing XLGenEPi-HEK clones within the microchannels post-functionalisation. **(D) Flow Circuit Assembly – Day 1.** Step-by-step illustration for assembling the flow circuit with the seeded-microfluidic device after XLGenEPi cells have properly attached within the microchannel. Schematics are not drawn to scale. Details of each step are described in **Section 3.7**.

3.6.1. The versatility of our developed system

To test if this culturing system is applicable with other cell types, I used the same microfluidic setup for HUVECs culture. My setup procedure remained unchanged from the above-described method (**Figure 3.8**). There were, however, minor adaptations that were made for optimal culturing of HUVECs within the microchannel. For example, instead of using fibronectin coating, 0.1% gelatine solution was used to coat the microchannel culturing surface the day before seeding the cells. Also, seeding of HUVECs was performed at a higher density, 15 million cells/ml, instead of 5 or 10 million cells/ml in the case of HEK cells. Again, the HUVECs culture took two days to form a near-confluence cellularised microfluidic device (**Figure 3.9**).

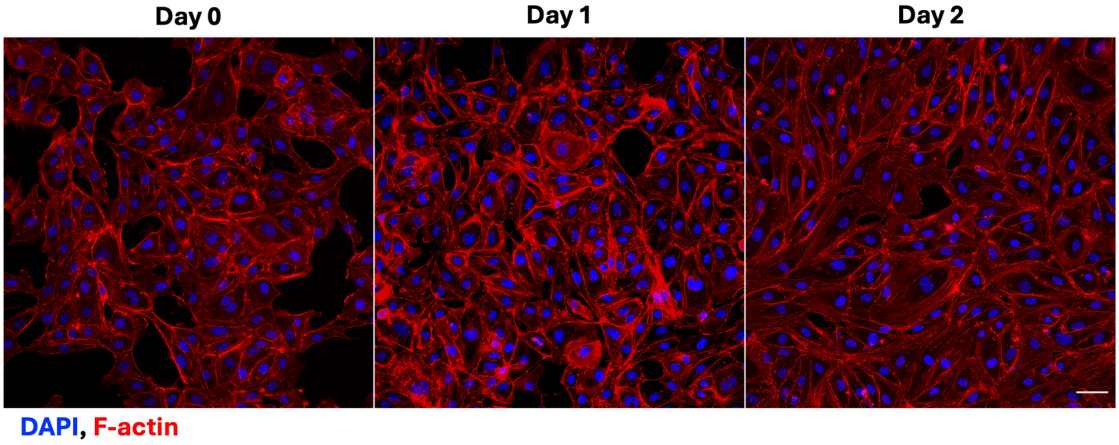


Figure 3.9. Culturing timeline for cellularising the rectangular microchannel with HUVECs. Representative confocal images of HUVECs seeded and cultured within our microfluidic-based set-up from Day 0 to Day 2. Celluarised microchannels were fixed at different time-points and stained for DAPI (blue) and F-actin (red) to illustrate the process of culturing HUVECs within our rectangular microfluidic devices. Confocal images presented at 60x magnification (taken with 20x dry objective, and 3x optical zoom factor). Scale bar = 15 µm.

In conclusion, I have developed a microfluidic-based culturing system, which has been optimised for my XLGenEPi-HEK 293T clones, but can be easily adapted to other cell types. From device fabrication to flow circuit setup, this microfluidic-based system has been designed and devised to be simple, yet compatible for precision imaging of cellular mechanical events under confocal microscopes.

3.6.2. Mechanical stretch-based system to study mechanosensitive proteins and cell processes

The system described in this thesis is developed based on organ-on-a-chip methodology. Organ-on-a-chip technology has emerged as an invaluable method in modelling crucial parts of human physiology *in vitro*, like cellular microenvironment. By integrating our genetically-encoded, Piezo1-specific sensor, GenEPi, into a microfluidic-based organ-on-a-chip platform, we are able to track and investigate the dynamic behaviour of cellular Piezo1. While I have successfully coupled a microfluidic-based system with advance imaging technique, this system may pose challenges related to other imaging modalities, such as optical access and high-resolution imaging. A microfluidic-based system, like ours, is also primarily designed to study fluid flow-induced mechanotransduction processes. Therefore, limiting the applicability of such system to selective cellular microenvironment context. However, there are other ways of organ-on-a-chip systems employed in previous research to capture and investigate mechanosensitive cellular processes.

Mechanical stretch-based organ-on-a-chip system is another widely used platform for studying dynamic cellular responses. Using either commercially available or custom-built cell stretchers, which are usually compatible with commercial confocal microscopes, we can induced controlled mechanical deformations on the cells or tissues. The versatility of experimental design from using a mechanical stretch system allow researchers to study the cellular effect of a range of mechanical stress, such as uni- and/or bi-axial mechanical stretch, cyclic strain, and even membrane compression. The mechanical stretcher system has also been shown to be highly compatible with advanced imaging techniques, such as live-cell microscopy, confocal microscopy, and AFM. Combining imaging modalities has yielded insights into dynamic changes in cell

morphology, cytoskeletal organization, and mechanosensitive protein localisation in response to mechanical forces. For example, Nava *et al*. (2020) revealed distinct time-dependent mechanoprotective response of the cell nucleus to prevent mechanical strain-induced DNA damage[211].

3.7. Statement of Contribution

The microfluidic work described in this chapter was carried out with the generous help of Ms Adele Lam Jing Ying (a fellow PhD student) and Dr Simon Tupin from the vBS group, supervised by Dr. Joseph van-Batenburg Sherwood.

4. Piezo1 dynamics dissected through GenEPi time-lapse, live-imaging system

"Research is what I'm doing when I don't know what I'm doing."

– Wernher von Braun

4.1. A microfluidic-based, live-imaging system for studying Piezo1 dynamics

Piezo1 is a mechanosensitive ion channel, which is activated upon changes in membrane tension caused by mechanical forces. The activation of Piezo1 causes the ion-conducting pore of the channel to open, which allows Ca^{2+} influx into the cytosol, leading to further downstream activities. Previous studies have also shown that wild-type Piezo1 exhibits dynamic activities, like diffusive motion, in the cell membrane[59,97,116]. The mobile behaviour in Piezo1 was subsequently replicated by Yaganoglu & Kalyviostis *et al.* (2023) when membrane GenEPi clusters appeared mobile in response to local cellular traction forces[1]. In addition, Piezo1-dependent Ca^{2+} flickers

were previously reported in response to local mechanical stimuli on the cell membrane[1,41,116].

In my current system, we apply laminar fluid shear stress through the microchannel to elicit uniform, global mechanical stimulation across. Imaging GenEPi-signal under altering shear stress level and duration allowed me to investigate the effects of perturbatory mechanical forces on membrane Piezo1 activities. Here, I explore the characterisation of Piezo1-specific dynamics in response to global mechanical stimuli (via fluid shear stress), using my microfluidic-based system.

4.2. Fluid shear stress on HEK 293 cells

In my microfluidic-based system, I have utilised HEK 293T cells as the cell model to dissect cellular-Piezo1 dynamics. As the rationale for developing such a system is to have a near-physiological study of the mechanosensitive ion channel, deriving the closest shear parameter in our experiments is important. The phenotypic nature and tissue origin of HEK 293 cells remained undetermined, though certain cellular characteristics traits had been identified from previous transcriptomics studies[202]. With kidney and pituitary tissue characteristics being picked out, Lin *et al*. (2014) concluded that HEK 293 and its derivatives possess epithelial, adrenal, and central nervous cell characteristics [202]. Therefore, the exact cell-type or location where the original cell samples were extracted remains unclear.

Table 4.1. List of shear stress magnitude ranges previously used on HEK 293 cells in literature.

Shear Stress Magnitudes	Purpose of Studies
Between 0.1 to 0.8 dynes/cm^2	Mainly for general culturing of “kidney”-natured cells in microfluidic chips.
Between 1 to 30 dynes/cm^2	Shear experiments to study the effects of shear on kidney cells.
> 30 dynes/cm^2 (Up to 70 dynes/cm^2)	Bioreactor culture studies (Mainly to find the optimal condition for big suspension HEK cultures).

Previous research using microfluidic technology to study HEK 293 and other renal cells has employed a wide range of shear stress magnitudes, between 0.1 to 70 dynes/cm^2 [201,203–206]. The shear stress magnitude varied depending on the intended purpose of the research (**summarised in Table 4.1**). Specifically, studies which investigated the sensitivity of HEK 293 cells to shear stress have reported force usage ranging from 0.1 to 10 dynes/cm^2. Exposing cells to shear stress above 10 dynes/cm^2 has been reported as the pathological condition of the renal proximal tubular cells[204,205]. Therefore, in our system, we cultured and exposed the XLGenEPi-HEK cells to varying shear stress levels, from 0.1 dyne/cm^2 to 50 dynes/cm^2.

4.3. Material & Methods

4.3.1. Cell Culture

To study the dynamics of Piezo1 activity, the XLGenEPi-HEK 293T clones generated for this PhD research work (**Chapter 2**) were used throughout. Like WT HEK 293T cells, the XLGenEPi clones are cultured at 37°C, 5% CO_2, in DMEM complete media, consisting of high glucose DMEM with GlutaMAX (ThermoFisher, 10569010), supplemented with 10% FBS (Sigma-Alrdrich, F7524) and 1x Penicillin-Streptomycin antibiotic solution (Thermo Fisher, 15140122).

HUVEC cultures were used to investigate the long-term effect of shear stress on Piezo1 dynamics in cells. HUVECs were cultured at 37°C, 5% CO_2, in EGM™-2 Endothelial Cell Growth Medium-2 BulletKit™ (Lonza, CC-3162). Medium kit system contains EBM™-2 Basal Medium (Lonza, CC-3156) and EGM™-2 SingleQuots™ Supplements (Lonza, CC-4176).

All cultures were routinely tested for mycoplasma infection using Mycoplasma detection kit (LuBioScience GmBH, B39032). For routine maintenance, culture media was changed

every two days and passaged at ~ 70% confluence using TrypLE™ (Gibco™, 12604-013). XLGenEPi-HEK 293T clones used were of P9-10, and HUVECs were of P3-4.

4.3.2. Microchannel Device Culturing

In order to study the mesoscopic dynamics of Piezo1 on a monolayer sheet of cells, we devised a microfluidic-based culturing and perfusing system. This system is adaptable to different cell types and applications. A detailed description of the system is being set up for our experiments has been elaborated in **Chapter 3**. Briefly, our microfluidic device is fabricated using soft lithography method, and the molded PDMS top-layer is trimmed and plasma-bounded onto a thickness #1 coverglass. After which, sterilised microfluidic devices are prepared for cell culturing by coating the glass culturing surface with either 1.5 μg/cm^2 fibronectin or 0.1% gelatin solution(s). XLGenEPi-HEK clones (or HUVECs) were seeded into coated devices the day after at a seeding density of 5 million cells/ml/. Once proper cellular attachment is achieved within the microchannels, the flow circuit would be assembled to perfuse fresh media for overnight culturing. Generally, 24 – 48 hours of media perfusion would establish a monolayer of HEK (or HUVECs) cells within the microchannel.

4.3.3. Fluid Shear Stress Applications

Fluid shear stress application was established using the PhD Ultra™ programmable syringe pump (Harvard Apparatus, 70-3007). Fluid flow rate was calculated and calibrated according to the channel's dimension to correspond to the respective shear levels. Depending on the level of fluid shear stress intended, the respective fluid flow rate will be input into the syringe pump system. Fluid flow rates corresponding to 0.1 – 10 dynes/cm^2 fluid shear stress were used, where 0.1 dyne/cm^2 for cell culturing and 1 – 10 dynes/cm^2 for shear experiments. Fluid flow rates corresponding to the different shear stress levels were calculated as according to the flow rate (Q) equation described in **Section 3.7.3**. The syringe pump is set on "Withdrawal" mode for cell culturing, and "Infusion" mode for experimental shear stress application.

4.3.4. Confocal and Time-lapse, Live-imaging

Images were acquired on a Leica SP8 confocal laser scanning microscope equipped with a white light laser (WLL, Leica) using an HC PL APO CS2 20x/0.75 dry objective. For time-lapse, live-imaging, images of cells were acquired at 8-bit depth, at 512 x 512 format, excited with 488 nm for GenEPi-signal, with photon-counting mode. An optical zoom factor up to 3 might be used to obtain higher magnification of the cells and their subcellular structures. To ensure fast image acquisition, we imaged small regions of interest within the field of view, recording a single z-plane over several minutes (pinhole size ranged from 3 Airy units to maximum pinhole size) using the maximum acquisition speed. When live-imaging was performed on the Leica SP8 confocal, bidirectional scanning with off-set correction was used to increase acquisition speed even more. Live imaging of cells was carried out in culture medium.

For fixed, confocal imaging, images of cells were acquired at 8-bit depth, at 1024 x 1024 format, excited with 405 nm for DAPI, 488 nm for Alexa Fluor Plus-488 reporter, and 647 nm for Alexa Fluor-647 Phalloidin, respectively. An optical zoom factor up to 3 might be used to obtain higher magnification of the cells and their subcellular structures. Z-stack images were acquired with an average z-stack size 20 µm at 0.88 µm optimal step-size.

4.3.5. Immunofluorescence Staining

To fix and stain the cells within the microfluidic device, the design of the system has allowed for direct pipetting of fixing and staining solutions through the microchannel from the inlet and outlet interfaces. Cells were fixed in 4% PFA (diluted from 16% concentrate solution, Thermo Fisher, 28908) for 10 minutes at 37^{o}C, permeabilized with DPBS supplemented with 0.1% TritonX-100 (Sigma-Aldrich, T8787) and blocked with 10% Donkey Serum (Jackson ImmunoResearch, 17-000-121) in DPBS supplemented with 0.1% TritonX-100. Samples were then incubated with anti-Piezo1 antibody (Proteintech; 15939-1-AP) diluted in 5% Donkey Serum (Jackson ImmunoResearch, 17-000-121) in DPBS supplemented with 0.1% TritonX-100. After several washing steps with DPBS, the samples were incubated donkey anti-rabbit IgG (H+L) Alexa Fluor Plus-488 (Thermo Fisher, A32790), Alexa Fluor-647 Phalloidin (Invitrogen, A22287), as well as DAPI (Thermo Fisher, 62248). Finally, washing with 1x DPBS was repeated at least five times,

before filling the microchannel with 15 µl of 1x DPBS (Sigma-Aldrich, D8537), making sure that a small amount of DPBS solution (approximately 30 µl) sat at both ends of the channel. Samples were stored in 4°C until imaging.

4.3.6. Image Processing and Analysis

ImageJ/Fiji [199] (release 1.53f51) was used for the post-processing of the confocal images acquired. For the immunofluorescence-stained confocal images, the maximum (X-Y plane) projection of the Z-stack images were made and subsequently merged to form the realised fluorescence images. For the live-imaging processing, GenEPi (Piezo1) clusters were segmented using the respective 8-bit single channel confocal images. Images were masked by (i) subtracting background (rolling ball radius of 2 pixels), (ii) applying a median filter (radius of 2 pixels) and (iii) thresholding (Otsu). The mask image was then subsequently watersheded, dilated before using it to obtain quantitative data, such as mean gray value, from the built-in "Analyse Particles" function of Fiji/ImageJ. Single-pixel measurements due to masking artifacts were excluded from the subsequent analysis. Any average camera noise was subtracted from images that are displayed.

To compute the GenEPi fluorescence intensity changes before and after shear stress application, $\frac{F}{F_0}$ images were calculated using the built-in image calculator function (where F_0 was the average of the 5 frames before shear stimulation was turned on during the time-lapse). Quantitative data of the $\frac{F}{F_0}$ changes over time were collected from individual cells or regions of interest using the plot z- axis profile (where z dimension was time, usually in milliseconds or seconds). Data were subsequently analysed and plotted in GraphPad Prism 9.

To track individual GenEPi (Piezo1) membrane clusters Trackmate[215] was used with LoG detector (Laplacian of Gaussian filter), estimated object diameter of 1 µm, quality threshold of 1.0 and sub-pixel localization. The tracker used was the simple LAP tracker with linking max distance of 1 µm, gap closing distance and frames of 1 µm and 20 frames, respectively. Data were saved as xml files and subsequently analysed with MATLAB (R2021b) and @msdanalyser[216]. To categorise the GenEPi tracks population,

the xml files were loaded into the TraJClassifier[207] plugin in ImageJ/Fiji. Data from @msdanalyser and TraJClassifier plugin were further analysed and plotted using GraphPad Prism 9.

To analyse the GenEPi (Piezo1) dynamics under fluid shear stress, we normalised the GenEPi signal according to the "response curve normalisation" approach used in Sun, *et al.* (2013) and Zamir, *et al.* (2022)[212,217]. The GenEPi response curve for each cell was defined as $R(t) = \frac{\Delta F}{F_0} = \frac{(F(t)-F_0)}{F_0}$, where *F(t)* was calculated as the mean GenEPi fluorescence intensity at time *t*, and the baseline F_0 was calculated as the mean of the first 5 frames (20 seconds) of *F(t)* before shear stimulation was turned on during the time-lapse. The *R(t)* provided a dimensionless measure for the GenEPi fluorescence intensity changes relative to the cell's basal intensity. To evaluate the changes in the GenEPi fluorescence intensity in response to systemic shear stress application, we derived GenEPi responses in time: $\widehat{R_i}(t) = \frac{dR_i}{dt}(t) - \langle\frac{dR_i}{dt}(t)\rangle$, where $\langle\frac{dR_i}{dt}(t)\rangle$ is the mean value of $\frac{dR_i}{dt}(t)$, and $\frac{dR_i}{dt}(t)$ was calculated as the derivative of the GenEPi responses against time elapsed. This temporal derivative of GenEPi responses, $\widehat{R_i}(t)$, is termed GenEPi dynamics. And the standard deviation of the individual cells' GenEPi dynamics is expressed as $\sigma\widehat{R_i}(t)$. Data were further analysed in GraphPad Prism 9 and plotted using the PlotTwist web app[209].

To quantify Piezo1 expression fluorescence intensity changes in the HUVECs shear stress experiments, images were opened on ImageJ/Fiji [199] (release 1.53f51) cell regions of interest were manually selected. Then, mean intensity values were exported to GraphPad Prism 9 for further analysis and graph-charting.

To measure the changes in nuclei size following externally applied shear stress, the DAPI (405 nm) 8-bit single channel confocal images were segmented and masked by (i) subtracting background (rolling ball radius of 2 pixels), (ii) applying a median filter (radius of 2 pixels) and (iii) thresholding (Otsu). The built-in "Analyse Particles" function of Fiji/ImageJ was used to obtain quantitative data, such as mean gray value, area,

perimeter, major axis, minor axis, and aspect ratio, on the processed nuclei images. Data were plotted and further analysed using GraphPad Prism 9.

4.3.7. Statistical Analysis

All data are expressed means ± SEM. Sample sizes (n) are provided in the text or figure legend of each experiment. Each experiment has been repeated independently at least 3 times. To determine whether the data set has a Gaussian distribution, data subjected to the Shapiro-Wilk normality test; $p>0.05$ indicated it has a Gaussian distribution, and $p<0.05$ indicated it did not. With Gaussian distribution confirmed for each data set, two-tailed Student's t-test was applied to compare two independent datasets; with an F-test to compare variances. When F-test resulted in $p<0.05$, Welch's correction was applied to the t-test. When more than 2 datasets were present with Gaussian distribution, one-way ANOVA was used to compare datasets, followed by multiple comparisons test. When at least one of the compared data sets did not have a Gaussian distribution, Mann-Whitney test was applied to compare two independent datasets; and Wilcoxon rank-sum test was applied when the data sets were paired. When more than 2 datasets were present without Gaussian distribution, Kruskal-Wallis test was applied, followed by Dunn's post hoc multiple comparisons test. For all statistics, either p-value number was reported or with n.s.=$p>0.05$, *=$p<0.05$, **=$p<0.01$, ***=$p<0.001$ and ****=$p<0.0001$. Mean Squared Displacement analysis and linear fitting of the GenEPi (Piezo1) membrane clusters tracking dynamics were performed using MATLAB (R2021b) and @msdanalyser[216].

4.4. Functional characterisation of Piezo1 dynamics

4.4.1. GenEPi fluorescence intensity increases after shear induction

Before diving into the investigation of Piezo1 dynamics, I first tested GenEPi's optical resolution in response to fluid shear stress within the system we developed. We exposed the cells to 0.1 dyne/cm^2 and 1 dyne/cm^2 in our experiments because the two magnitudes were associated with the shear stress commonly used in precious studies

and the physiological shear conditions[204,205]. I recorded the fluorescence signal across time to capture the changes in GenEPi fluorescence intensity in response to the shear stress (**Figure 4.1 a**). The calculated GenEPi-fluorescence intensity (annotated F/F_0; see **Section 4.3.6**) increased by at least 1.2-fold (20% increase in GenEPi fluorescence intensity) after inducing 1 dynes/cm^2 of shear stimulation (**Figure 4.1 b**). The level of fold increase observed in my experiments is comparable to what Yaganoglu & Kalyviotis *et al.* (2023) reported in the characterisation of the GenEPi-sensor[1]. Although there is no significant difference in the overall "Max F/F0" measurements, the analysis of GenEPi-responses of individual cells revealed that fluorescence intensities increased after shear stress induction (**Figure 4.1 c**). These results further strengthen the sensitivity of GenEPi as an optical tool to resolve activity dynamics of Piezo1 channels under fluid shear stress.

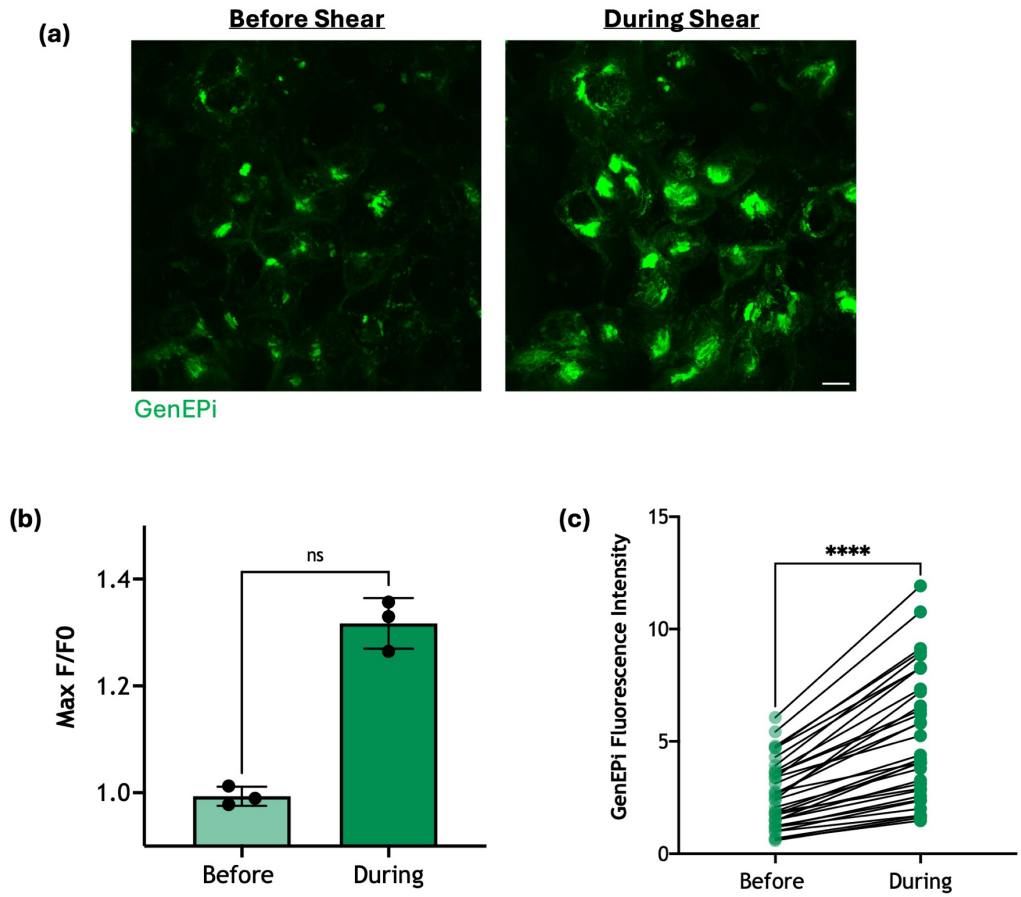


Figure 4.1. GenEPi fluorescence intensity increases after shear stress induction on XLGenEPi-HEK clones. (a) Representative max fluorescent-intensity projected confocal images of XLGenEPi-HEK cells before and after shear stress application. Confocal images were taken under time-lapse, live-imaging (with 20x dry objective, and 3x optical zoom factor) while shear stress was applied on the XLGenEPi-HEK clones. Max-intensity projected images presented at 60x magnification. Scale bar = 15 µm. **(b)** Representative bar graph showing the differences in GenEPi max fluorescence intensity (F/F_0)

in XLGenEPi-positive HEK clones before and after shear stress application. N = 34 cells both before and after shear stress stimulation. *** , p < 0.001. **(c)** Single cell comparison of GenEPi fluorescence intensity (F/F_0) changes in XLGenEPi-positive HEK clones before and after shear stress application. N = 3 experimental repeats (with an average of 34 cells analysed for the live-imaging data). n.s, non-significance, p>0.05, and **** , p<0.0001.

4.4.2. Cellular Piezo1 exhibits diffusive dynamics following shear stress induction

Previously we have shown that GenEPi displays similar dynamics as wt-Piezo1 channels in the cell membrane using time-lapse, Total Internal Reflection Fluorescence Microscopy (TIRFM) imaging[1]. Here, I wanted to investigate if Piezo1 exhibit the same dynamics when cells are subjected to global-scale mechanical stimuli, like fluid shear stress. I performed time-lapse, live-imaging on cellularised microchannels and applied fluid shear stress at different magnitudes, from 0 (static) to 10 dynes/cm^2, during the image acquisition process (**Figure 4.2 a**). ImageJ plugin/Fiji, TrackMate, was used and parameters for object identification were optimised (see **Section 4.7.6**) to accurately detect for individual GenEPi clusters (**Figure 4.2 b**). Fluid shear-induced time-lapse imaging of XLGenEPi-HEK clones revealed that Piezo1 clusters are mobile within cells. Cellular GenEPi clusters, following shear induction, were tracked to build the trajectories and plot the mean-squared displacement (MSD) of the GenEPi tracks (**Figure 4.2 c**). The apparent two-dimensional (2D) diffusion coefficient of ~0.0328 μm^2/s was derived from the slope of the MSD, which is within the range of previously reported values for Piezo1 clusters[1,97,116]. To confirm the membrane diffusiveness of cellular Piezo1 clusters, I employed the TraJClassifier[207] plugin on ImageJ/Fiji to dissect the distribution GenEPi track population upon shear stress application. The TraJClassifier[207] plugin segments and measures the GenEPi cluster motion tracks to classify the trajectory into four basic motion types – Confined, Normal Diffusion, Anomalous Diffusion and Directed Motion (see **Table 4.2** for definition of the motion types[208]).

Table. 4.2. Definition of the four basic motion types.

Motion Types	Definition
Confined Diffusion	The movement of particle (or cell) within a bounded region close to its starting point.
Normal Diffusion	The random molecular motion of particle (or cell), generally from an area of higher concentration to an area of lower concentration.

	Examples of normal diffusion in biological context: Ions and chemical compounds across a concentration gradient.
Anomalous Diffusion	The diffusion motion where the displacement of particle (or cell) is not in proportion to time progression. Examples of anomalous diffusion in biological context: Ion channels in the plasma membrane, and colloidal particle in the cytoplasm.
Directed Motion	The migratory motion of particle (or cell) in a direction or path of interest. Example of directed motion in biological context: Cell migration across a plane.

GenEPi responses to systemic mechanical forces applied by fluid shear stress indicated a less confined (and more directed) motion (**Figure 4.2 d and e**). This "loss of confined and gain in directed motion" phenomenon was more prevalent as the shear stress magnitude increased. My results support that Piezo1 clusters exhibit diffusive dynamics within the membrane, similar to previous studies[1,59,97,116]. I further establish the nature of the exhibited diffusive dynamics with the categorising of Piezo1 clusters' motion. My results also indicate that motions of Piezo1 clusters are directed upon mechanical force stimulation. Interestingly, I observed a huge proportion of GenEPi cluster tracks categorised as "Anomalous Diffusion", even in the absence of external systemic mechanical stimuli (**Figure 4.2 f**). These observations highlight the dynamic nature of Piezo1 channels on the membrane and warrant further refined analysis to dissect the mechanism of motion. Taken together, GenEPi robustly reveals the diffusion dynamics of cellular Piezo1 channels under systemic, global mechanical stimuli, like fluid shear stress.

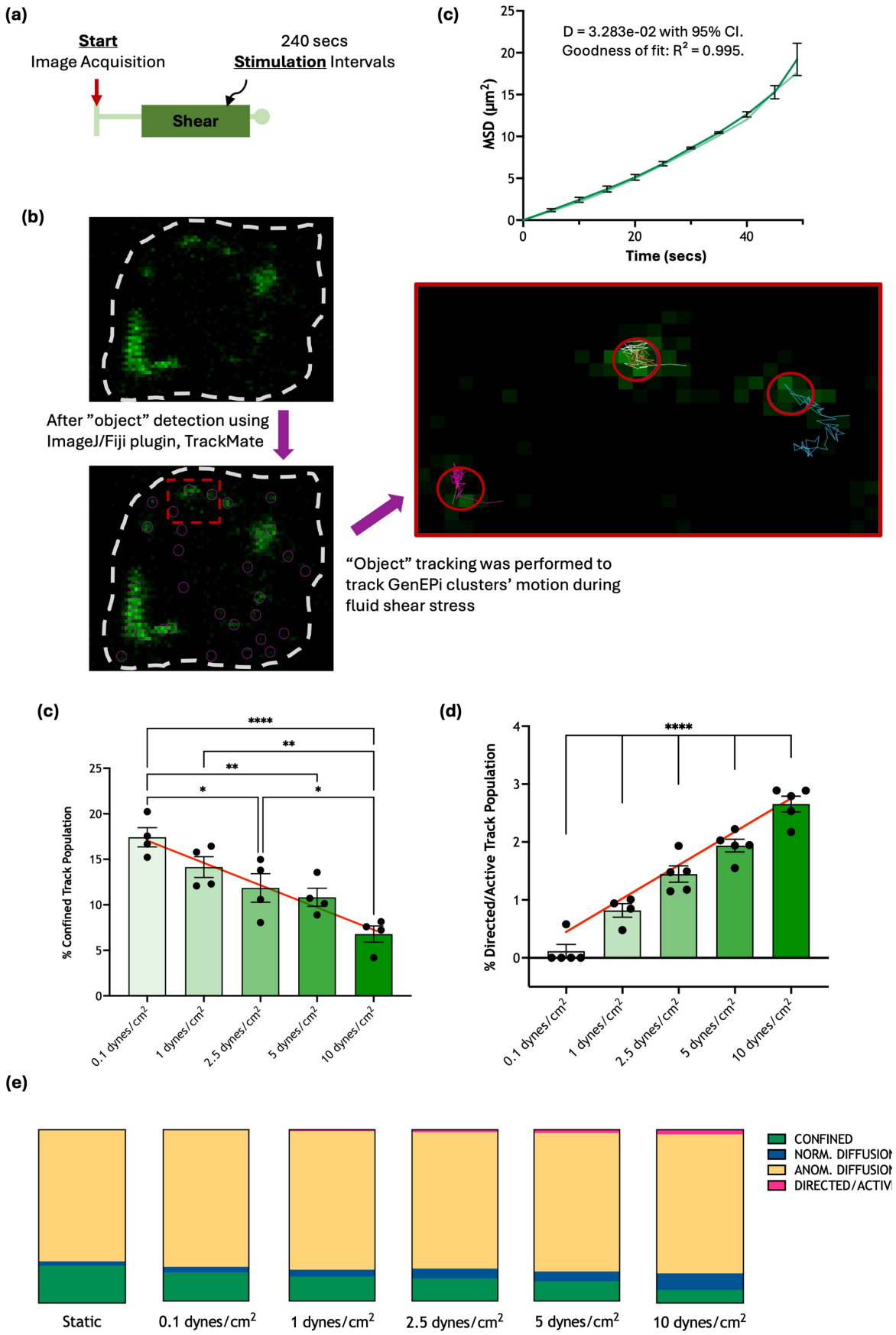


Figure 4.2. GenEPi (Piezo1) clusters displayed less confined diffusive motion within the cell membrane during shear stress stimulation. (a) Representative timeline depicting the shear stress stimulation cycle during the time-lapse, live imaging experiment. **(b)** "Object" identification and

tracking was performing, using ImageJ/Fiji plugin - TrackMate, to track the trajectories of individual GenEPi clusters within cells. **(c)** Mean-squared displacement (MSD) calculated from 4338 GenEPi cluster tracks plotted as a function of time. Data fit to a straight line with a slope corresponding to a two-dimensional (2D) diffusion coefficient (D) of 0.0033 $\mu m^2/s$. R^2 for linear fit to data is 0.995. **(d)** Representative bar graph tracking the population (%) of confined GenEPi (Piezo1) clusters during different shear stress magnitudes. The population of less confined Piezo1 clusters significantly decreased at shear stress magnitude 2.5 dynes/cm^2 and above. Data (red line) fitted to a linear regression model to depict the slope of decreasing confined GenEPi clusters within cells at increasing shear stress magnitudes. * , p<0.05, ** , p<0.01, and **** , p<0.0001. **(e)** Representative bar graph tracking the population (%) of directed diffusive GenEPi (Piezo1) clusters during different shear stress magnitudes. The population of Piezo1 clusters exhibiting directed diffusive motion significantly increased at shear stress magnitude 1 dyne/cm^2 and above. **** , p<0.0001. Data (red line) fitted to a linear fit model to depict the slope of increasing directed diffusive GenEPi clusters within cells at increasing shear stress magnitudes. **** , p<0.0001. **(f)** Summarised track motions of Piezo1 clusters within the population at different shear magnitudes. For the GenEPi dynamic live-imaging, N = 5 experimental repeats (with the following number of GenEPi cluster tracks analysed at different shear magnitudes: 0.1 dyne/cm^2 (616 tracks), 1 dyne/cm^2 (1068 tracks), 2.5 dynes/cm^2 (790 tracks), 5 dynes/cm^2 (609 tracks), and 10 dynes/cm^2 (1255 tracks)).

4.4.3. GenEPi responses are modulated dependent on the shear magnitudes

To begin dissecting the dynamics of Piezo1's activity in HEK 293T cells under fluid shear, I first looked at how GenEPi responded to shear stimulation at different levels. After inducing the expression of GenEPi through Dox-treatment, XLGenEPi-HEK clones were subjected to single pulse shear stimulation and imaged using time-lapse, live-imaging (see **Figure 4.2 a**). Between 1, 2.5 and 5 dynes/cm^2 shear stimuli, we observed at least a 2- and 3- fold decrease in GenEPi-signal response time (**Figure 4.3 a**). With an average GenEPi response time of 27.5 secs for 1 dyne/cm^2 stimulation, the response time decreased to 12.7 secs and 4.24 secs for 2.5 dynes/cm^2 and 5 dynes/cm^2 respectively. From these results, GenEPi-signal showed quicker response time with increasing shear magnitude. However, this trend was not observed in higher shear magnitudes. After 10 dynes/cm^2 stimulation, the response time of GenEPi-signal in cells did not decrease but became chaotic.

Apart from the dissimilarities in GenEPi response time across shear magnitudes, differing shear levels resulted in distinctive GenEPi response patterns. At 1 and 2.5 dynes/cm^2 shear stimulations, cellular GenEPi-response displayed a gradual increase in fluorescence intensity up to a peak value of 0.116 and 0.225 respective, which eventually plateaued out (**Figure 4.3 b**). The sustained activation of GenEPi-sensors remained steady throughout the 1 and 2.5 dynes/cm^2 mechanical stimulations (**Figure 4.3 c**).

Whereas upon 5 and 10 dynes/cm^2 shear level stimulation, the GenEPi-signal responded with a single-peak activation pattern, followed by a pronounced signal depression **(Figure 4.3 b and c**). The GenEPi-activation peak occurred 29.7 secs after exposure of XLGenEPi-HEK clones to 5 dynes/cm^2, whereas it took 72.1 secs for XLGenEPi-HEK clones exposed to 10 dynes/cm^2 to reach activation peak value (**Figure 4.3 c**). These results emphasise that the speed and pattern of HEK-Piezo1 activation are differentially modulated by the magnitudes of the shear stress. Furthermore, the difference in duration for GenEPi peak-signal to be reached under different shear stress magnitudes suggests that cellular Piezo1 activation occurs progressively.

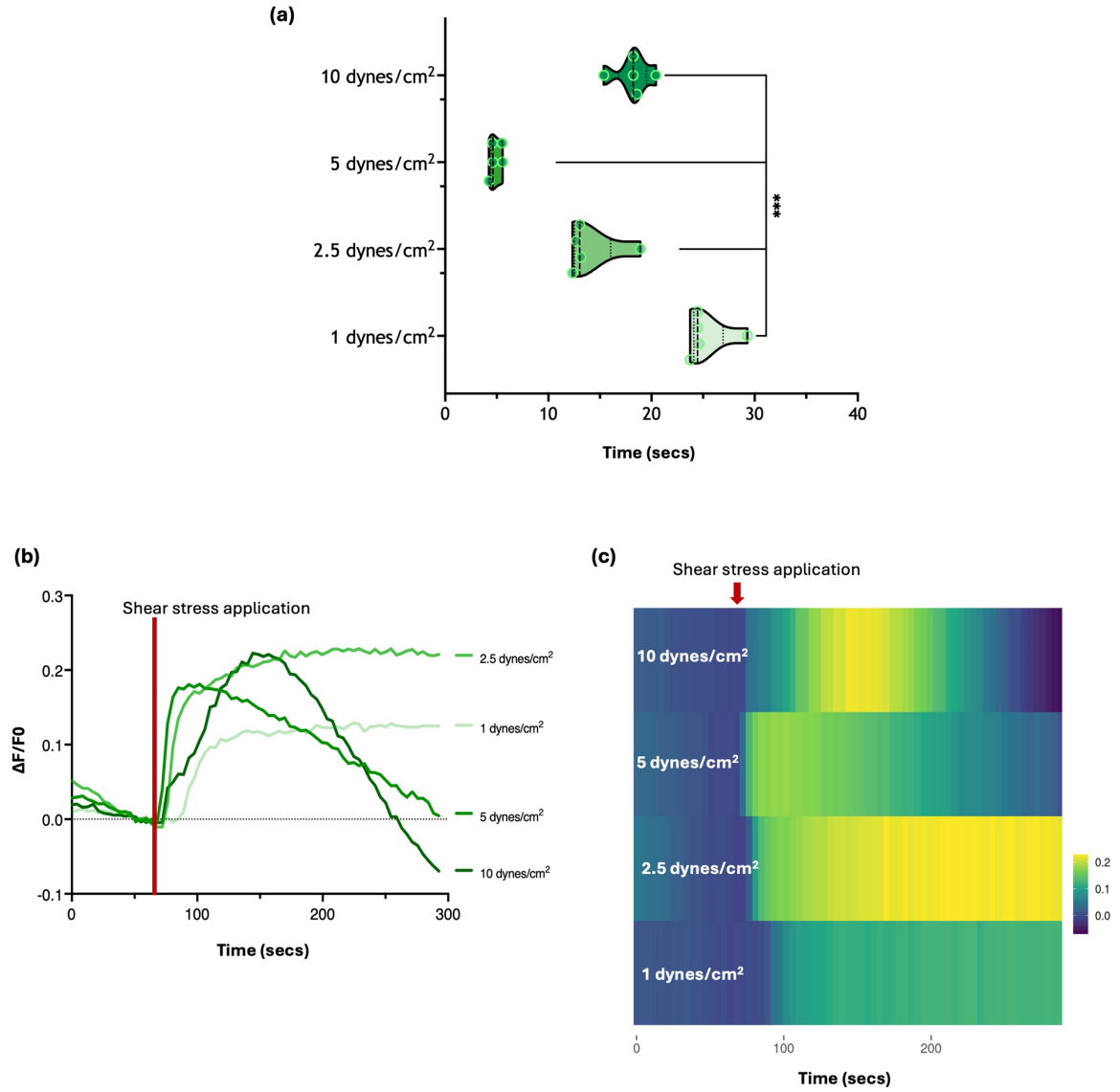


Figure 4.3. GenEPi (Piezo1) response-time and -pattern differed across shear stress magnitudes. **(a)** Representative single-cell violin plot depicting differences in Piezo1 response-time across increasing shear stress levels. *** , p<0.001. **(b)** GenEPi fluorescence intensity changes ($\Delta F/F_0$) curves

across different shear stress magnitudes. The red line indicates the point of shear stress application during the live-imaging experiment. **(c)** Representative heat-map of GenEPi $\Delta F/F_0$ plotted over time (secs). The red arrow indicates the point of shear stress application during the live-imaging experiment. Heat-map representative of GenEPi $\Delta F/F_0$ over time is generated using the PlotTwist web app[209]. For this set of experiments, N = 5 experimental repeats (with the following number of GenEPi cluster tracks analysed at different shear magnitudes: 1 dyne/cm^2 (47 tracks), 2.5 dynes/cm^2 (40 tracks), 5 dynes/cm^2 (50 tracks), and 10 dynes/cm^2 (49 tracks)).

4.4.4. GenEPi responses are graded over increasing shear stress of 1 – 5 dynes/cm^2 stimulation

Other than Piezo1 response speed to stimuli, we tested Piezo1 force sensitivity to differing magnitudes of fluidic shear stress. To do so, I elicited different magnitudes of shear stress on the XLGenEPi-HEK clones within the microchannel (**Figure 4.2 a**), and studied the changes in GenEPi-signal fluorescence intensity. To which, I calculated the GenEPi-signal responses or GenEPi-fluorescence intensity changes (annotated $\Delta F/F_0$; see **Section 4.3.6**) after cells were subjected to various levels of shear stresses, ranging from 1 to 10 dynes/cm^2. A graded increase in $\Delta F/F_0$ response of GenEPi-signal can be observed between mechanical stimuli of 1 – 5 dynes/cm^2 shear (**Figure 4.4 a**). However, that graded response stopped after 5 dynes/cm^2, as 10 dynes/cm^2 shear stimulation did not result in any significant difference in $\Delta F/F_0$ response of GenEPi-signal within cells. When the GenEPi-signal responses data was fitted with a simple linear regression model, GenEPi-responses showed correlation with the increment of shear stress stimulation (**Figure 4.4 b**). Altogether, these results confirm the force sensitivity of Piezo1 within our GenEPi-sensor. Furthermore, I affirm that the optical response of GenEPi is sensitive enough to display differences in signal amplitude across varying fluid shear stress. This observation highlights the diverse range of Piezo1 activity in response to a single mechanical stimulus. Therefore, future studies need to investigate the range of Piezo1 activities in a more complex, physiological microenvironment.

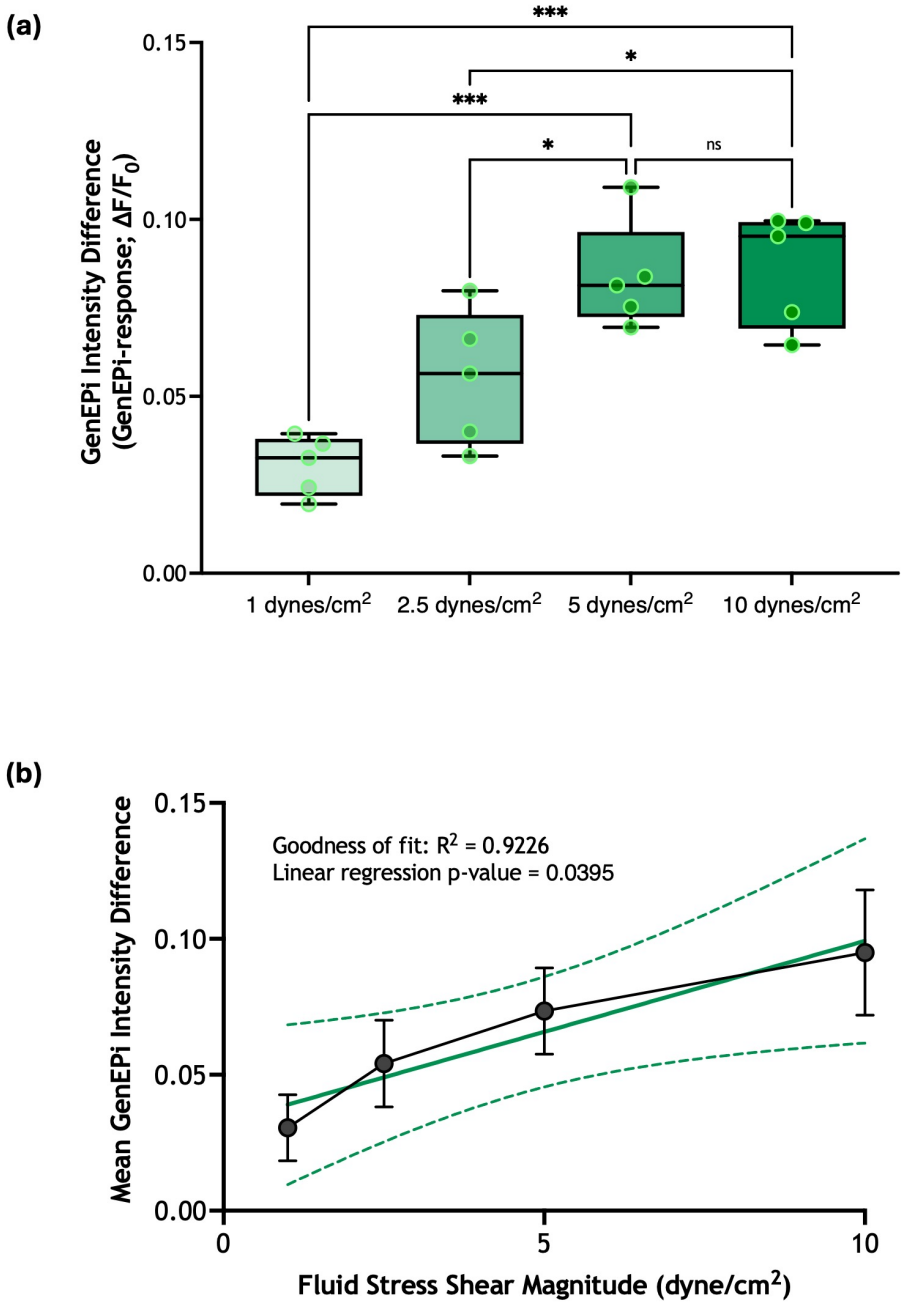


Figure 4.4. GenEPi (Piezo1) responses are graded over increasing shear stress levels. (a) Response of GenEPi-expressing XLGenEPi-HEK clones to a range of shear stress magnitudes. **(b)** GenEPi-signal response to mechanical stimulation strongly correlates with the magnitude of fluid shear stress. Simple linear regression model (solid green line) fitted on the means of each condition. 95% confidence interval (CI) shown as dashed lines, error bars: SEM. R^2=0.9226, with linear regression p-value = 0.0395. Response of GenEPi was calculated as GenEPi fluorescence intensity changes ($\Delta F/F_0$). For this set of experiments, N = 5 experimental repeats (with the following number of GenEPi cluster tracks analysed at different shear magnitudes: 1 dyne/cm^2 (47 tracks), 2.5 dynes/cm^2 (40 tracks), 5 dynes/cm^2 (50 tracks), and 10 dynes/cm^2 (49 tracks)). n.s, non-significance, p>0.05, *, p<0.05, and *** , p<0.001.

4.4.5. Shear stress-stimulated XLGenEPi-HEK cells display a response threshold at 5 dynes/cm²

To investigate if there is a threshold limit for activating membrane Piezo1 in HEK 293T cells, I devised repeated stimulation cycles of increment shear magnitudes, ranging from 0.1 dyne/cm^2 to 50 dynes/cm^2. Each cycle of shear stress onset lasted for 4 minutes at the respective shear stress magnitude (**Figure 4.5 a**). Like in **Section 4.4.4**, the GenEPi responses were observed by calculating the GenEPi-fluorescence intensity changes ($\Delta F/F_0$) across time (see **Section 4.3.6**). In my experiment, I reported Piezo1 activation occurring during the 1 dyne/cm^2 cycle, and peaked at the 5 dynes/cm^2 cycle (**Figure 4.5 b**). The behaviour of the GenEPi responses during sequential cycles of 1 and 5 dynes/cm^2 stimulation corresponded to the fluorescence intensity behaviour previously reported in **Section 4.4.3**, where I saw a sustained activation for 1 dyne/cm^2 and a one-peak activation for 5 dynes/cm^2 during shear stress onset (**Figure 4.5 b**). However, further cycles of shear stimuli at higher magnitudes (10 and 50 dynes/cm^2 respectively) resulted in a sharp decrease in GenEPi $\Delta F/F_0$ response. This sharp decrease in GenEPi-signal $\Delta F/F_0$, which I termed the GenEPi response depression, continued to fall below baseline fluorescence as fluid shear stress stimulation continued (**Figure 4.5 b**). I observed the same phenomenon when I replaced the 5 dynes/cm^2 shear cycle with 10 dynes/cm^2 (**Figure 4.5 c)**. As before, the 10 dynes/cm^2 shear stimulation, after the 1 dyne/cm^2 cycle, brought about a one-peak activation which is not as quick as the activation from 5 dynes/cm^2 (**Figure 4.5 c**). These results outline a mechanical threshold to Piezo1 peak activation within the HEK cells.

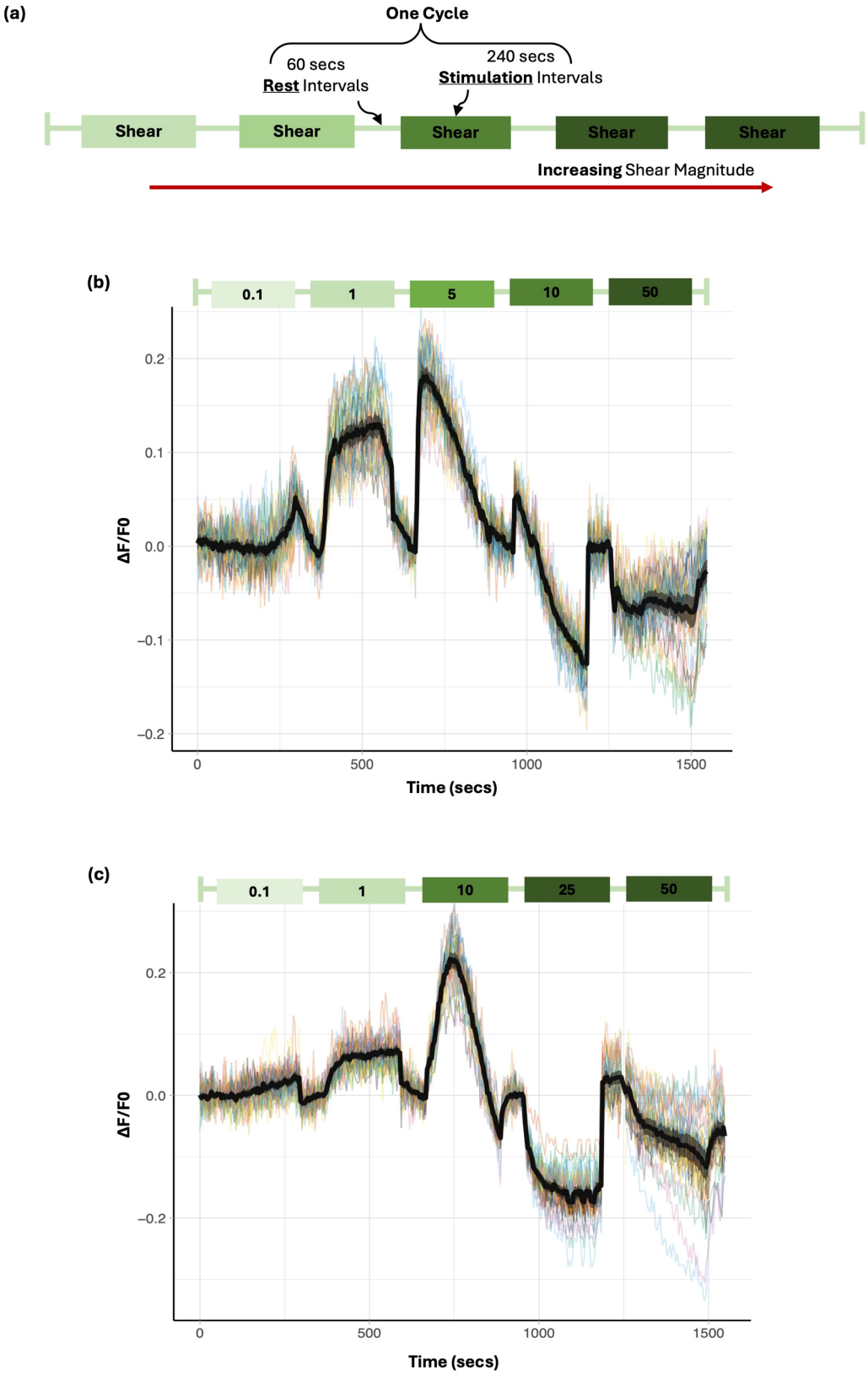


Figure 4.5. GenEPi (Piezo1) response peak is accompanied by signal depression after the shear stress threshold. (a) Representative timeline depicting the individual shear stress stimulation cycle during the time-lapse, live imaging experiment. **(b and c)** GenEPi response curves over increasing shear stress application with thresholding magnitudes at 5 and 10 dynes/cm^2 respectively. The GenEPi response curve is derived from GenEPi fluorescence intensity changes ($\Delta F/F_0$) across time. Single-cell $\Delta F/F_0$ plots are presented in colour, while overall mean $\Delta F/F_0$ across time is presented in black. Gray

shaded area represents the standard error (s.e.m) plots. GenEPi response curves were plotted using the PlotTwist web app[209]. For this set of experiments, N = 5 experimental repeats (with the following number of GenEPi cluster tracks analysed at different shear magnitudes: 45 tracks for 5 dynes/cm^2 and 39 tracks for 10 dynes/cm^2).

4.4.6. HEK-Piezo1 mechanical threshold triggers nuclei shrinkage within cells

To confirm if HEK-Piezo1's activation at 5 and 10 dynes/cm^2 shear stimuli caused any downstream cellular effect, I studied the extent of nucleus shrinkage after the respective shear onset. It was shown previously that nuclei shrinkage is a mechanoprotective response, which requires the involvement of Piezo1 activity, when cells are challenged mechanically[210,211]. Nava *et al*. (2020) further identified that the Piezo1-associated nuclei shrinkage occurs faster than the supracellular alignment response (including cytoskeleton reorganisation and cell orientation)[211]. Therefore, I investigated the extent of nucleus mechanoresponse during the onset of HEK-Piezo1 mechanical threshold stimulation. The general experiment is to label the nuclei and then measure their shape/axes. The nuclei's major and minor axis, as well as the aspect ratio, were measured before and after the respective cycle of shear onset (**Figure 4.6 a**). In both cases (5 and 10 dynes/cm^2 shear stimuli), I saw a significant decrease in the nuclei's major and minor axis, with the shrinkage more pronounced in cells sheared at 10 dynes/cm^2 (**Figure 4.6 b and c**). Although the nuclear major and minor axes showed a significant reduction in size at both 5 and 10 dynes/cm^2 shear stimulation, the nuclei's aspect ratio only decreased significantly in cells sheared at 10 dynes/cm^2 cycle, but not in cells sheared at 5 dynes/cm^2 cycle (**Figure 4.6 d**). The nuclear shrinkage in HEK cells observed after shear stimuli demonstrated that the onset of 5 and 10 dynes/cm^2 shear stimuli were sufficient to trigger prominent Piezo1-associated downstream effects. These results further corroborate that a magnitude threshold to Piezo1 activation is present, and that the observed GenEPi-signal depression following the 5 and 10 dynes/cm^2 shear onset could constitute a regulatory response of the molecular machinery of the cell when the mechanical threshold of Piezo1 activation is reached.

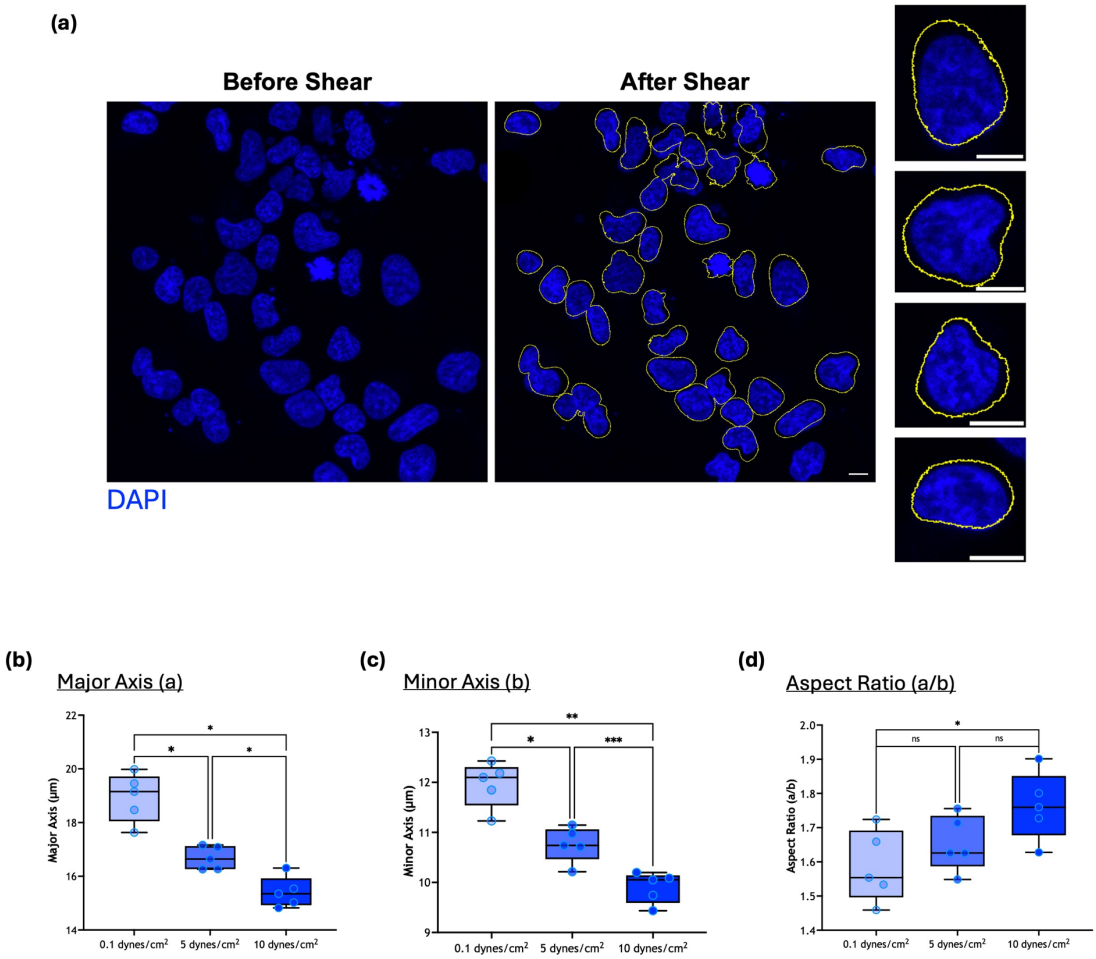


Figure 4.6. Nuclei shrinkage was observed after 5 and 10 dynes/cm² stimulatory cycle in XLGenEPi-HEK cells. (a) Representative confocal images of XLGenEPi-HEK cell nuclei before and after shear. Yellow perimeter drawings over the nuclei in the "After Shear " image depict the respective nuclei "Before Shear". Four zoomed-in nuclei within the field of view are presented on the right. XLGenEPi-HEK clones were stained with DAPI before time-lapse, live imaging experiment. Scale bar = 15 µm. **(b – d)** Representative graphs of the differences in nuclei measurements across different shear stress magnitudes. Nuclei measurements analysed and presented include: major axis (b), minor axis (c), and aspect ratio (d). For this set of experiments, N = 5 experimental repeats (with the following number of cell nuceli analysed at different shear magnitudes: 0.1 dyne/cm² (33 nuclei), 5 dynes/cm² (45 nuclei), and 10 dynes/cm² (39 nuclei)). n.s, non-significance, p>0.05, * , p<0.05, ** , p<0.01, and *** , p<0.001.

4.4.7. Repeated mechanical stimulation at lower shear stress eventually triggers the HEK-Piezo1 mechanical threshold effect in the GenEPi response

I investigated if repeating cycles of mechanical stimulation at lower shear magnitudes would eventually trigger the same depression effect observed in higher shear magnitudes with GenEPi-signal. I repeatedly stimulated the XLGenEPi-HEK cells within the microchannel at either 1 or 2.5 dynes/cm² and captured the fluorescent response using time-lapse, live-imaging. I observed that the changes in GenEPi-fluorescence intensity changes ($\Delta F/F_0$) decreased consistently across cycles and eventually fell below

baseline (**Figure 4.7 a and b**). On average, it took 5 cycles of 2.5 dynes/cm^2 and 12 cycles of 1 dyne/cm^2 repeated stimulations for the GenEPi-signal ($\Delta F/F_0$) to fall below baseline activity (**Figure 4.7 b**). The observed decrease in fluorescence intensity changes upon repetitive stimulation indicates that there is a force threshold present that is eventually reached after repetitive mechanical stimulation, which once reached, renders the cells insensitive to further force application.

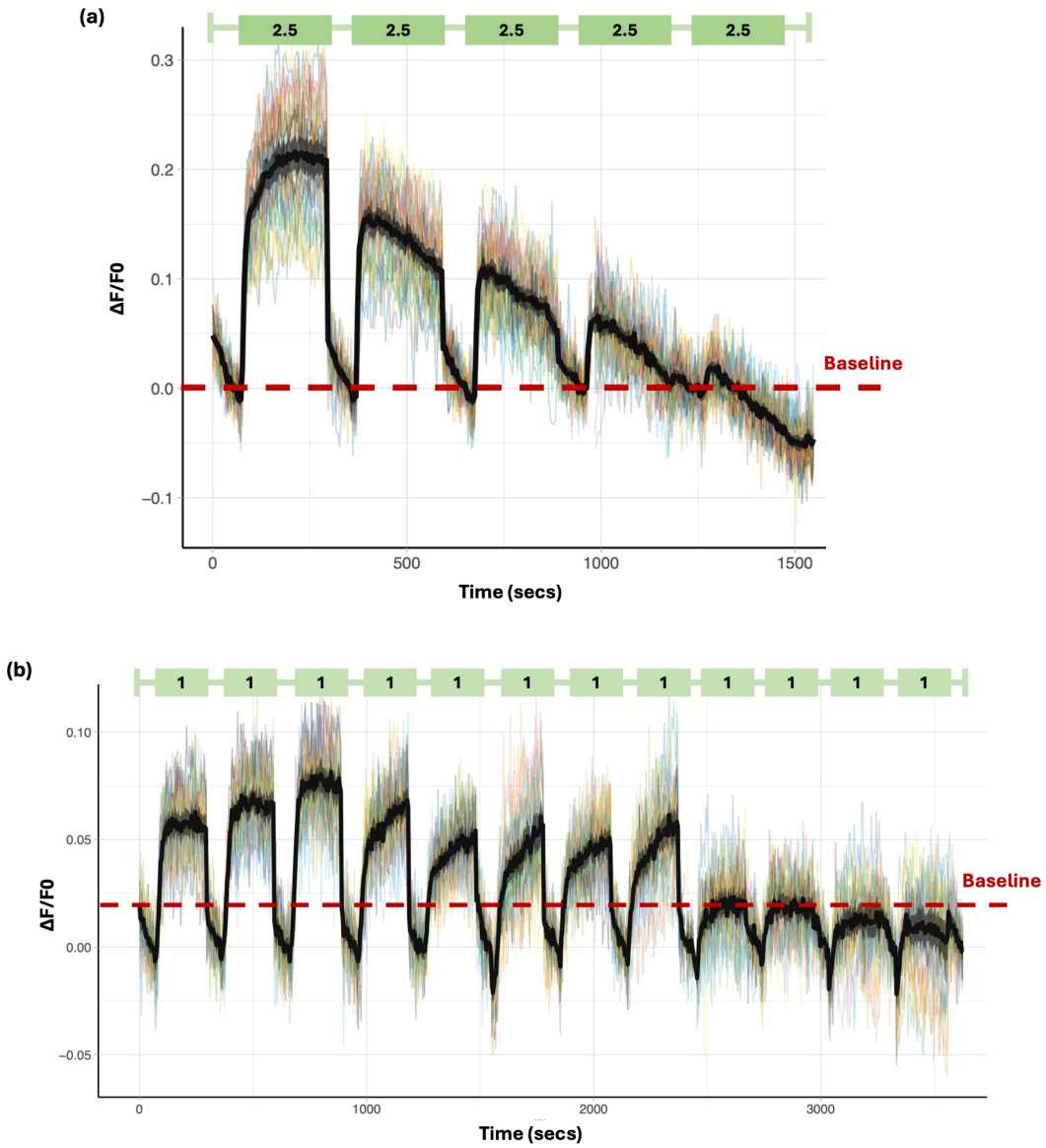


Figure 4.7. GenEPi (Piezo1) response depresses over time during sustained shear stimulation at lower magnitudes. GenEPi response curves over repeated 1 dyne/cm^2 **(a)** and 2.5 dynes/cm^2 **(b)** shear stress application. The GenEPi response curve is derived from GenEPi fluorescence intensity changes ($\Delta F/F_0$) across time. Single-cell $\Delta F/F_0$ plots are presented in colour, while overall mean $\Delta F/F_0$ across time is presented in black. Gray shaded area represents the standard error (s.e.m) plots. The red line across the plot(s) depicts the original GenEPi $\Delta F/F_0$ at baseline. GenEPi response curves were plotted using the PlotTwist web app[209]. For this set of experiments, N = 5 experimental repeats (with the

following number of GenEPi cluster tracks analysed at different shear magnitudes: 28 tracks for 2.5 dynes/cm^2 and 41 tracks for 1 dyne/cm^2).

Interestingly, when I analysed the $\Delta F/F_0$ peak averages for each response at lower shear stress levels, I noticed that Piezo1 activities peaked at different rates, complementing the results of differential GenEPi-response time (**Section 4.4.3**). The GenEPi-response peaked after the first cycle of 2.5 dynes/cm^2 and progressively declined with further repetitions, while the GenEPi-response peaked at the third cycle of 1 dyne/cm^2 (**Figure 4.8 a and b**). Furthermore, the GenEPi-signal always displayed a decaying fluorescence intensity trend after peak response. At 2.5 dynes/cm^2 repeated stimulation, the GenEPi-signal displayed a consistent declining trend after peak response, unlike the signal depression observed after 5—10 dynes/cm^2 threshold shear stimulation (**Figure 4.6**). Repeated cycles revealed a similar downward slope of -0.00023 to -0.00029 within each cycle (**Figure 4.7 a**). This moderate decay slope in GenEPi-signal points to a steady decline of Piezo1 activity when cells are subjected to lower shear magnitude (**Figure 4.8 a**).

Although there is no obvious depression in GenEPi-signal for the duration of repeated 1 dyne/cm^2, analysis of peak $\Delta F/F_0$ averages across cycles showed that GenEPi-responses consistently dropped (**Figure 4.8 b**). Interestingly, repeated 1 dyne/cm^2 shear stress presented a combination of both steep and gradual decline trends in GenEPi-responses across shear cycles.

- The steep decline trend occurred across cycles 3 to 4 and cycles 8 to 9 (**Figure 4.8 b, insert i**) which is similar to the GenEPi-signal depression slope after 5—10 dynes/cm^2 threshold shear stress.
- Whereas the gradual decay observed across cycles 5 to 7 and cycles 10 to 12 (**Figure 4.8 b, insert ii**) is comparable to the response declining trend in repeated 2.5 dynes/cm^2 shear stimulation.

The differences in the two declining slope trends are significant, with gradients of -0.00117 and -0.0115 for gradual and steep slopes, respectively (**Figure 4.8 c**). This difference in slope trends suggests the presence of different regulatory mechanisms for Piezo1 activities within cells. Most importantly, my findings confirm that the Piezo1

activity threshold can also be triggered by the shear amplitude, as well as the frequency of shear stimulation occurrence.

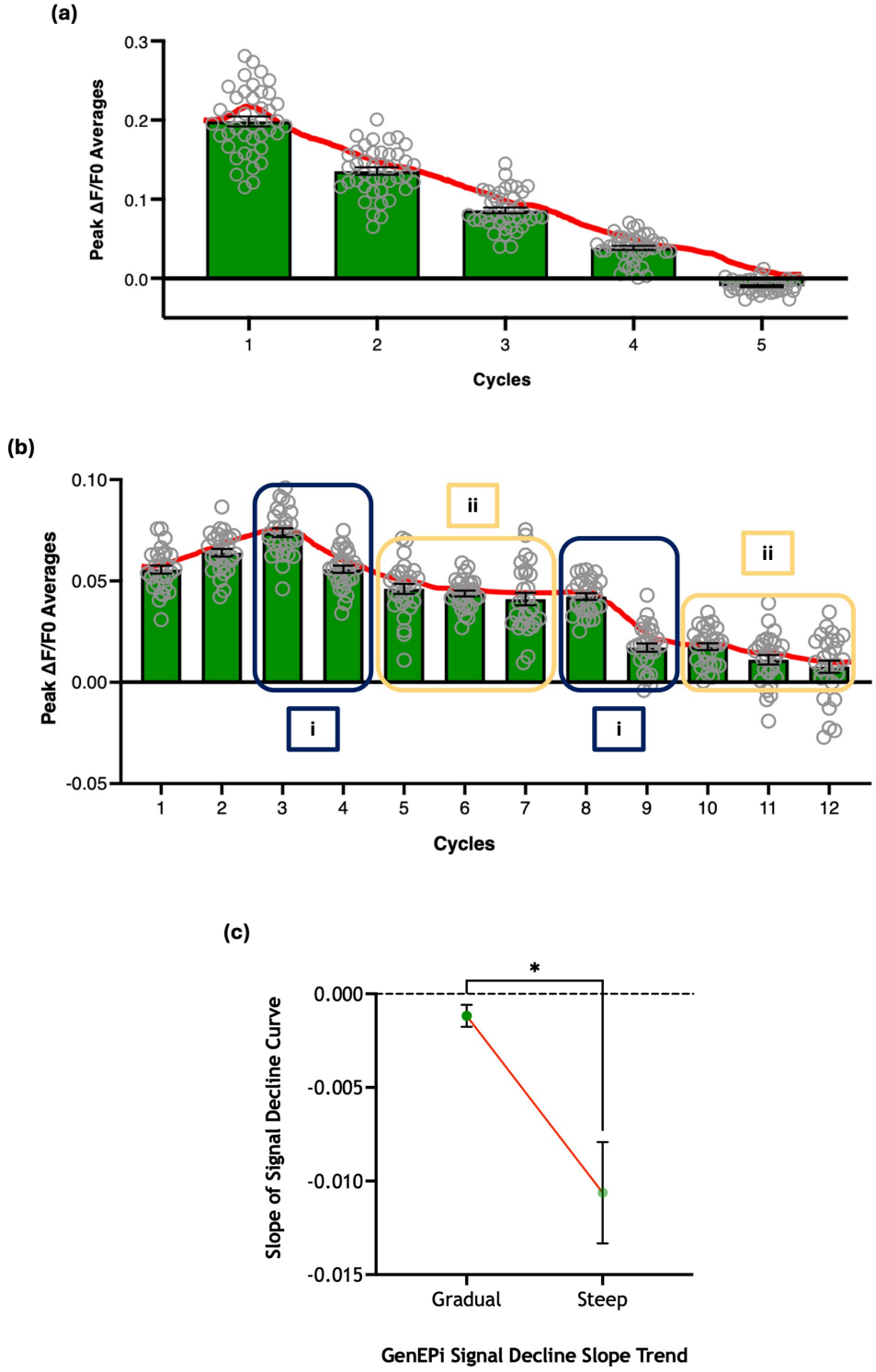


Figure 4.8. GenEPi (Piezo1) declining response exhibits two different slope depressive trends. Peak $\Delta F/F_0$ averages of XLGenEPi-HEK cells under repeated 2.5 dynes/cm^2 **(a)** and 1 dyne/cm^2 **(b)** shear stress application. Red line across the bar plot(s) depicts the slope for the peak $\Delta F/F_0$ average changes across the cycles. **(b, insert i)** Representation of steep GenEPi response declines within shear stress stimulation cycles. **(b, insert ii)** Representation of gentle GenEPi response declines over

multiple shear stress stimulation cycles. **(c)** Slope gradient analysis between the two declining GenEPi-responses trends. For this set of experiments, N = 5 experimental repeats (with the following number of GenEPi cluster tracks analysed at different shear magnitudes: 28 tracks for 2.5 dynes/cm^2 and 41 tracks for 1 dyne/cm^2). * , $p<0.05$.

4.4.8. Temporary downregulation of Piezo1 expression following sustained shear stress exposure in HUVECs

My observations reported above can be explained by two possible scenarios: (A) the closing of Piezo1 channels at the membrane or (B) the removal of Piezo1 channels to accomplish the reduced and(or) abolished GenEPi-reported activity. To test the second hypothesis, I exposed HUVECs, since I have previously cultured them in my microchannels (see **Section 3.6.1**), to 10 dynes/cm^2 shear stress for up to 48 hours. As endothelial cells highly express Piezo1 endogenously, IF staining was performed to study the changes in cellular Piezo1 expression under shear stress (**Figure 4.9 a**). Against static cultures, HUVECs-Piezo1 expression decreased significantly after 24 hours of shear stress exposure (**Figure 4.9 a and b**). The HUVECs-Piezo1 expression after 48 hours of 10 dynes/cm^2 perturbation was significantly higher than expression after 24 hours shear, but still lower than expression of those in static culture (**Figure 4.9 b**). This data demonstrates that there is a temporary downregulation of Piezo1 expression in the endothelial cells after 24 hours of shear stress exposure, which started to recover after 48 hours.

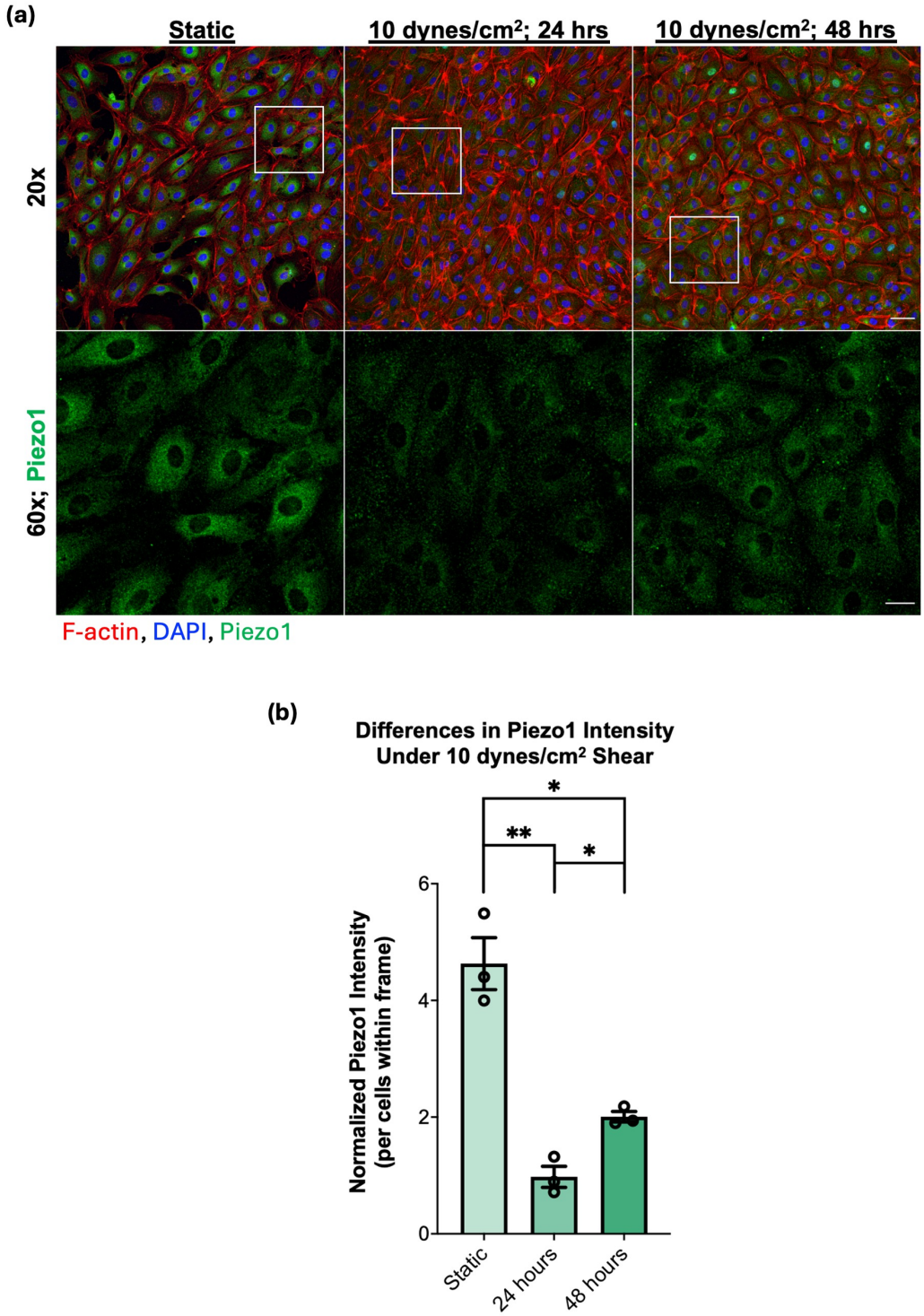


Figure 4.9. Endothelial-Piezo1 expression temporarily downregulated after 24 hours of constant 10 dynes/cm² shear stress. (a) Representative confocal images of endothelial cells (HUVECs) stained with Piezo1 (green), F-actin (red), and DAPI (blue). Rectangular box regions are areas for the respective 60x magnified confocal images. Scale bar for 20x confocal images = 25 µm, scale bar for 60x confocal images = 15 µm. **(b)** Representative bar graphs of normalised Piezo1 staining intensity under different durations of 10 dynes/cm² shear stress exposure. For this sets of experiments, N = three independent set of experiment. Within each experiment, n = 46 cells average for static condition, n = 56 cells average for 24 hours shear condition, and n = 47 cells average for 48 hours shear condition. * , $p<0.05$, and **, $p<0.01$.

4.4.9. GenEPi response is synchronised to mechanical shear triggers that becomes increasingly asynchronous under sustained shear stress

Synchronised multicellular dynamics is the basis of many molecular phenomena. One of the recently proven phenomena is the synchronising of Ca^{2+} signalling in endothelial cells exposed to systemic fluid shear stress[212]. Therefore, I investigated if the shear stress-induced GenEPi dynamics I observed in my experiment is temporally controlled by external mechanical stimuli. To do this, I compared the single-cell GenEPi-responses across individual cycles of repetitive 1 or 2.5 dynes/cm^2 shear stimulations. I reasoned that I could dissect the development of GenEPi dynamics synchronisation in the multicellular system by expressing GenEPi response changes ($\Delta F/F_0$) as a function of time (t). To display this function quantitatively, I modelled the function of the calcium dynamics derivative presented by Zamir, *et al.* (2022). Here, my measurement of GenEPi dynamics (annotated $\hat{R}_i(t)$; see **Section 4.3.6**) is the temporal derivative of the cells' GenEPi response to shear stimuli. During shear stimulation (both 1 or 2.5 dynes/cm^2), I recorded the peak increase in GenEPi dynamics shortly after the instance of stimulation, but declined over time (**Figure 4.10 a and b**). The same trend in GenEPi dynamics could be observed in repeated exposure to 1 or 2.5 dynes/cm^2 shear stimuli. However, under sustained shear stimulation, the variability in GenEPi dynamics increased and appeared to become more asynchronised (**Figure 4.10 c and d**). I also observed the increase in the standard deviation of the GenEPi dynamic across time (**Figure 4.10 e**). My results inform the asynchronism of Piezo1 activities following sustained mechanical stimulation.

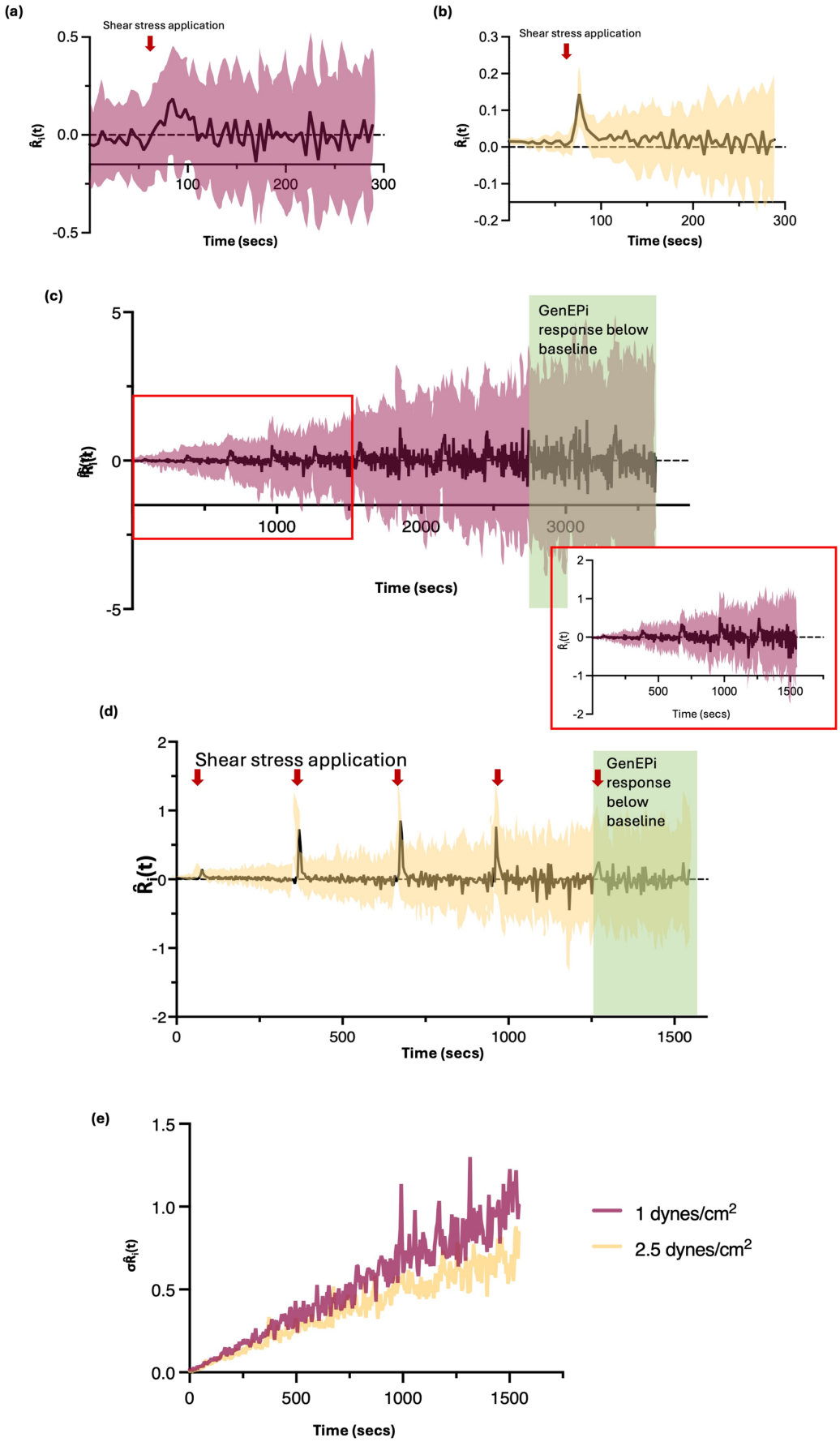


Figure 4.10. GenEPi dynamics are synchronised at the onset of mechanical stimulation, but becomes increasingly asynchronised under sustained stimulation. (a and b) GenEPi dynamics

($\hat{R}_i(t)$) curve over time in response to mechanical shear stress (a: 1 dyne/cm^2, b: 2.5 dynes/cm^2). GenEPi dynamics of each cell represent the time-derivative of GenEPi relative fluorescent intensity changes (see **Section 4.6.6**) over time. Red arrows indicate the onset of shear stress induction. Black line represents the mean GenEPi dynamics. Shaded area(s) displays the standard deviation of GenEPi dynamics over time. **(c)** GenEPi dynamics ($\hat{R}_i(t)$) curve over time in response to a repeated course of 1 dyne/cm^2 shear stress exposure. Black line represents the mean GenEPi dynamics. Red shaded area displays the standard deviation of GenEPi dynamics over time. Insert (in red box) zooms into the GenEPi dynamics within the first five cycles of 1 dyne/cm^2 shear stress exposure. **(d)** GenEPi dynamics ($\hat{R}_i(t)$) curve over time in response to a repeated course of 2.5 dynes/cm^2 shear stress exposure. Black line represents the mean GenEPi dynamics. Yellow shaded area displays the standard deviation of GenEPi dynamics over time. **(e)** Standard deviation of GenEPi dynamics ($\sigma\hat{R}_i(t)$) across time. Red: 1 dyne/cm^2 shear stimulation, yellow: 2.5 dynes/cm^2 shear stimulation. For this set of experiments, N = 5 experimental repeats (with the following number of GenEPi cluster tracks analysed at different shear magnitudes: 28 tracks for 2.5 dynes/cm^2 and 41 tracks for 1 dyne/cm^2).

4.5. Discussion

4.5.1. The use of GenEPi sensor reveals unique Piezo1 functional dynamics in HEK cells upon exposure to different shear stress magnitudes

In summary, my *in vitro* system established that GenEPi provides high spatiotemporal resolution and functional specificity to Piezo1-specific activity within cells. Using my developed system, I observed novel functional dynamics of HEK-Piezo1 within cells under different shear stress magnitudes. Here, I used the GenEPi-sensor to reliably capture Piezo1-specific activity to sustained, global mechanical stimuli across a monolayer of HEK-cells. By observing the speed, pattern, and magnitude of the Piezo1 activity response, I reveal that the channel response is dependent on both (i) magnitude and (ii) duration of mechanical forces. With increasing fluid shear stress, GenEPi response appeared quicker, and with graded increase. This observation is complementary to Piezo1's responses to increasing concentration of Yoda1 reported in Yaganoglu & Kalyviotis *et al.* (2023)[1]. Although the study confirmed a Piezo1 dose-

dependent response, intermittent Yoda1 concentration (between 5 to 25 μM) showed no significant increase in cellular Piezo1 activation[1]. Similarly, I observed a graded GenEPi-response as I increased the shear stress level from 0.1 to 5 dynes/cm^2. The graded GenEPi-response correlated to a progressive activation phenomenon of the Piezo1 population within cells. However, I reveal a Piezo1 activation ceiling when no further increase in GenEPi-signal response was observed when XLGenEPi-HEK cells were exposed to shear stress levels higher than 5 dynes/cm^2 (**Figure 4.3**). The discovery of an activation ceiling suggests that the cells present a response threshold to mechanical force, which can differ in cell-types.

By eliciting constant, global mechanical shear stress through my microchannels, I am also able to demonstrate GenEPi (Piezo1) clusters exhibiting dynamic behaviour on the cell membrane. Notably, the GenEPi-sensor robustly reports diffusive dynamics within the cell membrane, comparable to those reported in WT-Piezo1[1,59,97,116]. I showed that by increasing the mechanical force strength, GenEPi (Piezo1) clusters exhibit a less confined and more directed diffusive motion (**Figure 4.2**). This observation indicates that the motions of Piezo1 clusters are directed upon mechanical force stimulation. Future studies with a more refined methodology of analysis can investigate the relationship between Piezo1 cluster-directed motions and the mechanical force application. Interestingly, my Piezo1 clusters track analysis also revealed a huge population with anomalous diffusive motion. Previous work suggests a correlation between cellular/molecular crowding and spatial heterogeneity with anomalous diffusion[213,214]. The cell membrane layer is a complex and diverse system, with a dynamic organisation of lipids, proteins, and other macromolecules. In addition, the variety of lipid

components and receptor/cytoskeleton binding further contribute to the spatial heterogeneity of the cell membrane[214]. Therefore, it is unsurprising that Piezo1 channels (or other macromolecules) on the cell membrane layer exhibit anomalous diffusive motion.

4.5.2. Signal depression of GenEPi during persistent shear stress stimulation

When I applied repetitive shear stress stimulations with increasing magnitudes on the XLGenEPi-HEK cells, I saw a single GenEPi-response peak being triggered at 5 or 10 dynes/cm^2. The peak response was immediately followed by a sharp depression in GenEPi-signals in further stimulations. This observation further confirmed my hypothesis of a magnitude threshold for Piezo1 activation. Despite showing a consistent GenEPi-response pattern, repeated 1 or 2.5 dynes/cm^2 shear stress stimulations induced a gradual decline in GenEPi-signal response. At 1 dyne/cm^2, GenEPi-responses were generally sustained throughout the stimulation cycle (**Figure 4.7 b**). However, the average Piezo1-responses decreased across 1 dyne/cm^2 stimulation cycles, after peak response was achieved at the third cycle (**Figure 4.8 b**). On the other hand, I observed a gradual decrease in the GenEPi-signal responses during repeated 2.5 dynes/cm^2 stimulations (**Figures 4.7 a and 4.8 a**). This decrease in GenEPi-signal responses is unlike the steep depression in the signal recorded after peak 5 or 10 dynes/cm^2 shear stress application. Comparison between the two types of GenEPi-response decline revealed significant differences in their respective response curve slopes (**Figure 4.8 c**). Interestingly, both decline response trends were observable in continuous 1 dyne/cm^2 shear stress stimulation, up to 12 cycles (**Figure 4.8 b, inserts (i) and (ii)**). For the first time, I reported that Piezo1 response dynamics are gated by both the mechanical force

magnitude and duration of mechanical stimulation. The appearance of two different GenEPi-response declines suggests the possibility of inherent modulation mechanisms and regulatory "checkpoints" during Piezo1 activation. Further studies will need to explore the precise mechanisms in modulating cellular Piezo1 activities.

Alternative explanations debated for the signal depression of GenEPi-signal responses under persistent shear stress stimulation includes signal artifacts due to (i) focus drift during long-term, live-imaging, and (ii) GCaMP signal saturation. However, the association of our GenEPi-signal depression with a focus drift during imaging had been ruled out. In our experiments, we did not observe out-of-focus frames from our brightfield images of the imaged XLGenEPi-cells throughout the imaging period, especially during the onset of GenEPi-signal depression (data not included in this thesis). Z-plane focus drift is a common problem during long-term, live imaging experiments, one which we also observed during our early optimisation of the system. Visible in the brightfield images, this focus drift also results in the decrease in fluorescence intensity, which potential affects our analysis of GenEPi-fluorescence responses under sustained shear stress. However, to account and correct for the focus drift in our experiment, an auto-focus point has been set and the auto-focus function has been included in every third cycle during the imaging intervals (**Section 3.5, Figure 3.7**). Another plausible explanation for the observed signal depression trend is a saturation of the GCaMP indicator in our GenEP-sensor. As more Piezo1 channels get activated under persistent shear stress stimulation, there will be a saturation point when the concentration of Ca^{2+} influx is more than the detection limit of the GCaMP indicator. Although no Ca^{2+} concentration titration experiment has been performed using my system, Yaganoglu and

Kalyviotis *et al*. (2023) reported the GenEPi's GCaMP binding affinity to Ca^{2+} is 1.5 μM, with signal plateauing occurring in the mM range of Ca^{2+} concentration in their early experiments of the original GenEPi construct[1]. Given the Ca^{2+} detection resolution of our GenEPI's GCaMP, it is unlikely that the signal depression observed in our experiments is a result to the GCaMP saturation during increasing shear stress stimulation.

4.5.3. Piezo1 downregulation from cell membrane as cellular mechanoprotective response

Following the observation of GenEPi signal depression during sustained fluid shear stress stimulation, a potential regulatory mechanism of membrane Piezo1 we hypothesised is the downregulation of Piezo1 expression. Indeed, I observed in cells expressing high levels of Piezo1, like HUVECs, that Piezo1 expression was downregulated temporarily after 24 hours of constant, 10 dynes/cm^2 shear stress (**Figure 4.9**). Evidently, this downregulation period coincided with the reorganisation of HUVECs orientation within the microchannel. However, Piezo1 expression appeared to be gradually increasing following 48 hours of 10 dynes/cm^2 shear stress (**Figure 4.9**). The temporary downregulation of endothelial-Piezo1 after the first 24 hours of constant shear stress suggests that it is potentially a contending mechanoprotective reaction for cells exposed to sustained mechanical stress. Only when cells have recovered from the mechanical stress, will the expression of Piezo1 be returned to baseline. The downregulation of Piezo1 expression in HUVECs under long-term shear stress exposure also supports the decrease in GenEPi-signal observed in our HEK clones after exposure to 5 dynes/cm^2 threshold shear. The reduction in endothelial Piezo1 expression and abolition in HEK-GenEPi activity both indicate the possibility of Piezo1 channels removal

from the cell membrane after shear stress induction. My findings, here, propose that there are regulatory mechanisms in place to control Piezo1 activities in response to mechanical shear stress. After the cell's threshold stress level has been hit, it is plausible that the downregulation of Piezo1 channels from the cell membrane acts as a regulatory mechanism to prevent further external mechanical stimulation.

In summary, my results enhanced previously reported Piezo1 activities with insights into the ion channel's physiological dynamics. Moving away from *in vitro*, static cultures, and transient, local mechanical stimuli application, my system explored Piezo1 dynamics under a near-physiological context using a global, systemic mechanical force model. Using my *in vitro* microfluidic-based system, I demonstrate a robust and reliable system to generate physiologically relevant readouts and novel mechanosensitive dynamics on the cell membrane.

4.6. Statement of Contribution

The analysis carried out in this chapter were performed under the advisement of Dr. Jennifer Frattolin of Dr. Jimmy Moore's lab and Mr. Konstantinos Kalyviotis (a fellow PhD student, at the time this thesis is written) of the Pantazis lab.

5. Discussion

"Science is nothing but perceptions."

– Plato

Mechanical forces are important stimuli for ensuring development, maintaining homeostasis, and perpetuating pathophysiology. Their omnipresence plays a crucial role in the cellular microenvironment. The importance of mechanics has been increasingly proven to be important in cellular behaviours and functions. Therefore, there is a growing need to study the effect of mechanical forces across the scale of life, from cells to tissue and organs. However, investigating mechanical forces within the cell niche has fared poorer in contrast to studies done on chemical signals. This is largely due to factors requiring the studies to be done in a live context, and for experiments to recapitulate elements of the cell microenvironment. With the advancement in bio- and tissue- engineering, limitations are being addressed to create more a reliable and relevant experimental model for studying mechanosensation and mechanotransduction processes in the cells.

Piezo1 has been a major focus of cellular mechanosensation and mechanotransduction research. A decade of Piezo1 research has brought forth various physiological phenomena that were associated with the cells' innate ability to sense and transduce mechanical signals from their microenvironment. Previously in the Pantazis lab, we

designed and generated a Piezo1-specific reporter, termed GenEPi, to capture the ion channels' activity on the cell membrane. GenEPi has been shown to be reliable in reporting cellular Piezo1-specific activations in response to localised mechanical forces with high spatiotemporal resolution. The sensor's robustness is evident in cells, in 3D microtissues and live animal models. The work presented in this dissertation has aimed at developing an *in vitro* system to reliably investigate the mesoscopic dynamics of cellular Piezo1. To enhance the sensor's usability, I (a) modified the original GenEPi-construct, (b) developed a protocol for setting up a microfluidic-based culturing and imaging system to investigate the dynamic activities of cellular Piezo1 using GenEPi and (c) identified critical functionality behaviours of the Piezo1 channel under global, systemic mechanical stimulation.

In this chapter, I will discuss the findings of my research focusing on the following aspects: (i) GenEPi as an optical tool to resolve previously reported Piezo1-associated activity and novel Piezo1-specific dynamics, (ii) potential limitations of our microfluidic-based system and (iii) ongoing efforts and future Piezo1 research directions.

5.1. GenEPi, an optical tool for dissecting physiological Piezo1 dynamics

Continuing previous work in the lab, I developed an *in vitro* system with elements to recapitulate the physiological cell niche to study cellular Piezo1 dynamics. The adaptation of the GenEPi-construct was achieved by engineering the XLone-genetic backbone into the original construct. With the new XLGenEPi-construct, I was able to isolate positive clones that stably expressed our GenEPi-sensor upon Dox-induction. Concurrently, I developed an experimental model to support the investigation of cellular Piezo1 dynamics in response to mechanical forces in the cells' microenvironment. Finally, using my microfluidic-based system, I explored the extent the GenEPi-sensor can report various dynamics, both uncharacterised and previously reported, of Piezo1-specific activities.

Since the discovery of Piezo1, various aspects of the ion channel have been examined. Focusing on its ion-conducting capabilities yielded insights into Piezo1 channel activation and inactivation kinetics. Ca^{2+} imaging studies revealed Piezo1 clusters diffusivity within the membrane bilayer and other downstream signalling pathways associated with Piezo1 activity. Complementary, Piezo1 has been implicated in various physiological processes, including gene transcription, nuclear condensation, cell differentiation, migration, apoptosis and proliferation[17,18]. A hypothesis which emerged from the various studies is that Piezo1's role within the cellular mechanical microenvironment may be more complex and dynamics. For example, I reported that membrane Piezo1 channels have differential activation patterns in response to mechanical forces differing in amplitude and frequency (**Figures 4.3 and 4.7**), contrary to a straightforward "switch-like" functioning.

While characterising GenEPi-signal dynamics in response to global, systemic fluid shear stress (**Chapter 4**), I found the following dynamics in Piezo1 activity: (i) Piezo1 response is gated by both mechanical force magnitude and frequency, (ii) Piezo1 displays a mechanical threshold to peak activation in cells, (iii) there are different regulatory mechanisms during Piezo1 activation, and (iv) Piezo1 response becomes increasingly asynchronous under systemic stimulation.

I first observed, from the GenEPi fluorescence intensity changes, that Piezo1 response increases in activation speed and strength with increasing fluid shear stress magnitude. Similarly in Yaganoglu & Kalyviotis *et al*. (2023) where they concluded that Piezo1 responds with faster kinetics and higher strength after increasing compressive force[1], I observed that GenEPi responses earlier and in a graded manner with increasing shear amplitude from 0 to 5 dynes/cm^2 (**Figures 4.3 and 4.4**). This observation suggests that the Piezo1 activation mechanism occurs in a progressive manner, where more Piezo1 channels in individual cells are activated with increasing mechanical forces. However, there was no further increase in GenEPi response between 5 to 10 dynes/cm^2 shear stress increment (**Figure 4.4**), suggesting a mechanical threshold in Piezo1 peak activation. Previously, it was found that although GenEPi responded to the Piezo1-

specific agonist Yoda1 in a dose-dependent manner between 5 to 50 μM concentration, there were no significant changes in GenEPi responses between Yoda1 concentrations of 5 to 25 μM. The observation of a plateau in the GenEPi responses after certain shear stress magnitudes or Yoda1 concentrations indicates that there is possibly a threshold activation present in Piezo1 activity. Crucially, we also reported that the relationship between GenEPi graded response to increasing magnitude of fluid shear stress is linearly correlated (with linear regression *p*-value < 0.05; **Figure 4.4 b**). This suggests that the increase in GenEPi-signal response in our experiments is due to the increase in mechanical force stimulation XLGenEPi-HEK cells were exposed to. However, one should be careful to conclude that my current system can be used as a quantitative sensor, as GenEPi-signal response to higher magnitudes of fluid shear stress remain undetermined. Therefore, further experiments are needed to explore the sensitivity of our GenEPi-sensor to quantitatively report the magnitudes of fluid shear stress stimulation.

Using my setup, I identified distinct Piezo1 response patterns to different shear stress magnitudes (**Figure 4.3 b and c**). At lower shear stress magnitudes, between 1 and 2.5 dynes/cm^2, there is sustained activation of GenEPi throughout the shear stimulation period after the GenEPi responses reach their respective peaks. Whereas at 5 and 10 dynes/cm^2, GenEPi-signal responded with a single-peak, followed by a sharp depression in GenEPi-signal. Differential GenEPi response trends reinforce that Piezo1 activation occurred in a progressive manner (**Figure 5.1**), especially at lower mechanical stimulations.

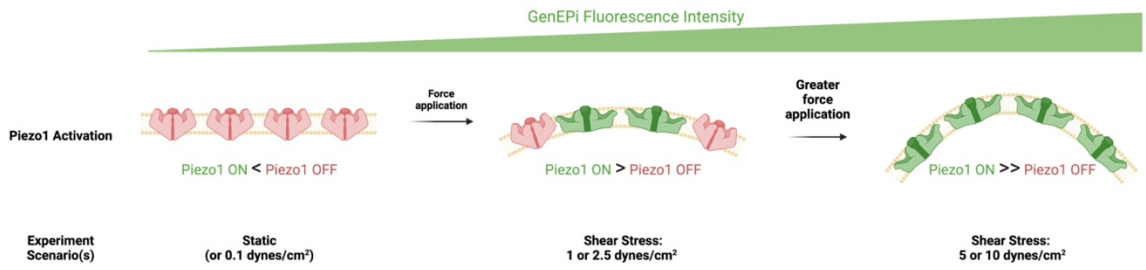


Figure 5.1. GenEPi (Piezo1) activation occurs in a graded and progressive manner. Our experimental results showing a graded activation response suggest that Piezo1 activation depends on the amplitude of the applied force. Altogether, our GenEPi system is useful for inter- and intra- cellular comparative studies in which different activation states can be correlated to GenEPi dynamics. (Illustration created with Biorender.com).

Moreover, the hypothesis of a Piezo1 activation threshold is further demonstrated when I continuously ramped up the shear stress magnitudes across the cellularised microchannel. I observed the same sustained activation of GenEPi during the 1 dyne/cm^2 cycle and a single peak at 5 dynes/cm^2 stimulations. A further increase in shear magnitudes brought about a stronger depression in the GenEPi response (**Figure 4.5 b**). My results cement the hypothesis that Piezo1 activation occurs progressively within individual cells until an activation threshold is reached. Notably, the activation threshold of 5 dynes/cm^2 shear stress was enough to trigger Piezo1-associated downstream cellular phenomena, like nuclei shrinkage (**Figure 4.6**). Therefore, I attribute the mechanical threshold to Piezo1 peak activation in cells, which triggers downstream cellular mechanoprotective responses to mechanical stress. At present, my GenEPi system cannot be used for quantitative force measurements, nevertheless, it has proven a setup for comparative studies to differentiate Piezo1 activation states using GenEPi fluorescence intensity changes (**Figure 5.1**).

I also identified two different declining slopes in GenEPi responses after Piezo1 peak activation is reached (**Figure 4.8**). A steep declining slope was reported after GenEPi peak response (**Figure 4.5 b and c**), while the gentler slope occurred between repetitive cycles of low magnitude stimulation (**Figure 4.8 a and b insert ii**). The presence of two differential GenEPi declining responses suggests two different Piezo1 activity modulation mechanisms. Sustained fluid shear stress has been associated to a long-lived inactivated state in Piezo1 channels, after peak activation[99,100,104,109]. A similar inactivation response pattern during continuous fluid shear stress exposure has been previously reported through electrophysiology readouts[104,109].

Finally, I also reported that GenEPi dynamics became increasingly asynchronised during prolonged, low-magnitude fluid shear stress (**Figure 4.10**). The GenEPi dynamics became significantly chaotic, especially after the fourth cycle of 1 dyne/cm^2 shear stress application. Complementary, that is the cycle right after the steep GenEPi response decline during sustained 1 dyne/cm^2 shear stress stimulation (**Figure 4.8 b**). In the future,

the investigation of cellular mechanisms modulating Piezo1 activities would be important to inform mechanosensation and mechanotransduction processes, especially in cells exposed to global, systemic mechanical forces in their microenvironment.

5.2. Limitations to our "XL-", microfluidic-based system

While my microfluidic-based setup overcomes many drawbacks in studying Piezo1 dynamics within cells *in vitro*, there remain limitations which warrant consideration when adopting this experimental system. Here, I will discuss three main limitations from factors like XLGenEPi construct to our microfluidic setup design.

5.2.1. Limitations to the "XL"-approach in GenEPi construct

The XLGenEPi construct enhances and improves user experience by providing an inducible expression system and construct integration into the host cell genome. Keeping the GenEPi-sensor under an inducible expression system helps limit the burden of our transgene expression in cells. Furthermore, integrating XLGenEPi construct into the host cell's genome not only eliminates non-expressing cells within the experimenting population, but also off-sets the transient transfection effect during the experiment. Although GenEPi expression is kept under an inducible control, when induced, GenEPi (functional Piezo1) is still being overexpressed for up to 3 days (**Figure 2.10**).

Protein expression is tightly regulated within cells and any dysregulation will cause an imbalance which could potentially be harmful for the cells. An overexpression system, like our "XLone-" system poses dysregulation when we induced GenEPi expression for our imaging experiment. Although no obvious detriments, like cell death, have been observed, pushing cells to produce more copies of a particular protein can pose a threat to cells through various other mechanisms. For instance, it can trigger or overwhelm certain cellular processes, interfere with regulatory functions, or result in the forming of unnecessary protein aggregates[218–221]. Ultimately, the overexpression of any protein increases the burden of cells as it depletes cellular energy and resources needed for

protein synthesis and transportation[222]. Research into protein overexpression has shown that there is a threshold at which the overexpressed copies can start becoming a burden and cause detrimental effects on the cells[192,223,224].

A strategy to address the limitations of an overexpression system is by using a CRISPR/Cas approach to knock-in the linker-GCaMP GECI module downstream of the host cell's Piezo1 gene. Work exploring the endogenous tagging of HEK-Piezo1 is already being developed in the lab. The success of this strategy will allow investigation of endogenous Piezo1 dynamics, and the interpretation of any cellular differences in Piezo1 activities. Furthermore, the CRISPR/Cas endogenous tagging strategy will be beneficial in studying of specific Piezo1 activities in sensitive cell types, for example in HUVECs.

5.2.2. Limitations to a GCaMP-based approach

The GenEPi-sensor, used in my research, was developed by incorporating a GCaMP molecule to the C-terminal of the human Piezo1 sequence. Employing this approach to create a Piezo1-specific reporter is advantageous because of its reliability to report Ca^{2+} influx from Piezo1 channel activation. It is highly sensitive to allow us to detect subtle changes in the Ca^{2+} concentration within individual Piezo1 channel's Ca^{2+} microdomain. In addition, have a genetically-encoded Ca^{2+} indicator tagged to Piezo1 channel enabled us to perform live-imaging to investigate the dynamic behaviours of Piezo1 (as described in this thesis). The specific GCaMP selected, GCaMP-G4, for the development of the GenEPi-sensor has a large dynamic range, which enable us to capture the linear response of Piezo1's response to increasing shear stress magnitudes.

However, there remains limitations to our system associated to the usage of a GCaMP indicator. Although GenEPi's GCaMP indicator provide high spatial resolution at the subcellular level, our GenEPi-sensor may not accurately localise to specific subcellular compartments or membrane microdomains where Piezo1 channels are localised. As shown in our results, our system allows the identification of Piezo1 clusters, but the resolution of a GCaMP-based indicator is not sensitive enough for me to discern between individual Piezo1 channels. This hinders the precise mapping of Piezo1 channels and our

ability to investigate Piezo1 channels' cooperative activation behaviours, which has previously been reported in other studies.

5.2.3. The HEK 293 cell model

As a proof of concept on the system developed here, HEK 293T cells were used mainly because of easy availability of the cell line and their amenability to genetic transfection[225]. However, our particular cell model poses two main disadvantages: (1) its vague cellular origin, and (2) the physiological context in Piezo1 research.

HEK 293 cell line was first derived from the kidney of an aborted human embryo. Viral transformation with genome fragments allowing for cell cycle and apoptosis interference enabled the immortalisation of cells[226]. Subsequently, multiple HEK 293 derivatives have been produced to enable different usages. For example, HEK 293T is a subset of HEK 293 lineage that was primed for cellular transformation and clone generation work or HEK 293S is optimally adapted for suspension culture[202]. Given its immortalised cell-line status, HEK 293 is reliable, easy to culture, and widely used in biological research. The HEK 293 cells are the second most-used cells, after HeLa cells, in the cell biology field, and the second most-used cells, after CHO cells, in the biopharmaceutical industry[202]. In addition, HEK 293 has been vital to the Piezo1 research, since its discovery, over the last two decades. Endogenously, HEK 293 cells exhibit a low expression of Piezo1. Dubin *et al*. (2017) and Zhao *et al*. (2017) concurrently reported that the Piezo1 genetic transcript is too low to be reliably detected by RT-qPCR [155,180]. Overexpression of Piezo1 has been a crucial methodology to investigate the function, as well as the importance, of this mechanosensitive ion channel. Furthermore, the HEK 293T derivative had been created with the sole objective of primed cellular cloning work[227]. The size of our XLGenEPi construct is approximately 14 kb, which has proven challenging in molecular cloning as cells might be less receptive to large plasmid transfection. As reported in **Chapter 2**, despite the large plasmid size, HEK293T cells remained receptive to our XLGenEPi construct, with transfection efficiency at 78%. Therefore, HEK 293T cells are, to a certain extent, a good starting cell model for our work.

Despite their wide usage, HEK 293 and its derivatives posed a problem for organ-specific cell-type research due to their unknown parenthood and tissue origin. A recent transcriptomics aimed to outline the background of the HEK 293 lineage by analysing the cell-lines' genetic expression profile gathered from their whole-genome sequencing data[202]. Although kidney and pituitary tissue characteristics were picked out from their study, it was reported that HEK 293 and its derivatives most closely resembled adrenal and central nervous cell-types. The usage of a diverse cellular nature cell-lines, like HEK 293T cells, in our research has confined our findings to the basic cell biological setting and will not inform further on the different organ-niche context. As different cells in different organs have diverse experiences and conditions from their niche. For example, endothelial cells within the blood vessels, experience a varying shear stress ranging from 10 to 80 dynes/cm^2, depending on the type and location of vessels[228,229]. Whereas, kidney epithelial cells generally are subjected to a shear rate of 10 to 30 dynes/cm^2, dependent on the location and the rate of the urine flow[201,203–206]. Therefore, the absence of a singular precise cell phenotype complicates the process of replicating the appropriate niche condition *in vitro*.

Secondly, immortalised cell lines, like HEK 293T cells, are usually inferior to primary cells (harvested directly from human or animal tissue samples) because they do not necessarily closely resemble *in vivo* situations. Primary cells, like HUVECs, are valuable models given that they are physiologically closer to the biochemical status of cells present *in vivo*[225]. Unfortunately, primary cells, among other sensitive cell types, are notoriously difficult to work with. Limited gene transfer and manipulation, slow proliferating rate, and restricted passage usage are some of the contributing factors[225]. Primary cells and other delicate cell-types, like stem cells, are also more sensitive to stress and manipulation. Therefore, changes in the culturing environment or tough chemical selection can damage them or cause them to (de)differentiate in cell nature.

HUVECs are a commonly used endothelial cell type in the cardiovascular research area. For example, HUVECs have been widely used to study the effect of shear stress on endothelial processes, as well as angiogenesis[21,151]. In my work, efforts to create a XLGenEPi-expressing clone have been undertaken, yet the highest genetic transfer

efficiency from an optimised lipofectamine transfection protocol was 5% (as reported in **Chapter 2**). Not only do HUVECs have limited gene transfer efficiency, but also our XLGenEPi construct size is significantly larger than a common EGFP-based construct. These two factors combined made the generation of XLGenEPi-expressing HUVECs tougher to achieve. In addition, the blasticidin (BSD)-clonal selection procedure, which required cells to be kept in culture for over 7 days, resulted in cell morphological changes. This indicates a fundamental change in cell nature, in other words, de-differentiation of the endothelial cells. This rendered my strategy incompatible with primary cells, like HUVECs.

To study the dynamics of Piezo1 in cells with a delicate nature, like HUVECs, a CRISPR/Ca gene editing strategy would be beneficial. By designing guide-RNAs to target the endogenous Piezo1 gene sequence, our linker-GECIs technology could be tagged onto the c-terminal tail of the Piezo1 gene transcript. Thus, enabling the recipient cells to express GenEPi endogenously. Efforts on this strategy have been underway within the research group.

5.2.4. Limitations in our fluidic handling method in the system

In my system, we used a syringe pump, one of the most common methods to apply fluid flow through the microfluidic channel. Syringe pumps are motor-driven, displacement-dependent devices used to apply a constant pressure or flow rate to the fluid. They are relatively easy to use and are widely available. However, there are limitations that can affect the accuracy and reproducibility of microfluidic experiments.

An important limitation that was considered in our research is the flow stability of the pump. As a syringe pump works by displacing the pistol, driven by a motor, to inject (or withdraw) fluid through the syringe, minimal movement of the motor induces a minimal injected volume. Therefore, it is common to observe a discrete flow profile of an oscillation flow, especially at a lower flow rate, because of the motor step. This oscillation of flow can cause an inaccuracy of flow rate measurement, which could potentially affect cellular behaviour manipulated within our experiments.

To limit the effect of oscillation flow within our system, pulseless syringe pumps were employed. In addition, syringe diameter sizes were controlled to match the intended flow rates elicited during the experiment. For example, smaller diameter syringes were used at a low shear rate (i.e. 1 µl/min, which corresponded to a 0.1 dyne/cm^2 shear level in our system). This is because the minimal infused (or withdrawn) volume, caused by the displacement of the pistol, is proportional to the syringe diameter.

While syringe pumps remain useful for our research to control fluid flow within a microfluidic device, they are not suitable for high-throughput applications. With no rapid and automated fluidic handling capabilities, it requires regular, manual intervention to change syringes and replenish fluid. The output of a syringe pump application is also directly dependent on the size of the syringe rack input. Generally, syringe pumps have a syringe rack input for two syringes, powering up to two microfluidic devices at once, without any parallelising of the flow circuit. Therefore, it is wise to consider other pump operation alternatives, such as peristatic or pneumatic pumps, when fluid recycling and high fluid handling accuracy are possible.

5.2.5. Limitations in confocal-based system

Our system which I presented in this thesis was developed based on standard confocal imaging. Offering good-resolution imaging capabilities and high optical sectioning, confocal imaging has long been the staple imaging technique in biological research. While our confocal-based imaging system has provided insightful findings presented in my thesis, confocal imaging has several limitations that can hinder its usage and should be considered in more intricate experiments of Piezo1 channel activities. One major limitation is its restricted penetration depth, particularly in thick or opaque specimens. Having restricted penetrance will limit the applicability for studying endogenous Piezo1 channels in deep tissue or animal organism *in vivo*. Moreover, confocal microscopy requires high-intensity laser illumination, which is prone to photobleaching and phototoxicity, especially during prolonged imaging. This limits the duration of live imaging experiments. Additionally, confocal imaging can be relatively slow, when compared to other microscopy methods, like spinning disk confocal or 2-photon imaging developed for studying rapid cellular events. This restriction in temporal resolution can

confound its suitability to capture fast dynamic processes, like mechanosensitive channel activities.

To address the limitations associated to confocal imaging system, 2-photon microscopy is a superior option to adapt for our system. Unlike confocal microscopy, 2-photon microscopy utilises longer excitation wavelengths, resulting in reduced scattering and increased penetration depth for deep tissue imaging. This will enabling subsequent studies on Piezo1 activities in intact tissues, organs with minimal light-induced damage. Moreover, 2-photon microscopy relies on nonlinear excitation, concentrating photon absorption at the focal point and reducing photobleaching and phototoxicity outside the focal plane. This makes it well-suited for long-term live-imaging experiments, preserving cellular viability and enabling the observation of dynamic cellular processes over extended periods. Additionally, 2-photon microscopy offers faster imaging speeds compared to confocal microscopy, allowing for high-speed imaging of dynamic biological processes with superior temporal resolution. Therefore, further application of our XLGenEPi system using 2-photon microscopy can offer a powerful imaging tool for investigating Piezo1 dynamic behaviours under chronic mechanical stress.

5.3. Ongoing work and future outlook

As described in this dissertation, we built a system which incorporated the GenEPi-sensor into a microfluidic-based platform to investigate the mesoscopic dynamics of cellular Piezo1. From my results, I suggest that our design system can serve as a model to study the activity of other mechanosensitive ion channels or proteins. Below, I discuss ongoing work in the lab and potential future research directions in the study of Piezo1 physiological activity within cells.

5.3.1. Red-GenEPi

Apart from the broad emission spectrum associated to the GCaMP-G4 present within the GenEPi-sensor, there are two other limitations with using a GFP-based Ca^{2+} indicator that would confine GenEPi-sensor usage for more sophisticated and future *in vivo*

experimental settings. Firstly, the overlapping of GenEPi's primary signal and cell autofluorescence range. Cell autofluorescence commonly occurs during certain cell processes and cell death[230,231]. This is due to the presence of certain endogenous molecules, like the various aromatic ring compounds – NADPH and riboflavin, which could have fluorescence capability under visible light excitation. Though often eliminable by image acquisition optimisation, cell autofluorescence is detectable within the 350 – 550 nm wavelength range, which coincides with the GenEPi-signal detectable range (i.e. 500 – 550 nm). Secondly, blue/green lights (i.e. 450 – 550 nm), used for the excitation of GFPs and GCaMPs, simply do not penetrate as deeply as orange/red lights (i.e. 600 – 750 nm) do[232]. This poses limitations especially when one is moving towards *in vivo* live-tissue imaging. However, these limitations with GFP- and GCaMP-based imaging can be eliminated by using red-shifted wavelength excitation indicators[233]. Therefore, efforts to create a red version of GenEPi have been underway (**Figure 5.2**).

Table 5.1. List of potential red-GECIs for generating red-GenEPi.

GECI(s)	Affinity to Ca^{2+} (Kd in nM)	Dynamic Range (F_{max}/F_{min})	Reference
GCaMP-G4	1400	31.0	[1]
CAR-GECO1	440	27.0	[235]
K-GECO1	165	12.0	[237]
O-GECO1	1300	146.0	[235]
R-GECO1	449	10.5	[234]
R-GECO1.2	1200	33.0	[235]
RCaMP1a	1300	7.2	[234]
RCaMP1b	770	4.2	[234]
RCaMP1c	922	7.5	[234]
RCaMP1d	1600	6.5	[234]
RCaMP1f	1900	12.3	[234]
RCaMP1h	1300	10.5	[234]

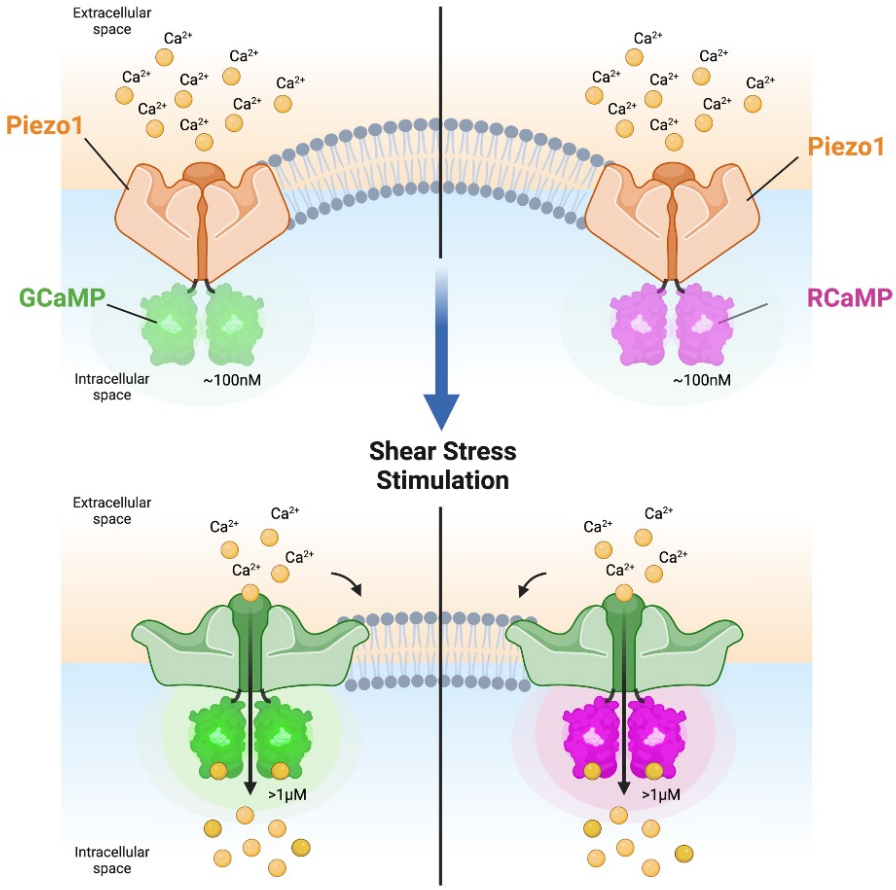


Figure 5.2. Engineering the red version of GenEPi. Current efforts have been focused on generating the red version of GenEPi, termed RGenEPi. The same strategy used to create our GenEPi construct has been employed. By the sub-cloning of red-GECIs to the C-terminal of the human Piezo1 sequence, we were able to create RGenEPi with similar dynamic range to our current GenEPi-sensor. (Illustration created using Biorender.com).

The GCaMP-G4 within the GenEPi-sensor is one of the many GECIs widely used to study Ca^{2+} dynamics within cells[172]. Recent advances in protein engineering led to a whole selection of novel GECIs with different fluorescent proteins[234]. The search for a potential red-GECIs to generate the red version of GenEPi needs to adhere to the sensor's Ca^{2+} affinity and a wide dynamic range, carefully calibrated in Yaganoglu, Y. & Kalyviotis, K. *et al.* (2023)[1]. Out of the library of red-GECIs (**Table 5.1**), two were selected based on their binding affinity to Ca^{2+} and dynamic range to GCaMP-G4. The two red-GECIs selected were O-GECO1 and RCamP1h, with Kd(s) to Ca^{2+} of 1300 nM and dynamic ranges of 146 and 10.5 respectively[234,235]. The O-GECO1 and RCamP1h are mApple- and mRuby-based GECIs, therefore they have an emission range of around 600 nm wavelength[236]. Molecular cloning was performed to replace the original GenEPi construct's GCaMP-G4

sequence and insert either the O-GECO1 or RCaMP1h sequence to create two red versions of GenEPi (**Figure 5.3 a**). The resultant two red-GenEPi constructs were termed O-GECO1-GenEPi and RCaMP1h-GenEPi. Following the creation of the two red-GenEPi(s), I investigated their transfectability on HUVECs (**Figure 5.3 b**), which was not much different from the original GenEPi construct. However, cloning efforts and further studies need to be done to insert the XLone-backbone for inducibility expression and characterise the red-GenEPi(s)' optical readouts.

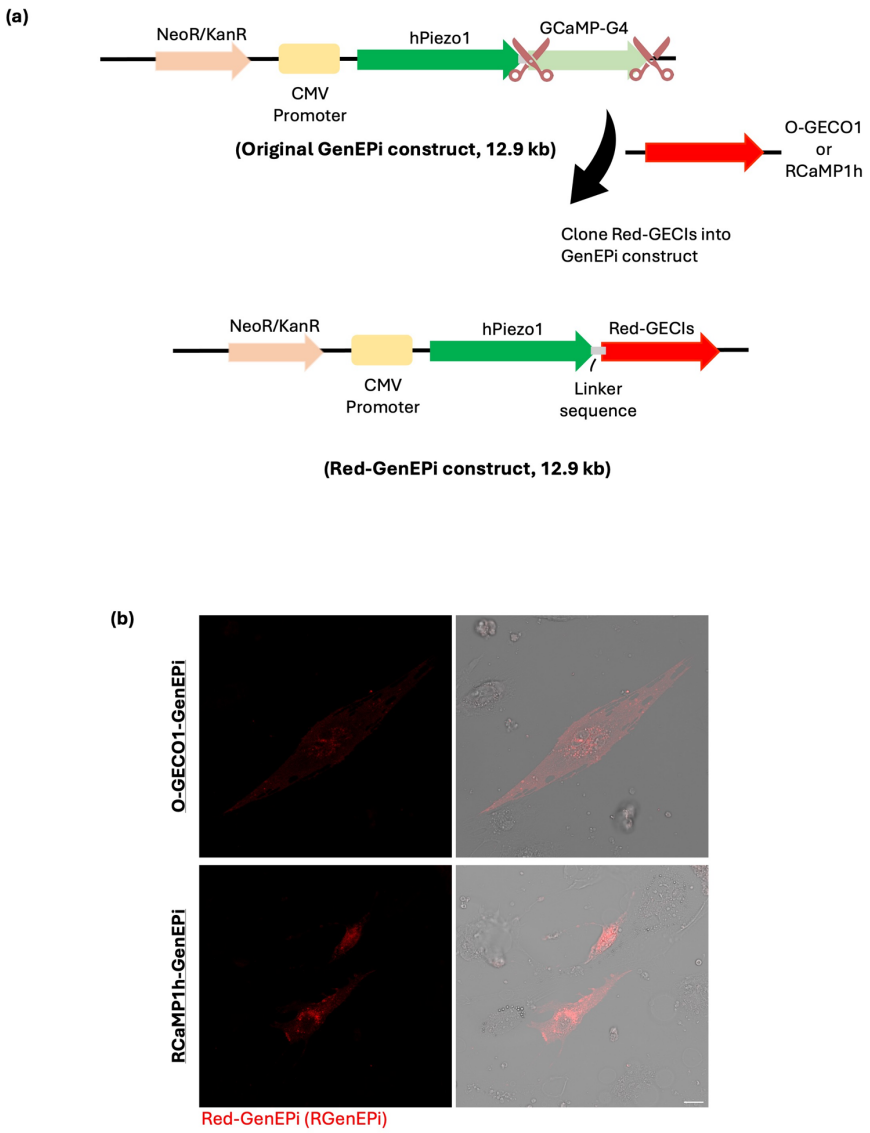


Figure 5.3. Red-GenEPi (or RGenEPi) is successfully expressed in HUVECs after transient transfection. (a) Molecular cloning strategy to sub-clone the selected red-GECIs (O-GECO1 and RCaMP1h) into the original GenEPi construct. Molecular cloning effort successfully generated the two versions of red-GenEPi (termed O-GECO1-GenEPi and RCaMP1h-GenEPi). **(b)** Representative confocal images of both red-GenEPi(s) transiently transfected into HUVECs. Both versions of red-GenEPi constructs achieved successful expression. Yoda1 treatment of transfected-HUVECs resulted in red

fluorescence display in red-GenEPi positive cells. Confocal images presented at 60x magnification (taken with 20x dry objective, and 3x optical zoom factor). Scale bar = 15 µm.

5.3.2. Endogenous Piezo1/GenEPi-tagging

So far, both original-GenEPi and XLGenEPi constructs have been readily implemented and yielded robust readouts in various models and different experimental setups. Although the incorporation of GenEPi-sensor is without any noticeable adverse effects on the cells, the expression of GenEPi still works under temporarily controlled overexpression. In addition, the usage of XLGenEPi-strategy remains challenging for primary cells, like HUVECs (discussed in **Section 5.2.3**). In such cases, it will be beneficial to employ genetic engineering strategy approaches to directly tag endogenous Piezo1 with a GCaMP or RCaMP. Endogenous tagging, like our already developed targeted CRISPR/Cas method, will enhance future studies investigating Piezo1 activity in response to both intrinsic and extrinsic stimuli, both mechanical and non-mechanical[238]. The study of Piezo1 activity is especially important for cells like endothelial cells, because the Piezo1 expression is relatively high. Furthermore, Piezo1 gene knockout is embryo lethal, due to the inability for vascular development[110]. Therefore, the use of endogenous GenEPi tagging in endothelial models will allow an in-depth understanding of the spatiotemporal dynamics of Piezo1's activity under constant fluid shear stress within the vasculature.

5.3.3. Compound screening and drug discovery pipeline

Despite its discovery one decade ago, there is still only one compound acting specifically on Piezo1. Yoda1, a Piezo1-specific agonist, acts by binding to Piezo1 channels and modulating their sensitivity to changes in the cell membrane tension. On the other hand, the availability of Piezo1 antagonists is restricted to GsMTx-4, which inhibits other stretch-activated channels (SACs), ruthenium red (RR) and Gadolinium (Gd^{3+}), which are broad spectrum Ca^{2+} ion channels inhibitors[99,155,156]. The absence of an inhibitor specific for Piezo1 brings challenges to conducting direct, isolated perturbatory experiments, without influencing other SACs or ion channels on the cell membrane. Hence, efforts for effective compound and drug screens can benefit from our system, using GenEPi as a direct optical readout for Piezo1 activity. Having a specific reporter, like GenEPi, provides

high spatiotemporal resolution readouts on cellular Piezo1 activity, which can be advantageous to precisely monitor the effects of compounds on Piezo1. My current microfluidic device design holds four microchannels in parallel, therefore, allowing the potential of having four cellularised channels for experimenting at once. The microfluidic device design can be modified to increase the number of holding microchannels. In addition, adaptations including recirculating media within the flow circuit will ensure the system is self-sustaining. Having a high-throughput system to detect Piezo1-specific dynamics ultimately allows high content screening for effective compound identification.

5.3.4. Understanding Piezo1 activity modulation

During the characterisation of GenEPi within our *in vitro* microfluidic model, I validated previously reported Piezo1-associated activities, e.g. Ca^{2+} flickers and membrane diffusivity, and described novel Piezo1 dynamics under global, systemic mechanical stimulus. Interestingly, I observed that Piezo1 response nature and dynamics can be differentially modulated depending on the force magnitude and frequency. As downstream mechanisms remain elusive for Piezo1 activity, dedicated efforts to investigate the machinery of differential Piezo1 activity modulation will be advantageous to understanding direct downstream mechanosensitive and mechanotransducive processes. This could involve the coupling of our GenEPi system with dynamic imaging of other mechanosensitive cellular components, like Yap/Taz and cytoskeleton, and other mechanoprotective phenomena, like nuclear condensation and cytoskeleton reorganisation.

Similarly, how, and the extent to, which Piezo1 dynamics are regulated by the lipid bilayer, cytoskeleton, Piezo1 clusters, and other associated partners remains to be deciphered. Finally, an in-depth investigation of Piezo1 activity and role within a complex environment, like the cell niche. In this PhD, I have incorporated the element of continuous, global mechanical stimulus into our culturing and experimental setup. Albeit better than *in vitro*, static models, the physiological cellular microenvironment is more dynamic. Therefore, the incorporation of other elements of the cellular niche, like other cell types and more components of ECM, will provide a wholesome picture of

mechanobiological phenomena in the cells' physiological environment. Ultimately, furthering research in Piezo1 dynamics will advance our understanding of the interplay between mechanical forces and cellular behaviour during development, homeostatic regulation, and disease pathophysiology.

5.4. Concluding remarks

In this project, I designed and developed a microfluidic-based system to study the mesoscopic dynamics of cellular Piezo1. Capitalising on GenEPi intensiometric readouts, I generated positive clonal cells, that stably express the GenEPi-sensor when induced, from my inducible XLGenEPi construct. I established a framework, from culturing to experimenting, to study Piezo1 dynamics in response to global, systemic mechanical stimulus. Using this system, I validated previously reported Piezo1 activities, and further outlined unique characteristics of Piezo1 dynamics within cells. This system which I developed can be multiplexed and be adapted for effective compound and drug for Piezo1 targeting. In sum, I hope this system can be a model or framework for others to adopt in investigating the dynamics of other mechanosensitive proteins expressed in the cells.

6. Bibliography

1. Yaganoglu, S., Kalyviotis, K., Vagena-Pantoula, C., Jülich, D., Gaub, B. M., Welling, M., Lopes, T., Lachowski, D., Tang, S. S., Del Rio Hernandez, A., Salem, V., Müller, D. J., Holley, S. A., Vermot, J., Shi, J., Helassa, N., Török, K., & Pantazis, P. (2023). Author Correction: Highly specific and non-invasive imaging of Piezo1-dependent activity across scales using GenEPi. *Nature communications*, **14**(1), 5787.

2. Spradling, A., Drummond-Barbosa, D. & Kai, T. (2001). Stem cells find their niche. *Nature,* **414**, 98–104.

3. Brafman D. A. (2013). Constructing stem cell microenvironments using bioengineering approaches. *Physiological genomics,* **45**(23), 1123–1135.

4. Huang G, Li F, Zhao X, Ma Y, Li Y, Lin M, Jin G, Lu TJ, Genin GM, Xu F. (2017). Functional and Biomimetic Materials for Engineering of the Three-Dimensional Cell Microenvironment. *Chem Rev.*, **117**(20):12764-12850.

5. Voog, J., & Jones, D. L. (2010). Stem cells and the niche: a dynamic duo. *Cell stem cell*, **6**(2), 103–115.

6. Kiefer J. C. (2011). Primer and interviews: The dynamic stem cell niche. *Developmental dynamics,* **240**(3), 737–743.

7. Yeung, T. M., Chia, L. A., Kosinski, C. M., & Kuo, C. J. (2011). Regulation of self-renewal and differentiation by the intestinal stem cell niche. *Cellular and molecular life sciences*, **68**(15), 2513–2523.

8. Vigetti, D., Götte, M., Pavão, M. S., & Theocharis, A. D. (2013). Cellular microenvironment in human pathologies. *BioMed research international,* 2013, 946958.

9. Lee, N., Kim, WU. (2017). Microbiota in T-cell homeostasis and inflammatory diseases. *Exp Mol Med,* 49, e340.

10. Zhang, J., & Li, L. (2008). Stem Cell Niche: Microenvironment and Beyond*. *Journal of Biological Chemistry,* 283, 9499 - 9503.

11. Tokoyoda, K., Egawa, T., Sugiyama, T., Choi, B., & Nagasawa, T. (2004). Cellular niches controlling B lymphocyte behavior within bone marrow during development. *Immunity,* **20**(6), 707-18 .

12. Badylak, S.F. (2002). The extracellular matrix as a scaffold for tissue reconstruction. *Seminars in cell & developmental biology,* **13**(5), 377-83 .

13. Karamanos, N., Theocharis, A.D., Piperigkou, Z., Manou, D., Passi, A., Skandalis, S.S., Vynios, D.H., Orian-Rousseau, V., Ricard-Blum, S., Schmelzer, C.E., Duca, L., Durbee, M., Afratis, N.A., Troeberg, L., Franchi, M., Masola, V., & Onisto, M. (2021). A guide to the composition and functions of the extracellular matrix. *The FEBS Journal,* 288.

14. Zito F. (2012). Role of extracellular matrix in regulating embryonic epithelial-mesenchymal transition. *Biomolecular concepts*, **3**(4), 333–344.

15. Kang, Y., & Massagué, J. (2004). Epithelial-mesenchymal transitions: twist in development and metastasis. *Cell,* **118**(3), 277–279.

16. Moustakas, A., & Heldin, C. H. (2007). Signaling networks guiding epithelial-mesenchymal transitions during embryogenesis and cancer progression. *Cancer science,* **98**(10), 1512–1520.

17. Gumbiner B. M. (1996). Cell adhesion: the molecular basis of tissue architecture and morphogenesis. *Cell,* **84**(3), 345–357.

18. Chaudhuri, O., Cooper-White, J., Janmey, P. A., Mooney, D. J., & Shenoy, V. B. (2020). Effects of extracellular matrix viscoelasticity on cellular behaviour. *Nature,* **584**(7822), 535–546.

19. Sun, Y., Yong, K. M., Villa-Diaz, L. G., Zhang, X., Chen, W., Philson, R., Weng, S., Xu, H., Krebsbach, P. H., & Fu, J. (2014). Hippo/YAP-mediated rigidity-dependent motor neuron differentiation of human pluripotent stem cells. *Nature materials,* **13**(6), 599–604.

20. Zhu, Y., Li, X., Janairo, R. R. R., Kwong, G., Tsou, A. D., Chu, J. S., Wang, A., Yu, J., Wang, D., & Li, S. (2019). Matrix stiffness modulates the differentiation of neural crest stem cells *in vivo*. *Journal of cellular physiology,* **234**(5), 7569–7578.

21. Ott, M. J., & Ballermann, B. J. (1995). Shear stress-conditioned, endothelial cell-seeded vascular grafts: improved cell adherence in response to *in vitro* shear stress. *Surgery,* **117**(3), 334–339.

22. Steward, R., Jr, Tambe, D., Hardin, C. C., Krishnan, R., & Fredberg, J. J. (2015). Fluid shear, intercellular stress, and endothelial cell alignment. American journal of physiology. *Cell physiology,* **308**(8), C657–C664.

23. Liotta, L. A., & Kohn, E. C. (2001). The microenvironment of the tumour-host interface. *Nature,* **411**(6835), 375–379.

24. Nyberg, P., Salo, T., & Kalluri, R. (2008). Tumor microenvironment and angiogenesis. *Frontiers in bioscience*, 13, 6537–6553.

25. Jung, H. Y., Fattet, L., & Yang, J. (2015). Molecular pathways: linking tumor microenvironment to epithelial-mesenchymal transition in metastasis. *Clinical cancer research,* **21**(5), 962–968.

26. Fenner, J., Stacer, A. C., Winterroth, F., Johnson, T. D., Luker, K. E., & Luker, G. D. (2014). Macroscopic stiffness of breast tumors predicts metastasis. *Scientific reports,* 4, 5512.

27. Liu, C., Li, M., Dong, Z. X., Jiang, D., Li, X., Lin, S., Chen, D., Zou, X., Zhang, X. D., & Luker, G. D. (2021). Heterogeneous microenvironmental stiffness regulates pro-metastatic functions of breast cancer cells. *Acta biomaterialia,* 131, 326–340.

28. Chatzizacharias, N. A., Kouraklis, G. P., & Theocharis, S. E. (2007). Focal adhesion kinase: a promising target for anticancer therapy. *Expert opinion on therapeutic targets,* **11**(10), 1315–1328.

29. Lee, B. Y., Timpson, P., Horvath, L. G., & Daly, R. J. (2015). FAK signaling in human cancer as a target for therapeutics. *Pharmacology & therapeutics,* 146, 132–149.

30. Masugi Y. (2022). The Desmoplastic Stroma of Pancreatic Cancer: Multilayered Levels of Heterogeneity, Clinical Significance, and Therapeutic Opportunities. *Cancers,* **14**(13), 3293.

31. Baghban, R., Roshangar, L., Jahanban-Esfahlan, R., Seidi, K., Ebrahimi-Kalan, A., Jaymand, M., Kolahian, S., Javaheri, T., & Zare, P. (2020). Tumor microenvironment complexity and therapeutic implications at a glance. *Cell communication and signaling,* **18**(1), 59.

32. Carton, F., & Malatesta, M. (2022). *in Vitro* Models of Biological Barriers for Nanomedical Research. *International journal of molecular sciences,* **23**(16), 8910.

33. Peyton, S. R., Ghajar, C. M., Khatiwala, C. B., & Putnam, A. J. (2007). The emergence of ECM mechanics and cytoskeletal tension as important regulators of cell function. *Cell biochemistry and biophysics,* **47**(2), 300–320.

34. Shemesh, J., Jalilian, I., Shi, A., Heng Yeoh, G., Knothe Tate, M. L., & Ebrahimi Warkiani, M. (2015). Flow-induced stress on adherent cells in microfluidic devices. *Lab on a chip,* **15**(21), 4114–4127.

35. Lesman, A., Blinder, Y., & Levenberg, S. (2010). Modeling of flow-induced shear stress applied on 3D cellular scaffolds: Implications for vascular tissue engineering. *Biotechnology and bioengineering,* **105**(3), 645–654.

36. Huh, D., Hamilton, G. A., & Ingber, D. E. (2011). From 3D cell culture to organs-on-chips. *Trends in cell biology,* **21**(12), 745–754.

37. Bhatia, S. N., & Ingber, D. E. (2014). Microfluidic organs-on-chips. *Nature biotechnology,* **32**(8), 760–772.

38. Gupta, A., Lutolf, M. P., Hughes, A. J., & Sonnen, K. F. (2021). Bioengineering *in vitro* models of embryonic development. *Stem cell reports,* **16**(5), 1104–1116.

39. Hofer, M., & Lutolf, M. P. (2021). Engineering organoids. *Nature reviews. Materials,* **6**(5), 402–420.

40. Fu, J., Warmflash, A., & Lutolf, M. P. (2021). Stem-cell-based embryo models for fundamental research and translation. *Nature materials,* **20**(2), 132–144.

41. Pathak, M. M., Nourse, J. L., Tran, T., Hwe, J., Arulmoli, J., Le, D. T., Bernardis, E., Flanagan, L. A., & Tombola, F. (2014). Stretch-activated ion channel Piezo1 directs lineage choice in human neural stem cells. *Proceedings of the National Academy of Sciences of the United States of America,* **111**(45), 16148–16153.

42. Arulmoli, J., Pathak, M. M., McDonnell, L. P., Nourse, J. L., Tombola, F., Earthman, J. C., & Flanagan, L. A. (2015). Static stretch affects neural stem cell differentiation in an extracellular matrix-dependent manner. *Scientific reports,* 5, 8499.

43. Oyama, H., Nukuda, A., Ishihara, S., & Haga, H. (2021). Soft surfaces promote astrocytic differentiation of mouse embryonic neural stem cells via dephosphorylation of MRLC in the absence of serum. *Scientific reports,* **11**(1), 19574.

44. Li, X. J., Valadez, A. V., Zuo, P., & Nie, Z. (2012). Microfluidic 3D cell culture: potential application for tissue-based bioassays. *Bioanalysis,* **4**(12), 1509–1525.

45. Mierke C. T. (2023). Physical and biological advances in endothelial cell-based engineered co-culture model systems. *Seminars in cell & developmental biology,* 147, 58–69.

46. Hoffman B. D. (2014). The detection and role of molecular tension in focal adhesion dynamics. *Progress in molecular biology and translational science,* 126, 3–24.

47. Gobaa, S., Gayet, R. V., & Lutolf, M. P. (2018). Artificial niche microarrays for identifying extrinsic cell-fate determinants. *Methods in cell biology,* 148, 51–69.

48. Muñoz-Garcia, J., Babic, J., & Coudreuse, D. (2018). Drug delivery and temperature control in microfluidic chips during live-cell imaging experiments. *Methods in cell biology,* 147, 3–28.

49. Di, X., Gao, X., Peng, L., Ai, J., Jin, X., Qi, S., Li, H., Wang, K., & Luo, D. (2023). Cellular mechanotransduction in health and diseases: from molecular mechanism to therapeutic targets. *Signal transduction and targeted therapy,* **8**(1), 282.

50. Vining, K. H., & Mooney, D. J. (2017). Mechanical forces direct stem cell behaviour in development and regeneration. *Nature reviews. Molecular cell biology,* **18**(12), 728–742.

51. Martino, F., Perestrelo, A. R., Vinarský, V., Pagliari, S., & Forte, G. (2018). Cellular Mechanotransduction: From Tension to Function. *Frontiers in physiology,* 9, 824.

52. Uray, I. P., & Uray, K. (2021). Mechanotransduction at the Plasma Membrane-Cytoskeleton Interface. *International journal of molecular sciences,* **22**(21), 11566.

53. Holle, A. W., Young, J. L., Van Vliet, K. J., Kamm, R. D., Discher, D., Janmey, P., Spatz, J. P., & Saif, T. (2018). Cell-Extracellular Matrix Mechanobiology: Forceful Tools and Emerging Needs for Basic and Translational Research. *Nano letters,* **18**(1), 1–8.

54. Heisenberg, C. P., & Bellaïche, Y. (2013). Forces in tissue morphogenesis and patterning. *Cell,* **153**(5), 948–962.

55. Lecuit, T., Lenne, P. F., & Munro, E. (2011). Force generation, transmission, and integration during cell and tissue morphogenesis. *Annual review of cell and developmental biology,* 27, 157–184.

56. Chan, C. J., Heisenberg, C. P., & Hiiragi, T. (2017). Coordination of Morphogenesis and Cell-Fate Specification in Development. *Current,* **27**(18), R1024–R1035.

57. Petridou, N. I., Spiró, Z., & Heisenberg, C. P. (2017). Multiscale force sensing in development. *Nature cell biology,* **19**(6), 581–588.

58. Humphrey, J. D., Dufresne, E. R., & Schwartz, M. A. (2014). Mechanotransduction and extracellular matrix homeostasis. Nature reviews. *Molecular cell biology,* **15**(12), 802–812.

59. Holt, J. R., Zeng, W. Z., Evans, E. L., Woo, S. H., Ma, S., Abuwarda, H., Loud, M., Patapoutian, A., & Pathak, M. M. (2021). Spatiotemporal dynamics of PIEZO1 localization controls keratinocyte migration during wound healing. *eLife,* 10, e65415.

60. Kai, F., Laklai, H., & Weaver, V. M. (2016). Force Matters: Biomechanical Regulation of Cell Invasion and Migration in Disease. *Trends in cell biology*, **26**(7), 486–497.

61. Panciera, T., Azzolin, L., Cordenonsi, M., & Piccolo, S. (2017). Mechanobiology of YAP and TAZ in physiology and disease. *Nature reviews. Molecular cell biology,* **18**(12), 758–770.

62. Eyckmans, J., Boudou, T., Yu, X., & Chen, C. S. (2011). A hitchhiker's guide to mechanobiology. *Developmental cell,* **21**(1), 35–47.

63. Swaminathan, V., & Gloerich, M. (2021). Decoding mechanical cues by molecular mechanotransduction. *Current opinion in cell biology,* 72, 72–80.

64. Hamill, O. P., & Martinac, B. (2001). Molecular basis of mechanotransduction in living cells. *Physiological reviews,* **81**(2), 685–740.

65. Cox, C. D., Bavi, N., & Martinac, B. (2019). Biophysical Principles of Ion-Channel-Mediated Mechanosensory Transduction. *Cell reports,* **29**(1), 1–12.

66. McIntosh, T. J., & Simon, S. A. (1986). Hydration force and bilayer deformation: a reevaluation. *Biochemistry*, **25**(14), 4058–4066.

67. Onal, S., Alkaisi, M. M., & Nock, V. (2022). Microdevice-based mechanical compression on living cells. *iScience*, **25**(12), 105518.

68. Fanfone, D., Wu, Z., Mammi, J., Berthenet, K., Neves, D., Weber, K., Halaburkova, A., Virard, F., Bunel, F., Jamard, C., Hernandez-Vargas, H., Tait, S. W. G., Hennino, A., & Ichim, G. (2022). Confined migration promotes cancer metastasis through resistance to anoikis and increased invasiveness. *eLife*, 11, e73150.

69. Denais, C. M., Gilbert, R. M., Isermann, P., McGregor, A. L., te Lindert, M., Weigelin, B., Davidson, P. M., Friedl, P., Wolf, K., & Lammerding, J. (2016). Nuclear envelope rupture and repair during cancer cell migration. *Science*, **352**(6283), 353–358.

70. Ammendolia, D. A., Bement, W. M., & Brumell, J. H. (2021). Plasma membrane integrity: implications for health and disease. *BMC biology*, **19**(1), 71.

71. Wang, J. H., & Thampatty, B. P. (2006). An introductory review of cell mechanobiology. *Biomechanics and modeling in mechanobiology*, **5**(1), 1–16.

72. Cui, Y., Hameed, F. M., Yang, B., Lee, K., Pan, C. Q., Park, S., & Sheetz, M. (2015). Cyclic stretching of soft substrates induces spreading and growth. *Nature communications*, 6, 6333.

73. Prinz, W. A., & Hinshaw, J. E. (2009). Membrane-bending proteins. *Critical reviews in biochemistry and molecular biology*, **44**(5), 278–291.

74. White, C. R., & Frangos, J. A. (2007). The shear stress of it all: the cell membrane and mechanochemical transduction. *Philosophical transactions of the Royal Society of London. Series B, Biological sciences*, **362**(1484), 1459–1467.

75. Espina, J. A., Cordeiro, M. H., Milivojevic, M., Pajić-Lijaković, I., & Barriga, E. H. (2023). Response of cells and tissues to shear stress. *Journal of cell science*, **136**(18), jcs260985.

76. Amiri, S., Muresan, C., Shang, X., Huet-Calderwood, C., Schwartz, M. A., Calderwood, D. A., & Murrell, M. (2023). Intracellular tension sensor reveals mechanical anisotropy of the actin cytoskeleton. *Nature communications*, **14**(1), 8011.

77. Fletcher, D. A., & Mullins, R. D. (2010). Cell mechanics and the cytoskeleton. *Nature*, **463**(7280), 485–492.

78. Addae-Mensah, K. A., & Wikswo, J. P. (2008). Measurement techniques for cellular biomechanics *in vitro*. *Experimental biology and medicine*, **233**(7), 792–809.

79. Moeendarbary, E., & Harris, A. R. (2014). Cell mechanics: principles, practices, and prospects. *Wiley interdisciplinary reviews. Systems biology and medicine*, **6**(5), 371–388.

80. Kim, S., Uroz, M., Bays, J. L., & Chen, C. S. (2021). Harnessing Mechanobiology for Tissue Engineering. *Developmental cell*, **56**(2), 180–191.

81. Melo-Fonseca, F., Carvalho, O., Gasik, M., Miranda, G., & Silva, F. S. (2023). 'Mechanical stimulation devices for mechanobiology studies: a market, literature, and patents review'. *Bio-Design and Manufacturing*, **6**(3), 340–371.

82. Oddershede L. B. (2012). Force probing of individual molecules inside the living cell is now a reality. *Nature chemical biology*, **8**(11), 879–886.

83. Gautier, H. O., Thompson, A. J., Achouri, S., Koser, D. E., Holtzmann, K., Moeendarbary, E., & Franze, K. (2015). Atomic force microscopy-based force measurements on animal cells and tissues. *Methods in cell biology*, 125, 211–235.

84. Gaub, B. M., & Müller, D. J. (2017). Mechanical Stimulation of Piezo1 Receptors Depends on Extracellular Matrix Proteins and Directionality of Force. *Nano letters*, **17**(3), 2064–2072.

85. Bambardekar, K., Clément, R., Blanc, O., Chardès, C., & Lenne, P. F. (2015). Direct laser manipulation reveals the mechanics of cell contacts *in vivo*. *Proceedings of the National Academy of Sciences of the United States of America*, **112**(5), 1416–1421.

86. Savin, T., Kurpios, N. A., Shyer, A. E., Florescu, P., Liang, H., Mahadevan, L., & Tabin, C. J. (2011). On the growth and form of the gut. *Nature*, **476**(7358), 57–62.

87. Fukui, H., Chow, R. W., Xie, J., Foo, Y. Y., Yap, C. H., Minc, N., Mochizuki, N., & Vermot, J. (2021). Bioelectric signaling and the control of cardiac cell identity in response to mechanical forces. *Science*, **374**(6565), 351–354.

88. Sugimura, K., Lenne, P. F., & Graner, F. (2016). Measuring forces and stresses in situ in living tissues. *Development*, **143**(2), 186–196.

89. Liu, N., Zhang, X. P., Guo, Q. X., Wu, T., Wang, Y. F. (2022). 3D Bioprinted Scaffolds for Tissue Repair and Regeneration. *Frontiers in Materials*, 9, 925321.

90. Erdemir, A., Guess, T. M., Halloran, J., Tadepalli, S. C., & Morrison, T. M. (2012). Considerations for reporting finite element analysis studies in biomechanics. *Journal of biomechanics*, **45**(4), 625–633.

91. Bachir, A. I., Horwitz, A. R., Nelson, W. J., & Bianchini, J. M. (2017). Actin-Based Adhesion Modules Mediate Cell Interactions with the Extracellular Matrix and Neighboring Cells. *Cold Spring Harbor perspectives in biology*, **9**(7), a023234.

92. Yamaguchi, N., & Knaut, H. (2022). Focal adhesion-mediated cell anchoring and migration: from *in vitro* to *in vivo*. *Development*, **149**(10), dev200647.

93. Goult, B. T., Brown, N. H., & Schwartz, M. A. (2021). Talin in mechanotransduction and mechanomemory at a glance. *Journal of cell science*, **134**(20), jcs258749.

94. Ridone, P., Vassalli, M., & Martinac, B. (2019). Piezo1 mechanosensitive channels: what are they and why are they important. *Biophysical reviews*, **11**(5), 795–805.

95. Jin, P., Jan, L. Y., & Jan, Y. N. (2020). Mechanosensitive Ion Channels: Structural Features Relevant to Mechanotransduction Mechanisms. *Annual review of neuroscience*, 43, 207–229.

96. Martinac B. (2004). Mechanosensitive ion channels: molecules of mechanotransduction. *Journal of cell science*, **117**(Pt 12), 2449–2460.

97. Ridone, P., Pandzic, E., Vassalli, M., Cox, C. D., Macmillan, A., Gottlieb, P. A., & Martinac, B. (2020). Disruption of membrane cholesterol organization impairs the activity of PIEZO1 channel clusters. *The Journal of general physiology*, **152**(8), e201912515.

98. Cox, C. D., Bae, C., Ziegler, L., Hartley, S., Nikolova-Krstevski, V., Rohde, P. R., Ng, C. A., Sachs, F., Gottlieb, P. A., & Martinac, B. (2016). Removal of the mechanoprotective influence of the cytoskeleton reveals PIEZO1 is gated by bilayer tension. *Nature communications*, 7, 10366.

99. Coste, B., Mathur, J., Schmidt, M., Earley, T. J., Ranade, S., Petrus, M. J., Dubin, A. E., & Patapoutian, A. (2010). Piezo1 and Piezo2 are essential components of distinct mechanically activated cation channels. *Science*, **330**(6000), 55–60.

100. Coste, B., Xiao, B., Santos, J. S., Syeda, R., Grandl, J., Spencer, K. S., Kim, S. E., Schmidt, M., Mathur, J., Dubin, A. E., Montal, M., & Patapoutian, A. (2012). Piezo proteins are pore-forming subunits of mechanically activated channels. *Nature*, **483**(7388), 176–181.

101. Uhlén, M., Fagerberg, L., Hallström, B. M., Lindskog, C., Oksvold, P., Mardinoglu, A., Sivertsson, Å., Kampf, C., Sjöstedt, E., Asplund, A., Olsson, I., Edlund, K., Lundberg, E., Navani, S., Szigyarto, C. A., Odeberg, J., Djureinovic, D., Takanen, J. O., Hober, S., Alm, T., ... Pontén, F. (2015). Proteomics. Tissue-based map of the human proteome. *Science*, **347**(6220), 1260419.

102. Nourse, J. L., & Pathak, M. M. (2017). How cells channel their stress: Interplay between Piezo1 and the cytoskeleton. *Seminars in cell & developmental biology,* 71, 3–12.

103. Murthy, S. E., Dubin, A. E., & Patapoutian, A. (2017). Piezos thrive under pressure: mechanically activated ion channels in health and disease. *Nature reviews. Molecular cell biology*, **18**(12), 771–783.

104. Lewis, A. H., Cui, A. F., McDonald, M. F., & Grandl, J. (2017). Transduction of Repetitive Mechanical Stimuli by Piezo1 and Piezo2 Ion Channels. *Cell reports,* **19**(12), 2572–2585.

105. Saotome, K., Murthy, S. E., Kefauver, J. M., Whitwam, T., Patapoutian, A., & Ward, A. B. (2018). Structure of the mechanically activated ion channel Piezo1. *Nature*, **554**(7693), 481–486.

106. Tang, H., Zeng, R., He, E., Zhang, I., Ding, C., & Zhang, A. (2022). Piezo-Type Mechanosensitive Ion Channel Component 1 (Piezo1): A Promising Therapeutic Target and Its Modulators. *Journal of medicinal chemistry*, **65**(9), 6441–6453.

107. Jiang, Y., Yang, X., Jiang, J., & Xiao, B. (2021). Structural Designs and Mechanogating Mechanisms of the Mechanosensitive Piezo Channels. *Trends in biochemical sciences,* **46**(6), 472–488.

108. Zhao, Q., Zhou, H., Li, X., & Xiao, B. (2019). The mechanosensitive Piezo1 channel: a three-bladed propeller-like structure and a lever-like mechanogating mechanism. *The FEBS journal*, **286**(13), 2461–2470.

109. Gottlieb, P. A., Bae, C., & Sachs, F. (2012). Gating the mechanical channel Piezo1: a comparison between whole-cell and patch recording. *Channels*, **6**(4), 282–289.

110. Li, J., Hou, B., Tumova, S., Muraki, K., Bruns, A., Ludlow, M. J., Sedo, A., Hyman, A. J., McKeown, L., Young, R. S., Yuldasheva, N. Y., Majeed, Y., Wilson, L. A., Rode, B., Bailey, M. A., Kim, H. R., Fu, Z., Carter, D. A., Bilton, J., Imrie, H., ... Beech, D. J. (2014). Piezo1 integration of vascular architecture with physiological force. *Nature*, **515**(7526), 279–282.

111. Ranade, S. S., Qiu, Z., Woo, S. H., Hur, S. S., Murthy, S. E., Cahalan, S. M., Xu, J., Mathur, J., Bandell, M., Coste, B., Li, Y. S., Chien, S., & Patapoutian, A. (2014). Piezo1, a mechanically activated ion channel, is required for vascular development in mice. *Proceedings of the National Academy of Sciences of the United States of America,* **111**(28), 10347–10352.

112. Gudipaty, S. A., Lindblom, J., Loftus, P. D., Redd, M. J., Edes, K., Davey, C. F., Krishnegowda, V., & Rosenblatt, J. (2017). Mechanical stretch triggers rapid epithelial cell division through Piezo1. *Nature*, **543**(7643), 118–121.

113. Lacroix, J. J., Botello-Smith, W. M., & Luo, Y. (2018). Probing the gating mechanism of the mechanosensitive channel Piezo1 with the small molecule Yoda1. *Nature communications,* **9**(1), 2029.

114. Syeda, R., Florendo, M. N., Cox, C. D., Kefauver, J. M., Santos, J. S., Martinac, B., & Patapoutian, A. (2016). Piezo1 Channels Are Inherently Mechanosensitive. *Cell reports,* **17**(7), 1739–1746.

115. Hung, W. C., Yang, J. R., Yankaskas, C. L., Wong, B. S., Wu, P. H., Pardo-Pastor, C., Serra, S. A., Chiang, M. J., Gu, Z., Wirtz, D., Valverde, M. A., Yang, J. T., Zhang, J., & Konstantopoulos, K. (2016). Confinement Sensing and Signal Optimization via Piezo1/PKA and Myosin II Pathways. *Cell reports,* **15**(7), 1430–1441.

116. Ellefsen, K. L., Holt, J. R., Chang, A. C., Nourse, J. L., Arulmoli, J., Mekhdjian, A. H., Abuwarda, H., Tombola, F., Flanagan, L. A., Dunn, A. R., Parker, I., & Pathak, M. M. (2019). Myosin-II mediated traction forces evoke localized Piezo1-dependent Ca^{2+} flickers. *Communications biology*, 2, 298.

117. Fang, X. Z., Zhou, T., Xu, J. Q., Wang, Y. X., Sun, M. M., He, Y. J., Pan, S. W., Xiong, W., Peng, Z. K., Gao, X. H., & Shang, Y. (2021). Structure, kinetic properties and biological function of mechanosensitive Piezo channels. *Cell & bioscience,* **11**(1), 13.

118. Yang, S., Miao, X., Arnold, S., Li, B., Ly, A. T., Wang, H., Wang, M., Guo, X., Pathak, M. M., Zhao, W., Cox, C. D., & Shi, Z. (2022). Membrane curvature governs the distribution of Piezo1 in live cells. *Nature communications,* **13**(1), 7467.

119. Gnanasambandam, R., Bae, C., Gottlieb, P. A., & Sachs, F. (2015). Ionic Selectivity and Permeation Properties of Human PIEZO1 Channels. *PloS one,* **10**(5), e0125503.

120. Lewis, A. H., & Grandl, J. (2020). Inactivation Kinetics and Mechanical Gating of Piezo1 Ion Channels Depend on Subdomains within the Cap. *Cell reports*, **30**(3), 870–880.e2.

121. Brohawn, S. G., Su, Z., & MacKinnon, R. (2014). Mechanosensitivity is mediated directly by the lipid membrane in TRAAK and TREK1 K+ channels. *Proceedings of the National Academy of Sciences of the United States of America,* **111**(9), 3614–3619.

122. Poole, K., Herget, R., Lapatsina, L., Ngo, H. D., & Lewin, G. R. (2014). Tuning Piezo ion channels to detect molecular-scale movements relevant for fine touch. *Nature communications*, 5, 3520.

123. Qi, Y., Andolfi, L., Frattini, F., Mayer, F., Lazzarino, M., & Hu, J. (2015). Membrane stiffening by STOML3 facilitates mechanosensation in sensory neurons. *Nature communications*, 6, 8512.

124. Wu, J., Lewis, A. H., & Grandl, J. (2017). Touch, Tension, and Transduction - The Function and Regulation of Piezo Ion Channels. *Trends in biochemical sciences*, **42**(1), 57–71.

125. Albuisson, J., Murthy, S. E., Bandell, M., Coste, B., Louis-Dit-Picard, H., Mathur, J., Fénéant-Thibault, M., Tertian, G., de Jaureguiberry, J. P., Syfuss, P. Y., Cahalan, S., Garçon, L., Toutain, F., Simon Rohrlich, P., Delaunay, J., Picard, V., Jeunemaitre, X., & Patapoutian, A. (2013). Dehydrated hereditary stomatocytosis linked to gain-of-function mutations in mechanically activated PIEZO1 ion channels. *Nature communications*, 4, 1884.

126. Andolfo, I., Alper, S. L., De Franceschi, L., Auriemma, C., Russo, R., De Falco, L., Vallefuoco, F., Esposito, M. R., Vandorpe, D. H., Shmukler, B. E., Narayan, R., Montanaro, D., D'Armiento, M., Vetro, A., Limongelli, I., Zuffardi, O., Glader, B. E., Schrier, S. L., Brugnara, C., Stewart, G. W., … Iolascon, A. (2013). Multiple clinical forms of dehydrated hereditary stomatocytosis arise from mutations in PIEZO1. *Blood*, **121**(19), 3925–S12.

127. Fotiou, E., Martin-Almedina, S., Simpson, M. A., Lin, S., Gordon, K., Brice, G., Atton, G., Jeffery, I., Rees, D. C., Mignot, C., Vogt, J., Homfray, T., Snyder, M. P., Rockson, S. G., Jeffery, S., Mortimer, P. S., Mansour, S., & Ostergaard, P. (2015). Novel mutations in PIEZO1 cause an autosomal recessive generalized lymphatic dysplasia with non-immune hydrops fetalis. *Nature communications*, 6, 8085.

128. Lukacs, V., Mathur, J., Mao, R., Bayrak-Toydemir, P., Procter, M., Cahalan, S. M., Kim, H. J., Bandell, M., Longo, N., Day, R. W., Stevenson, D. A., Patapoutian, A., & Krock, B. L. (2015). Impaired PIEZO1 function in patients with a novel autosomal recessive congenital lymphatic dysplasia. *Nature communications*, 6, 8329.

129. Archer, N. M., Shmukler, B. E., Andolfo, I., Vandorpe, D. H., Gnanasambandam, R., Higgins, J. M., Rivera, A., Fleming, M. D., Sachs, F., Gottlieb, P. A., Iolascon, A.,

Brugnara, C., Alper, S. L., & Nathan, D. G. (2014). Hereditary xerocytosis revisited. *American journal of hematology*, **89**(12), 1142–1146.

130. Ma, S., Cahalan, S., LaMonte, G., Grubaugh, N. D., Zeng, W., Murthy, S. E., Paytas, E., Gamini, R., Lukacs, V., Whitwam, T., Loud, M., Lohia, R., Berry, L., Khan, S. M., Janse, C. J., Bandell, M., Schmedt, C., Wengelnik, K., Su, A. I., Honore, E., ... Patapoutian, A. (2018). Common PIEZO1 Allele in African Populations Causes RBC Dehydration and Attenuates Plasmodium Infection. *Cell*, **173**(2), 443–455.e12.

131. Wang, S., Chennupati, R., Kaur, H., Iring, A., Wettschureck, N., & Offermanns, S. (2016). Endothelial cation channel PIEZO1 controls blood pressure by mediating flow-induced ATP release. *The Journal of clinical investigation*, **126**(12), 4527–4536.

132. Cudmore, R. H., & Santana, L. F. (2022). Piezo1 Tunes Blood Flow in the Central Nervous System. *Circulation research*, **130**(10), 1547–1549.

133. Zhang, L., Liu, X., Gao, L., Ji, Y., Wang, L., Zhang, C., Dai, L., Liu, J., & Ji, Z. (2020). Activation of Piezo1 by ultrasonic stimulation and its effect on the permeability of human umbilical vein endothelial cells. *Biomedicine & pharmacotherapy*, 131, 110796.

134. Eisenhoffer, G. T., Loftus, P. D., Yoshigi, M., Otsuna, H., Chien, C. B., Morcos, P. A., & Rosenblatt, J. (2012). Crowding induces live cell extrusion to maintain homeostatic cell numbers in epithelia. *Nature*, **484**(7395), 546–549.

135. McHugh, B. J., Murdoch, A., Haslett, C., & Sethi, T. (2012). Loss of the integrin-activating transmembrane protein Fam38A (Piezo1) promotes a switch to a reduced integrin-dependent mode of cell migration. *PloS one*, **7**(7), e40346.

136. Miyamoto, T., Mochizuki, T., Nakagomi, H., Kira, S., Watanabe, M., Takayama, Y., Suzuki, Y., Koizumi, S., Takeda, M., & Tominaga, M. (2014). Functional role for Piezo1 in stretch-evoked Ca^{2+} influx and ATP release in urothelial cell cultures. *The Journal of biological chemistry*, **289**(23), 16565–16575.

137. Peyronnet, R., Martins, J. R., Duprat, F., Demolombe, S., Arhatte, M., Jodar, M., Tauc, M., Duranton, C., Paulais, M., Teulon, J., Honoré, E., & Patel, A. (2013). Piezo1-dependent stretch-activated channels are inhibited by Polycystin-2 in renal tubular epithelial cells. *EMBO reports*, **14**(12), 1143–1148.

138. Nakada, D., Levi, B. P., & Morrison, S. J. (2011). Integrating physiological regulation with stem cell and tissue homeostasis. *Neuron*, **70**(4), 703–718.

139. Li, X., Han, L., Nookaew, I., Mannen, E., Silva, M. J., Almeida, M., & Xiong, J. (2019). Stimulation of Piezo1 by mechanical signals promotes bone anabolism. *eLife*, 8, e49631.

140. Wang, L., You, X., Lotinun, S., Zhang, L., Wu, N., & Zou, W. (2020). Mechanical sensing protein PIEZO1 regulates bone homeostasis via osteoblast-osteoclast crosstalk. *Nature communications*, **11**(1), 282.

141. Zheng, Q., Liu, H., Yu, W., Dong, Y., Zhou, L., Deng, W., & Hua, F. (2023). Mechanical properties of the brain: Focus on the essential role of Piezo1-mediated mechanotransduction in the CNS. *Brain and behavior*, **13**(9), e3136.

142. Zhu, T., Guo, J., Wu, Y., Lei, T., Zhu, J., Chen, H., Kala, S., Wong, K. F., Cheung, C. P., Huang, X., Zhao, X., Yang, M., & Sun, L. (2023). The mechanosensitive ion channel Piezo1 modulates the migration and immune response of microglia. *iScience*, **26**(2), 105993.

143. Ma, N., Chen, D., Lee, J. H., Kuri, P., Hernandez, E. B., Kocan, J., Mahmood, H., Tichy, E. D., Rompolas, P., & Mourkioti, F. (2022). Piezo1 regulates the regenerative capacity of skeletal muscles via orchestration of stem cell morphological states. *Science advances*, **8**(11), eabn0485.

144. Yu, Y., Wu, X., Liu, S., Zhao, H., Li, B., Zhao, H., & Feng, X. (2021). Piezo1 regulates migration and invasion of breast cancer cells via modulating cell mechanobiological properties. *Acta biochimica et biophysica Sinica*, **53**(1), 10–18.

145. Li, C., Rezania, S., Kammerer, S., Sokolowski, A., Devaney, T., Gorischek, A., Jahn, S., Hackl, H., Groschner, K., Windpassinger, C., Malle, E., Bauernhofer, T., & Schreibmayer, W. (2015). Piezo1 forms mechanosensitive ion channels in the human MCF-7 breast cancer cell line. *Scientific reports*, 5, 8364.

146. Guillou, L., Babataheri, A., Puech, P. H., Barakat, A. I., & Husson, J. (2016). Dynamic monitoring of cell mechanical properties using profile microindentation. *Scientific reports*, 6, 21529.

147. Campàs O. (2016). A toolbox to explore the mechanics of living embryonic tissues. Seminars in cell & developmental biology, 55, 119–130.

148. Campàs, O., Mammoto, T., Hasso, S., Sperling, R. A., O'Connell, D., Bischof, A. G., Maas, R., Weitz, D. A., Mahadevan, L., & Ingber, D. E. (2014). Quantifying cell-generated mechanical forces within living embryonic tissues. *Nature methods*, **11**(2), 183–189.

149. Grannemann, C., Pabst, A., Honert, A., Schieren, J., Martin, C., Hank, S., Böll, S., Bläsius, K., Düsterhöft, S., Jahr, H., Merkel, R., Leube, R., Babendreyer, A., & Ludwig, A. (2023). Mechanical activation of lung epithelial cells through the ion channel Piezo1 activates the metalloproteinases ADAM10 and ADAM17 and promotes growth factor and adhesion molecule release. *Biomaterials advances*, 152, 213516.

150. Swain, S. M., & Liddle, R. A. (2021). Piezo1 acts upstream of TRPV4 to induce pathological changes in endothelial cells due to shear stress. *The Journal of biological chemistry*, 296, 100171.

151. Gordon, E., Schimmel, L., & Frye, M. (2020). The Importance of Mechanical Forces for *in vitro* Endothelial Cell Biology. *Frontiers in physiology*, 11, 684.

152. Syeda, R., Xu, J., Dubin, A. E., Coste, B., Mathur, J., Huynh, T., Matzen, J., Lao, J., Tully, D. C., Engels, I. H., Petrassi, H. M., Schumacher, A. M., Montal, M., Bandell, M., & Patapoutian, A. (2015). Chemical activation of the mechanotransduction channel Piezo1. *eLife*, 4, e07369.

153. Evans, E. L., Cuthbertson, K., Endesh, N., Rode, B., Blythe, N. M., Hyman, A. J., Hall, S. J., Gaunt, H. J., Ludlow, M. J., Foster, R., & Beech, D. J. (2018). Yoda1 analogue (Dooku1) which antagonizes Yoda1-evoked activation of Piezo1 and aortic relaxation. *British journal of pharmacology*, **175**(10), 1744–1759.

154. Wang, Y., Chi, S., Guo, H., Li, G., Wang, L., Zhao, Q., Rao, Y., Zu, L., He, W., & Xiao, B. (2018). A lever-like transduction pathway for long-distance chemical- and mechano-gating of the mechanosensitive Piezo1 channel. *Nature communications*, **9**(1), 1300.

155. Zhao, Q., Wu, K., Geng, J., Chi, S., Wang, Y., Zhi, P., Zhang, M., & Xiao, B. (2016). Ion Permeation and Mechanotransduction Mechanisms of Mechanosensitive Piezo Channels. *Neuron*, **89**(6), 1248–1263.

156. Suchyna, T. M., Johnson, J. H., Hamer, K., Leykam, J. F., Gage, D. A., Clemo, H. F., Baumgarten, C. M., & Sachs, F. (2000). Identification of a peptide toxin from Grammostola spatulata spider venom that blocks cation-selective stretch-activated channels. *The Journal of general physiology*, **115**(5), 583–598.

157. Bae, C., Sachs, F., & Gottlieb, P. A. (2011). The mechanosensitive ion channel Piezo1 is inhibited by the peptide GsMTx4. *Biochemistry*, **50**(29), 6295–6300.

158. Bowman, C. L., Gottlieb, P. A., Suchyna, T. M., Murphy, Y. K., & Sachs, F. (2007). Mechanosensitive ion channels and the peptide inhibitor GsMTx-4: history, properties, mechanisms and pharmacology. *Toxicon*, **49**(2), 249–270.

159. Bosmans, F., & Swartz, K. J. (2010). Targeting voltage sensors in sodium channels with spider toxins. *Trends in pharmacological sciences*, **31**(4), 175–182.

160. Gottlieb P. A. (2017). A Tour de Force: The Discovery, Properties, and Function of Piezo Channels. *Current topics in membranes*, 79, 1–36.

161. Qiu, Z., Guo, J., Kala, S., Zhu, J., Xian, Q., Qiu, W., Li, G., Zhu, T., Meng, L., Zhang, R., Chan, H. C., Zheng, H., & Sun, L. (2019). The Mechanosensitive Ion Channel

Piezo1 Significantly Mediates *In Vitro* Ultrasonic Stimulation of Neurons. *iScience*, 21, 448–457.

162. Parekh A. B. (2011). Decoding cytosolic Ca^{2+} oscillations. *Trends in biochemical sciences*, **36**(2), 78–87.

163. Stewart, T. A., & Davis, F. M. (2019). An element for development: Calcium signaling in mammalian reproduction and development. Biochimica et biophysica acta. *Molecular cell research*, **1866**(7), 1230–1238.

164. Berridge, M. J., Lipp, P., & Bootman, M. D. (2000). The versatility and universality of calcium signalling. *Nature reviews. Molecular cell biology*, **1**(1), 11–21.

165. Eggermann, E., Bucurenciu, I., Goswami, S. P., & Jonas, P. (2011). Nanodomain coupling between Ca^{2+} channels and sensors of exocytosis at fast mammalian synapses. *Nature reviews. Neuroscience*, **13**(1), 7–21.

166. Mehta, S., & Zhang, J. (2015). Dynamic visualization of calcium-dependent signaling in cellular microdomains. *Cell calcium*, **58**(4), 333–341.

167. Rose, T., Goltstein, P. M., Portugues, R., & Griesbeck, O. (2014). Putting a finishing touch on GECIs. *Frontiers in molecular neuroscience*, 7, 88.

168. Pendin, D., Greotti, E., Lefkimmiatis, K., & Pozzan, T. (2017). Exploring cells with targeted biosensors. *The Journal of general physiology*, **149**(1), 1–36.

169. Rodriguez, E. A., Campbell, R. E., Lin, J. Y., Lin, M. Z., Miyawaki, A., Palmer, A. E., Shu, X., Zhang, J., & Tsien, R. Y. (2017). The Growing and Glowing Toolbox of Fluorescent and Photoactive Proteins. *Trends in biochemical sciences*, **42**(2), 111–129.

170. Nagai, T., Sawano, A., Park, E. S., & Miyawaki, A. (2001). Circularly permuted green fluorescent proteins engineered to sense Ca^{2+}. *Proceedings of the National Academy of Sciences of the United States of America*, **98**(6), 3197–3202.

171. Nakai, J., Ohkura, M., & Imoto, K. (2001). A high signal-to-noise Ca(2+) probe composed of a single green fluorescent protein. *Nature biotechnology*, **19**(2), 137–141.

172. Pérez Koldenkova, V., & Nagai, T. (2013). Genetically encoded Ca(2+) indicators: properties and evaluation. *Biochimica et biophysica acta*, **1833**(7), 1787–1797.

173. Zhao, Y., Araki, S., Wu, J., Teramoto, T., Chang, Y. F., Nakano, M., Abdelfattah, A. S., Fujiwara, M., Ishihara, T., Nagai, T., & Campbell, R. E. (2011). An expanded palette of genetically encoded Ca^{2+} indicators. *Science*, **333**(6051), 1888–1891.

174. Palmer, A. E., & Tsien, R. Y. (2006). Measuring calcium signaling using genetically targetable fluorescent indicators. *Nature protocols*, **1**(3), 1057–1065.

175. Randolph, L. N., Bao, X., Zhou, C., & Lian, X. (2017). An all-in-one, Tet-On 3G inducible PiggyBac system for human pluripotent stem cells and derivatives. *Scientific reports*, **7**(1), 1549.

176. Das, A. T., Tenenbaum, L., & Berkhout, B. (2016). Tet-On Systems For Doxycycline-inducible Gene Expression. *Current gene therapy*, **16**(3), 156–167.

177. Edbauer, D., Kaether, C., Steiner, H., & Haass, C. (2004). Co-expression of nicastrin and presenilin rescues a loss of function mutant of APH-1. *The Journal of biological chemistry*, **279**(36), 37311–37315.

178. Oka, T., Mazack, V., & Sudol, M. (2008). Mst2 and Lats kinases regulate apoptotic function of Yes kinase-associated protein (YAP). *The Journal of biological chemistry*, **283**(41), 27534–27546.

179. Tomecki, R., Drazkowska, K., Kucinski, I., Stodus, K., Szczesny, R. J., Gruchota, J., Owczarek, E. P., Kalisiak, K., & Dziembowski, A. (2014). Multiple myeloma-associated hDIS3 mutations cause perturbations in cellular RNA metabolism and suggest hDIS3 PIN domain as a potential drug target. *Nucleic acids research*, **42**(2), 1270–1290.

180. Dubin, A. E., Murthy, S., Lewis, A. H., Brosse, L., Cahalan, S. M., Grandl, J., Coste, B., & Patapoutian, A. (2017). Endogenous Piezo1 Can Confound Mechanically Activated Channel Identification and Characterization. *Neuron*, **94**(2), 266–270.e3.

181. Sachs F. (2015). Mechanical transduction by ion channels: A cautionary tale. *World journal of neurology*, **5**(3), 74–87.

182. Pezzoli, D., Giupponi, E., Mantovani, D., & Candiani, G. (2017). Size matters for *in vitro* gene delivery: investigating the relationships among complexation protocol, transfection medium, size and sedimentation. *Scientific reports*, 7, 44134.

183. Wang, T., Larcher, L. M., Ma, L., & Veedu, R. N. (2018). Systematic Screening of Commonly Used Commercial Transfection Reagents towards Efficient Transfection of Single-Stranded Oligonucleotides. *Molecules*, **23**(10), 2564.

184. Cormack, B. P., Valdivia, R. H., & Falkow, S. (1996). FACS-optimized mutants of the green fluorescent protein (GFP). *Gene*, **173**(1 Spec No), 33–38.

185. Yang, Y., Liu, N., He, Y., Liu, Y., Ge, L., Zou, L., Song, S., Xiong, W., & Liu, X. (2018). Improved calcium sensor GCaMP-X overcomes the calcium channel perturbations induced by the calmodulin in GCaMP. *Nature communications*, **9**(1), 1504.

186. Parpaite, T., & Coste, B. (2017). Piezo channels. *Current biology*, **27**(7), R250–R252.

187. Riba, A., Di Nanni, N., Mittal, N., Arhné, E., Schmidt, A., & Zavolan, M. (2019). Protein synthesis rates and ribosome occupancies reveal determinants of translation elongation rates. *Proceedings of the National Academy of Sciences of the United States of America*, **116**(30), 15023–15032.

188. Stepanenko, O. V., Stepanenko, O. V., Kuznetsova, I. M., Verkhusha, V. V., & Turoverov, K. K. (2013). Beta-barrel scaffold of fluorescent proteins: folding, stability and role in chromophore formation. *International review of cell and molecular biology*, 302, 221–278.

189. Li, Z. W., & Dalton, W. S. (2006). Tumor microenvironment and drug resistance in hematologic malignancies. *Blood reviews*, **20**(6), 333–342.

190. Chisholm, R. H., Lorenzi, T., & Clairambault, J. (2016). Cell population heterogeneity and evolution towards drug resistance in cancer: Biological and mathematical assessment, theoretical treatment optimisation. *Biochimica et biophysica acta*, **1860**(11 Pt B), 2627–2645.

191. Gillies, R. J., Verduzco, D., & Gatenby, R. A. (2012). Evolutionary dynamics of carcinogenesis and why targeted therapy does not work. *Nature reviews. Cancer*, **12**(7), 487–493.

192. Bolognesi, B., & Lehner, B. (2018). Protein Overexpression: Reaching the limit. *eLife*, 7, e39804.

193. Zhou, Z., Li, J. V., Martinac, B., & Cox, C. D. (2021). Loss-of-Function Piezo1 Mutations Display Altered Stability Driven by Ubiquitination and Proteasomal Degradation. *Frontiers in pharmacology*, 12, 766416.

194. Maltsev, V. A., Kyle, J. W., Mishra, S., & Undrovinas, A. (2008). Molecular identity of the late sodium current in adult dog cardiomyocytes identified by Nav1.5 antisense inhibition. *American journal of physiology. Heart and circulatory physiology*, **295**(2), H667–H676.

195. Cohen, L. D., Zuchman, R., Sorokina, O., Müller, A., Dieterich, D. C., Armstrong, J. D., Ziv, T., & Ziv, N. E. (2013). Metabolic turnover of synaptic proteins: kinetics, interdependencies and implications for synaptic maintenance. *PloS one*, **8**(5), e63191.

196. Mathieson, T., Franken, H., Kosinski, J., Kurzawa, N., Zinn, N., Sweetman, G., Poeckel, D., Ratnu, V. S., Schramm, M., Becher, I., Steidel, M., Noh, K. M., Bergamini, G., Beck, M., Bantscheff, M., & Savitski, M. M. (2018). Systematic analysis of protein turnover in primary cells. *Nature communications*, **9**(1), 689.

197. Dörrbaum, A. R., Kochen, L., Langer, J. D., & Schuman, E. M. (2018). Local and global influences on protein turnover in neurons and glia. *eLife*, 7, e34202.

198. Mahmood, T., & Yang, P. C. (2012). Western blot: technique, theory, and trouble shooting. *North American journal of medical sciences*, **4**(9), 429–434.

199. Schindelin, J., Arganda-Carreras, I., Frise, E., Kaynig, V., Longair, M., Pietzsch, T., Preibisch, S., Rueden, C., Saalfeld, S., Schmid, B., Tinevez, J. Y., White, D. J., Hartenstein, V., Eliceiri, K., Tomancak, P., & Cardona, A. (2012). Fiji: an open-source platform for biological-image analysis. *Nature methods*, **9**(7), 676–682.

200. Pathania, M., De Jay, N., Maestro, N., Harutyunyan, A. S., Nitarska, J., Pahlavan, P., Henderson, S., Mikael, L. G., Richard-Londt, A., Zhang, Y., Costa, J. R., Hébert, S., Khazaei, S., Ibrahim, N. S., Herrero, J., Riccio, A., Albrecht, S., Ketteler, R., Brandner, S., Kleinman, C. L., … Salomoni, P. (2017). H3.3K27M Cooperates with Trp53 Loss and PDGFRA Gain in Mouse Embryonic Neural Progenitor Cells to Induce Invasive High-Grade Gliomas. *Cancer cell*, **32**(5), 684–700.e9.

201. Georg, M., Fernández-Cabada, T., Bourguignon, N., Karp, P., Peñaherrera, A. B., Helguera, G., Lerner, B., Pérez, M. S., & Mertelsmann, R. (2018). Development of image analysis software for quantification of viable cells in microchips. *PloS one*, **13**(3), e0193605.

202. Lin, Y. C., Boone, M., Meuris, L., Lemmens, I., Van Roy, N., Soete, A., Reumers, J., Moisse, M., Plaisance, S., Drmanac, R., Chen, J., Speleman, F., Lambrechts, D., Van de Peer, Y., Tavernier, J., & Callewaert, N. (2014). Genome dynamics of the human embryonic kidney 293 lineage in response to cell biology manipulations. *Nature communications*, 5, 4767.

203. Stathopoulos, N. A., & Hellums, J. D. (1985). Shear stress effects on human embryonic kidney cells *in Vitro*. *Biotechnology and bioengineering*, **27**(7), 1021–1026.

204. Zhou J. (2009). Polycystins and primary cilia: primers for cell cycle progression. *Annual review of physiology*, 71, 83–113.

205. Maggiorani, D., Dissard, R., Belloy, M., Saulnier-Blache, J. S., Casemayou, A., Ducasse, L., Grès, S., Bellière, J., Caubet, C., Bascands, J. L., Schanstra, J. P., & Buffin-Meyer, B. (2015). Shear Stress-Induced Alteration of Epithelial Organization in Human Renal Tubular Cells. *PloS one*, **10**(7), e0131416.

206. Concilia, G., Lai, A., Thurgood, P., Pirogova, E., Baratchi, S., & Khoshmanesh, K. (2022). Investigating the mechanotransduction of transient shear stress mediated by Piezo1 ion channel using a 3D printed dynamic gravity pump. *Lab on a chip*, **22**(2), 262–271.

207. Wagner, T., Kroll, A., Haramagatti, C. R., Lipinski, H. G., & Wiemann, M. (2017). Classification and Segmentation of Nanoparticle Diffusion Trajectories in Cellular Micro Environments. *PloS one*, **12**(1), e0170165.

208. Frattolin, J., Watson, D. J., Bonneuil, W. V., Russell, M. J., Fasanella Masci, F., Bandara, M., Brook, B. S., Nibbs, R. J. B., & Moore, J. E., Jr (2021). The Critical Importance of Spatial and Temporal Scales in Designing and Interpreting Immune Cell Migration Assays. *Cells*, **10**(12), 3439.

209. Goedhart J. (2020). PlotTwist: A web app for plotting and annotating continuous data. *PLoS biology*, **18**(1), e3000581.

210. Jetta, D., Gottlieb, P. A., Verma, D., Sachs, F., & Hua, S. Z. (2019). Shear stress-induced nuclear shrinkage through activation of Piezo1 channels in epithelial cells. *Journal of cell science*, **132**(11), jcs226076.

211. Nava, M. M., Miroshnikova, Y. A., Biggs, L. C., Whitefield, D. B., Metge, F., Boucas, J., Vihinen, H., Jokitalo, E., Li, X., García Arcos, J. M., Hoffmann, B., Merkel, R., Niessen, C. M., Dahl, K. N., & Wickström, S. A. (2020). Heterochromatin-Driven Nuclear Softening Protects the Genome against Mechanical Stress-Induced Damage. *Cell*, **181**(4), 800–817.e22.

212. Zamir, A., Li, G., Chase, K., Moskovitch, R., Sun, B., & Zaritsky, A. (2022). Emergence of synchronized multicellular mechanosensing from spatiotemporal integration of heterogeneous single-cell information transfer. *Cell systems*, **13**(9), 711–723.e7.

213. Weigel, A. V., Simon, B., Tamkun, M. M., & Krapf, D. (2011). Ergodic and nonergodic processes coexist in the plasma membrane as observed by single-molecule tracking. *Proceedings of the National Academy of Sciences of the United States of America*, **108**(16), 6438–6443.

214. Woringer, M., Izeddin, I., Favard, C., & Berry H. (2020). Anomalous Subdiffusion in Living Cells: Bridging the Gap Between Experiments and Realistic Models Through Collaborative Challenges. *Frontiers in Physics*, 8, 134.

215. Tinevez, J. Y., Perry, N., Schindelin, J., Hoopes, G. M., Reynolds, G. D., Laplantine, E., Bednarek, S. Y., Shorte, S. L., & Eliceiri, K. W. (2017). TrackMate: An open and extensible platform for single-particle tracking. *Methods*, 115, 80–90.

216. Tarantino, N., Tinevez, J. Y., Crowell, E. F., Boisson, B., Henriques, R., Mhlanga, M., Agou, F., Israël, A., & Laplantine, E. (2014). TNF and IL-1 exhibit distinct ubiquitin requirements for inducing NEMO-IKK supramolecular structures. *The Journal of cell biology*, **204**(2), 231–245.

217. Sun, B., Duclos, G., & Stone, H. A. (2013). Network characteristics of collective chemosensing. *Physical review letters*, **110**(15), 158103.

218. Vavouri, T., Semple, J. I., Garcia-Verdugo, R., & Lehner, B. (2009). Intrinsic protein disorder and interaction promiscuity are widely associated with dosage sensitivity. *Cell*, **138**(1), 198–208.

219. Birchler, J. A., & Veitia, R. A. (2012). Gene balance hypothesis: connecting issues of dosage sensitivity across biological disciplines. *Proceedings of the National Academy of Sciences of the United States of America*, **109**(37), 14746–14753.

220. Tang, Y. C., & Amon, A. (2013). Gene copy-number alterations: a cost-benefit analysis. *Cell*, **152**(3), 394–405.

221. Bolognesi, B., Lorenzo Gotor, N., Dhar, R., Cirillo, D., Baldrighi, M., Tartaglia, G. G., & Lehner, B. (2016). A Concentration-Dependent Liquid Phase Separation Can Cause Toxicity upon Increased Protein Expression. *Cell reports*, **16**(1), 222–231.

222. Stoebel, D. M., Dean, A. M., & Dykhuizen, D. E. (2008). The cost of expression of Escherichia coli lac operon proteins is in the process, not in the products. *Genetics*, **178**(3), 1653–1660.

223. Eguchi, Y., Makanae, K., Hasunuma, T., Ishibashi, Y., Kito, K., & Moriya, H. (2018). Estimating the protein burden limit of yeast cells by measuring the expression limits of glycolytic proteins. *eLife*, 7, e34595.

224. Rice, A. M., & McLysaght, A. (2017). Dosage-sensitive genes in evolution and disease. *BMC biology*, **15**(1), 78.

225. Gresch, O., & Altrogge, L. (2012). Transfection of difficult-to-transfect primary mammalian cells. *Methods in molecular biology*, 801, 65–74.

226. Kavsan, V. M., Iershov, A. V., & Balynska, O. V. (2011). Immortalized cells and one oncogene in malignant transformation: old insights on new explanation. *BMC cell biology*, 12, 23.

227. Rio, D. C., Clark, S. G., & Tjian, R. (1985). A mammalian host-vector system that regulates expression and amplification of transfected genes by temperature induction. *Science* (New York, N.Y.), **227**(4682), 23–28.

228. Roux, E., Bougaran, P., Dufourcq, P., & Couffinhal, T. (2020). Fluid Shear Stress Sensing by the Endothelial Layer. *Frontiers in physiology*, 11, 861.

229. Jackson, M. L., Bond, A. R., & George, S. J. (2023). Mechanobiology of the endothelium in vascular health and disease: *in vitro* shear stress models. *Cardiovascular drugs and therapy*, **37**(5), 997–1010.

230. Surre, J., Saint-Ruf, C., Collin, V., Orenga, S., Ramjeet, M., & Matic, I. (2018). Strong increase in the autofluorescence of cells signals struggle for survival. *Scientific reports*, **8**(1), 12088.

231. Bertolo, A., Baur, M., Guerrero, J., Pötzel, T., & Stoyanov, J. (2019). Autofluorescence is a Reliable *in vitro* Marker of Cellular Senescence in Human Mesenchymal Stromal Cells. *Scientific reports*, **9**(1), 2074.

232. Deliolanis, N. C., Kasmieh, R., Wurdinger, T., Tannous, B. A., Shah, K., & Ntziachristos, V. (2008). Performance of the red-shifted fluorescent proteins in deep-tissue molecular imaging applications. *Journal of biomedical optics*, **13**(4), 044008.

233. Molina, R. S., Qian, Y., Wu, J., Shen, Y., Campbell, R. E., Drobizhev, M., & Hughes, T. E. (2019). Understanding the Fluorescence Change in Red Genetically Encoded Calcium Ion Indicators. *Biophysical journal*, **116**(10), 1873–1886.

234. Akerboom, J., Carreras Calderón, N., Tian, L., Wabnig, S., Prigge, M., Tolö, J., Gordus, A., Orger, M. B., Severi, K. E., Macklin, J. J., Patel, R., Pulver, S. R., Wardill, T. J., Fischer, E., Schüler, C., Chen, T. W., Sarkisyan, K. S., Marvin, J. S., Bargmann, C. I., Kim, D. S., … Looger, L. L. (2013). Genetically encoded calcium indicators for multi-color neural activity imaging and combination with optogenetics. *Frontiers in molecular neuroscience*, 6, 2.

235. Wu, J., Liu, L., Matsuda, T., Zhao, Y., Rebane, A., Drobizhev, M., Chang, Y. F., Araki, S., Arai, Y., March, K., Hughes, T. E., Sagou, K., Miyata, T., Nagai, T., Li, W. H., & Campbell, R. E. (2013). Improved orange and red Ca^2± indicators and photophysical considerations for optogenetic applications. *ACS chemical neuroscience*, **4**(6), 963–972.

236. Dana, H., Mohar, B., Sun, Y., Narayan, S., Gordus, A., Hasseman, J. P., Tsegaye, G., Holt, G. T., Hu, A., Walpita, D., Patel, R., Macklin, J. J., Bargmann, C. I., Ahrens, M. B., Schreiter, E. R., Jayaraman, V., Looger, L. L., Svoboda, K., & Kim, D. S. (2016). Sensitive red protein calcium indicators for imaging neural activity. *eLife*, 5, e12727.

237. Shen, Y., Dana, H., Abdelfattah, A. S., Patel, R., Shea, J., Molina, R. S., Rawal, B., Rancic, V., Chang, Y. F., Wu, L., Chen, Y., Qian, Y., Wiens, M. D., Hambleton, N., Ballanyi, K., Hughes, T. E., Drobizhev, M., Kim, D. S., Koyama, M., Schreiter, E. R., … Campbell, R. E. (2018). A genetically encoded Ca^{2+} indicator based on circularly permutated sea anemone red fluorescent protein eqFP578. *BMC biology*, **16**(1), 9.

238. Moroni, M., Servin-Vences, M. R., Fleischer, R., Sánchez-Carranza, O., & Lewin, G. R. (2018). Voltage gating of mechanosensitive PIEZO channels. *Nature communications*, **9**(1), 1096.

Appendix

Appendix A1.

Sequencing Primer 1	GAGGTCTATATAAGCAGAGCTGG
Sequencing Primer 2	CTACCTGCTGCTCTTCCTGG
Sequencing Primer 3	CTGTATGGGATGACGCTGTG
Sequencing Primer 4	CTCACAGGCAGGATGCAGTG
Sequencing Primer 5	CAGCTGGACCAGGATCTGC
Sequencing Primer 6	CGTCACCGTCATCATCTCCAA
Sequencing Primer 7	GAACAGGCAGGACAGCTACC
Sequencing Primer 8	ATCCCGAGGCCCAGCAA
Sequencing Primer 9	ATCATCATTTTTGGCTTCTGGGC
Sequencing Primer 10	CTGTTCACCATGAGCGCC
Sequencing Primer 11	GACCGCATCCTCAAGCTCT
Sequencing Primer 12	GGCAAGCTGACCCTGAAGTT
Sequencing Primer 13	CCGCCATGCATTAGTTAATCACCTCGAGTTTACTCCCTA
Sequencing Primer 14	GTCCGGTAGCGCTAGCGGGTACCTTTACGAGGGTAGGAA

Table A1. Primer sequence for XLGenEPi sequencing. A total of 14 primers were generated using the NCBI Primer-BLAST designing tool to screen for both the quality and the integrity of the XLGenEPi generated from the molecular cloning.

Appendix A2.

Target XLGenEPi Element	Primers Sequence (5'-3')	Annealing temperature (T_a)	Product size (bp)
GCaMP-G4	GACTCGTGAGAAGGAGACCG	54 ℃	1414
	GAGCTCTAGGGCCGCTTTTT		
TRE3G	CCCAACTTCTCGGGGACTGT	55 ℃	472
	GTGCGGCTCCATGCGATAA		
Tet-On	AATCGTCAAGAGCGTCAGCA	55 ℃	614
	TGAGCAGCCTACCCTGTACT		
Blasticidin-resistance gene	CAGAGGGCAGCAATTCACGA	55 ℃	153
	TCGTCGCGATCGGAAATGAG		

Table A2. Primer pair sequence for four key elements of XLGenEPi construct. A total of 4 primer pairs were generated using the NCBI Primer-BLAST designing tool to screen for the presence of the four main elements in the XLGenEPi, namely (1) GCaMP-G4 sequence, (2) TRE-promoter sequence, (3) Tet-On gene sequence, and (4) blasticidin-resistance gene sequence.

Appendix A3.

CMV FW Primer	CCCCGAAAAGTGCCACCTGGTTAATAGTAATCAATTACGGGG
CMV RV Primer	ATTCACCGGGGATCCTGGCGGATCTGACGGTTCACTAAAC

Table A3. Primer sequence for the PCR cloning of CMV-pBase constuct. The forward (FW) and reverse (RV) primers used to clone the CMV-promoter site into the pBase construct backbone, as described in Chapter 2, **Section 2.3.3**.